

Advances in Optical Technologies

Biophotonics

Guest Editors: Stoyan Tanev, Brian C. Wilson,
Valery V. Tuchin, and Dennis Matthews





Biophotonics

Advances in Optical Technologies

Biophotonics

Guest Editors: Stoyan Tanev, Brian C. Wilson,
Valery V. Tuchin, and Dennis Matthews



Copyright © 2008 Hindawi Publishing Corporation. All rights reserved.

This is a special issue published in volume 2008 of “Advances in Optical Technologies.” All articles are open access articles distributed under the Creative Commons Attribution License, which permits unrestricted use, distribution, and reproduction in any medium, provided the original work is properly cited.

Editor-in-Chief

H. John Caulfield, Fisk University and Alabama A&M University Research Institute, USA

Associate Editors

Mustafa A. G. Abushagur, USA

Partha P. Banerjee, USA

Ralph Barry Johnson, USA

Steve Blair, USA

Maria Luisa Calvo, Spain

Pierre Chavel, France

Michael A. Fiddy, USA

Patti Gillespie, USA

Richard B. Hoover, USA

Saulius Juodkazis, Japan

Mark A. Kahan, USA

Liren Liu, China

Mikhail Noginov, USA

Mikhail P. Petrov, Russia

Joseph Rosen, Israel

Colin J. R. Sheppard, Singapore

Theo Tschudi, Germany

Leonid P. Yaroslavsky, Israel

Contents

Biophotonics, Stoyan Tanev, Brian C. Wilson, Valery V. Tuchin, and Dennis Matthews
Volume 2008, Article ID 134215, 2 pages

A Ratiometric Fluorescence Imaging System for Surgical Guidance, Eduardo H. Moriyama, Anthony Kim, Arjen Bogaards, Lothar Lilge, and Brian C. Wilson
Volume 2008, Article ID 532368, 10 pages

5-ALA Mediated Fluorescence Detection of Gastrointestinal Tumors, Ekaterina Borisova, Borislav Vladimirov, and Latchezar Avramov
Volume 2008, Article ID 862081, 7 pages

The Impact of Autonomic Dysreflexia on Blood Flow and Skin Response in Individuals with Spinal Cord Injury, J. C. Ramella-Roman and J. M. Hidler
Volume 2008, Article ID 797214, 7 pages

Optical Clearing of Cranial Bone, Elina A. Genina, Alexey N. Bashkatov, and Valery V. Tuchin
Volume 2008, Article ID 267867, 8 pages

Optical Biomedical Diagnostics: Sensors with Optical Response Based on Two-Photon Excited Luminescent Dyes for Biomolecules Detection, V. M. Yashchuk, S. M. Yarmoluk, V. Yu. Kudrya, M. Yu. Losytskyy, V. P. Tokar, V. M. Kravchenko, V. B. Kovalska, A. O. Balanda, and D. V. Kryvorotenko
Volume 2008, Article ID 908246, 11 pages

Sensitive Label-Free Biomolecular Detection Using Thin Silicon Waveguides, A. Densmore, D.-X. Xu, S. Janz, P. Waldron, J. Lapointe, T. Mischki, G. Lopinski, A. Del age, J. H. Schmid, and P. Cheben
Volume 2008, Article ID 725967, 9 pages

Nanotomography of Cell Surfaces with Evanescent Fields, Michael Wagner, Petra Weber, Wolfgang S. L. Strauss, Henri-Pierre Lassalle, and Herbert Schneckeburger
Volume 2008, Article ID 254317, 7 pages

A Proposed Method for Thermal Specific Bioimaging and Therapy Technique for Diagnosis and Treatment of Malignant Tumors by Using Magnetic Nanoparticles, Iddo M. Gescheit, Moshe Ben-David, and Israel Gannot
Volume 2008, Article ID 275080, 7 pages

Ultrashort Laser Pulse Heating of Nanoparticles: Comparison of Theoretical Approaches, Renat R. Letfullin, Thomas F. George, Galen C. Duree, and Brett M. Bollinger
Volume 2008, Article ID 251718, 8 pages

A New 3D Simulation Method for the Construction of Optical Phase Contrast Images of Gold Nanoparticle Clusters in Biological Cells, Stoyan Tanev, James Pond, Paul Paddon, and Valery V. Tuchin
Volume 2008, Article ID 727418, 9 pages

Editorial

Biophotonics

Stoyan Tanev,¹ Brian C. Wilson,² Valery V. Tuchin,³ and Dennis Matthews⁴

¹ *Department of Systems and Computer Engineering, Faculty of Engineering and Design, Carleton University, Ottawa, ON, Canada K1S 5B6*

² *Division of Biophysics and Bioimaging, Ontario Cancer Institute, University Health Network and University of Toronto, Toronto, ON, Canada M5G 2M9*

³ *Research-Educational Institute of Optics and Biophotonics, Saratov State University, 410012 Saratov, Russia*

⁴ *Center for Biophotonics Science and Technology and Lawrence Livermore National Laboratory, University of California Davis, CA 95817, USA*

Correspondence should be addressed to Stoyan Tanev, tanev@sce.carleton.ca

Received 19 November 2008; Accepted 19 November 2008

Copyright © 2008 Stoyan Tanev et al. This is an open access article distributed under the Creative Commons Attribution License, which permits unrestricted use, distribution, and reproduction in any medium, provided the original work is properly cited.

The application of innovative optical technologies in medicine, biology, agriculture, environmental sciences, and public health has emerged as one of the new paradigms in today's knowledge economy. This convergence between optical and biosciences is due to the recent significant advances of photonics and biotechnologies driven by the various health, environment, and defense challenges faced by humanity at the beginning of 21st century.

Biophotonics technologies can impact biomedical research and human health, since they can yield the critical information bridging molecular structure and physiological function, which is the most important process in understanding, treating, and preventing a disease, as well as in pathology in general. As increasingly aging world population represents new health problems, biophotonics offer great hope for the early detection of diseases and for new technologies for light-guided and light-activated therapies. These technologies continue to advance at a spectacular rate, contributing to the growth of novel platforms that affect medical healthcare in virtually all medical specialties.

Advances in photonics have contributed dramatically to the biological revolution that is being currently witnessed. Very few biological science disciplines have not been touched by photonics, since optical methods play a critical role in biotechnologies, ranging from genomics to cell-based assays, providing new knowledge on individual life forms and their related biochemistry, on how living things interact with each other, and on how new and emerging optical technologies could be used to measure, quantify, and understand their

biological properties. Biology has also advanced photonics, since biomaterials have shown a great promise as new photonic media for technological applications. The collective effects of this revolution have already influenced the quality of human life and behavior in a way that was never imagined before.

Along with the positive aspects of this revolution, there come some potential negative aspects. They include, to name a few, an increased potential for human plagues caused by the increased rates of human contact and resistance to antibiotics, agricultural plagues exacerbated by extensive use of single-genetic-strain crops and livestock, and purposely induced plagues of human or agricultural pathogens: bio- and agroterrorism. Significant international medical, agricultural, and environmental science research activities are directed to the development of pathogen detection and identification systems that are lower in cost, more biochemically specific, more accurate, faster, smaller, less demanding of infrastructure, and more accessible to a larger number of people. The role of biophotonics in these research and development efforts is significant.

The aim of this special issue is to provide a snapshot of recent progress in biophotonics and point out the emerging future developments in this broad and rapidly evolving field. The guest editors have previously cooperated in running a similar project (*Advances in Biophotonics*, B. C. Wilson, V. V. Tuchin and S. Tanev, Eds., NATO Science Series I: Life and Behavioural Sciences, vol. 369, IOS Press, Amsterdam, 2005), and are firmly convinced in the value of such initiatives. Although the objectives of this special issue and of our

previous publication are practically the same, there are a number of qualitative points of difference that are largely due to the way biophotonics research and development (R&D) has progressed in the last four years. Biophotonics R&D in 2009 could be characterized by a greater focus on (i) nano-biophotonics and, specifically, nanoplasmonics, (ii) a higher degree of applicability of biosensing techniques, and (iii) a stronger link to the clinical realm.

These three trends are clearly visible in the articles published in this issue. All the articles are invited reviews or invited research papers by leading biophotonics researchers and research groups from universities, as well as industry and government laboratories, and they can be structured in three major themes: (i) biophotonics instrumentation and experimental techniques, (ii) biophotonic sensors, and (iii) nano-biophotonics:

(I) Biophotonics instrumentation and experimental techniques

“A ratiometric fluorescence imaging system for surgical guidance” by E. Moriyama et al.; “5-ALA mediated fluorescence detection of gastrointestinal tumors” by E. Borisova et al.; “The impact of autonomic dysreflexia on blood flow and skin response in individuals with spinal cord injury” by J. C. Ramella-Roman et al.; and “Optical clearing of cranial bone” by E. Genina et al.

(II) Biophotonics sensors

“Optical biomedical diagnostics: sensors with optical response based on two-photon excited luminescent dyes for biomolecule detection” by V. Yashchuk et al. and “Sensitive label-free biomolecular detection using thin silicon waveguides” by Adam Densmore et al.

(III) Nano-biophotonics

“Nanotomography of cell surfaces with evanescent fields” by M. Wagner et al.; “A proposed method for thermal specific bioimaging and therapy technique for diagnostic and treatment of malignant tumors by using magnetic nanoparticles” by I. M. Gescheit et al.; “Ultra-short laser pulse heating of nanoparticles: Comparison of theoretical approaches” by Renat Letfullin et al.; and “A new 3D simulation method for the construction of optical phase contrast images of gold nanoparticle clusters in biological cells” by S. Tanev et al.

The authors are grateful to all contributors for their constructive cooperation in providing informative overviews of their respective topics and new insights into ongoing and potential developments. They have greatly enjoyed the design and preparation of this special issue and strongly believe that it will be valuable to those working in this multidisciplinary field by helping its advances in new and inspiring directions.

*Stoyan Tanev
Brian C. Wilson
Valery V. Tuchin
Dennis Matthews*

Research Article

A Ratiometric Fluorescence Imaging System for Surgical Guidance

Eduardo H. Moriyama,^{1,2} Anthony Kim,¹ Arjen Bogaards,¹ Lothar Lilge,¹ and Brian C. Wilson¹

¹ Division of Biophysics and Bioimaging, Ontario Cancer Institute, University Health Network, 610 University Avenue 7-420, Toronto, ON, Canada M5G 2M9

² Department of Physics, Ryerson University, 350 Victoria Street, Toronto, ON, Canada M5B 2K3

Correspondence should be addressed to Brian C. Wilson, wilson@uhnres.utoronto.ca

Received 3 March 2008; Accepted 28 June 2008

Recommended by Stoyan Tanev

A 3-chip CCD imaging system has been developed for quantitative *in vivo* fluorescence imaging. This incorporates a ratiometric algorithm to correct for the effects of tissue optical absorption and scattering, imaging “geometry” and tissue autofluorescence background. The performance was characterized, and the algorithm was validated in tissue-simulating optical phantoms for quantitative measurement of the fluorescent molecule protoporphyrin IX (PpIX). The technical feasibility to use this system for fluorescence-guided surgical resection of malignant brain tumor tissue was assessed in an animal model in which PpIX was induced exogenously in the tumor cells by systemic administration of aminolevulinic acid (ALA).

Copyright © 2008 Eduardo H. Moriyama et al. This is an open access article distributed under the Creative Commons Attribution License, which permits unrestricted use, distribution, and reproduction in any medium, provided the original work is properly cited.

1. INTRODUCTION

Intracranial brain tumors are the most common and aggressive primary tumors in the central nervous system (CNS) and carry one of the worst prognosis of all types of cancers. Advances in surgery, radiotherapy, and chemotherapy have resulted in only modest improvement in patient survival [1]. Radical surgical resection is considered the standard procedure for treatment of high-grade gliomas, and maximizing the degree of tumor resection has been related to improvement of patient survival [2, 3]. However, due to the infiltrative nature of most of the gliomas, complete resection is difficult to achieve, resulting in high risk of tumor recurrence [2]. Hence, more sensitive and specific techniques are needed to aid in the identification of malignant tissue intraoperatively and, thereby, to increase the completeness of tumor resection without damaging adjacent critical normal brain structures and function [4]. Such techniques include magnetic resonance imaging (MRI) [5, 6], ultrasound [7], and optical technologies [8–10].

Fluorescence imaging is particularly promising to identify malignant tissues *in vivo*, exploiting either intrinsic fluorescence characteristics (autofluorescence) [11–13] or the preferential accumulation or targeting of administered

(exogenous) fluorophores [14–16]. Fluorescent agents such as fluorescein [17] and porphyrins [8, 18, 19] are suitable agents for detection of neoplastic cells during intraoperative tumor removal, on account of their preferential accumulation and/or retention in malignant tissues. Recently, the main effort has been on fluorescence-guided resection (FGR) of brain tumors using protoporphyrin IX (PpIX), which is preferentially synthesized in brain tumor cells relative to normal brain following administration of aminolevulinic acid (ALA). This approach has demonstrated more complete resection of brain tumors compared to surgery under white light alone, in both preclinical animal models [20, 21] and in patients [18, 22]. However, making FGR using exogenous fluorophores, including ALA-PpIX, a quantitative and hence, objective and reproducible technique is challenging, due to the effects of multiple scattering and absorption of the excitation and emission light and the background of tissue autofluorescence. To date, only semiquantitative information on the concentration and distribution of fluorescent probes *in vivo* [23–25] has been possible.

Several approaches have been investigated for quantitative fluorescence measurements *in vivo*, including tomographic imaging [26, 27], fluorescence lifetime imaging [28], fiberoptic point fluorescence spectroscopies [29, 30], and

ratiometric correction methods [31–33]. Here, we will focus on the last of these, in which the objective is to make multiple spectral measurements that are then combined through an empirical or biophysical model to correct for the tissue attenuation and/or autofluorescence effects. As we will demonstrate, the advantage is that this can be implemented in real-time imaging mode, which is clinically desirable. In the simplest approach, correction is performed using single excitation and emission wavelengths [34, 35], but this does not correct for tissue autofluorescence [36]. As we recently showed in a modeling study [37], the use of multiple excitation and/or emission wavelengths can virtually eliminate the tissue autofluorescence and also enable quantitative measurements of fluorophores [36–40], such that the fluorescent signal depends only on the concentration of the fluorophore. This has been validated in phantoms for a wide range of fluorophore concentrations (in the case of PpIX, e.g., to $<0.1 \mu\text{g mL}^{-1}$) and tissue optical properties [41].

Here, we present a prototype FGR instrument that provides video-rate digital fluorescence imaging incorporating a double-ratiometric correction method that is optimized for intraoperative identification of brain tumors. Validation studies in phantoms are presented to demonstrate the performance of the system, and preliminary experiments are presented in resection of intracranial brain tumor in a rat model *in vivo* to illustrate its practicality and functionality.

2. MATERIALS AND METHODS

2.1. System description

The fluorescence imaging system was designed primarily for surgical guidance and is shown in Figure 1. The light source comprises a 300 W xenon lamp (Cermax, Perkin Elmer, CA, USA) focused through a filter wheel into a 5 mm diameter liquid light guide (Model 495 FR, Karl Storz, Tuttlingen, Germany) that is coupled into a 10 mm diameter rigid clinical laparoscope (Model 871 1AA, Karl Storz, Tuttlingen Germany). The collection component of the imaging system is based on a 3-CCD compact camera (DXC-C33, Sony, ON, Canada) operating at 30 frames s^{-1} (NTSC) with 796×494 pixels and 8-bit dynamic range. A long-pass 500 nm filter (Custom made, Chroma Technologies, VT, USA) is placed between the camera and the laparoscope. This filter deliberately leaks a small fraction ($\sim 10^{-4}$) of the UV/blue excitation light to allow measurement of the diffuse reflectance signal from the tissue for the ratiometric algorithm described below. Spectral response curves for the red, green, and blue channels of the CCD were measured using a standard color target (ColorChecker Chart: Gretag Macbeth, Grand Rapids, MI, USA) illuminated by a tungsten-halogen light source (LS-1: Ocean Optics, Dunedin, FL, USA). For this, the images of the color target were taken through the laparoscope without the fluorescence emission filter installed. Serial filters spanning from 420 to 750 nm were placed in front of the laparoscope lens for each of the color target images. The spectral response of the camera-laparoscope optical chain

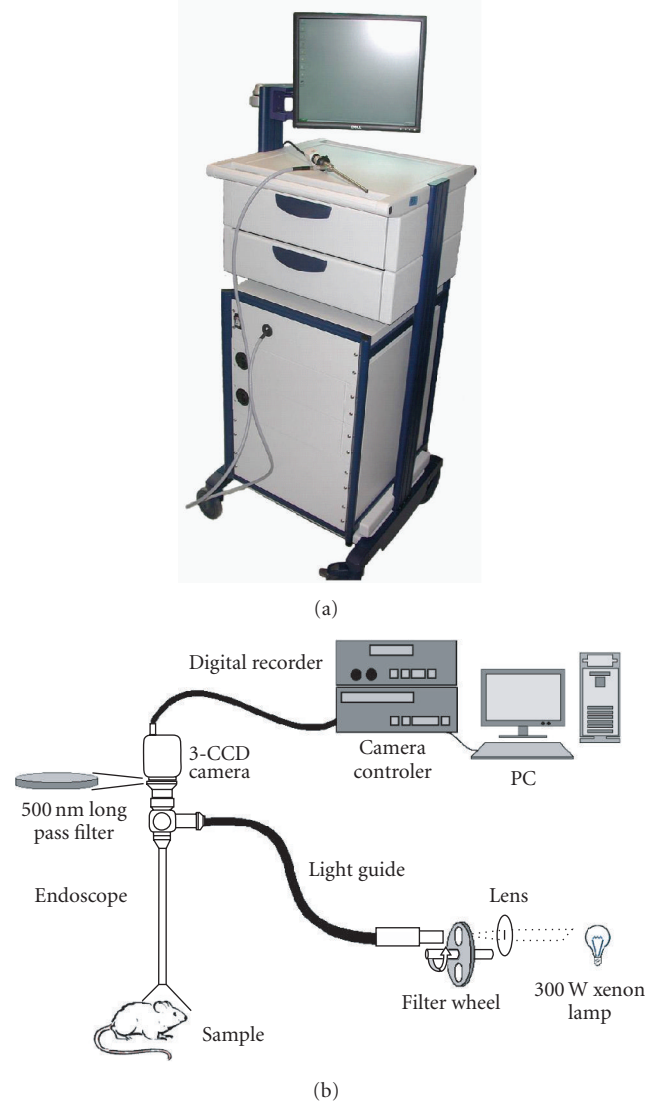


FIGURE 1: (a) Photograph and (b) schematic of the system.

was determined and averaged from 4 spectrally-neutral shades.

The fluorescence imaging system features a dual-excitation capability. The filter wheel holds two different excitation filters, and its rotation rate is such that consecutive camera frames are excited by alternating excitation wavelengths. For the present study, the excitation filters had central wavelengths, $\lambda_{\text{ex}1}$, at the PpIX Soret maxima of 405 nm (full width at half maximum, FWHM = 96 nm) and at 440 nm (FWHM = 60 nm). The latter was chosen as the shortest wavelength lying above the main PpIX Soret band in order to allow for correction for the tissue autofluorescence. It is assumed then that the tissue optical properties are comparable at these two wavelengths, since they are not too far apart. Both wavelengths can induce high levels of autofluorescence in tumor and normal tissues. The delivered power at each wavelength was approximately 50 mW cm^{-2} at a typical working distance of 2 cm from

TABLE 1: Optical properties of the liquid phantoms at 635 nm.

	Reduced scattering coefficient μ_s' (cm^{-1})	Absorption coefficient μ_a (cm^{-1})
Phantom A	7	1.6
Phantom B	7	3.2
Phantom C	14	1.6
Phantom D	14	3.2

the tissue surface. The digital video output is captured by a laptop computer and can be displayed for visualization of the processed fluorescence images in real time. The image processing software (Hytek Automation, Waterloo, ON, Canada) was based on LabVIEW (National Instruments Corp., Austin, TX, USA) and could execute multiplication, division, addition, or subtraction on each channel.

2.2. System characterization

The spatial resolution of the imaging system was determined using a standard 1951 USAF glass slide resolution target (Edmund Optics, NJ, USA) placed 2 cm from the front end of the laparoscope, resulting in a field of view of 12.7×8.2 mm. To characterize the system performance for fluorescence imaging, tissue-simulating liquid phantoms were prepared, comprising PpIX (Sigma-Aldrich, ON, Canada) dissolved in 1 mM dimethyl sulfoxide (DMSO) with methylene blue dye added as the optical absorber and the lipoprotein emulsion Intralipid (Fresenius Kabi, Uppsala, Sweden) to provide optical scattering [42]. The corresponding absorption and reduced scattering coefficients are given in Table 1, based on well-established literature values. The system sensitivity was measured using varying PpIX concentrations: 2.5, 1.25, 0.62, 0.31, 0.15, 0.075, and $0.039 \mu\text{g mL}^{-1}$. At each concentration, fluorescence images were taken at both excitation wavelengths at distances of 2, 3, 4, or 5 cm from the phantom surface, with the camera focused at the 2 cm working distance. The signal in the red channel of the 3-CCD was plotted as a function of PpIX concentration. The fluorescence signal was collected at 0° , 15° , or 30° from the vertical axis to determine the influence of the imaging geometry.

The ratiometric method applied here was developed by our group previously and is based on using 2 excitation and 2 emission wavelengths [41]. The first excitation wavelength is in the absorption peak of PpIX ($\lambda_{\text{ex1}} = 405$ nm) and, for each image pixel, the emitted red fluorescence (560–750 nm) is divided by the signal from the diffusely reflected excitation light. Next, this fluorescence/reflectance ratio is divided by the same ratio calculated using the second-excitation wavelength ($\lambda_{\text{ex2}} = 440$ nm). Thus, the signal, Q , in each pixel is given by

$$Q = \frac{F(\lambda_{\text{ex1}}, \lambda_{\text{em1}})}{R(\lambda_{\text{ex1}})} \times \frac{R(\lambda_{\text{ex2}})}{F(\lambda_{\text{ex2}}, \lambda_{\text{em1}})}. \quad (1)$$

2.3. In vivo tests

To test the feasibility and functionality of this imaging system and the double-ratio algorithm *in vivo*, PpIX fluorescence and diffuse reflectance images were acquired in an established rat brain tumor model [39] undergoing fluorescence-guided tumor resection. The rat glioma tumor model, CNS-1, was chosen as being highly infiltrative, a common characteristic of high-grade human gliomas that should present a valid test of the ability to detect residual tumor at the surgical margins. FGR was performed at 21 days following implantation of luciferase-transfected CNS-1^{luc} cells (3×10^5 cells, 2 mm below the dura, $n = 2$ per ALA dose) in the left brain hemisphere of Lewis rats (Charles River, MA, USA). PpIX was induced by administering aminolevulinic acid (ALA) in hydrochloride form (Sigma, Oakville, ON, Canada). This was dissolved in phosphate-buffered saline (20 mg mL^{-1}) with the pH adjusted to ~ 5.5 by 1N NaOH and then injected intraperitoneally (i.p.) at 20, 50, or 100 mg kg^{-1} at 2–4 hours before the surgical procedure/imaging. The animals were subdued by an i.p. mixture of ketamine and xylazine (80 and 13 mg kg^{-1} , resp.). A 2 cm incision was made in the scalp along the midline and held open by a retractor. A 1 cm craniotomy was performed using a burr drill, and the dura was carefully removed. To measure the uptake of PpIX in tumors, PpIX fluorescence spectra (450–750 nm) were acquired by means of a $400 \mu\text{m}$ fiberoptic probe, coupled to a spectrometer (Model S2000, Ocean Optics, FL, USA), placed in gentle contact with the tissue surface, and compared with PpIX fluorescence spectra from CNS-1^{luc} cell lysates measured using a spectrofluorimeter (SpectraMax M5; Molecular Devices, CA, USA) at 405 nm excitation after incubation with 1 mM ALA for 4 hours. FGR was performed by positioning the laparoscope tip at 2 cm above the surgical site. Tumor was identified by areas of evident red fluorescence and resected by means of suction through a glass tip with 0.5 mm inner diameter. Spectral images were acquired during tumor resection, which was terminated when red fluorescence was no longer detectable on the video monitor. The resected tissue was fixed in 10% formalin for sectioning H&E staining. Following resection, the presence of residual tumor cells was assessed semiquantitatively by applying $100 \mu\text{L}$ of 1 mM luciferin (Xenogen, Alameda, CA, USA) in PBS as the substrate for bioluminescence, which was observed *in vivo* using a commercial bioluminescence imaging system (IVIS, Xenogen). Immediately afterwards, the animals were sacrificed by intracardiac injection of 1 mg kg^{-1} of sodium pentobarbital (Euthanyl, MTC Pharmaceuticals, Cambridge, ON, Canada), and the whole brain was removed intact for sectioning and H&E staining for histopathological assessment.

3. RESULTS

3.1. System performance

Figure 2(a) shows the spectral response of the CCD camera in each of the 3 channels. The spatial modulation transfer function (MTF), measured using the resolution pattern at

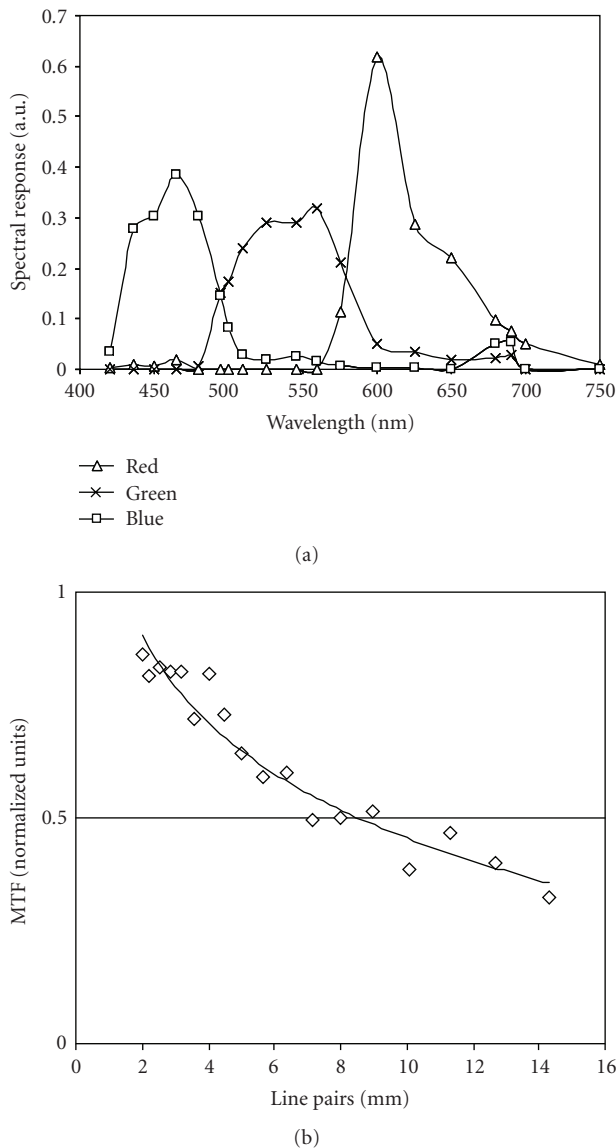


FIGURE 2: (a) Spectral response curves for the red, green, and blue channels of the 3-chip CCD, (b) fluorescence modulation transfer function measured at 2 cm working distance. The solid line is a logarithmic fit to the experimental data points.

a working distance of 2 cm from the laparoscope tip, is shown in Figure 2(b). The spatial resolution, defined at an MTF value of 50%, is 0.12 mm (8.5 line pairs per mm).

3.2. Efficacy of the ratiometric algorithm

The red-channel signal, corresponding to PpIX fluorescence, is plotted as a function of PpIX concentration for phantoms of different optical properties in Figure 3(a) and for different laparoscope-tissue distances in Figure 3(c). These demonstrate the strong dependence of the “raw” fluorescence signal on the tissue characteristics (due to attenuation of the excitation and fluorescent light) and imaging geometry, confirming the need to apply corrections to the data. Figures

3(b) and 3(d) show that the double-ratio method markedly reduces these differences, for example, at $2.5 \mu\text{g mL}^{-1}$ (i.e., the highest concentration used), the relative standard deviations of the fluorescence signal (i.e., $\text{stdev}/\text{mean} * 100\%$) are 26.1%, 13.1%, 28.2%, and 10.1% for Figures 3(a)–3(d), respectively. Figure 4 shows the corresponding data for varying angle between the laparoscope and the tissue surface.

3.3. Biological studies

In vitro and *in vivo* spectroscopic analysis of CNS-1 cells and tumors after administration of ALA for 4 hours (1 mM and 100 mg kg^{-1} , resp.) confirmed the presence of the PpIX fluorescence peak at 635 nm (see Figure 5(a)). Figures 5(b)–5(d) show examples that demonstrate the quality of the fluorescence images obtained with the system. Evident red fluorescence was observed from tumor areas at all ALA doses, demonstrating the capability to discriminate between tumor and normal brain tissues. The tumor-associated fluorescence increased from the lowest to the highest ALA dose, roughly proportionally. The normal brain showed no such trend. However, there was high variability in the fluorescence signals that was likely due in part to the small number of animals used in this feasibility study and in part to the intrinsic heterogeneity of the tumor model. The imaging system also detected diffuse and specular reflectance in the blue component, which aids in overall tissue orientation during surgery. No significant differences in PpIX fluorescence were found in normal brain tissues between the tumor-bearing and contralateral hemispheres (data not shown).

We also tested the system’s ability to monitor fluorescence-guided resection of tumor. As illustrated by the example in Figure 6, it was possible in all animals to completely resect the visible fluorescing (tumor) tissue, as confirmed by histopathology (see Figure 7(c)). Despite this, bioluminescence imaging (see Figures 7(a)–7(b)) indicated the presence of small amounts of residual tumor, corresponding to ~ 100 cells at or close to the resection surface (as estimated from the bioluminescence signal).

4. DISCUSSION

The ability to accurately quantify fluorescence signals in optically-turbid media such as tissue is challenging, due to its complex dependence on many factors in addition to the fluorophore concentration, and in particular the tissue absorption and scattering properties, the measurement geometry and the background tissue autofluorescence. These issues have been discussed in many papers, as summarized by Bradley and Thorniley [36] and Bogaards et al. [41]. Several different fluorescence imaging systems have also been developed for *in vivo* applications, including the purpose of guiding tumor surgery and particularly in the brain. The intent in developing the present instrument was two-fold. Firstly, we wished to make a device that is compact and independent of any other surgical instrumentation. The approach implemented by Stummer and colleagues [18, 22, 43], for example, is to integrate fluorescence capabilities into an

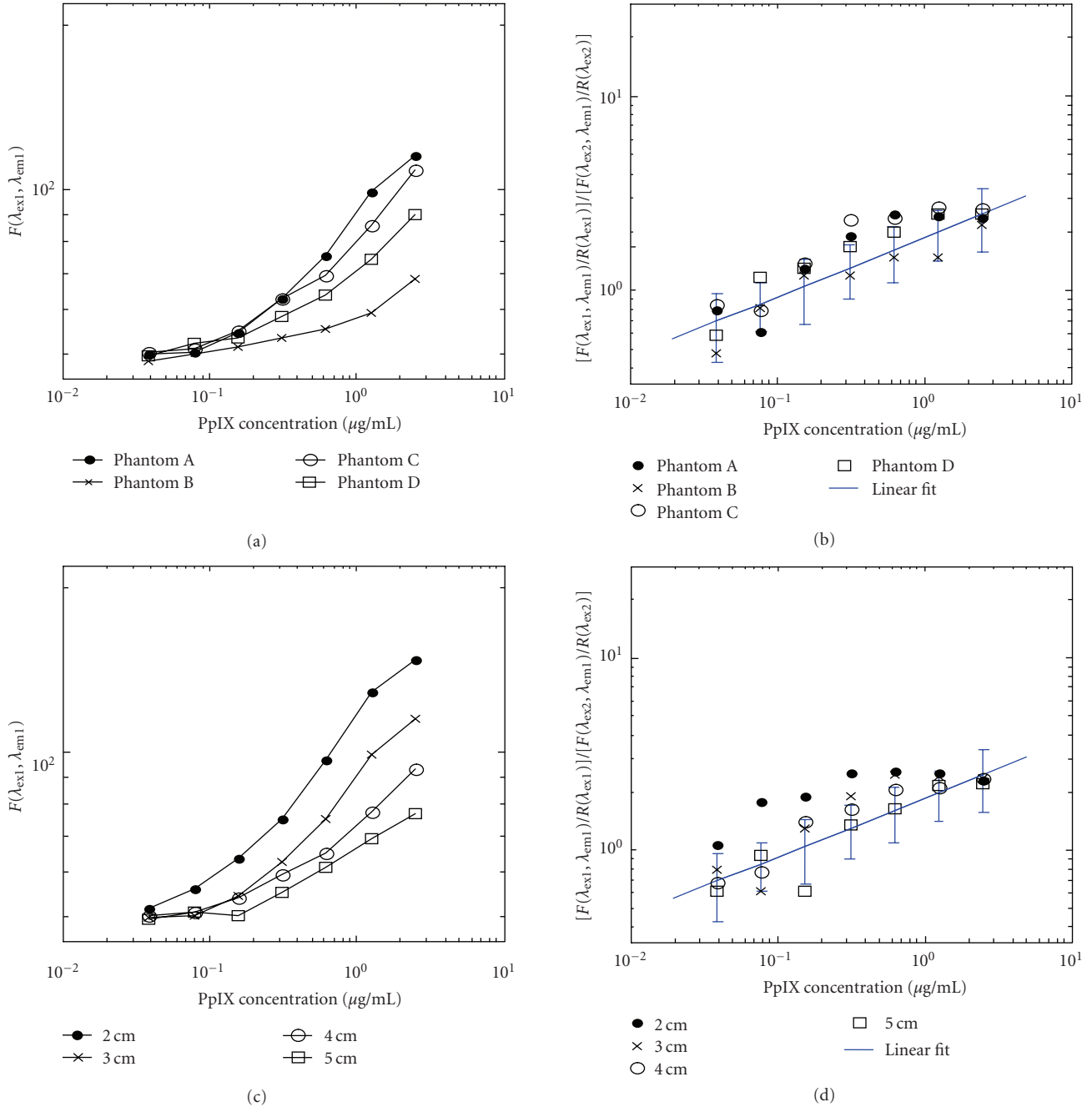


FIGURE 3: (a), (c) Relative PpIX fluorescence intensities as a function of PpIX concentration before and (b), (d) after application of the double-ratio algorithm, measured in the phantoms under different conditions. Linear regression fits to the combined data are shown in the corrected plots.

operating microscope. This certainly is a valid approach and has advantages in terms of ease of use, but limits its general surgical applicability. We intend in the near future to carry out a direct comparison of the performance of the present open-field device with the through-microscope technique. The second intent was to implement the double-wavelength ratiometric algorithm. While single-ratio correction has been used in other studies as a method to improve the information content in fluorescence-based diagnostics (e.g., $R_1 =$

$F(\lambda_{ex1}, \lambda_{em1})/R(\lambda_{ex1})$, or $R_2 = F(\lambda_{ex2}, \lambda_{em2})/R(\lambda_{ex2})$) [32, 39, 44], the 2-excitation/2-detection wavelengths algorithm developed previously by our group [41] and implemented here appears to be particularly effective in minimizing the effects of tissue autofluorescence, geometric effects, and optical attenuation. The phantom studies presented above on the latter two factors confirm our previous modeling study of the efficacy of different correction algorithms [41]. In particular, including the reflectance signal (by allowing

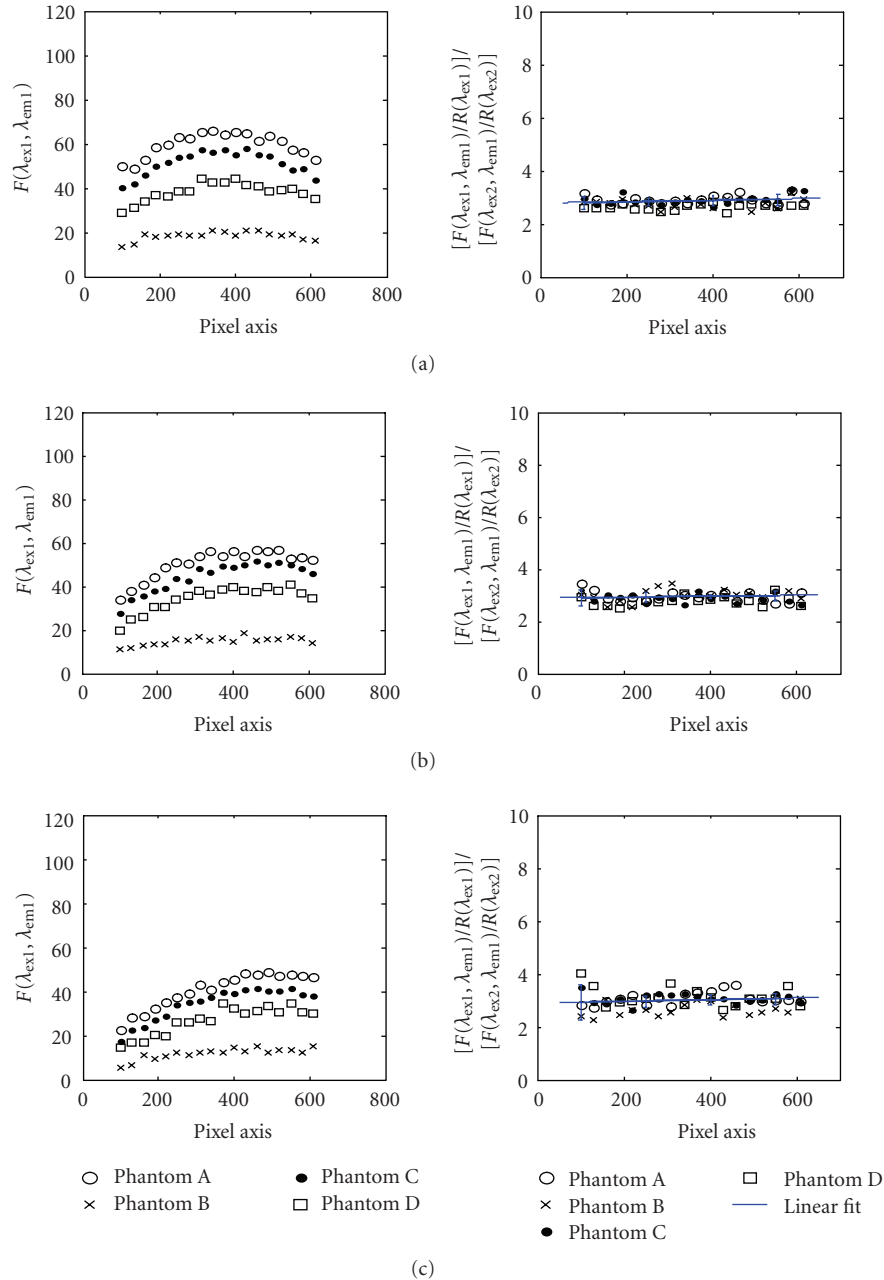
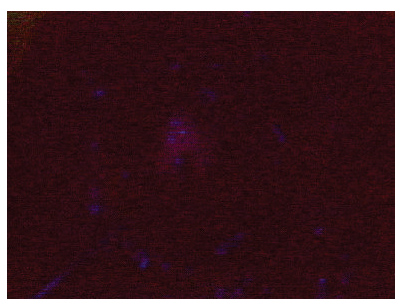
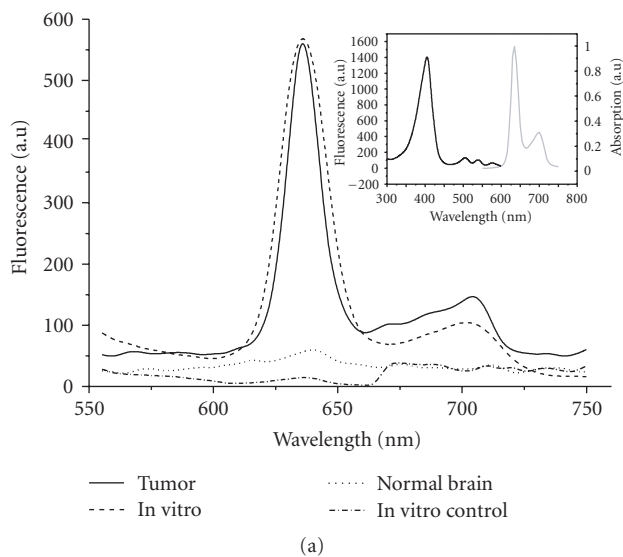


FIGURE 4: Relative PpIX fluorescence intensities as a function on position on the CCD image (centered at the 400 pixel value), showing how this varies with the angle between the optical axis (i.e., laparoscope direction) and the tissue surface, for the different optical properties: (a) 0°, (b) 15°, (c) 30°. Graphs on the left are the uncorrected data; those on the right are after applying the double-ratio algorithm (with linear fits to the combined data). In each plot, the signals are summed along the axis perpendicular to the x-axis of the graphs on the 3D CCD array. All measurements were made at 2 cm working distance.

a small fraction of the excitation light to leak through the excitation filter) minimizes the dependence on variations in autofluorescence. As shown by the phantom studies (see Figures 3 and 4), the algorithm also largely removes the dependence on the tissue optical properties and imaging geometry, since the effects of these factors are similar at the 2 excitation wavelengths, so that they are largely cancelled by taking the ratio of the signals at these wavelengths, which

aids in applying an objective and quantitative criterion (e.g., a threshold concentration) to differentiate between diseased and non-diseased tissues. This overcomes a significant weakness of previous studies, including clinical trials, in which only subjective and qualitative criteria were applied [45].

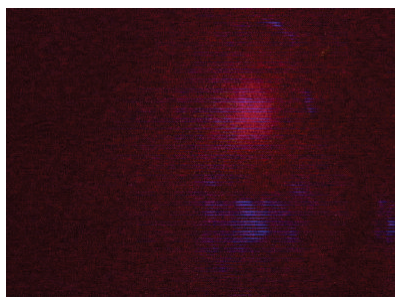
The principal advantage of using a 3-chip CCD camera in this device is that the red, green, and blue components can



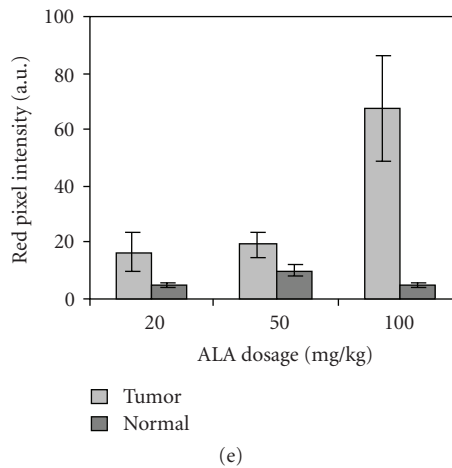
(b)



(c)



(d)



(e)

FIGURE 5: (a) Normalized PpIX fluorescence spectra of tumor and normal contralateral brain *in vivo*, 4 hours after i.p. administration of 100 mg kg⁻¹ of ALA, and corresponding spectra in CNS-1 cells *in vitro* compared to controls (no ALA). The insert shows the excitation and emission spectra of PpIX in solution. (b)–(d) *In vivo* fluorescence images of PpIX in tumor after i.p. injection of 20, 50, and 100 mg kg⁻¹ ALA, respectively. (e) PpIX fluorescence from tumor-bearing animals 4 hours after injection of different ALA doses in tumor and contralateral normal brain (means ± 1 standard deviation: N = 2).

be independently augmented or attenuated in the resulting image, depending on the spectral band that exhibits the highest contrast between tumor and normal tissue. Custom software integrates the dual excitation and RGB components

into a real-time (video rate) composite that can be tailored to enhance a large number of different fluorophores.

The spectral images of PpIX in phantoms and *in vivo* demonstrated excellent spatial resolution and contrast for

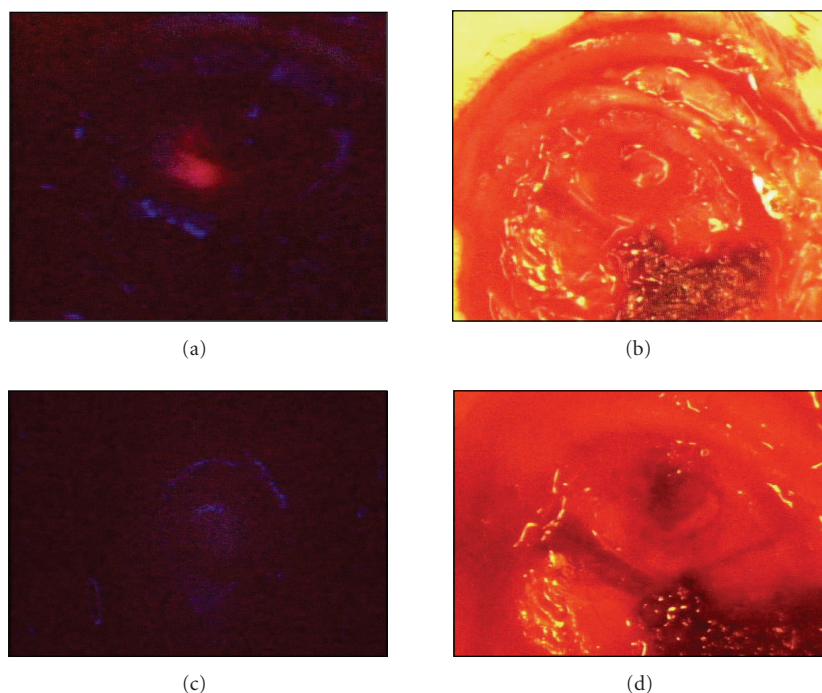


FIGURE 6: (a), (c) Example of *in vivo* PpIX fluorescence (λ_{ex} : 405 nm) and (b), (d) white light images in the tumor resection cavity pre (a), (b) and post fluorescence-guided resection (c), (d). Surgery was performed 4 hours after ALA injection (100 mg kg^{-1} , i.p.). The blue areas represent specular reflection from the tissue surface.

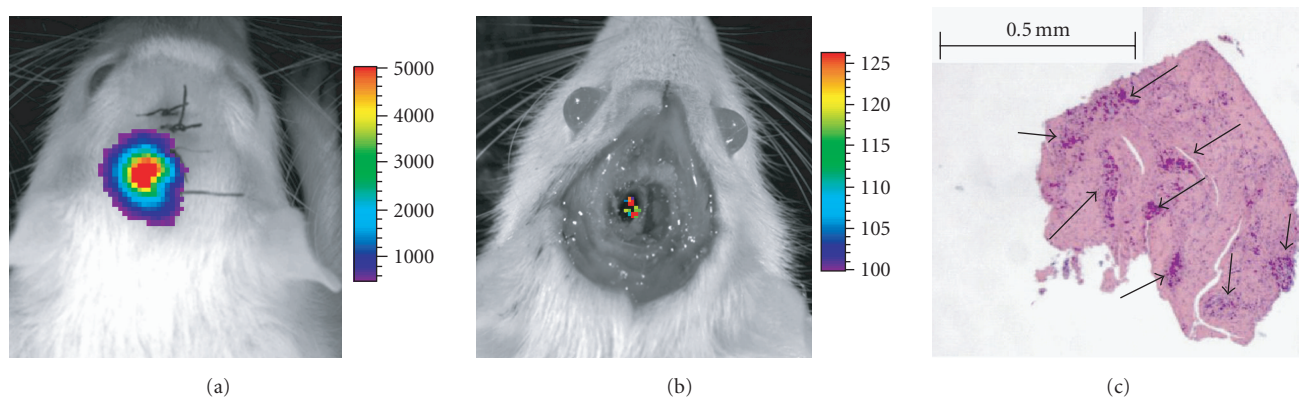


FIGURE 7: Example of *in vivo* bioluminescence imaging pre (a) and post (b) fluorescence-guided resection. The bioluminescence imaging of residual CNS-1^{huc} cells immediately after FGR corresponds to approximately 100 cells detected at the surface of the resection cavity. (c) H&E stained tissue section from the red-positive region in Figure 6(a). The arrows show nests of tumor cells.

visualization of residual tumors and the margins between normal and tumor tissues (see Figure 5). Hence, the technology should “extend the surgeon’s eye” in the identification and localization of tumor tissue. In particular, the system should work better than simply imaging the uncorrected fluorescence signal, especially in areas of low fluorescence intensity, due to reduction of the dependence on tissue autofluorescence. Again, this will be evaluated by head-to-head comparisons in phantoms, animal models, and patients.

One of the most exciting possibilities for this method of ALA-PpIX fluorescence imaging for guiding brain tumor

resection is to combine it with photodynamic therapy (PDT), and several groups, including our own, are pursuing this approach [20, 39]. The advantage of ALA-PpIX is that the same agent can serve both purposes, since PpIX is also well established as a PDT sensitizer. Further, since the PpIX is endogenously synthesized, we and others have shown its high selectivity for brain tumor relative to normal brain tissues, especially white matter [46–48].

As indicated in the Introduction, ALA-PpIX-based FGR has been shown to improve the completeness of glioma resection compared to standard white-light visualization [18–21]. However, the present study (see Figure 7), and

earlier work in a different brain tumor model [49] using bioluminescence post resection, show the likelihood of there being small amounts of residual tumor tissue that is below the fluorescence detection threshold. Hence, PDT applied intraoperatively immediately after resection should offer an additional level of tumor destruction and such combination studies are in progress, both preclinically [20, 42] and in human trials [50].

In conclusion, to date this instrument has met our objectives of a free-standing, easy-to-use, and highly sensitive intraoperative fluorescence imaging system for improved tumor resection. The phantom and previous modeling studies [41] have demonstrated the effectiveness of the double-ratio algorithm. Although limited in extent, the initial *in vivo* studies presented here have demonstrated the technical feasibility of the system to be used for fluorescence image-guided resection. Work is in progress in the CNS-1^{luc} brain tumor model using the system to optimize the ALA dose and the time interval between its administration and the resection to give the highest sensitivity and specificity. We have also confirmed the technical feasibility of the instrument in preliminary clinical tests in patients carried out during prostatectomy and in assessment of recurrent vulvar malignancy (data not shown). Systematic clinical tests are in progress or planned for a number of different tumor sites.

ACKNOWLEDGMENTS

This work was supported by NIH Grant PO1-CA43892. A. Kim was supported by NIH Grant RO1-NS052274. The authors thank Dr. Kai Zhang for his assistance with the imaging system and Mathieu Roy for preparing the phantoms.

REFERENCES

- [1] F. G. Barker II, S. M. Chang, P. H. Gutin, et al., "Survival and functional status after resection of recurrent glioblastoma multiforme," *Neurosurgery*, vol. 42, no. 4, pp. 709–723, 1998.
- [2] M. Lacroix, D. Abi-Said, D. R. Fourney, et al., "A multivariate analysis of 416 patients with glioblastoma multiforme: prognosis, extent of resection, and survival," *Journal of Neurosurgery*, vol. 95, no. 2, pp. 190–198, 2001.
- [3] J. Yoshida, Y. Kajita, T. Wakabayashi, and K. Sugita, "Long-term follow-up results of 175 patients with malignant glioma: importance of radical tumour resection and postoperative adjuvant therapy with interferon, ACNU and radiation," *Acta Neurochirurgica*, vol. 127, no. 1-2, pp. 55–59, 1994.
- [4] R. Zakhary, G. E. Keles, and M. S. Berger, "Intraoperative imaging techniques in the treatment of brain tumors," *Current Opinion in Oncology*, vol. 11, no. 3, pp. 152–156, 1999.
- [5] M. J. McGirt, K. R. Bulsara, T. J. Cummings, et al., "Prognostic value of magnetic resonance imaging-guided stereotactic biopsy in the evaluation of recurrent malignant astrocytoma compared with a lesion due to radiation effect," *Journal of Neurosurgery*, vol. 98, no. 1, pp. 14–20, 2003.
- [6] C. Nimsky, O. Ganslandt, M. Buchfelder, and R. Fahlbusch, "Intraoperative visualization for resection of gliomas: the role of functional neuronavigation and intraoperative 1.5 T MRI," *Neurological Research*, vol. 28, no. 5, pp. 482–487, 2006.
- [7] D. Lindner, C. Trantakis, C. Renner, et al., "Application of intraoperative 3D ultrasound during navigated tumor resection," *Minimally Invasive Neurosurgery*, vol. 49, no. 4, pp. 197–202, 2006.
- [8] V. X. D. Yang, P. J. Muller, P. Herman, and B. C. Wilson, "A multispectral fluorescence imaging system: design and initial clinical tests in intra-operative photofrin-photodynamic therapy of brain tumors," *Lasers in Surgery and Medicine*, vol. 32, no. 3, pp. 224–232, 2003.
- [9] R. Tréhin, J.-L. Figueiredo, M. J. Pittet, R. Weissleder, L. Josephson, and U. Mahmood, "Fluorescent nanoparticle uptake for brain tumor visualization," *Neoplasia*, vol. 8, no. 4, pp. 302–311, 2006.
- [10] H. Stepp, T. Beck, T. Pongratz, et al., "ALA and malignant glioma: fluorescence-guided resection and photodynamic treatment," *Journal of Environmental Pathology, Toxicology and Oncology*, vol. 26, no. 2, pp. 157–164, 2007.
- [11] M. A. Kara, F. P. Peters, F. J. W. ten Kate, S. J. van Deventer, P. Fockens, and J. J. G. H. M. Bergman, "Endoscopic video autofluorescence imaging may improve the detection of early neoplasia in patients with Barrett's esophagus," *Gastrointestinal Endoscopy*, vol. 61, no. 6, pp. 679–685, 2005.
- [12] S. Andersson-Engels, C. Klinteberg, K. Svanberg, and S. Svanberg, "In vivo fluorescence imaging for tissue diagnostics," *Physics in Medicine and Biology*, vol. 42, no. 5, pp. 815–824, 1997.
- [13] M. L. Harries, S. Lam, C. MacAulay, J. Qu, and B. Palcic, "Diagnostic imaging of the larynx: autofluorescence of laryngeal tumours using the helium-cadmium laser," *The Journal of Laryngology & Otology*, vol. 109, no. 2, pp. 108–110, 1995.
- [14] W. Alian, S. Andersson-Engels, K. Svanberg, and S. Svanberg, "Laser-induced fluorescence studies of meso-tetra(hydroxyphenyl)chlorin in malignant and normal tissues in rats," *British Journal of Cancer*, vol. 70, no. 5, pp. 880–885, 1994.
- [15] J. Blais, C. Amirand, J. P. Ballini, P. Debey, M. T. Foulter, and T. Patrice, "Photofrin-induced fluorescence in progressive and regressive murine colonic cancer cells: correlation with cell photosensitivity," *Journal of Photochemistry and Photobiology B*, vol. 27, no. 3, pp. 225–231, 1995.
- [16] T. S. Mang, C. McGinnis, C. Liebow, U. O. Nseyo, D. H. Crean, and T. J. Dougherty, "Fluorescence detection of tumors: early diagnosis of microscopic lesions in preclinical studies," *Cancer*, vol. 71, no. 1, pp. 269–276, 1993.
- [17] J. Shinoda, H. Yano, S.-I. Yoshimura, et al., "Fluorescence-guided resection of glioblastoma multiforme by using high-dose fluorescein sodium. Technical note," *Journal of Neurosurgery*, vol. 99, no. 3, pp. 597–603, 2003.
- [18] W. Stummer, S. Stocker, S. Wagner, et al., "Intraoperative detection of malignant gliomas by 5-aminolevulinic acid-induced porphyrin fluorescence," *Neurosurgery*, vol. 42, no. 3, pp. 518–526, 1998.
- [19] K. M. Hebeda, J. G. Wolbers, H. J. C. M. Sterenborg, W. Kamphorst, M. J. C. van Gemert, and H. A. M. van Alphen, "Fluorescence localization in tumour and normal brain after intratumoral injection of haematoporphyrin derivative into rat brain tumour," *Journal of Photochemistry and Photobiology B*, vol. 27, no. 1, pp. 85–92, 1995.
- [20] A. Bogaards, A. Varma, K. Zhang, et al., "Fluorescence image-guided brain tumour resection with adjuvant metronomic photodynamic therapy: pre-clinical model and technology development," *Photochemical & Photobiological Sciences*, vol. 4, no. 5, pp. 438–442, 2005.
- [21] A. Bogaards, A. Varma, S. P. Collens, et al., "Increased brain tumor resection using fluorescence image guidance in

- a preclinical model," *Lasers in Surgery and Medicine*, vol. 35, no. 3, pp. 181–190, 2004.
- [22] W. Stummer, A. Novotny, H. Stepp, C. Goetz, K. Bise, and H. J. Reulen, "Fluorescence-guided resection of glioblastoma multiforme by using 5-aminolevulinic acid-induced porphyrins: a prospective study in 52 consecutive patients," *Journal of Neurosurgery*, vol. 93, no. 6, pp. 1003–1013, 2000.
- [23] V. Ntziachristos, C. Bremer, and R. Weissleder, "Fluorescence imaging with near-infrared light: new technological advances that enable in vivo molecular imaging," *European Radiology*, vol. 13, no. 1, pp. 195–208, 2003.
- [24] B. W. Pogue, S. L. Gibbs, B. Chen, and M. Savellano, "Fluorescence imaging in vivo: raster scanned point-source imaging provides more accurate quantification than broad beam geometries," *Technology in Cancer Research & Treatment*, vol. 3, no. 1, pp. 15–21, 2004.
- [25] V. Ntziachristos, E. A. Schellenberger, J. Ripoll, et al., "Visualization of antitumor treatment by means of fluorescence molecular tomography with an annexin V-Cy5.5 conjugate," *Proceedings of the National Academy of Sciences of the United States of America*, vol. 101, no. 33, pp. 12294–12299, 2004.
- [26] E. E. Graves, D. Yessayan, G. Turner, R. Weissleder, and V. Ntziachristos, "Validation of in vivo fluorescence concentrations measured using fluorescence molecular tomography," *Journal of Biomedical Optics*, vol. 10, no. 4, Article ID 044019, 10 pages, 2005.
- [27] S. V. Patwardhan, S. Bloch, S. Achilefu, and J. P. Culver, "Quantitative small animal fluorescence tomography using an ultrafast gated image intensifier," in *Proceedings of the 28th Annual International Conference of the IEEE Engineering in Medicine and Biology Society (EMBS '06)*, vol. 1, pp. 2675–2678, New York City, NY, USA, August–September 2006.
- [28] D. Hall, G. Ma, F. Lesage, and Y. Wang, "Simple time-domain optical method for estimating the depth and concentration of a fluorescent inclusion in a turbid medium," *Optics Letters*, vol. 29, no. 19, pp. 2258–2260, 2004.
- [29] K. R. Diamond, M. S. Patterson, and T. J. Farrell, "Quantification of fluorophore concentration in tissue-simulating media by fluorescence measurements with a single optical fiber," *Applied Optics*, vol. 42, no. 13, pp. 2436–2442, 2003.
- [30] B. W. Pogue and G. Burke, "Fiber-optic bundle design for quantitative fluorescence measurement from tissue," *Applied Optics*, vol. 37, no. 31, pp. 7429–7436, 1998.
- [31] J. R. Mansfield, K. W. Gossage, C. C. Hoyt, and R. M. Levenson, "Autofluorescence removal, multiplexing, and automated analysis methods for in-vivo fluorescence imaging," *Journal of Biomedical Optics*, vol. 10, no. 4, Article ID 041207, 9 pages, 2005.
- [32] J. C. Finlay and T. H. Foster, "Recovery of hemoglobin oxygen saturation and intrinsic fluorescence with a forward-adjoint model," *Applied Optics*, vol. 44, no. 10, pp. 1917–1933, 2005.
- [33] A. E. Profio, O. J. Balchum, and F. Carstens, "Digital background subtraction for fluorescence imaging," *Medical Physics*, vol. 13, no. 5, pp. 717–721, 1986.
- [34] R. Weersink, M. S. Patterson, K. Diamond, S. Silver, and N. Padgett, "Noninvasive measurement of fluorophore concentration in turbid media with a simple fluorescence/reflectance ratio technique," *Applied Optics*, vol. 40, no. 34, pp. 6389–6395, 2001.
- [35] H. J. C. M. Sterenberg, A. E. Saarnak, R. Frank, and M. Motamedi, "Evaluation of spectral correction techniques for fluorescence measurements on pigmented lesions in vivo," *Journal of Photochemistry and Photobiology B*, vol. 35, no. 3, pp. 159–165, 1996.
- [36] R. S. Bradley and M. S. Thorniley, "A review of attenuation correction techniques for tissue fluorescence," *Journal of the Royal Society Interface*, vol. 3, no. 6, pp. 1–13, 2006.
- [37] A. Bogaards, H. J. C. M. Sterenberg, and B. C. Wilson, "In vivo quantification of fluorescent molecular markers in real-time: a review to evaluate the performance of five existing methods," *Photodiagnosis and Photodynamic Therapy*, vol. 4, no. 3, pp. 170–178, 2007.
- [38] M. Sinaasappel and H. J. C. M. Sterenberg, "Quantification of the hematoporphyrin derivative by fluorescence measurement using dual-wavelength excitation and dual-wavelength detection," *Applied Optics*, vol. 32, no. 4, pp. 541–548, 1993.
- [39] R. Baumgartner and E. Unsöld, "High contrast fluorescence imaging using two-wavelength laser excitation and image processing," *Journal of Photochemistry and Photobiology B*, vol. 1, no. 1, pp. 130–132, 1987.
- [40] H. J. C. M. Sterenberg, A. E. Saarnak, R. Frank, and M. Motamedi, "Evaluation of spectral correction techniques for fluorescence measurements on pigmented lesions in vivo," *Journal of Photochemistry and Photobiology B*, vol. 35, no. 3, pp. 159–165, 1996.
- [41] A. Bogaards, H. J. C. M. Sterenberg, J. Trachtenberg, B. C. Wilson, and L. Lilge, "In vivo quantification of fluorescent molecular markers in real-time by ratio imaging for diagnostic screening and image-guided surgery," *Lasers in Surgery and Medicine*, vol. 39, no. 7, pp. 605–613, 2007.
- [42] M. Roy and B. C. Wilson, "An accurate homogenized tissue phantom for broad spectrum autofluorescence studies: a tool for optimizing quantum dot-based contrast agents," in *Design and Performance Validation of Phantoms Used in Conjunction with Optical Measurements of Tissue*, vol. 6870 of *Proceedings of SPIE*, pp. 1–12, San Jose, Calif, USA, January 2008.
- [43] W. Stummer, H. Stepp, G. Möller, A. Ehrhardt, M. Leonhard, and H. J. Reulen, "Technical principles for protoporphyrin-IX-fluorescence guided microsurgical resection of malignant glioma tissue," *Acta Neurochirurgica*, vol. 140, no. 10, pp. 995–1000, 1998.
- [44] S. Lam, J. Hung, and B. Palcic, "Mechanism of detection of early lung cancer by ratio fluorometry," *Lasers in the Life Sciences*, vol. 4, no. 2, pp. 67–73, 1991.
- [45] F. Duffner, R. Ritz, D. Freudenstein, M. Weller, K. Dietz, and J. Wessels, "Specific intensity imaging for glioblastoma and neural cell cultures with 5-aminolevulinic acid-derived protoporphyrin IX," *Journal of Neuro-Oncology*, vol. 71, no. 2, pp. 107–111, 2005.
- [46] H. Heyerdahl, I. Wang, D. L. Liu, et al., "Pharmacokinetic studies on 5-aminolevulinic acid-induced protoporphyrin IX accumulation in tumours and normal tissues," *Cancer Letters*, vol. 112, no. 2, pp. 225–231, 1997.
- [47] A. Orenstein, G. Kostenich, and Z. Malik, "The kinetics of protoporphyrin fluorescence during ALA-PDT in human malignant skin tumors," *Cancer Letters*, vol. 120, no. 2, pp. 229–234, 1997.
- [48] L. Lilge and B. C. Wilson, "Photodynamic therapy of intracranial tissues: a preclinical comparative study of four different photosensitizers," *Journal of Clinical Laser Medicine and Surgery*, vol. 16, no. 2, pp. 81–91, 1998.
- [49] E. H. Moriyama, S. K. Bisland, L. Lilge, and B. C. Wilson, "Bioluminescence imaging of the response of rat gliosarcoma to ALA-PpIX-mediated photodynamic therapy," *Photochemistry and Photobiology*, vol. 80, no. 2, pp. 242–249, 2004.
- [50] P. J. Muller and B. C. Wilson, "Photodynamic therapy of brain tumors—a work in progress," *Lasers in Surgery and Medicine*, vol. 38, no. 5, pp. 384–389, 2006.

Research Article

5-ALA Mediated Fluorescence Detection of Gastrointestinal Tumors

Ekaterina Borisova,¹ Borislav Vladimirov,² and Latchezar Avramov¹

¹*Institute of Electronics, Bulgarian Academy of Sciences, 72 Tsarigradsko Chaussee Boulevard, 1784 Sofia, Bulgaria*

²*Gastroenterology Department, University Hospital "Queen Giovanna", 8 Bjalo More Street, 1527 Sofia, Bulgaria*

Correspondence should be addressed to Ekaterina Borisova, borisova@ie.bas.bg

Received 7 March 2008; Revised 7 May 2008; Accepted 19 June 2008

Recommended by Stoyan Tanev

Delta-aminolevulinic acid/protoporphyrin IX is applied for fluorescent tumor detection in the upper part of gastrointestinal tract. The 5-ALA is administered per os six hours before measurements at dose 20 mg/kg weight. High-power light-emitting diode at 405 nm is used as an excitation source. Special opto-mechanical device is built to use the light guide of standard video-endoscopic system. Through endoscopic instrumental channel a fiber is applied to return information about fluorescence to microspectrometer. In such way, 1D detection and 2D visualization of the lesions' fluorescence are received, and both advantages and limitations of these methodologies are discussed in relation to their clinical applicability. Comparison of the spectra received from normal mucosa, inflammatory, and tumor areas is applied to evaluate the feasibility for development of simple but effective algorithm based on dimensionless ratio of the fluorescence signals at 560 and 635 nm, for differentiation of normal/abnormal gastrointestinal tissues.

Copyright © 2008 Ekaterina Borisova et al. This is an open access article distributed under the Creative Commons Attribution License, which permits unrestricted use, distribution, and reproduction in any medium, provided the original work is properly cited.

1. INTRODUCTION

The limitations of standard endoscopy for detection and evaluation of cancerous changes in gastrointestinal tract are significant challenge and initiative development of new diagnostic modalities, including optical detection of tissues alterations. One of the most widely examined spectroscopic techniques is laser- or light-induced fluorescence spectroscopy (LIFS), because of its rapid and highly sensitive response to early biochemical and morphological changes in the tissues. Fluorescent diagnosis of tumor tissues becomes a valuable tool in the clinical practice. This technique could be applied for detection and evaluation of tumors in different localizations using endoscopic equipment. Such combined white-light and fluorescent mode endoscopic systems are already developed and introduced in the clinic for the needs of bronchoscopy and lung cancer diagnosis, like D-Light system of Karl Storz GmbH, Tuttlingen, Germany, diagnostic autofluorescence endoscope (DAFE) system of Richard Wolf GmbH, Knittlingen, Germany, lung fluorescence endoscopy (LIFE) system of Xillix Technologies Corp., Richmond, Canada [1–4].

However, fluorescent gastroscopes are still on its research and development phases and from the best we know that the few existing systems, such as Olympus Evis Lucera, have not received yet approvals from FDA for access to the broad clinical market [5]. This system is a digestive tract videoscope used for observing blood vessels in mucous membranes under infrared light in the regions 790–820 nm and 905–970 nm. Variation of Xillix fluorescent endoscopic system is Xillix-LIFE-GI which is applied for autofluorescence detection of stomach neoplasia and has approval for Japan and European countries.

Several fluorescent endoscopy systems are developed and proposed also for practical applications by different research teams, demonstrating very good clinical results [4, 6–8], using autofluorescence or exogenous fluorescence detection of gastrointestinal neoplasia.

Despite of the fluorescent endoscopic systems developed mentioned above, the fluorescent diagnosis of tumors of the upper part of gastrointestinal tract still is very interesting and extensive research and development task worldwide. Spectral diagnosis can provide imaging and point spectroscopic information in both morphological and biochemical data

modes [1, 4, 9]. With the optimization of the procedures and evaluation of this technique diagnostic added value, through development of appropriate algorithms based on fluorescence properties of the investigated sites, a novel high-sensitive diagnostic tool could be successfully applied as complementary to the standard white light endoscopy [10–13].

In the case of autofluorescence detection, high sensitivity and specificity could be achieved if complex algorithms are applied for differentiation of the spectra [14]. However, on the current moment detecting the difference in autofluorescence as a gastroendoscopic image still has been relatively difficult task because of its faintness. Only combination of powerful light sources and highly sensitive detectors will lead to the development of autofluorescence gastroscopy clinical systems [1, 13]. Therefore, recent real-time gastrointestinal fluorescence endoscopy is all based on the use of exogenous fluorophores [1, 8, 12], as the addition of exogenous fluorescent compounds increases the contrast, improves endoscopic resolution and sampling, and could be used to receive better 2D visualization for the needs of clinicians.

Unfortunately, one typical problem of exogenous fluorophores' application, for example 5-ALA/PpIX for detection of gastrointestinal tumors, is the moderate specificity achieved. High false-positive values are obtained, mainly due to inflammation areas in the organs under interest. Sensitivity and specificity reported in different studies related to detection of esophageal neoplasia are 76% and 63% [15], 77% and 71% [16], 80% and 56% [17], respectively. Moreover, these values undergo significant changes in dependence of the amount of the photosensitizer applied—5, 10, 20, or 30 mg/kg 5-ALA and the way of sensitization—orally, using enema, or spray catheter [17, 18]. These differences are quite large—as the sensitivity and specificity for the cases of 10 mg/kg and 30 mg/kg oral application are 80% and 56%, as well as 100% and 27%, respectively. Local application of 5-ALA using spray catheter also reveals better values for sensitivity of the dysplastic lesions evaluation in colon than oral application of the drug, but specificity is lower—62% versus 73% (in the case of 20 mg/kg oral application) [18]. With increasing of the 5-ALA concentration orally applied, the specificity decreases very rapidly. Therefore, to achieve some optimization of the procedures and proper diagnosis, it is proposed to work with orally applied aminolevulinic acid, with concentration in the frames of 15–20 mg/kg for the gastrointestinal tract tumor detection [17, 18].

In the recent study, delta-aminolevulinic acid/protoporphyrin IX (5-ALA/PpIX) is also applied as fluorescent marker for tumor detection in esophagus and stomach. Normal and cancerous mucosas of esophagus and stomach as well as inflammatory areas fluorescence spectra are detected and compared in this study. Rapid lesions border determination using exogenous fluorescence signal is obtained in 1D scanning spectroscopic mode. Our results from in vivo detection show very good differentiation between normal and abnormal tissues in 1D spectroscopic regime, but moderate discrimination in 2D imaging. In the case of 2D video visualization, the problem of high autofluorescence signal in the red spectral region gives low contrast between

normal and abnormal mucosas when standard CCD camera of the endoscope is applied. This problem is in a process of resolve in our further investigations.

2. METHODS AND MATERIALS

Two variants of the fluorescent complimentary equipment to the standard gastroscope were applied for the needs of fluorescent diagnosis of the neoplasia in upper part of gastrointestinal tract. In the first one, we built light source that replace standard white light illuminator of the endoscope, and through instrumental channel a fluorescence collecting fiber (quartz-polymer single fiber, $d = 600 \mu\text{m}$, $NA = 0.22$) was applied. In the second variant, a fiber bundle was applied through instrumental channel of the endoscope, as the excitation light was delivered through central 1 fiber, and fluorescence response of the tissue was collected by surrounding 7 fibers and delivered to microspectrometer. The fiber bundle is specially developed for endoscopic applications in gastrointestinal tract (Polironik Ltd., Moscow, Russia), as the bundle used in this case consists of 8 quartz fibers, central one with diameter $200 \mu\text{m}$, and surrounding 7 fibers with diameter $100 \mu\text{m}$, all of them with numerical aperture 0.22. The central fiber is detached by thin aluminum folio from the surrounding fibers to avoid cross-signal between the fibers. Special resin is used on the end tip of the fiber bundle applied, due to its application in gastrointestinal tract—for patient safety and for enlarged resistance on the severe conditions in stomach environment. Both modalities have their advantages and disadvantages that will be described below.

In the first case, a special light source was developed for the needs of our experimental work, based on 405 nm high-power light-emitting diode OTLH-0360-UV-UV HIGH FLUX LED ILLUMINATOR (25 mW, Rhopoint Components Ltd, Oxted-Surrey, UK). This opto-mechanical device could replace common white light source of the standard endoscopic equipment (Olympus Corporation, Hertfordshire, UK) that is in use in the University Hospital “Queen Giovanna,” Sofia, Bulgaria. Through endoscopic instrumental channel, a quartz-polymer fiber was applied to return information about fluorescence to microspectrometer USB4000 (spectral range—350–1000 nm, FWHM~2 nm, Ocean Optics Inc., Fla, USA). A computer was used to control the spectrometric system and to store and display the data measured using specialized software Spectra Suite (Ocean Optics Inc.). Usage of the standard light guide of the endoscope for delivery of excitation light is beneficial due to the same geometry of illumination—view angle and illuminated area are preserved as for the white-light illumination mode. However, the optics of the light guide was not optimized for the short wavelength range and strong losses appeared in this case, therefore 2D visualization of the lesions obtained was not optimal for clinical observation needs [13].

In the second variant, excitation source was light emitting diode illuminator—AFS-405 (Polironik Ltd., Moscow, Russia) on 405 nm with 25 mW output power on the end of the fiber tip. Numerical aperture of the fiber was lower than that

one of light guide of the endoscope itself, and about 60% of the view area was illuminated in this case, reducing the field of view for the clinicians. However, in this case excitation light intensity was not faded by delivery optics, and bright 2D video visualization was achieved.

In the both cases, spectroscopic 1D measurements were with very good quality (high value of the signal-to-noise ratio), due to the significant sensitivity of the microspectrometer applied.

In the study, delta-aminolevulinic acid/protoporphyrin IX (“ALASENS,” NIOPIK JSCo, Russia) was used as fluorescent marker for dysplasia and tumor detection in esophagus and stomach. The δ -ALA is administered per os six hours before measurements at dose 20 mg/kg weight, according to clinical experience in gastrointestinal diagnostic applications of δ -ALA/PpIX fluorescence [4, 17].

Fluorescence diagnosis of esophageal and stomach lesions was made during standard endoscopic examinations of the patients in Gastroenterology Department of University Hospital “Queen Giovanna.” Twelve esophageal tumors and fifteen stomach tumors were detected using fluorescence endoscopy. The spectral measurements are made on several anatomic points during endoscopic procedures—on normal mucosa and cancerous sites. In the case of stomach endoscopic observations, spectral data from inflammatory areas were also detected and stored for subsequent analysis. All procedures are developed after local ethical committee approval received for the protocol of exogenous fluorescence diagnostic modality verification.

Five to seven points were measured from every section and averaged spectrum was used for evaluation of their state. The resultant spectrum was smoothed using Savitzky-Golay algorithm to reduce instrumental noise of the spectrometric system used. All results presented from spectral measurements in this paper are normalized with respect to back-scattered excitation signal at 405 nm from the mucosa surface for appropriate comparison of the signals obtained.

Measurements of the fluorescence spectra were made in 1D using spectrometer fibers and 2D visualization, and record of protoporphyrin IX distribution in the mucosa was made using video system of the endoscopic equipment. Up to three biopsy samples are collected from every suspicious area observed during observations of the patients using standard endoscopic biopsy clips and send for histological evaluation. Standard histology of all suspicious areas was used as “gold” standard, for comparison with the results obtained from spectral measurements.

3. RESULTS

The spectral measurements *in vivo* were made on several anatomic points during endoscopic procedures—on normal mucosa and suspicious sites, known from the previous diagnostic evaluation of the exact patient or where some red fluorescence signal was observed during current endoscopic observation. Standard histology applied as a “gold” standard for comparison with the results obtained from spectral measurements, revealed very good correlation between the fluorescence signals detected and histology examination results.

The fluorescence detected from tumor sites has very complex spectral origins. It consists of autofluorescence, fluorescence from exogenous fluorophores, and reabsorption from the chromophores accumulated in the tissue under investigation [1, 7–15, 19].

Spectral features observed during endoscopic investigations could be distinct as the next regions, according to their origin and spectral region appearance, after excitation at 405 nm:

- (i) 450–650 nm region, where tissue autofluorescence is observed;
- (ii) 630–710 nm region, where fluorescence of PpIX is clearly pronounced;
- (iii) 530–580 nm region, where minima in the autofluorescence signal are observed, related to reabsorption of oxy-hemoglobin in this spectral area.

Normal mucosa has bright autofluorescence, related mainly to the emission of coenzymes and protein cross-links [19]. The intensity of autofluorescence in the case of neoplasia rapidly decreases, which could be used as additional indicator of pathology evaluation; see Figures 1(a) and 1(b).

On Figure 1 are presented spectra of normal mucosa and tumor sites for esophagus and stomach for two patients. Standard deviation presented is a result of averaging of the spectra detected from different points of the pathological and normal tissues surface, respectively. In the case of stomach, autofluorescence of normal mucosa was significantly higher than that of tumor, and the contrast observed in green spectral area is usually higher than 3,5:1. For the esophagus fluorescence, this difference is not so strongly pronounced, but the autofluorescence of normal mucosa was also higher for all cases observed.

Such high autofluorescence leads to problems in 2D video-observation of the stomach tumor fluorescence, as the values of the area of the autofluorescence spectrum of normal mucosa for the region >600 nm in comparison with the same region for tumor fluorescence are comparable, and the ratio values between total areas of normal versus tumor spectra in the region 600–800 nm vary from 0.7 to 1.1 for different patients. This effect could not be avoided by application of filter before CCD camera, as the long-pass filter (>600 nm) passed both signals—from normal mucosa autofluorescence and from exogenous PpIX tumor fluorescence.

For both anatomic areas, esophagus and stomach, the same procedure was applied, 20 mg/kg 5-ALA oral application 6 hours before endoscopic observations. However, we received relatively big deviations of the fluorescence intensity of PpIX emission for both localizations for different patients, as in esophagus neoplastic lesions the fluorescence intensity of exogenous fluorophore was higher as a general than that for the stomach cancer sites; see Figures 2(a) and 2(b). On Figure 2 schematically are presented two endmost cases—of the highest signal detected from tumor—“Tumor 1” and the lowest signal detected from tumor—“Tumor 2” for both localizations—esophagus and stomach. All spectra are normalized with respect to the back-scattered

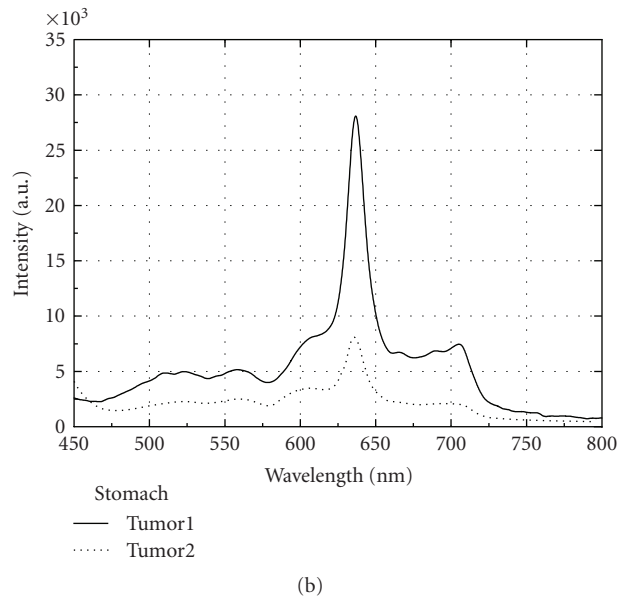
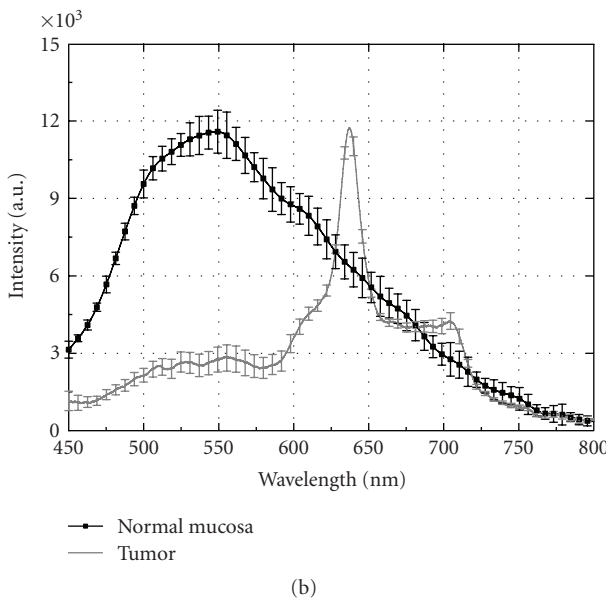
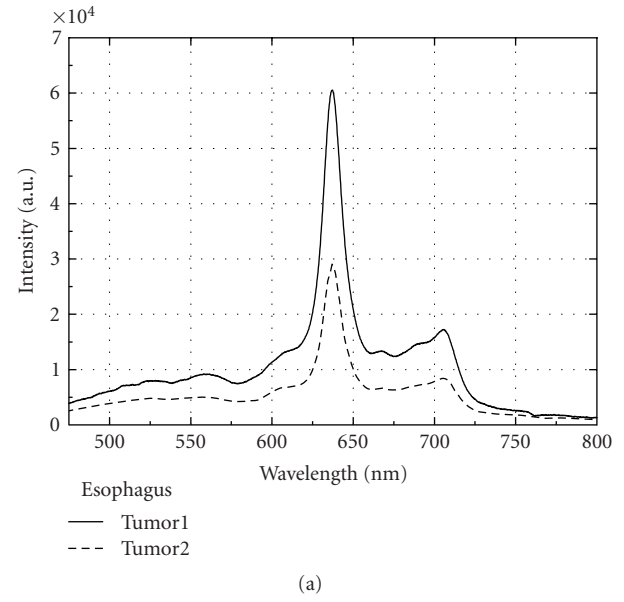
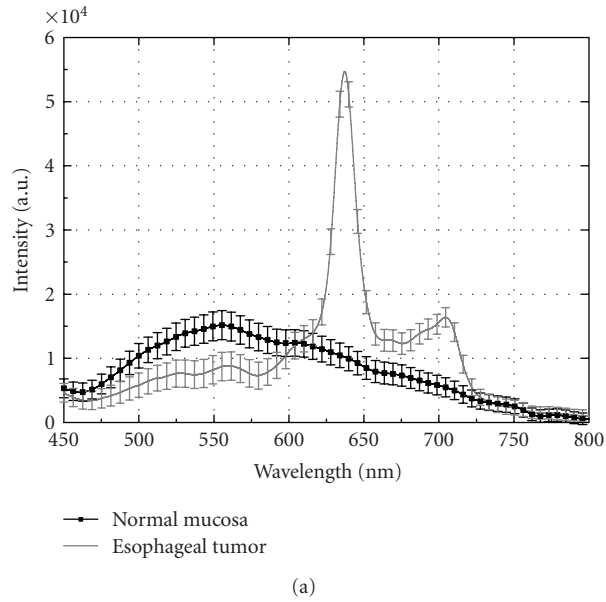


FIGURE 1: Fluorescence spectra of normal mucosa and tumor of patient with (a) esophageal carcinoma and patient with (b) stomach carcinoma at 405 nm excitation. Spectra are presented with their standard deviation, resulting of calculation of the mean value from the spectra detected from one section.

FIGURE 2: Fluorescence spectra of the lesions of two different patients with (a) esophageal tumors and two patients with (b) stomach tumors at 405 nm excitation. Spectra presented outlying cases of the highest (“Tumor 1”) and the lowest (“Tumor 2”) signals received from tumors in both localizations in different patients.

excitation signal at 405 nm. In general, stomach tumor PpIX fluorescence is about two times lower than that from esophagus neoplastic areas. It could be related to differences in the time of accumulation or the specific accumulation in both anatomic areas.

When inflammatory areas occurred in the organ under investigation, red fluorescence is also observed, which could give false-positive results for tumor determination, during observation in video channel of the endoscope. This fluorescence is observed due to the accumulation of PpIX in the both tumor and inflammatory areas. These signals could be

distinguished when 1D measurements of the inflammation are carried out; see Figure 3. The contrast between the fluorescent signals at 635 nm between tumor regions and inflammations observed in all patients, where such comparison was possible, usually is higher than two. In such way, we could be sure in general that by using this detection approach one could distinguish inflammation from tumor site, and moreover, could distinguish inflammatory areas from normal mucosa.

However, the fluorescent intensities of the maximum at 635 nm of inflammatory area detected from stomach

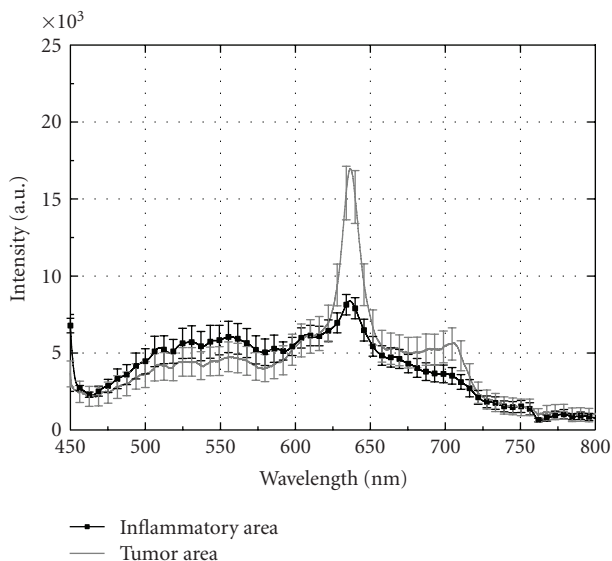


FIGURE 3: Fluorescence spectra of stomach inflammation and tumor of one patient, using excitation at 405 nm. Spectra are presented with their standard deviation, received after averaging of several point measurements in the respective abnormal mucosa areas.

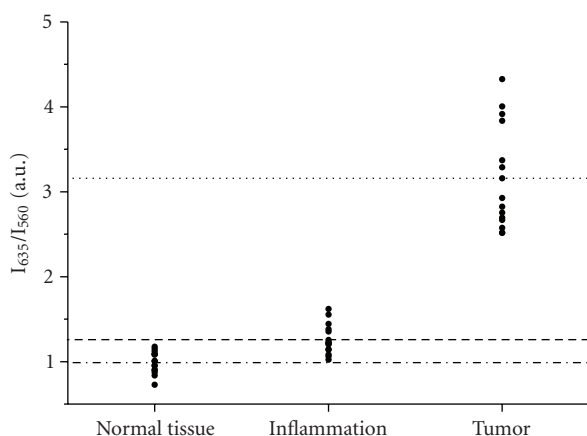


FIGURE 4: Dimensionless ratio (\bullet) $R = I_{635}/I_{560}$ calculated for all cases detected from normal mucosa, inflammation, and tumor of stomach. Lines represent the mean values of this ratio calculated.

wall are close to the lowest signals received from tumors (see Figure 2(b)). Therefore, an additional criterion could be applied for better differentiation of inflammation from tumor. We used for these goals a dimensionless ratio $R = I_{635}/I_{560}$. In such way, we received excellent differentiation of malignancies from benign and normal tissues of the stomach with significant gap between values corresponded; see Figure 4.

On Figure 4 are presented values of the dimensionless ratio of the all cases detected with tumors and inflammations in stomach wall, compared with normal mucosa values. Using this simple algorithm, very good differentiation tumor/inflammation is obtained that could be applied for clinical practice needs.

Moreover, similar approaches are proposed by other research groups for differentiation of normal and cancerous sites in bronchi and lungs. Using green and red band-pass filters, two complimentary images are received and ratio between them is calculated to receive more contrast image and to improve sensitivity and specificity of the fluorescent endoscopy approach [8, 20, 21].

4. DISCUSSION

Gastrointestinal tumors have major place in the statistics of newly developed cancers every year, and usually the tumors are detected on advanced III and IV stages, where perspectives for the patients are not very optimistic. Up to now, white light endoscopy is the main method in detection of gastrointestinal tumors. White-light endoscopy is well-established and wide used modality. However, despite the many technological advances that have been occurred, conventional white-light endoscopy is suboptimal and usually detects lesions, which already have symptoms of obstruction, bleeding and pain, related to tumor growth. Misdiagnoses, related to difficulties in differentiation of inflammatory from initial stage adenocarcinoma, also have negative effect on the diagnostic accuracy [1]. Only experienced gastroenterologists with long practice in endoscopy observations could find slight initial changes to dysplastic and neoplastic stages of esophageal, stomach or colon mucosa.

In gastroenterology, several optical methods are applied recently, such as optical coherent tomography [7], chromoendoscopy, confocal fluorescent microscopy [10], Raman spectroscopy [22], reflectance spectroscopy [11], and laser- and light-induced fluorescence spectroscopy [4, 15–17]. Combination of optical techniques (laser autofluorescence and diffuse reflectance) is also applied to increase the values of sensitivity and specificity of diagnostic procedure up to 93% and 100%, respectively [11].

Exogenous fluorescence spectroscopy is suggested to be very promising modality for early diagnosis of gastrointestinal tumors, and one of the most widely applied compound is delta-aminolevulinic acid/protoporphyrin IX [9, 16, 17]. 5-ALA is a natural precursor of heme, which induces the formation of endogenous PpIX. The administration of exogenous 5-ALA results in the accumulation of PpIX in tissue due to feedback inhibition of the final step of the heme biosynthetic cycle. Enzymatic differences in dysplastic tissue (e.g., decreased ferrochelatase activity) can lead to an increase in PpIX fluorescence in the tumor cells. Fluorescence spectroscopy of gastrointestinal tract is not yet in routine clinical use, but increasingly compelling data in patients will likely lead to its introduction to the diagnostic practice in near future.

In the current study are presented data from exogenous fluorescence spectroscopy of esophageal and stomach tumors in vivo after oral application of 20 mg/kg 5-ALA six hours before spectroscopic measurements and video visualization of the patients using excitation at 405 nm. The spectra received in 1D point spectroscopic measurements consist from three fundamental compounds—autofluorescence of endogenous fluorophores, fluorescence of exogenous

protoporphyrin IX, and reabsorption of their emission from the hemoglobin. Video 2D observation which is the most user—friendly tool for the needs of anatomically connected visualization of the pathology from the clinicians is not presented, as due to high level of autofluorescence of the gastrointestinal wall in the red spectral region, it is not representative enough. Similar observations were found from other investigators for detection of esophageal carcinoma lesions [23]. This problem could be solved by change of excitation wavelength applied and this task is in a process of solving in our further investigations using longer wavelengths for excitation of PpIX (e.g., its peaks of absorption at 509 nm, 544 nm, or 584 nm), where autofluorescence is not so strong factor, as well as back scattered excitation light from the mucosal surface does not lie in the spectral region of PpIX fluorescence itself.

In the case of normal mucosa, the hemoglobin reabsorption is not strongly pronounced. The mucosal autofluorescence is observed in the region of 450–700 nm and could be related to signals from protein cross-links, coenzymes, and phospholipids, using excitation at 405 nm [4, 19, 24–26]. The lack of fluorescence peaks at 636 nm and 704 nm for normal mucosa is an indication for highly selective accumulation of 5-ALA/PpIX only in abnormal sites and gives high contrast when lesion borders are determined. In the cases of advanced tumor progress, where necrosis appears, a lack of autofluorescence or exogenous signal is noticed, which visually is observed as a dark spot in the center of tumor lesion.

In the case of inflammation and tumor very strong minima are presented in the spectra at 545 and 573 nm, related to oxy-hemoglobin reabsorption of the autofluorescence signals from these areas. These strongly pronounced minima in the green spectral region could be used as additional indication of abnormality of the tissue investigated.

Dimensionless ratio at two wavelengths 560 nm and 635 nm is proposed to be used for better differentiation of tumors from inflammatory areas. This ratio allows receiving of 100% selective discrimination of tumors versus mucosal inflammation. However, additional comparison must be applied when dysplasia is evaluated. On this stage, only three cases of dysplasia are evaluated during clinical observations and their ratio' values lie between values of inflammations' and tumors' spectral ratios, namely, values of R for detected spectra of inflammation are between $1 < R < 1,6$, of dysplasia— $1,5 < R < 2,3$, and $2,5 < R < 4,4$ for the tumors' fluorescence spectra measured.

5. CONCLUSIONS

Advances in spectroscopic instruments will improve imaging's role as a facilitator of research translation. Results received in our study could serve for development of novel tools for quantifying in vivo tumor growth and origin and for accelerating the transition from preclinical studies to early clinical trials and to routine diagnostic practice. Fluorescent spectroscopy and imaging will help for further understanding of gastrointestinal tract tumors and to improve cancer patients' lives.

ACKNOWLEDGMENTS

This work was supported by the Bulgarian Ministry of Education and Science under Grant VU-L-01/05 "Optical biopsy of dysplasia and tumors in upper part of gastrointestinal tract."

REFERENCES

- [1] R. S. DaCosta, B. C. Wilson, and N. E. Marcon, "Photodiagnostic techniques for the endoscopic detection of premalignant gastrointestinal lesions," *Digestive Endoscopy*, vol. 15, no. 3, pp. 153–173, 2003.
- [2] T. Gabrecht, B. Lovisa, F. Borle, and G. Wagnieres, "Design of an endoscopic optical referent to be used for autofluorescence bronchoscopy with a commercially available diagnostic autofluorescence endoscopy (DAFE) system," *Physics in Medicine and Biology*, vol. 52, pp. 163–171, 2007.
- [3] "Xillix and Olympus Finalize Distribution and Development Agreement—Product Launch Scheduled for Early 1997," *Business Wire*, January 1997.
- [4] V. Chissov, V. Sokolov, N. Bulgakova-Zharkova, and E. Filonenko, "Fluorescence endoscopy, dermoscopy and spectrophotometry for diagnosis of malignant tumors," *Russian Biotherapeutic Journal*, vol. 4, pp. 45–56, 2003.
- [5] "World's First Auto Fluorescent Endoscope, medGadget—Internet Journal of Emerging Medical Technologies," April 2007, <http://www.medgadget.com/>.
- [6] G. V. Papayan and U. Kang, "Fluorescence endoscopic video system," *Journal of Optical Technology*, vol. 73, no. 10, pp. 739–743, 2006.
- [7] A. R. Tumlinson, L. P. Hariri, U. Utzinger, and J. K. Barton, "Miniature endoscope for simultaneous optical coherence tomography and laser-induced fluorescence measurement," *Applied Optics*, vol. 43, no. 1, pp. 113–121, 2004.
- [8] V. V. Sokolov, E. V. Filonenko, L. V. Telegina, N. N. Boulgakova, and V. V. Smirnov, "Combination of fluorescence imaging and local spectrophotometry in fluorescence diagnostics of early cancer of larynx and bronchi," *Quantum Electronics*, vol. 32, no. 11, pp. 963–969, 2002.
- [9] S. Svanberg, "Environmental and medical applications of photonic interactions," *Physica Scripta*, vol. T110, pp. 39–50, 2004.
- [10] R. DaCosta and N. Marcon, "Neue dimensionen in der bildgebung: bioendoskopie," *Endo Heute*, vol. 16, no. 2, pp. 75–90, 2003.
- [11] I. Georgakoudi, B. C. Jacobson, J. Van Dam, et al., "Fluorescence, reflectance, and light-scattering spectroscopy for evaluating dysplasia in patients with Barrett's esophagus," *Gastroenterology*, vol. 120, no. 7, pp. 1620–1629, 2001.
- [12] R. L. Probst and J. Gahlen, "Fluorescence diagnosis of colorectal neoplasms: a review of clinical applications," *International Journal of Colorectal Disease*, vol. 17, no. 1, pp. 1–10, 2002.
- [13] E. G. Borisova, B. G. Vladimirov, I. G. Angelov, and L. A. Avramov, "Fluorescence spectroscopy of gastrointestinal tumors using δ -ALA," in *14th International School on Quantum Electronics: Laser Physics and Applications*, vol. 6604 of *Proceedings of SPIE*, pp. 1–5, Sunny Beach, Bulgaria, September 2006.
- [14] C. Ell, "Improving endoscopic resolution and sampling: fluorescence techniques," *Gut*, vol. 52, supplement 4, pp. 30–33, 2003.
- [15] M.-A. E. J. Ortner, B. Ebert, E. Hein, et al., "Time gated fluorescence spectroscopy in Barrett's oesophagus," *Gut*, vol. 52, no. 1, pp. 28–33, 2003.

- [16] S. Brand, T. D. Wang, K. T. Schomacker, et al., "Detection of high-grade dysplasia in Barrett's esophagus by spectroscopy measurement of 5-aminolevulinic acid-induced protoporphyrin IX fluorescence," *Gastrointestinal Endoscopy*, vol. 56, no. 4, pp. 479–487, 2002.
- [17] E. Endlicher, R. Knuechel, T. Hauser, R. Szeimies, J. Scholmerich, and H. Messmann, "Endoscopic fluorescence detection of low and high grade dysplasia in Barrett's oesophagus using systemic or local 5-aminolevulinic acid sensitization," *Gut*, vol. 48, no. 3, pp. 314–319, 2001.
- [18] H. Messmann, E. Endlicher, G. Freunek, P. Rummele, J. Scholmerich, and R. Knuchel, "Fluorescence endoscopy for the detection of low and high grade dysplasia in ulcerative colitis using systemic or local 5-aminolevulinic acid sensitization," *Gut*, vol. 52, no. 7, pp. 1003–1007, 2003.
- [19] L. M. Song and K. K. Wang, "Optical detection and eradication of dysplastic Barrett's esophagus," *Technology in Cancer Research & Treatment*, vol. 2, no. 4, pp. 289–302, 2003.
- [20] D. Goujon, M. Zellweger, H. van den Bergh, and G. Wagnières, "Autofluorescence imaging in the tracheo-bronchial tree," *Photodynamics News*, vol. 3, no. 3, pp. 11–14, 2000.
- [21] V. Sokolov, V. Chissov, E. Filonenko, et al., "Fluorescence diagnostics of early central cancer of the lung," *Pulmonology*, vol. 1, pp. 107–116, 2005.
- [22] X.-L. Yan, R.-X. Dong, L. Zhang, X.-J. Zhang, and Z.-W. Zhang, "Raman spectra of single cell from gastrointestinal cancer patients," *World Journal of Gastroenterology*, vol. 11, no. 21, pp. 3290–3292, 2005.
- [23] M.-A. E. J. Ortner, K. Zumbusch, J. Liebetrueth, et al., "Is topical δ -aminolevulinic acid adequate for photodynamic therapy in Barrett's esophagus? A pilot study," *Endoscopy*, vol. 34, no. 8, pp. 611–616, 2002.
- [24] S. Andersson-Engels, C. A. Klinteberg, K. Svanberg, and S. Svanberg, "In vivo fluorescence imaging for tissue diagnostics," *Physics in Medicine and Biology*, vol. 42, no. 5, pp. 815–824, 1997.
- [25] P. Wilder-Smith, T. Krasieva, W.-G. Jung, et al., "Noninvasive imaging of oral premalignancy and malignancy," *Journal of Biomedical Optics*, vol. 10, no. 5, Article ID 051601, 8 pages, 2005.
- [26] G. Zonios, R. Cotheren, J. Crawford, et al., "Spectral pathology," in *Advances in Optical Biopsy and Optical Mammography*, R. Alfano, Ed., vol. 838, pp. 108–115, Annals of the New York Academy of Sciences, New York, NY, USA, 1998.

Research Article

The Impact of Autonomic Dysreflexia on Blood Flow and Skin Response in Individuals with Spinal Cord Injury

J. C. Ramella-Roman and J. M. Hidler

Department of Biomedical Engineering, The Catholic University of America, 620 Michigan Avenue, N.E. Washington, DC 20064, USA

Correspondence should be addressed to J. C. Ramella-Roman, ramella@cua.edu

Received 5 March 2008; Accepted 1 June 2008

Recommended by Stoyan Tanev

Autonomic dysreflexia (AD) is an inappropriate response of the sympathetic nervous system that commonly occurs when individuals with spinal cord injury (SCI), at or above the sixth thoracic (T6) vertebra, are subjected to a noxious stimulus below the level of injury. An AD event can be put into motion by something as simple as an ingrown toenail or a full bladder, with symptoms ranging from headache, high blood pressure, and even stroke. We have characterized the onset of AD and resulting autonomic events in an individual with SCI using a fiberoptic-based probe. Two probes were located above and below the injury level, on the subjects forearm and thigh, respectively, and were connected to a dual channel spectrophotometer. Oxygen saturation was calculated using the reflectance spectra and an algorithm based on melanin and hemoglobin absorption. We noticed that during an AD event the amount of oxygen in the skin below the injury level dropped by as much as 40%, while above the injury level, skin oxygenation remained constant. In addition, we found that the level of skin perspiration below the level of injury increased significantly. We hypothesize that the combination of AD-related ischemia with pressure-related ischemia and increased perspiration places individuals with spinal cord injury level at T6 or above at an elevated risk for developing a pressure sore below the injury site.

Copyright © 2008 J. C. Ramella-Roman and J. M. Hidler. This is an open access article distributed under the Creative Commons Attribution License, which permits unrestricted use, distribution, and reproduction in any medium, provided the original work is properly cited.

1. INTRODUCTION

Autonomic dysreflexia (AD) is an inappropriate response of the sympathetic nervous system in individuals with spinal cord injuries at or above the sixth thoracic vertebra (T6). Some common symptoms of AD include excessive sweating, piloerector erection of skin hairs, headache, hypertension, blurring of vision, and more rarely convulsion, loss of consciousness, cerebral hemorrhage, and death [1]. An AD event is often induced by a noxious stimulus below the level of injury, such as a full bladder, an ingrown nail, or a pressure sore.

The autonomic nervous system is responsible for maintaining the body's homeostasis via the parasympathetic nervous system and the sympathetic nervous system. These two systems have in most cases complementary roles and exist in two different locations of the central nervous system. In patients with T6 injuries or higher, the communication between the parasympathetic nervous system and the

sympathetic nervous system is interrupted, so that the stimulation of one branch no longer corresponds to the suppression of the other, resulting in the negative feedback loop of both systems no longer working appropriately. A noxious stimulus below T6 can cause a sympathetic response resulting in vasoconstriction, headaches, pallor, and chills below the injury level. Vasoconstriction produces a rise in blood pressure and consequent reflex bradycardia through the baroreceptor reflex [1, 2]. Because of disruptions in descending neural pathways, the parasympathetic nervous system is unable to send or receive information regarding the status of the body below the injury level, but tries to maintain the body's homeostasis by slowing down the heart rate. As a result, above the injury level the patient will experience a vagal response with vasodilation and bradycardia. An AD episode can normally be stopped quickly by removing the painful stimulus that triggered it; however, if no action is taken, the individual will experience elevating levels of symptoms. AD has been the focus of many studies for its

cardiovascular effects [3], however, no study to date has evaluated its effect on pressure sore formation. We believe that the circulatory dysfunction caused by AD (hypoxia and ischemia) can negatively impact the health of the skin contributing to the formation of skin ulcers.

Skin hypoxia is often referred to as a one of the main causes of skin damage [4, 5]. Several studies have shown that hypoxic wounds do not heal as quickly as well oxygenated wounds [5], forcing an investigation on the pathophysiological impact of hypoxia on healthy skin [6]. Previous studies have shown that hypoxia leads to tissue angiogenesis, vascular leakage, and consequently to skin deterioration [7]. A mediator in these alterations is the vascular permeability factor [8] (VPF, also known as vascular endothelial growth factor (VEGF)). Steinbrech et al. [9] have shown a time-dependent change in levels of VEGF and type II collagen under hypoxic condition. Levels of VEGF mRNA in normal human dermal fibroblast increased by 140% after 6 hours of hypoxia. Likewise, collagen mRNA expression increased by 170% after 24 hours of hypoxia. Finally Yamanaka and Ishikawa [5] showed that decreasing the oxygen tension to 2% increased mRNA of type I collagen from cultured human skin. Recently Dalton et al. [6] have shown each of these factors contribute to dermal failure and the formation of leg ulcers. Ischemia is also a recognized risk factor in skin ulcer formation. Thorfinn et al. [10, 11] have shown that sitting on a hard surface reduces perfusion to a biological zero.

Several studies used reactive hyperemia [12–14] as a way to measure perfusion response to load and skin stress. Herrman et al. [15] used a rat model to show that long-term ischemia (5 hours) due to elevated surface pressure causes a persistent hyperemic response, suggesting a compromise in the vasodilator mechanisms. In fact, persistent hyperemia is considered stage I skin breakdown in the National Pressure Ulcer Advisory Panel (NPUAP) definitions. In a related study by Thorfinn et al. [11], it was found that through the use of laser doppler flowmetry (LDF), perfusion in the skin over the ischial tuberosities of individuals with SCI after short and long periods of loading was higher than in normal individuals although the initial hyperemic response was significantly lower for SCI patients. Munstoe et al. [16, 17] have studied the role of ischemic-reperfusion injury in chronic wounds and have pointed out that the related inflammatory mechanism caused by a release of free radicals could lead to pressure ulcers. Finally, recent studies [18] on animal models have shown that the onset of anoxia on an already ischemic environment may cause a restructuring of the capillary bed with a permanent increase in skin perfusion. Stover et al. [19, 20] have shown that AD is a possible cause of skin restructuring. In studying skin thickening in SCI patients with and without AD symptoms it was shown that 80% of individuals with severe AD (grade 3) developed skin thickening compared to the 22% of patients without AD symptoms. The reduction of oxygenated flow coming from the femoral artery, characteristic of autonomic dysreflexia, is likely to exacerbate the ischemic hypoxia due to pressure. AD also causes increased perspiration that has been linked to skin ulcer formation [21]. The goal of this study

was to quantify blood flow rate, skin oxygenation levels, the amount of skin perspiration, and other autonomically related events during an episode of autonomic dysreflexia in an individual with spinal cord injury. We hypothesize that during AD, the blood flow rate below the injury level will drop significantly, translating into meaningful decreases in skin oxygen levels. Additionally, we hypothesize that during AD, the amount of skin perspiration will increase below the injury level.

2. MATERIAL AND METHODS

Our preliminary measurements were made on an individual with a T6 level injury classified as ASIA A on the American Spinal Injury Association sensory and motor impairment scale. As such, this individual had no sensation or volitional movement below the T6 injury level. Five different diagnostic modalities were measured: blood pressure, lower limb temperature, femoral artery blood flow velocity, pulse oximetry in the right thumb and right toe, and oxygen saturation in the forearm skin (above injury level), and thigh skin (below injury level). Measurements were first taken from the subject 15 minutes after the subject emptied his bladder. The subject then began consuming water, slowly filling his bladder. The test was interrupted when the subject acknowledged persistent symptoms of AD resulting from a full bladder, while his blood pressure remained under 150/100 mm Hg. All measurements were conducted in 5 minutes intervals apart from skin oxygenation that was measured automatically every 30 seconds. Systolic and diastolic pressures were measured with an electronic blood pressure measuring device (Jobar International, China). A thermocouple attached to the patients left leg measured surface temperature. The femoral artery blood velocity was measured with an ultrasound probe (HP Sonos 2000, Palo Alto CA). Measurement of oxygen saturation on the patients thumb and toe were done with a portable pulse oximeter (Digit, Smiths Medical, Waukesha, Wis, USA). Finally, skin oxygenation was measured spectroscopically.

Our spectroscopic technique measures local oxygen saturation StO_2 in the skin microcirculation and differs from pulse oximetry which measures oxygen saturation in arterial blood only. Our experimental apparatus consisted of two custom-made optical probes constructed with two optical fibers (Figure 1), and a dual channel spectrophotometer (Ocean Optics, Dunedin, Fla, USA).

Fiber diameter and separation were chosen in order to obtain a shallow probing depth (<1.5 mm). This ensured correct measurement of superficial skin. Two 0.6 mm diameter multimode fibers (Ocean Optics, Dunedin, Fla, USA) were positioned at 2.2 mm center to center and were supported by a Delrin casing. One fiber was used as the light source and was attached to a tungsten halogen lamp (Ocean Optics, Dunedin, Fla, USA); the second fiber was used as a detector and was connected to one channel of the spectrophotometer (Ocean Optics, Dunedin, Fla, USA). Finally the device was tested on a custom-made reflectance standard described by Moffitt et al. [22]. Similar probes have been used recently to measure tumor oxygenation in vivo [23], as well as optical

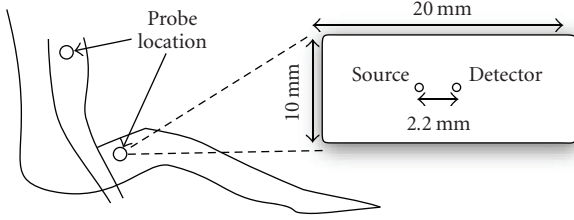


FIGURE 1: Measurement location of the fiber optic probe used in the skin oxygen saturation measurements. The fiber optics were enclosed in a black Delrin case with a fiber to fiber separation of 2.2 mm, both fibers were 0.6 mm in diameter.

properties of scattering biological tissues [24, 25], and are ideal for measurements where the penetration depth is low. The probing depth of our system was assessed with the aid of Monte Carlo simulations of light propagation into skin. Figure 2 shows the results of a simulation conducted with 3 million photons.

Skin was represented by two layers of different optical properties. The top most layer represented the epidermis and was $60 \mu\text{m}$ in thickness ($\mu_a = 35 \text{ cm}^{-1}$, $\mu_s = 450 \text{ cm}^{-1}$, and $g = 0.78$ at 540 nm); the second layer, representing the dermis, was semiinfinite ($\mu_a = 5 \text{ cm}^{-1}$, $\mu_s = 450 \text{ cm}^{-1}$, and $g = 0.81$ at 540 nm); the skin optical properties for each layer were from [26] by van Gemert et al. The Monte Carlo program followed the general structure of MCML [27] and was able to handle layers but did not consider Fresnel reflections at the interfaces. Photons were launched by a source fiber $600 \mu\text{m}$ in diameter, $\text{NA} = 0.39$, and collected by an identical detector fiber at 0.22 mm distance from the source. The propagation media was divided in square bins $10 \mu\text{m} \times 10 \mu\text{m}$ in size, initially all the bins were set to a zero value. Only the trajectories of the photons leaving the source fiber and reaching the detector fiber were tracked. Each time a photon reached a location in the media the value of the corresponding bin was increased by one fold (see insert in Figure 2).

Moore et al. [28] have measured dermis thickness using ultrasound both for able-bodied individuals as well as individuals with systemic sclerosis showing no significant difference among the two populations, dermis thickness in the right thigh was $1.379 \pm 0.217 \text{ mm}$ for controls and $0.8 \pm 0.13 \text{ mm}$ in the upper arm. In light of these measurements and looking at Figure 2, we can note that the photons traveling from the source to the collector fiber reached depths as far as 1.5 mm , spanning the full length of a normal epidermis and dermis [26, 28]. From this simple simulation we can assume that the probe design is suitable to measure superficial skin hemodynamics.

2.1. Phantom measurements

Calibration of the fiber optic probe was accomplished with an optical phantom, whose optical properties had been characterized as described in the paper by Moffitt et al. [22]. From the calibrated optical properties, and using Farrel's equation [29], we calculated the total reflectance

captured by a fiber optic layout with 2.2 mm center-to-center fiber separation (thin line). Finally, we experimentally measured the standard reflectance using the fiber probe and spectrometer as discussed in the previous section. The fiber tip/phantom interface was matched using a water droplet, and a 99% Spectralon reflectance standard was used to normalize the experimental results, both experimental and calibrated values are shown in Figure 3.

2.2. Analysis of spectral data

Two different algorithms yielding similar results were used to model the reflectance spectra acquired with the spectrophotometer. The first algorithm is described by Kollias and Baqer [25] and uses the curve of absorbance of skin, which is simply the logarithm of the ratio of the skin diffused reflectance to a reflectance standard (Spectralon standard 99% reflectance). The total absorbance curve of skin is corrected for melanin absorption by subtracting its contribution from the general data. Skin pigmentation is approximated as the slope of a fitted straight line between the values of absorbance at 620 nm and 720 nm , the absorbance curve of melanin decreasing monotonically between 600 nm and 750 nm . Oxygen saturation is calculated by using tabulated absorption curves of oxygenated and deoxygenated hemoglobin to fit the experimental data in the range 550 nm to 580 nm . In this range both curves exhibit local maxima [30].

The second algorithm used to model reflectance spectra is based on the Farrel's equation and has been used by Bargo et al. [23, 24]. Tabulated skin chromophores spectra [30, 31] are used to model the skin absorption μ_a and reduced scattering coefficient μ'_s . The model considers the effect of the absorption of oxygenated hemoglobin μ_a^{oxy} , deoxygenated hemoglobin μ_a^{deoxy} , water μ_a^{water} , and melanin μ_a^{melanin} . The scattering coefficient of skin is modeled as a combination of Mie (M) and Rayleigh (R) scatterers [32]:

$$\begin{aligned} M &= 4.5910^3 \text{ nm}^{-0.913} [\text{cm}^{-1}], \\ R &= 1.7410^{12} \text{ nm}^{-4} [\text{cm}^{-1}], \\ \mu'_s &= a(M + R) [\text{cm}^{-1}]. \end{aligned} \quad (1)$$

The total absorption in the skin is given by

$$\mu_a = B(\text{StO}_2 \mu_a^{\text{oxy}} + (1 - \text{StO}_2) \mu_a^{\text{deoxy}}) + W \mu_a^{\text{water}} [\text{cm}^{-1}]. \quad (2)$$

The calculated optical coefficients μ_a and μ'_s are used in combination with fiber separation and interface index of reflection in the Farrel's equation to calculate total reflectance (R_{Farrel}) from skin in the range of wavelengths of interest ($500\text{--}700 \text{ nm}$). The impact of melanin is finally added to the model using a simple Beer-Lambert law as shown below:

$$\text{Total}_R = C e^{-N \mu_a^{\text{melanin}} 2L_{\text{epidermis}}} R_{\text{Farrel}}, \quad (3)$$

where $\mu_a^{\text{melanin}} = 6.610^{11} \text{ nm}^{-3.33}$ [32] and the photon trajectory in and out of the epidermis is taken into account by

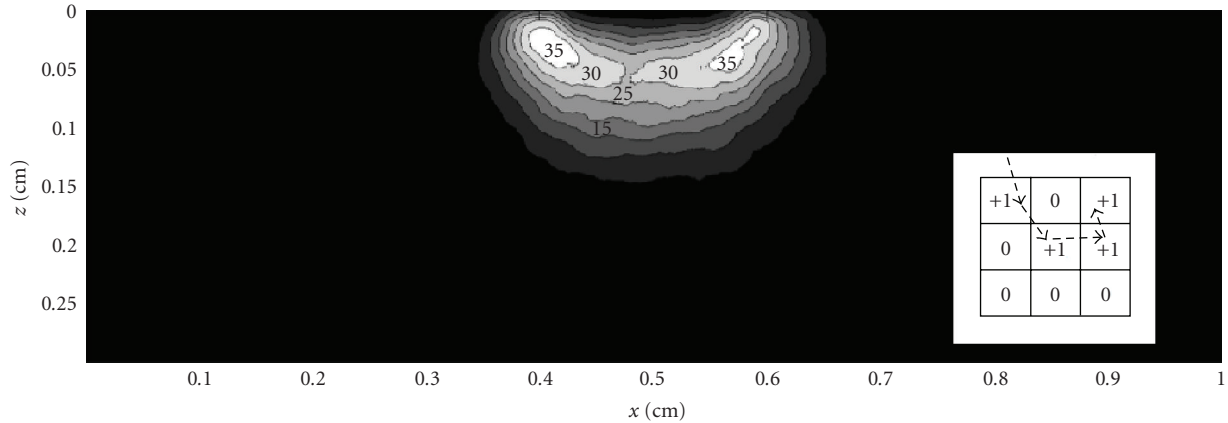


FIGURE 2: Monte Carlo simulation of light propagation in tissue. The different contours represent the number of photons reaching different depths (bin). In the insert, a pictorial description of our approach, every time a photon reaches a particular location the bin values are increased (+1). The graphs shows that photons will reach depths as far as 1.2 mm and still be able to return to the collection fiber. An averaging filter (20×20 pixels in size) was used to smooth the figure and to generate legible contours; the general trend shown in the graph did not change with the addition of the filter.

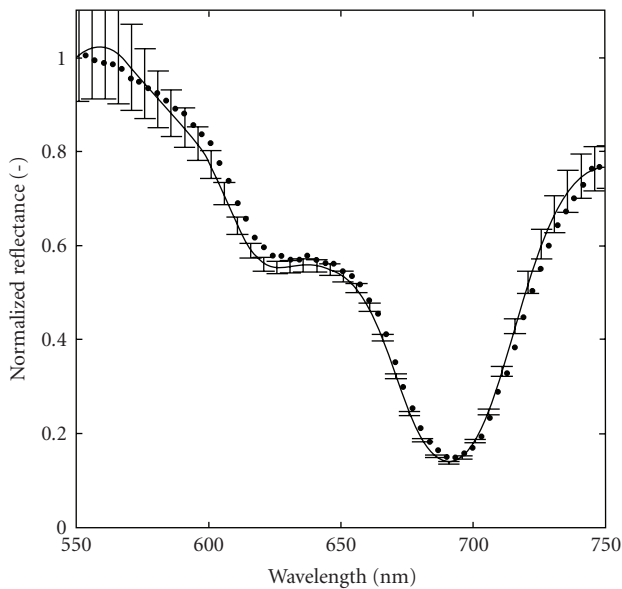


FIGURE 3: Calibration of the fiber optic probe. The solid symbols represent the values obtained experimentally with the fiber probe and the Ocean Optics spectrometer. The dashes represent the calculated reflectance for a set of experimentally measured optical properties. The optical properties of the standard had a larger margin of uncertainty at lower wavelengths as shown by the large standard deviation. The experimental results and theoretical findings were both normalized by the 550 nm reflectance.

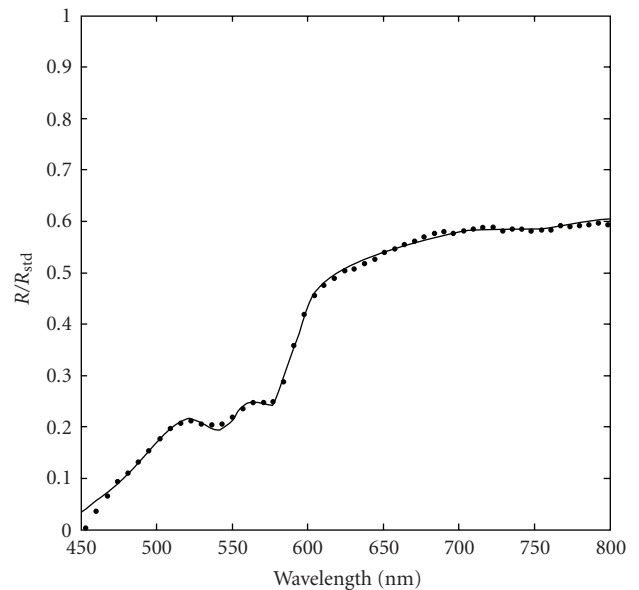


FIGURE 4: Normalized data (filled circles) and corresponding least square fit (line) obtained with the model by Bargo et al. Values of StO_2 for this particular fit were 0.58, the fraction of water was 0.65, and the blood volume fraction was 0.0009.

multiplying the epidermis thickness by 2. For these models we considered the epidermis to be $60 \mu\text{m}$ in thickness. A least square mechanism is finally used to fit the theoretical results to the experimental data, fitting parameters are oxygen saturation (StO_2), water content (W), blood fraction (B), scattering fraction (a), and melanin fraction (N). A wavelength-independent parameter C is used to account for

the effect of fiber collection efficiency [24]. This method has the advantage of obtaining information not only for oxygen saturation, but also for the skin components previously mentioned. These parameters can then be used to assess the quality and stability of the model. A typical least square fit obtained with this model is shown in Figure 4.

Both models yield similar results showing a decrease of oxygen saturation in the skin below the injury level at the onset of AD. Although the general temporal trend was identical for both algorithms, the numerical values of StO_2 were at times different, up to 10%. This difference

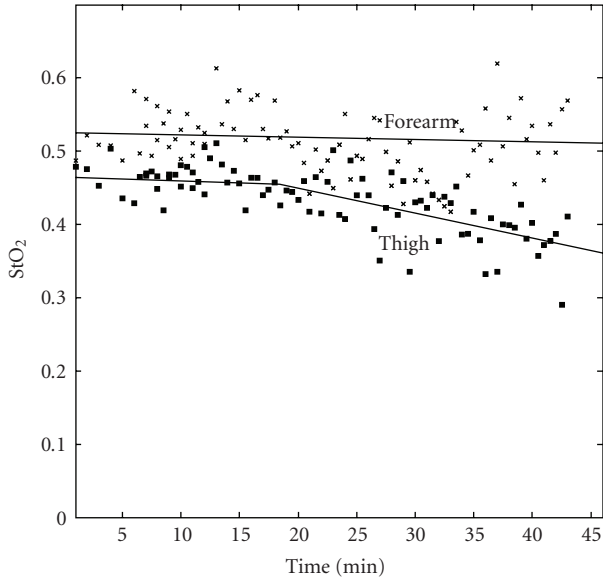


FIGURE 5: The effect of AD on the skin of an individual with complete SCI. The measurement on the forearm albeit noisy is stable around ($StO_2 \sim 52\%$), while the measurement on the thigh decreases over time going from 52% down to $\sim 37\%$.

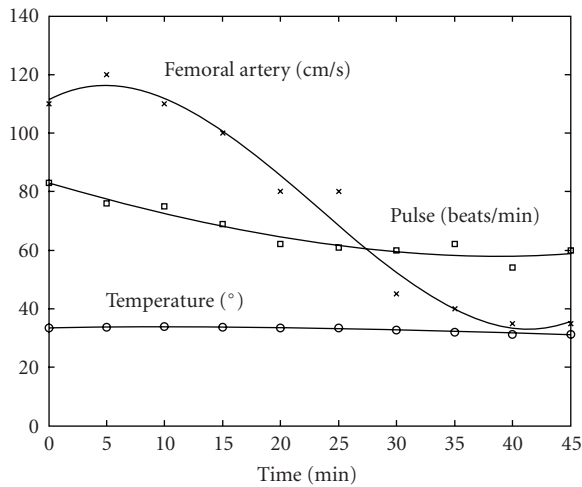


FIGURE 6: Measured modalities during an AD event, the lines 2nd order fits to the data.

can be minimized by changing the starting parameters of Bargo’s algorithm. In this paper we will show the StO_2 results obtained with the algorithm by Kollias et al.

3. RESULTS

Typical results obtained with the spectrophotometer and the fiber-optic probes over the experimental test session are shown in Figure 5. Two measurements were taken simultaneously on the subjects forearm and thigh using a dual channel spectrophotometer. AD causes a dilation of the vessel above the injury level and a constriction of the

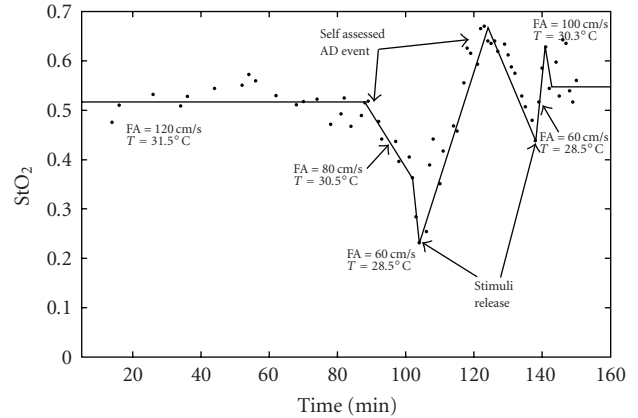


FIGURE 7: Two sequential AD events as detected by a SCI individual. At stimulus release oxygen saturation increases and overshoots to values above the norm. The patient relieved himself twice during this test at about 100 minutes and 140 minutes from the start of the test. Lines were manually drawn to pinpoint the AD events.

vessels below it. The purpose of this test was to show the effect of vessel constriction on the skin surface. Values of skin oxygenation (StO_2) were constant at the beginning of the measurement for the first 15 minutes. However, as the subject started experiencing AD, oxygen saturation decreased quickly. Similar trends are observed in other diagnostic modalities (Figure 6).

The temperature in the subjects lower extremities decreased from $33^\circ C$ to $31.2^\circ C$ over the course of the experiment, while femoral artery systolic velocity dropped from ~ 110 cm/sec to ~ 40 cm/sec. Interestingly, the pulse rate progressively slowed during the AD event, however we did not notice a significant increase in blood pressure as cited by the literature [21]. During the measurement the test subject described an increase in perspiration, and indeed an independent observation was made that the skin was noticeably moist to the touch; this is an important finding since humidity is considered a risk factor in the formation of skin ulcer, surprisingly analysis conducted with Bargo’s model did not show any change in skin water content. Finally the pulse oximetry measurements on the thumb and toe remained constant at a $97\% (\pm 1\%)$ level (not shown in graph). It is worth noting that while oxygen values in the main vessels remained constant, insufficient blood and oxygen reached the skin capillaries, possibly due to the vasoconstriction below T6.

During the entire experiment, we carefully monitored the well-being of the test subject, specifically the subjects systolic and diastolic blood pressure levels, as well as the subjects discomfort level. The first identification of AD symptoms came from the individual 15 minutes into the test; the test was interrupted at the patients request after 45 minutes.

Relieving the noxious stimulus by draining the bladder had an immediate impact on the AD symptoms, as shown in Figure 7. The release events are clearly observed in the oxygen saturation curve following an AD event. During AD oxygen content in the skin decreased to 22%. Interestingly,

a second AD event occurred caused by a re-filling of the bladder due to the large quantity of water consumed. During this second, less serious episode of AD, oxygen content in the skin decreased to 42%, which immediately recovered after the bladder was drained for a second time. Oxygen saturation values increased dramatically in a very brief time interval after the bladder was drained, surpassing normal values. This is indicative of a rush of oxygenated blood to the superficial capillary bed possibly causing reperfusion injury [17].

4. CONCLUSIONS

Autonomic dysreflexia is a fairly common event for people with spinal cord injury at or above the T6 level. Unfortunately, few SCI individuals or clinicians are aware of the potential consequences of its symptoms. The long-term effects of AD have not been explored to their full extent. One study [19] has shown that patients experiencing high levels of AD develop skin thickening, and since AD influences the circulatory system it is very possible that the skin capillary bed is also impacted. In this study we have demonstrated a quantitative method to measure the effect of AD on the skin oxygenation. Oxygen saturation is reduced to 40% of its original value and skin temperature is reduced of 2 to 3 degrees Centigrade possibly due to a decreased skin perfusion.

It is interesting to note that measurements of pulse oximetry in the thumb and toe of the test subject did not show any change with the onset of AD contrary to what was measured with the fiber probe. Pulse oximetry is a technique that measures arterial oxygenation by relying on its pulsatile nature, [33]. It is commonly accepted that the signal in pulse oximetry derives from the arterioles in the junction of dermis and hypodermis [34], this junction can be as deep as 2 mm in the skin and it is beyond the probing depth capability of our fiber optics (Figure 2). The signal measured in this paper comes from the non-pulsatile capillary blood flow in the dermis and papillary-plexus, part of the DC signal that is eliminated in pulse oximetry. Since the oxygen saturation values measured with the pulse oximeter did not change during AD, we can deduce that we are measuring a local reduction in blood flow and oxygen in lieu of a systemic physiological event. The real origin of the measured signal would be better understood with a combination of reflectance spectroscopy and laser Doppler (LD) monitoring. An independent measurement of perfusion such as the one offered by the LD would clarify the impact on the signal due to a decrease in blood volume in the capillary bed as opposed to a reduction of the oxyhemoglobin molecules. Future work will be directed to such a study. Finally we want to recognize that much work remains to be done in generalizing these findings to a larger sample group, and our measurements are to be considered preliminary, but nevertheless the effect of AD on the circulatory system has been well documented [2–4], and a clear consequence of vasoconstriction is a peripheral decrease in perfusion, which ultimately points to skin deperfusion and deoxygenation.

ACKNOWLEDGMENTS

The authors gratefully acknowledge funding from the Christopher and Dana Reeve foundation. The authors want to thank Ted Moffit of the Oregon Medical Laser Center for providing the calibrated optical phantom. Parts of this paper have appeared in the Proceedings of SPIE—Volume 6852, Optical Fibers and Sensors for Medical Diagnostics and Treatment Applications VIII, “A fiber optic probe for measurement of an autonomic dysreflexia event on SCI patients.”

REFERENCES

- [1] D. Walker, *Autonomic dysreflexia*, B.S. thesis, University of Northampton, School of Health, Northampton, UK, 2000.
- [2] A. Curt, B. Nitsche, B. Rodic, B. Schurch, and V. Dietz, “Assessment of autonomic dysreflexia in patients with spinal cord injury,” *Journal of Neurology, Neurosurgery & Psychiatry*, vol. 62, no. 5, pp. 473–477, 1997.
- [3] A.-K. Karlsson, “Autonomic dysfunction in spinal cord injury: clinical presentation of symptoms and signs,” *Progress in Brain Research*, vol. 152, pp. 1–8, 2005.
- [4] F. U. Sack, W. Funk, F. Hammersen, and K. Messer, “Microvascular injury in skeletal muscle and skin after different periods of pressure induced ischemia,” in *Microcirculation and Inflammation: Vessel Wall—Inflammatory Cells—Mediator Interaction*, vol. 12 of *Progress in Applied Microcirculation*, pp. 282–288, S. Karger, Basel, Switzerland, 1987.
- [5] M. Yamanaka and O. Ishikawa, “Hypoxic conditions decrease the mRNA expression of pro α 1(I) and (III) collagens and increase matrix metalloproteinases-1 of dermal fibroblasts in three-dimensional cultures,” *Journal of Dermatological Science*, vol. 24, no. 2, pp. 99–104, 2000.
- [6] S. J. Dalton, D. C. Mitchell, C. V. Whiting, and J. F. Tarlton, “Abnormal extracellular matrix metabolism in chronically ischemic skin: a mechanism for dermal failure in leg ulcers,” *Journal of Investigative Dermatology*, vol. 125, no. 2, pp. 373–379, 2005.
- [7] D. R. Knighton, T. K. Hunt, H. Scheuenstuhl, B. J. Halliday, Z. Werb, and M. J. Banda, “Oxygen tension regulates the expression of angiogenesis factor by macrophages,” *Science*, vol. 221, no. 4617, pp. 1283–1285, 1983.
- [8] M. Detmar, L. F. Brown, B. Berse, et al., “Hypoxia regulates the expression of vascular permeability factor/vascular endothelial growth factor (VPF/VEGF) and its receptors in human skin,” *Journal of Investigative Dermatology*, vol. 108, no. 3, pp. 263–268, 1997.
- [9] D. S. Steinbrech, M. T. Longaker, B. J. Mehrara, et al., “Fibroblast response to hypoxia: the relationship between angiogenesis and matrix regulation,” *Journal of Surgical Research*, vol. 84, no. 2, pp. 127–133, 1999.
- [10] J. Thorfinn, F. Sjöberg, and D. Lidman, “Sitting pressure and perfusion of buttock skin in paraplegic and tetraplegic patients, and in healthy subjects: a comparative study,” *Scandinavian Journal of Plastic and Reconstructive Surgery and Hand Surgery*, vol. 36, no. 5, pp. 279–283, 2002.
- [11] J. Thorfinn, F. Sjöberg, L. Sjöstrand, and D. Lidman, “Perfusion of the skin of the buttocks in paraplegic and tetraplegic patients, and in healthy subjects after a short and long load,” *Scandinavian Journal of Plastic and Reconstructive Surgery and Hand Surgery*, vol. 40, no. 3, pp. 153–160, 2006.

- [12] V. Schubert and B. Fagrell, "Local skin pressure and its effect on skin microcirculation as evaluated by laser—Doppler fluxmetry," *Clinical Physiology*, vol. 9, no. 6, pp. 535–545, 1989.
- [13] P. G. Agache and A. S. Dupond, "Recent advances in non-invasive assessment of human skin blood flow," *Acta Dermatovenereologica. Supplementum*, vol. 185, pp. 47–51, 1994.
- [14] F. U. Sack, W. Funk, F. Hammersen, and K. Messer, "Microvascular injury in skeletal muscle and skin after different periods of pressure induced ischemia," in *Microcirculation and Inflammation: Vessel Wall—Inflammatory Cells—Mediator Interaction*, vol. 12 of *Progress in Applied Microcirculation*, pp. 282–288, S. Karger, Basel, Switzerland, 1987.
- [15] E. C. Herrman, C. F. Knapp, J. C. Donofrio, and R. Salcido, "Skin perfusion responses to surface pressure-induced ischemia: implication for the developing pressure ulcer," *Journal of Rehabilitation Research and Development*, vol. 36, no. 2, pp. 109–120, 1999.
- [16] T. Mustoe, "Understanding chronic wounds: a unifying hypothesis on their pathogenesis and implications for therapy," *American Journal of Surgery*, vol. 187, no. 5, supplement 1, pp. 65S–70S, 2004.
- [17] T. A. Mustoe, K. O'Shaughnessy, and O. Kloeters, "Chronic wound pathogenesis and current treatment strategies: a unifying hypothesis," *Plastic and Reconstructive Surgery*, vol. 117, supplement 7, pp. 35S–41S, 2006.
- [18] A. D. Shaw, N. Aravindan, Z. Li, and B. J. C. J. Riedel, "Temporal variation in tissue oxygen tension and perfusion response to hypoxia and ischaemia: the importance of local control of the microcirculation," *The Internet Journal of Emergency and Intensive Care Medicine*, vol. 7, 2003.
- [19] S. L. Stover, A. M. Hale, and A. B. Buell, "Skin complications other than pressure ulcers following spinal cord injury," *Archives of Physical Medicine and Rehabilitation*, vol. 75, no. 9, pp. 987–993, 1994.
- [20] S. L. Stover, E. F. Omura, and A. B. Buell, "Clinical skin thickening following spinal cord injury studied by histopathology," *The Journal of the American Paraplegia Society*, vol. 17, no. 2, pp. 44–49, 1994.
- [21] R. P. Erickson, "Autonomic hyperreflexia: pathophysiology and medical management," *Archives of Physical Medicine and Rehabilitation*, vol. 61, no. 10, pp. 431–440, 1980.
- [22] T. Moffitt, Y.-C. Chen, and S. A. Prah, "Preparation and characterization of polyurethane optical phantoms," *Journal of Biomedical Optics*, vol. 11, no. 4, Article ID 041103, 10 pages, 2006.
- [23] P. R. Bargo, S. A. Prah, T. T. Goodell, et al., "In vivo determination of optical properties of normal and tumor tissue with white light reflectance and an empirical light transport model during endoscopy," *Journal of Biomedical Optics*, vol. 10, no. 3, Article ID 034018, 15 pages, 2005.
- [24] P. R. Bargo, S. A. Prah, and S. L. Jacques, "Optical properties effects upon the collection efficiency of optical fibers in different probe configurations," *IEEE Journal on Selected Topics in Quantum Electronics*, vol. 9, no. 2, pp. 314–321, 2003.
- [25] N. Kollias and A. H. Baqer, "Quantitative assessment of UV-induced pigmentation and erythema," *Photodermatology*, vol. 5, no. 1, pp. 53–60, 1988.
- [26] M. J. C. Van Gemert, S. L. Jacques, H. J. C. M. Sterenborg, and W. M. Star, "Skin optics," *IEEE Transactions on Biomedical Engineering*, vol. 36, no. 12, pp. 1146–1154, 1989.
- [27] L. Wang, S. L. Jacques, and L. Zheng, "MCML—Monte Carlo modeling of light transport in multi-layered tissues," *Computer Methods and Programs in Biomedicine*, vol. 47, no. 2, pp. 131–146, 1995.
- [28] T. L. Moore, M. Lunt, B. McManus, M. E. Anderson, and A. L. Herrick, "Seventeen-point dermal ultrasound scoring system—a reliable measure of skin thickness in patients with systemic sclerosis," *Rheumatology*, vol. 42, no. 12, pp. 1559–1563, 2003.
- [29] T. J. Farrell, M. S. Patterson, and B. Wilson, "A diffusion theory model of spatially resolved, steady-state diffuse reflectance for the noninvasive determination of tissue optical properties in vivo," *Medical Physics*, vol. 19, no. 4, pp. 879–888, 1992.
- [30] S. Takatani and M. D. Graham, "Theoretical analysis of diffuse reflectance from a two-layer tissue model," *IEEE Transactions on Biomedical Engineering*, vol. 26, no. 12, pp. 656–664, 1979.
- [31] G. M. Hale and M. R. Querry, "Optical constants of water in the 200 nm to 200 μm wavelength region," *Applied Optics*, vol. 12, no. 3, pp. 555–563, 1973.
- [32] S. L. Jacques and D. J. McAuliffe, "The melanosome: threshold temperature for explosive vaporization and internal absorption coefficient during pulsed laser irradiation," *Photochemistry and Photobiology*, vol. 53, no. 6, pp. 769–775, 1991.
- [33] J. F. Kelleher, "Pulse oximetry," *Journal of Clinical Monitoring and Computing*, vol. 5, no. 1, pp. 37–62, 1989.
- [34] J. L. Reuss and D. Siker, "The pulse in reflectance pulse oximetry: modeling and experimental studies," *Journal of Clinical Monitoring and Computing*, vol. 18, no. 4, pp. 289–299, 2004.

Research Article

Optical Clearing of Cranial Bone

Elina A. Genina,¹ Alexey N. Bashkatov,¹ and Valery V. Tuchin^{1,2}

¹ *Research-Educational Institute of Optics and Biophotonics, Saratov State University, Astrakhanskaya Street, 83, Saratov 410012, Russia*

² *Laser Diagnostics of Technical and Living Systems Lab, Institute of Precise Mechanics and Control of RAS, 24 Rabochaya Street, Saratov 410028, Russia*

Correspondence should be addressed to Elina A. Genina, eagenina@yandex.ru

Received 20 February 2008; Accepted 2 April 2008

Recommended by Stoyan Tanev

We present experimental results on optical properties of cranial bone controlled by administration of propylene glycol and glycerol. Both transmittance and reflectance spectra of human and porcine cranial bone *in vitro* were measured. For estimation of absorption and reduced scattering coefficients of the bone, the inverse adding-doubling method was used. The decrease of reflectance of the samples under action of the immersion agents was demonstrated. The experiments have shown that administration of the immersion liquids allows for effective controlling of tissue optical characteristics that makes bone more transparent, thereby increasing the ability of light penetration through the tissue. The presented results can be used in developing of functional imaging techniques, including OCT.

Copyright © 2008 Elina A. Genina et al. This is an open access article distributed under the Creative Commons Attribution License, which permits unrestricted use, distribution, and reproduction in any medium, provided the original work is properly cited.

1. INTRODUCTION

Interest in using optical methods in the development of noninvasive clinical functional cerebral imaging systems for physiological-condition monitoring [1, 2], cancer diagnostics, and therapies [3, 4] increases due to their simplicity, safety, and low cost in contrast to conventional X-ray computed tomography, magnetic resonance imaging, and ultrasound imaging [5–8]. Spectroscopic techniques are capable of deep imaging of tissues that could provide information of blood oxygenation and tissue metabolism [1, 2, 9, 10] and detect brain malignancies [4, 11, 12]. However, the main limitations of the optical imaging techniques, including diffusion optical tomography, optical coherent tomography, and reflectance spectroscopy deal with the strong light scattering in superficial tissues, which cause decrease of spatial resolution, low contrast, and small penetration depth. One of the prospective solutions of the problem is a reduction of light scattering of the upper tissue layers that provides improvement of image quality and precision of spectroscopic information getting from tissue depth [5, 13–15].

It is well known that the major source of scattering in tissues and cell structures is a refractive index mismatch

between cell organelles, like mitochondria and cytoplasm, extracellular media and tissue structural components such as collagen and elastin fibres [5]. The tissue scattering properties can be significantly changed due to action of immersion liquids [15–20]. Administration of the immersion liquid having a refractive index higher than that of tissue interstitial fluid and/or hyperosmotic properties induces a partial replacement of the interstitial fluid by immersion substance and hence matching of refractive indices of tissue scatterers and the modified interstitial fluid. The matching, correspondingly, causes the decrease of scattering. As immersion liquids aqueous solutions of glucose and mannitol, propylene glycol, glycerol, and other biocompatible chemicals are used [15–20].

The possibility of selective translucence of cranial bone can be very useful in developing techniques of brain functional imaging. A potential benefit of the optical clearing technique is an improvement of laser therapeutic techniques that rely on sufficient light penetration to a target embedded in tissue. Combining optical clearing with laser radiation could reduce the laser fluence required for a therapeutic effect. Another application of the optical method is a noninvasive visualization of brain blood vessels, hematomas, and small pathologic structures (including cancerous growth)

with a high resolution. This is important for diagnosis and treatment of many diseases such as tumors of brain, vascular pathologies, and so forth. However, despite the numerous studies of optical clearing of such tissues as skin, sclera, *dura mater*, and so forth, the bone optical clearing is not investigated enough up to now.

In this study, we investigate optical clearing of both human and porcine cranial bone *in vitro* under the action of propylene glycol and glycerol.

2. BONE STRUCTURE AND PHYSICAL PROPERTIES

The structural components of the bones consist of an inorganic matrix (largely mineralised) and an organic matrix [21, 22]. The inorganic matrix contains calcium hydroxyapatite, which is responsible for the compressive strength of bone, and osteocalcium phosphate. The main components of the organic matrix are collagen, proteins, blood cells, and lipids [23]. The amount of bone mineral matrix is 16%, the lipid content is 54%, the proteins content is 16%, and water contributes 16% [23]. It is the calcium and phosphorus component of the inorganic matrix that makes bone hard and rigid, and the arrangement of the collagen fibres in the organic matrix that makes it strong. Porosity of the bones is 5–10% [23].

At microstructural length scales, cortical bone is organised into 200–300 μm diameter secondary osteons [24], which are composed of large vascular channels (50–90 μm diameter) surrounded by circumferential lamellar rings (3–7 μm thick), with the so-called “cement lines” at the outer boundary [25]. At the nanostructural level, the lamellae are composed of organic type-I mineralised collagen fibres (up to 15 μm in length, 50–70 nm in diameter, and formed by regular arrangement of subnanostructural collagen molecules) bound and impregnated with inorganic carbonated apatite nanocrystals (about 30 nm in length and width, 2–3 nm in thickness) [26, 27].

Water is of significant importance for the living bone and is one of its major components. Bone water occurs at various locations and in different binding states. Water in bone may be found associated with the mineral phase, bound to the organic phase (collagen and cement substance), or free (bulk water) [28, 29]. The most tightly bound water is the one occupying the calcium ion coordination sites in the apatite-like crystals (about 35 mg of water/g mineral) [30]. A significant less tightly bound fraction is water associated with collagen fibrils. In the unmineralised state as the bone matrix is laid down by osteoblasts, the collagen fibers produced contain a large volume fraction of water (up to 60%) [31]. During calcification, however, apatite crystals are deposited in the organic matrix, gradually displacing the osteoid water and reducing it down to a 20% volume fraction. Eventually, this fraction drops to 10% in senile bone [32]. Bulk water fills the pores of the calcified matrix, which form a network of interconnecting channels (the lacunocanalicular system), which communicate the Haversian canals (the bone vascular system) with the osteocytes, embedded in the mineralized matrix [28, 31]. This communication network serves for transport of nutrients, waste products, and signaling

molecules from the vascular system to the osteocytes and vice versa. The water channels are also the transport pathways for calcium and phosphate ions flowing in and out of bone tissue, which acts as a mineral reservoir for the rest of the organism [28].

Refractive index of the whole cranial bone has been estimated by Ascenzi and Fabry [33] at various stages of mineralisation to range from 1.555 to 1.564. Components of the tissue have the following refractive indices: apatite: > 1.623 [34], hydrated collagen (type I): 1.43 [35], and lipids ~1.45 [36].

3. MATERIALS AND METHODS

3.1. Materials

For this study, five porcine and ten human cranial bone samples were used. All bone samples were cortical (or compact) bones. The samples of human cranial bone were obtained from *postmortem* examinations. All samples were kept in saline at temperature about 5°C until spectroscopic measurements. The bone samples were measured during 4–6 hours after autopsy. The area of the samples was about 25 × 25 mm². The thickness of each bone sample was measured with a micrometer in several points over the sample surface and averaged. Precision of the single measurement was ±50 μm . Thickness of the samples varied from 1.6 ± 0.1 to 5.0 ± 0.5 mm.

In this study, the commercially available propylene glycol (“Reactive,” Russia) and glycerol (“Ph. Eur.,” Germany) have been used as clearing agents. The refractive index of propylene glycol and glycerol has been measured by Abbe refractometer at wavelength 589 nm as 1.43 and 1.47, respectively.

3.2. Experimental setups

The measurements of bone reflectance have been performed in the spectral range 450–1000 nm using a commercially available optical multichannel spectrometer LESA-5 (“BioSpec,” Moscow, Russia) with a fiber-optical probe. The scheme of the experimental setup is shown in Figure 1. The fiber optical probe consists of seven optical fibers. All fibers had 200 μm core diameter and a numerical aperture of 0.22. The central fiber delivers incident light to the tissue surface, and six fibers, placed around the central fiber, collect reflected light. Distance between the delivering and receiving fibers is 290 μm . As a reference, a white slab BaSO₄ with a smooth surface has been used. The sample of bone was placed into cuvette with the immersion liquid. For spectrophotometric measurements, each sample was removed from the cuvette. Then the sample was again placed in the cuvette.

The total transmittance and diffuse reflectance measurements have been performed in the 800–2000 nm wavelength range using the commercially available spectrophotometer CARY-2415 (“Varian,” Australia) with an integrating sphere (Figure 2). Inner diameter of the sphere is 100 mm, size of the entrance port is 20 × 20 mm, and diameter of the exit port is

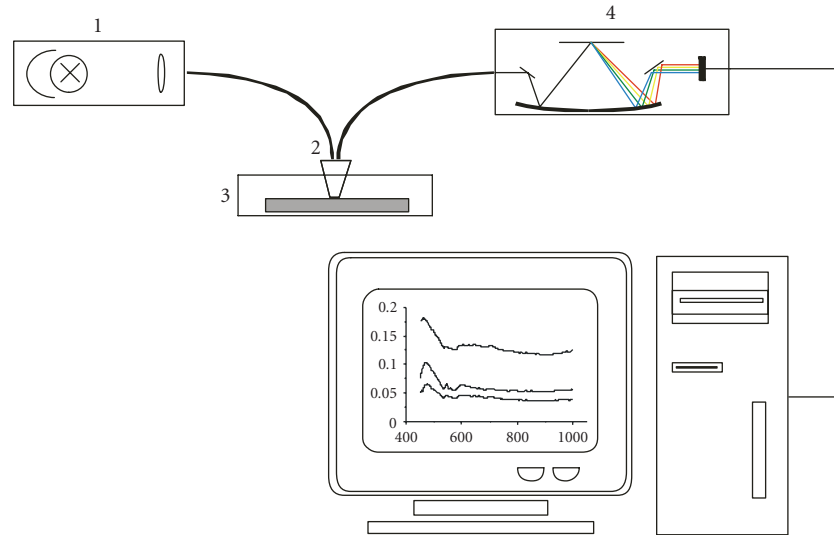


FIGURE 1: The geometry of the measurements in reflectance mode with the spectrometer LESA-5: (1) halogen lamp (2) fiber-optical probe (3) cuvette with a bone sample (4) grating and photodiode array.

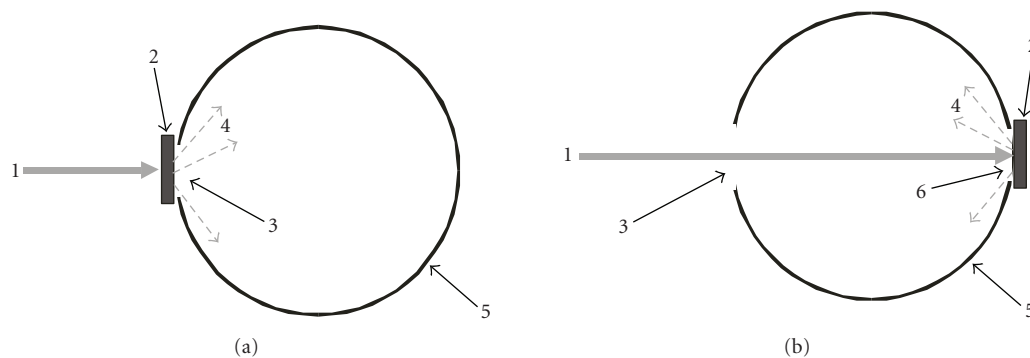


FIGURE 2: The geometry of the measurements in: (a) transmittance mode, (b) reflectance mode: (1) the incident beam (diameter 3 mm) (2) the bone sample (3) the entrance port (square 20×20 mm) (4) the transmitted (or diffuse reflected) radiation (5) the integrating sphere (inner diameter is 100 mm) and (6) the exit port (diameter 16 mm).

16 mm. As a light source, a halogen lamp with filtering of the radiation in the studied spectral range has been used in the measurements. The diameter of incident light beam on the tissue sample is 3 mm. Scan rate is 2 nm/s.

The measurements were carried out at room temperature about 20°C .

Images of cranial porcine bone during optical clearing under action of pure propylene glycol during 24 hours were obtained by a digital camera with crossed polarizers.

3.3. Processing of experimental data

For processing the experimental data and determination the change of the optical properties of tissue, the inverse adding-doubling (IAD) method developed by Prahl et al. [37] has been used. The method is widely used in tissue optics for processing the experimental data of spectrophotometry with integrating spheres [38, 39]. An important advantage of the IAD method when applied to tissue optics is a possibility of

rapidly obtaining iterative solutions with the aid of up-to-date microcomputers [5].

This method allows one to determine the absorption (μ_a) and the reduced scattering coefficients ($\mu'_s = \mu_s(1 - g)$) of a tissue from the measured values of the total transmittance and the diffuse reflectance. Here, μ_s is the scattering coefficient, and g is the anisotropy factor of scattering. In these calculations, the anisotropy factor has been fixed as 0.9, since this value is typical for the tissue in the visible and NIR spectral ranges [5].

4. RESULTS AND DISCUSSION

Result of cranial bone clearing can be illustrated by Figure 3. The complete clearing of the bone took place in about 24 hours. Figure 3 shows images of cranial porcine bone before (a) and after (b) optical clearing by propylene glycol during 24 hours. The cross drawn on a paper was covered by the bone to observe the increase of the sample translucence. The

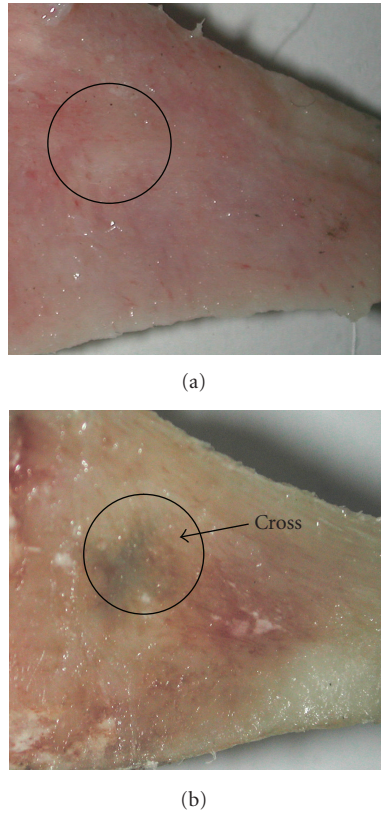


FIGURE 3: The bone sample before (a) and after (b) optical clearing by propylene glycol during 24 hours. The cross-observed through the bone is marked by an arrow.

thickness of the sample was 1.5 ± 0.2 mm. It is well seen that before immersion agent action the tissue was turbid, and the image of cross was not seen. After 24 hours, the bone became more transparent and the cross image was observed. Besides, blood vessels being under the bone surface were also clearly seen.

In Figure 4, spectra of reflectance of cranial porcine bone during the action of propylene glycol are presented. In the spectra, three spectral bands corresponding to blood absorption in the visible range are well seen. They are the α -band with maximum at 537 nm and the β -band with maximum at 568 nm of oxyhemoglobin absorption [40]. Decrease of reflectance in the short-wavelength range from 450 to 470 nm can be connected with absorption in long-wavelength wing of the Soret band of oxyhemoglobin with maximum at 415 nm [40]. The action of immersion agent produces the decrease of the reflectance of the bone tissue (due to decreasing light scattering in the tissue) in whole studied spectral range that indicates that bone becomes more transparent.

In the visible spectral range, significant decrease of reflectance of the sample wetted in propylene glycol in comparison with untreated sample is observed during the first few minutes. It can be explained by effective immersion of the upper layers of the sample. Further decrease of the

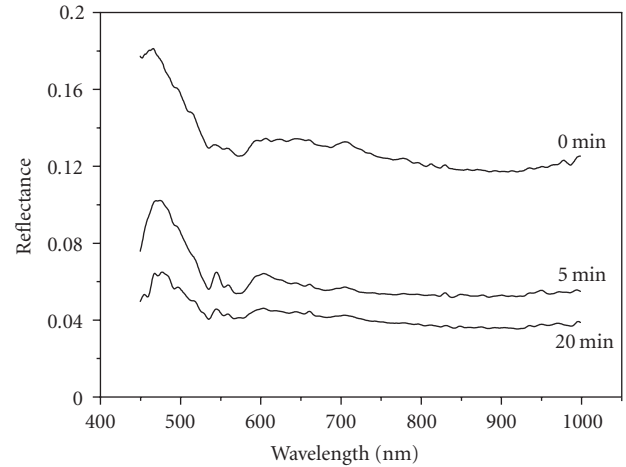


FIGURE 4: The reflectance spectra of the bone sample measured concurrently with administration of propylene glycol at different time intervals.

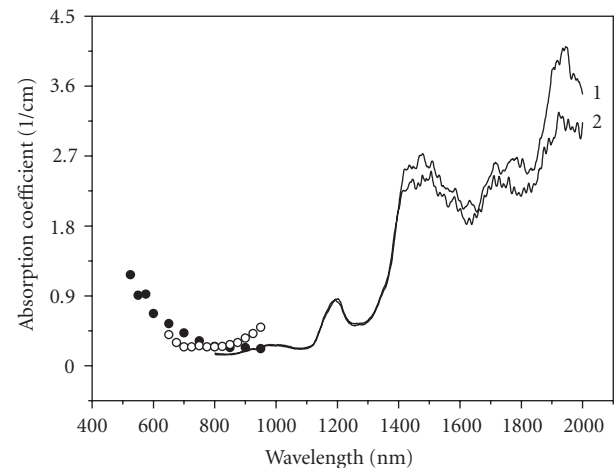


FIGURE 5: The absorption spectra of bone sample measured before (1) and after administration of glycerol (2) during an hour. Black circles correspond to data presented in [41], and open circles correspond to data presented in [42].

bone reflectance is caused by penetration of immersion agent into the sample on the depth of probing (about $100 \mu\text{m}$ for the given centre-to-centre separation of the source and detector fibers) and partial matching of refractive indices of both inorganic matrix and interstitial substance.

Figures 5 and 6 demonstrate dynamics of optical properties of human cranial bone after administration of glycerol in spectral range 800–2000 nm calculated by IAD method on the basis of measured values of the total transmittance and the diffuse reflectance. Figure 5 presents typical wavelength dependence of the bone absorption coefficient before glycerol administration and after an hour of glycerol action. Figure 6 shows typical wavelength dependence of the reduced scattering coefficient of the bone sample before glycerol administration and after an hour of glycerol action.

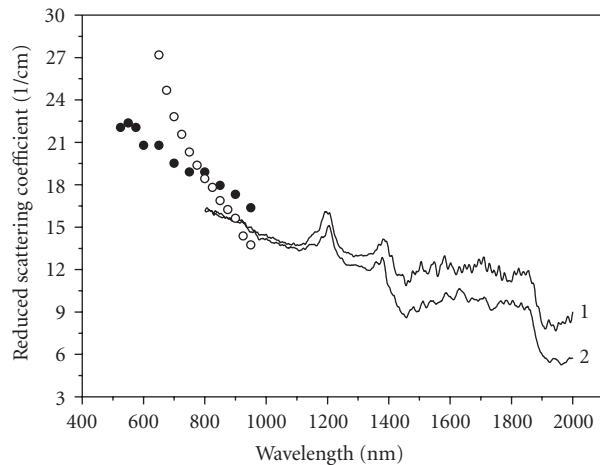


FIGURE 6: The reduced scattering spectra of bone sample measured before (1) and after administration of glycerol (2) during an hour. Black circles correspond to data presented in [41], and open circles correspond to data presented in [42].

In the near infrared (NIR) spectral range, the absorption bands of water with maximums at 978, 1192, 1464, and 1930 nm are observed [43, 44]. Absorption band with maximum at 1745 nm corresponds to absorption band of lipids [45]. Comparison of the data obtained in this study and presented by other authors [41, 42] shows accordance between them in the spectral range 800–1000 nm. Insignificant differences between these data can be explained by differences in the used measuring techniques and the tissue samples preparation and storage methods [46].

It is well seen that administration of hyperosmotic solutions into cranial bone tissue allows for effective controlling its optical properties in NIR range. The transparence of the bone increases due to matching of the refractive indices of the hydroxyapatite matrix and the interstitial substance. Scatterers in bone tissues are large osteons with diameter 200–300 μm and cavities between osteons with diameter 50–90 μm as well as nanostructures that cause complex character of light scattering.

Figure 6 shows that the reduced scattering coefficient decreases with wavelength increasing, which, in general, corresponds to spectral behaviour of the scattering characteristics of most of tissues [5, 37, 39]. A comparison of the data obtained by us in the spectral range 800–950 nm with the data presented by Ugryumova et al. [41] and Firbank et al. [42] shows an accordance between them (see Figures 5 and 6). Discrepancy between these data does not prevail 20% [46]. In the spectral range from 1000 to 2000 nm, the reduced scattering coefficient decreases nonmonotonically with increasing of wavelength with peaks corresponding to the absorption bands in contrast to spectral behaviour of bone scattering in the spectral range from 800 to 1000 nm, where the reduced scattering coefficient decreases smoothly with wavelength increasing. It can be explained by significant decrease of the anisotropy factor in the range of water absorption bands that produces the increase of the reduced scattering coefficient and appearance of bands in its spectrum [47, 48].

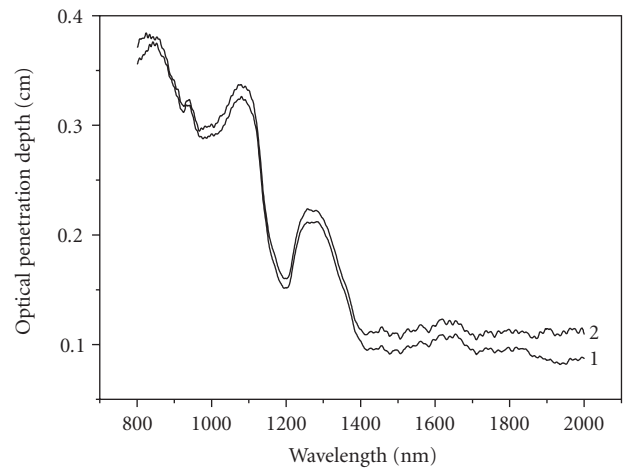


FIGURE 7: The optical penetration depth δ of light into human bone tissue over the wavelength range from 800 to 2000 nm before (1) and after administration of glycerol (2) during an hour.

The decrease of both absorption and scattering coefficients of bone tissue under action of immersion agent (see Figures 5, 6) is not uniform in the studied range. It is well seen that in the wavelength range from 800 to 1400 nm, absorption coefficient of the bone sample does not change. In the range from 1400 to 2000 nm, the decrease of the absorption coefficient is observed in the following way: the average decreasing was about 8% in the range 1400–1800 nm and about 20% in the range 1800–2000 nm. It can be explained by replacing of bone water by the surrounding glycerol solution. Since bone absorption properties in the spectral ranges are determined by water absorption, then replacing of bone water by dehydrogenated glycerol produced decrease of bone absorption coefficient. Another explanation of the decreasing of the bone absorption coefficient can be connected with the change of regime of photon scattering from the multiple to a low-scattering mode. In this case, the increase of photons free path length should be observed and, thus, more photons pass the tissue layer almost without absorption.

The decrease of tissue reduced scattering coefficient is observed in whole studied wavelength range. With increasing of wavelength, the effect also becomes more significant. Analysis of the experimental results has shown that the average decreasing of the coefficient was about 2% in the range 800–1100 nm, about 8% in the range 1100–1400 nm, and about 30% in the range 1400–2000 nm.

Numerous publications discuss the mechanisms of clearing of soft tissues (i.e., skin, *dura mater*, sclera, and others) [5, 15–20, 49, 50]. The main mechanisms of light scattering reduction induced by immersion agents are (1) dehydration of tissue constituents, (2) partial replacement of the interstitial fluid by the immersion substance, and (3) structural modification or dissociation of collagen [5, 15–20, 49, 50]. We may hypothesise that dissociation of collagen of bone is not of great importance for the clearing as it may be in soft tissues because of a rigid structure of bone tissue. We believe that the main role in the clearing process has the replacement of water in the interstitial space by the immersion substance

that leads to matching of the refractive indices between tissue scatterers and ground matter. Both glycerol and propylene glycol, as hypersosmotic agents, stimulate diffusion flow of bulk water from tissue to surrounding agent solution which also leads to additional refractive index matching between scatterers and interstitial space materials. On the other hand, they prevent total dehydration of tissue due to holding water inside, as water dilutes initial agent solution [49].

The depth penetration of light into a biological tissue is an important parameter for the correct determination of the irradiation dose in photothermal and photodynamic therapy of various diseases [5]. Estimation of the light penetration depth δ can be performed with the relation [51]

$$\delta = \frac{1}{\sqrt{3\mu_a(\mu_a + \mu'_s)}}. \quad (1)$$

Calculation of the optical penetration depth has been performed with the absorption and the reduced scattering coefficient values presented in Figures 5 and 6, respectively, and the result is presented in Figure 7. In Figure 7, it is seen that in dependence on the wavelength, the penetration depth varies considerably. The penetration depth is maximal in the spectral ranges 800–900 nm and 1000–1100 nm, where the optical radiation penetrates up to depths of 0.32–0.37 cm (light attenuation of 2.7-fold) in intact cranial bone. During an hour after administration of glycerol, the optical penetration depth increases by 5% in this spectral range. In the spectral range 1400–2000 nm, the penetration depth increases more than 20%.

5. CONCLUSION

The changes of optical properties of the human cranial bone in vitro under action of glycerol have been determined over the wavelength range 800–2000 nm using the integrating sphere technique and the inverse adding-doubling method. The reflectance change of the porcine cranial bone in vitro under action of propylene glycol has been determined over the wavelength range 450–1000 nm using the optical multichannel spectrometer. The decrease of both absorption and reduced scattering coefficient of the samples up to 20% and 30%, respectively, under action of glycerol has been demonstrated. The decrease of bone reflectance under action of propylene glycol was up to 70%.

The experiments have shown that administration of the immersion liquids allows for effective control of bone optical characteristics that makes bone more transparent, thereby increasing the ability of light penetration through the tissue. The presented results can be used in the developing of functional imaging techniques, including OCT and reflectance spectroscopy.

ACKNOWLEDGMENTS

The research described in this publication has been made possible, in part, by Grants of CRDF RNP.2.1.1.4473, Grant of RFBR no. 06-02-16740, and Russian Federation President's Grant no. 208-2008.2 "Supporting of Scientific

Schools." The authors would like to thank Professors V. I. Kochubey and Ms. N. A. Lakodina (Department of Optics and Biomedical Physics of Saratov State University) for the help in the experiments. They also would like to thank Dr. S. V. Eremina (Department of English and Intercultural Communication of Saratov State University) for the help in manuscript translation into English.

REFERENCES

- [1] R. D. Frostig, Ed., *In Vivo Optical Imaging of Brain Function*, CRC Press, Boca Raton, Fla, USA, 2002.
- [2] E. Gratton, V. Toronov, U. Wolf, M. Wolf, and A. Webb, "Measurement of brain activity by near-infrared light," *Journal of Biomedical Optics*, vol. 10, no. 1, Article ID 011008, 13 pages, 2005.
- [3] S. Krishnamurthy, S. K. Powers, P. Witmer, and T. Brown, "Optimal light dose for interstitial photodynamic therapy in treatment for malignant brain tumors," *Lasers in Surgery and Medicine*, vol. 27, no. 3, pp. 224–234, 2000.
- [4] V. X. D. Yang, P. J. Muller, P. Herman, and B. C. Wilson, "A multispectral fluorescence imaging system: design and initial clinical tests in intra-operative photofrin-photodynamic therapy of brain tumors," *Lasers in Surgery and Medicine*, vol. 32, no. 3, pp. 224–232, 2003.
- [5] V. V. Tuchin, *Tissue Optics: Light Scattering Methods and Instruments for Medical Diagnosis*, SPIE Press Monograph Vol. PM166, SPIE Press, Bellingham, Wash, USA, 2nd edition, 2007.
- [6] W. A. Kalender, "X-ray computed tomography," *Physics in Medicine and Biology*, vol. 51, no. 13, pp. R29–R43, 2006.
- [7] Y. Chen, D. R. Taylor, X. Intes, and B. Chance, "Correlation between near-infrared spectroscopy and magnetic resonance imaging of rat brain oxygenation modulation," *Physics in Medicine and Biology*, vol. 48, no. 4, pp. 417–427, 2003.
- [8] X. Wang, Y. Pang, G. Ku, X. Xie, G. Stoica, and L. V. Wang, "Noninvasive laser-induced photoacoustic tomography for structural and functional in vivo imaging of the brain," *Nature Biotechnology*, vol. 21, no. 7, pp. 803–806, 2003.
- [9] D. A. Benaron, S. R. Hintz, A. Villringer, et al., "Noninvasive functional imaging of human brain using light," *Journal of Cerebral Blood Flow and Metabolism*, vol. 20, no. 3, pp. 469–477, 2000.
- [10] J. C. Hebden, A. Gibson, T. Austin, et al., "Imaging changes in blood volume and oxygenation in the newborn infant brain using three-dimensional optical tomography," *Physics in Medicine and Biology*, vol. 49, no. 7, pp. 1117–1130, 2004.
- [11] F. Bevilacqua, D. Piguet, P. Marquet, J. D. Gross, B. J. Tromberg, and C. Depeursinge, "In vivo local determination of tissue optical properties: applications to human brain," *Applied Optics*, vol. 38, no. 22, pp. 4939–4950, 1999.
- [12] W.-C. Lin, S. A. Toms, M. Johnson, E. D. Jansen, and A. Mahadevan-Jansen, "In vivo brain tumor demarcation using optical spectroscopy," *Photochemistry and Photobiology*, vol. 73, no. 4, pp. 396–402, 2001.
- [13] D. A. Boas, "A fundamental limitation of linearized algorithms for diffuse optical tomography," *Optics Express*, vol. 1, no. 13, pp. 404–413, 1997.
- [14] C. L. Smithpeter, A. K. Dunn, A. J. Welch, and R. Richards-Kortum, "Penetration depth limits of in vivo confocal reflectance imaging," *Applied Optics*, vol. 37, no. 13, pp. 2749–2754, 1998.

- [15] V. V. Tuchin, "A clear vision for laser diagnostics (review)," *IEEE Journal on Selected Topics in Quantum Electronics*, vol. 13, no. 6, pp. 1621–1628, 2007.
- [16] R. Cicchi, F. S. Pavone, D. Massi, and D. D. Sampson, "Contrast and depth enhancement in two-photon microscopy of human skin ex vivo by use of optical clearing agents," *Optics Express*, vol. 13, no. 7, pp. 2337–2344, 2005.
- [17] I. V. Meglinski, A. N. Bashkatov, E. A. Genina, D. Y. Churmakov, and V. V. Tuchin, "The enhancement of confocal images of tissues at bulk optical immersion," *Laser Physics*, vol. 13, no. 1, pp. 65–69, 2003.
- [18] E. D. Jansen, P. M. Pickett, M. A. Mackanos, and J. Virostko, "Effect of optical tissue clearing on spatial resolution and sensitivity of bioluminescence imaging," *Journal of Biomedical Optics*, vol. 11, no. 4, Article ID 041119, 7 pages, 2006.
- [19] M. G. Ghosn, V. V. Tuchin, and K. V. Larin, "Depth-resolved monitoring of glucose diffusion in tissues by using optical coherence tomography," *Optics Letters*, vol. 31, no. 15, pp. 2314–2316, 2006.
- [20] I. V. Larina, E. F. Carbajal, V. V. Tuchin, M. E. Dickinson, and K. V. Larin, "Enhanced OCT imaging of embryonic tissue with optical clearing," *Laser Physics Letters*, vol. 5, pp. 476–480, 2008.
- [21] A. Boskey and R. Mendelsohn, "Infrared analysis of bone in health and disease," *Journal of Biomedical Optics*, vol. 10, no. 3, Article ID 031102, 9 pages, 2005.
- [22] J. W. Ager III, R. K. Nalla, K. L. Breeden, and R. O. Ritchie, "Deep-ultraviolet Raman spectroscopy study of the effect of aging on human cortical bone," *Journal of Biomedical Optics*, vol. 10, no. 3, Article ID 034012, 8 pages, 2005.
- [23] A. Pifferi, A. Torricelli, P. Taroni, et al., "Optical biopsy of bone tissue: a step toward the diagnosis of bone pathologies," *Journal of Biomedical Optics*, vol. 9, no. 3, pp. 474–480, 2004.
- [24] J. Currey, "'Osteons' in biomechanical literature," *Journal of Biomechanics*, vol. 15, no. 9, p. 717, 1982.
- [25] S. Weiner and H. D. Wagner, "The material bone: structure-mechanical function relations," *Annual Review of Materials Science*, vol. 28, no. 1, pp. 271–298, 1998.
- [26] A. S. Posner, "Bone mineral and the mineralisation process," in *Bone and Mineral Research*, W. A. Peck, Ed., Elsevier, Amsterdam, The Netherlands, 1987.
- [27] J.-Y. Rho, L. Kuhn-Spearing, and P. Zioupos, "Mechanical properties and the hierarchical structure of bone," *Medical Engineering & Physics*, vol. 20, no. 2, pp. 92–102, 1998.
- [28] M. A. Fernández-Seara, S. L. Wehrli, and F. W. Wehrli, "Diffusion of exchangeable water in cortical bone studied by nuclear magnetic resonance," *Biophysical Journal*, vol. 82, no. 1, pp. 522–529, 2002.
- [29] E. E. Wilson, A. Awonusi, M. D. Morris, D. H. Kohn, M. M. J. Tecklenburg, and L. W. Beck, "Three structural roles for water in bone observed by solid-state NMR," *Biophysical Journal*, vol. 90, no. 10, pp. 3722–3731, 2006.
- [30] W. F. Neuman and M. W. Neuman, *Skeletal Dynamics the Chemical Dynamics of Bone Mineral*, University of Chicago Press, Chicago, Ill, USA, 1958.
- [31] F. W. Wehrli and M. A. Fernández-Seara, "Nuclear magnetic resonance studies of bone water," *Annals of Biomedical Engineering*, vol. 33, no. 1, pp. 79–86, 2005.
- [32] R. F. Robinson, "An electron-microscopy study of the crystalline inorganic component of bone and its relationship to the organic matrix," *Journal of Bone and Joint Surgery*, vol. 34-A, no. 2, pp. 389–435, 1952.
- [33] A. Ascenzi and C. Fabry, "Technique for dissection and measurement of refractive index of osteones," *Journal of Biophysical and Biochemical Cytology*, vol. 6, pp. 139–143, 1959.
- [34] F. A. Duck, *Physical Properties of Tissue: A Comprehensive Reference Book*, Academic Press, London, UK, 1990.
- [35] X.-J. Wang, T. E. Milner, M. C. Chang, and J. S. Nelson, "Group refractive index measurement of dry and hydrated type I collagen films using optical low-coherence reflectometry," *Journal of Biomedical Optics*, vol. 1, no. 2, pp. 212–216, 1996.
- [36] V. V. Tuchin, *Optical Clearing of Tissues and Blood*, SPIE Press Monograph Vol. PM154, SPIE Press, Bellingham, Wash, USA, 2005.
- [37] S. A. Prahl, M. J. C. van Gemert, and A. J. Welch, "Determining the optical properties of turbid media by using the adding-doubling method," *Applied Optics*, vol. 32, no. 4, pp. 559–568, 1993.
- [38] A. N. Bashkatov, E. A. Genina, V. I. Kochubey, and V. V. Tuchin, "Optical properties of human skin, subcutaneous and mucous tissues in the wavelength range from 400 to 2000 nm," *Journal of Physics D*, vol. 38, no. 15, pp. 2543–2555, 2005.
- [39] D. K. Sardar, G.-Y. Swanland, R. M. Yow, R. J. Thomas, and A. T. C. Tsin, "Optical properties of ocular tissues in the near infrared region," *Lasers in Medical Science*, vol. 22, no. 1, pp. 46–52, 2007.
- [40] S. A. Prahl, "Optical absorption of hemoglobin," 1999, <http://omlc.ogi.edu/spectra/hemoglobin/>.
- [41] N. Ugryumova, S. J. Matcher, and D. P. Attenburrow, "Measurement of bone mineral density via light scattering," *Physics in Medicine and Biology*, vol. 49, pp. 469–483, 2004.
- [42] M. Firbank, M. Hiraoka, M. Essenpreis, and D. T. Delpy, "Measurement of the optical properties of the skull in the wavelength range 650–950 nm," *Physics in Medicine and Biology*, vol. 38, no. 4, pp. 503–510, 1993.
- [43] K. F. Palmer and D. Williams, "Optical properties of water in the near infrared," *Journal of the Optical Society of America*, vol. 64, no. 8, pp. 1107–1110, 1974.
- [44] L. Kou, D. Labrie, and P. Chylek, "Refractive indices of water and ice in the 0.65–2.5 μm spectral range," *Applied Optics*, vol. 32, no. 19, pp. 3531–3543, 1993.
- [45] K. A. Martin, "Direct measurement of moisture in skin by NIR spectroscopy," *Journal of the Society of Cosmetic Chemists*, vol. 44, pp. 249–261, 1993.
- [46] A. N. Bashkatov, E. A. Genina, V. I. Kochubey, and V. V. Tuchin, "Optical properties of human cranial bone in the spectral range from 800 to 2000 nm," in *Saratov Fall Meeting 2005: Optical Technologies in Biophysics and Medicine VII*, vol. 6163 of *Proceedings of SPIE*, p. 11, Saratov, Russia, July 2006.
- [47] Y. Du, X. H. Hu, M. Caiveau, X. Ma, G. W. Kalmus, and J. Q. Lu, "Optical properties of porcine skin dermis between 900 nm and 1500 nm," *Physics in Medicine and Biology*, vol. 46, no. 1, pp. 167–181, 2001.
- [48] J.-P. Ritz, A. Roggan, C. Isbert, G. Müller, H. J. Buhr, and C.-T. Germer, "Optical properties of native and coagulated porcine liver tissue between 400 and 2400 nm," *Lasers in Surgery and Medicine*, vol. 29, no. 3, pp. 205–212, 2001.
- [49] E. A. Genina, A. A. Korobko, A. N. Bashkatov, V. V. Tuchin, I. V. Yaroslavsky, and G. B. Altshuler, "Investigation of skin water loss and glycerol delivery through stratum corneum," in *Saratov Fall Meeting 2006: Optical Technologies in Biophysics and Medicine VIII*, vol. 6535 of *Proceedings of SPIE*, Saratov, Russia, September 2007.

- [50] J. Hirshburg, B. Choi, J. S. Nelson, and A. T. Yeh, "Collagen solubility correlates with skin optical clearing," *Journal of Biomedical Optics*, vol. 11, no. 4, Article ID 040501, 3 pages, 2006.
- [51] J.-P. Ritz, A. Roggan, C. Isbert, G. Müller, H. J. Buhr, and C.-T. Germer, "Optical properties of native and coagulated porcine liver tissue between 400 and 2400 nm," *Lasers in Surgery and Medicine*, vol. 29, no. 3, pp. 205–212, 2001.

Research Article

Optical Biomedical Diagnostics: Sensors with Optical Response Based on Two-Photon Excited Luminescent Dyes for Biomolecules Detection

V. M. Yashchuk,¹ S. M. Yarmoluk,² V. Yu. Kudrya,¹ M. Yu. Losytskyy,^{1,2} V. P. Tokar,^{1,2} V. M. Kravchenko,¹ V. B. Kovalska,² A. O. Balanda,² and D. V. Kryvorotenko²

¹Department of Physics, Taras Shevchenko Kyiv University, Build.1, Academic Glushkov's Street 2, Kyiv 03680, Ukraine

²Institute of Molecular Biology and Genetics, National Academy of Sciences of Ukraine, Zabolotnogo Street 150, Kyiv 03143, Ukraine

Correspondence should be addressed to V. M. Yashchuk, vmyashchuk@univ.kiev.ua

Received 29 February 2008; Accepted 4 April 2008

Recommended by Stoyan Tanev

The spectral properties of novel styryl dyes developed for the biomacromolecules (such as DNA) detection and imaging were investigated. The energy structures of dye molecules were examined. The spectral data prove that dyes aggregate and interact with DNA. The essential increase of the fluorescence intensity of dyes in the presence of DNA was observed. The photostability and phototoxic influence on the DNA of several styryl dyes were studied by analyzing absorption, fluorescence, and phosphorescence spectra of these dyes and dye-DNA systems. Changes of the optical density value of dye-DNA solutions caused by the irradiation were fixed in the DNA and dye absorption wavelength regions. Fluorescence emission of dye-DNA complexes upon two-photon excitation at wavelength 1064 nm with the 20-nanosecond pulsed YAG:Nd³⁺ laser and at 840 nm with the 90 femtosecond pulsed Ti:sapphire laser was registered. The values of two-photon absorption cross-sections of dye-DNA complexes were evaluated.

Copyright © 2008 V. M. Yashchuk et al. This is an open access article distributed under the Creative Commons Attribution License, which permits unrestricted use, distribution, and reproduction in any medium, provided the original work is properly cited.

1. INTRODUCTION

Fluorescent probes are widely used in biological and medical studies for the detection of biological molecules and fluorescent imaging of biological objects [1]. The two important properties of these probes permitting their application for fluorescent detection are (1) strong affinity of the probe binding to the biological molecule of interest, and (2) sharp enhancement of the fluorescence intensity of the probe upon such binding. Commonly, the fluorescence of the probes is excited with either ultraviolet (UV) or visible light, so that the probe molecule is excited by one absorbed photon (single photon excitation). The single photon excitation (SPE) approach has several disadvantages. First, the light in UV and visible regions (250–700 nm) cannot penetrate deep into the biological tissue, being both absorbed and scattered, and hence is not useful for the tissue fluorescent scanning. The probes with absorption in the region 700–1000 nm, where the majority of biological objects are transparent, are not easy to design, and if designed such probes would

fluoresce in infrared (IR) region, which is not convenient for observation. Second, using SPE (especially with UV light) causes significant damage of the studied biological objects, not only in the point of detection, but also on the whole way of the beam. Third, when used for three-dimensional (3D) scanning microscopy, SPE results in rather restricted resolution in the two directions perpendicular to the beam and in very poor resolution along the direction parallel to the beam propagation.

The problems mentioned above could be overcome with the help of two-photon excitation (TPE) of the fluorescent probe. By TPE, which is a nonlinear process, one probe molecule is excited by two photons absorbed simultaneously (or, to be more precise, in a very short period of time). Hence, the TPE efficiency is proportional to the square of the excitation beam intensity, which permits the localization of the excitation only at the focusing point, and not on the whole way of the beam. Moreover, the wavelength of the exciting beam for TPE is about 2 times higher than this for SPE beam for the same probe, which permits excitation

of visual fluorescence in the transparency region of biological objects (700–1000 nm), besides, the higher excitation wavelength means the lower scattering of excitation beam. Thus, using two-photon excitation of fluorescent probes in procedures of biological objects detection permits deeper penetration of exciting beam into the tissue, excitation of visual fluorescence in near infrared spectral region, where the majority of biological objects are transparent, decreased photodamage of the studied object, and obtaining of well-resolved three-dimensional image of biological object [2, 3].

The efficiency of TPE of a molecule at the constant excitation intensity is determined by the value of two-photon absorption cross-section. The higher the value of two-photon absorption cross-section is, the lower excitation intensity is required to obtain the same fluorescence intensity. And lower excitation intensity means (1) cheaper and simpler equipment needed and (2) lower photodamage of the sample. Thus, the successful application of the TPE for the detection of biological molecules requires the fluorescent probes with (1) high affinity to the biological molecules of interest, and (2) high value of the two-photon absorption cross section. Unfortunately, such probes are not developed at all for the moment.

It is important that the luminescent biomedical probe-sensor could be applied to the study of the living cells (e.g., with the fluorescent microscopy). It was shown in a number of papers that the widely used fluorescent probes photochemically destroy the biological objects (DNA, RNA, etc.). So probes have to be nonphototoxic. Besides, the probe should be photostable so that the biomolecule could be studied for the long enough period of time without the probe damage. The phototoxic influence of the dye molecule on the DNA or RNA can take place either directly via the excitation energy transfer from the dye to the nucleotide bases or indirectly via the third molecule (e.g., by the triplet excitation energy transfer to the oxygen molecule resulting in the generation of the toxic singlet oxygen [4, 5]). It was shown [6–15] that the absorption bands (connected with the first electronic transition) of the DNA, RNA, and nucleotide bases are located in the near UV spectral region with the maximum near 260 nm. At the same time, the corresponding absorption bands of the majority of dyes used as luminescent probes are located in the visual spectral region (>400 nm) [1]. The fact that the first excited singlet and triplet energy levels of dyes are situated essentially lower than correspondent levels of any nucleotides does not allow the excitation energy transfer from the dye to the DNA thus making impossible the direct phototoxic influence of the dye on the DNA. Nevertheless, the molecules such as porphyrines or other pigments that destroy the DNA indirectly by the generation of singlet oxygen are well known and used in the photodynamic therapy.

In the presented work we study the styryl dyes as the probes for the TPE fluorescent detection of DNA. Styryl dyes are known as having high two-photon absorption cross-section values [2, 16]; one of the benzothiazolium styryls was shown to give strong fluorescence upon TPE by 1064 nm irradiation [17]. On the other hand, significant fluorescent response on the dsDNA presence is observed for these

dyes [18–21]. Recently series of monomer and homodimer benzothiazolium styrylcyanines was synthesized and studied for their efficiency as TPE nucleic acids sensitive dyes. It was shown that dyes modified with spermine-like linkage/tail group demonstrate increased sensitivity to DNA [19]. They have low intrinsic emission intensity and enhance their fluorescence intensity up to three orders of magnitude in presence of DNA. We believe that the influence of spermine-like linkage/tail group on the dye sensitivity to DNA is due to the additional interaction of the positively charged nitrogen atom with the DNA. Complexes of studied dyes with DNA also demonstrate intensive emission upon the TPE [19].

In the presented work, two-photon excited fluorescence of monomer and homodimer styrylcyanine dyes based on benzothiazole, naphthothiazole, benzoimidazole, pyridinium, quinoline, and 4-oxo-thieno[2,3-d]pyrimidinium heterocyclic residues and containing charged spermine-like linkage/tail groups was studied in the presence of DNA. Besides, for several dyes the fluorescent and phosphorescent properties at low temperature, as well as photochemical stability and phototoxicity to the DNA, were investigated.

2. METHODOLOGY

The total DNA from chicken erythrocytes was purchased from Sigma-Aldrich Inc (St. Louis, Mo, USA). The dye Dst-MdO (Figure 1) was obtained by the boiling of quaternary salt and *p*-dimethylaminobenzaldehyde in acetic anhydride. Dyes Bos-1, DBos-21, DBos-24, DBos-25, DBos-28, and DBos-30 (Figure 1) were obtained as described in [19]. Dyes S-3, S-20, S-33, S-45, and S-46 (Figure 1) were obtained as described in [21]. Dyes F, Sbt, Sil, Dst-6, Dst-10, Dbt-10, and Dil-10 (Figure 1) were synthesized according to the procedures described in [18]. The synthesis of dyes S-48, Tio-1, and S-40 (Figure 1) was described in [20]. The structures of the dyes were confirmed with ^1H NMR and element analysis.

The samples were prepared in distilled water and 0.05 M TRIS-HCl buffer, pH 8.0. The concentrations of dye and DNA were, respectively, 10^{-5} M and 6×10^{-5} M b.p. (base pairs) for the absorption measurements and photodamage experiment, and 10^{-4} M and 6×10^{-4} M b.p., respectively, for the low-temperature luminescence measurements. For the low-temperature measurements, the prepared solutions were poured out into the special cell so that the upper surface is open, and then frozen at the temperature of the boiling nitrogen (77 K). The excitation beam was directed to the open surface, and from the same surface the luminescence was registered.

The steady state fluorescence and phosphorescence measurements were performed using laboratory-designed equipment; absorption spectra were recorded with the help of a Specord UV-VIS spectrophotometer. The photodamage of dyes and the DNA+dye systems was performed by exposition of the corresponding solution to the visible spectrum irradiation of the 1 kW Hg-lamp.

The measurements were carried out at 77 K and ambient temperatures.

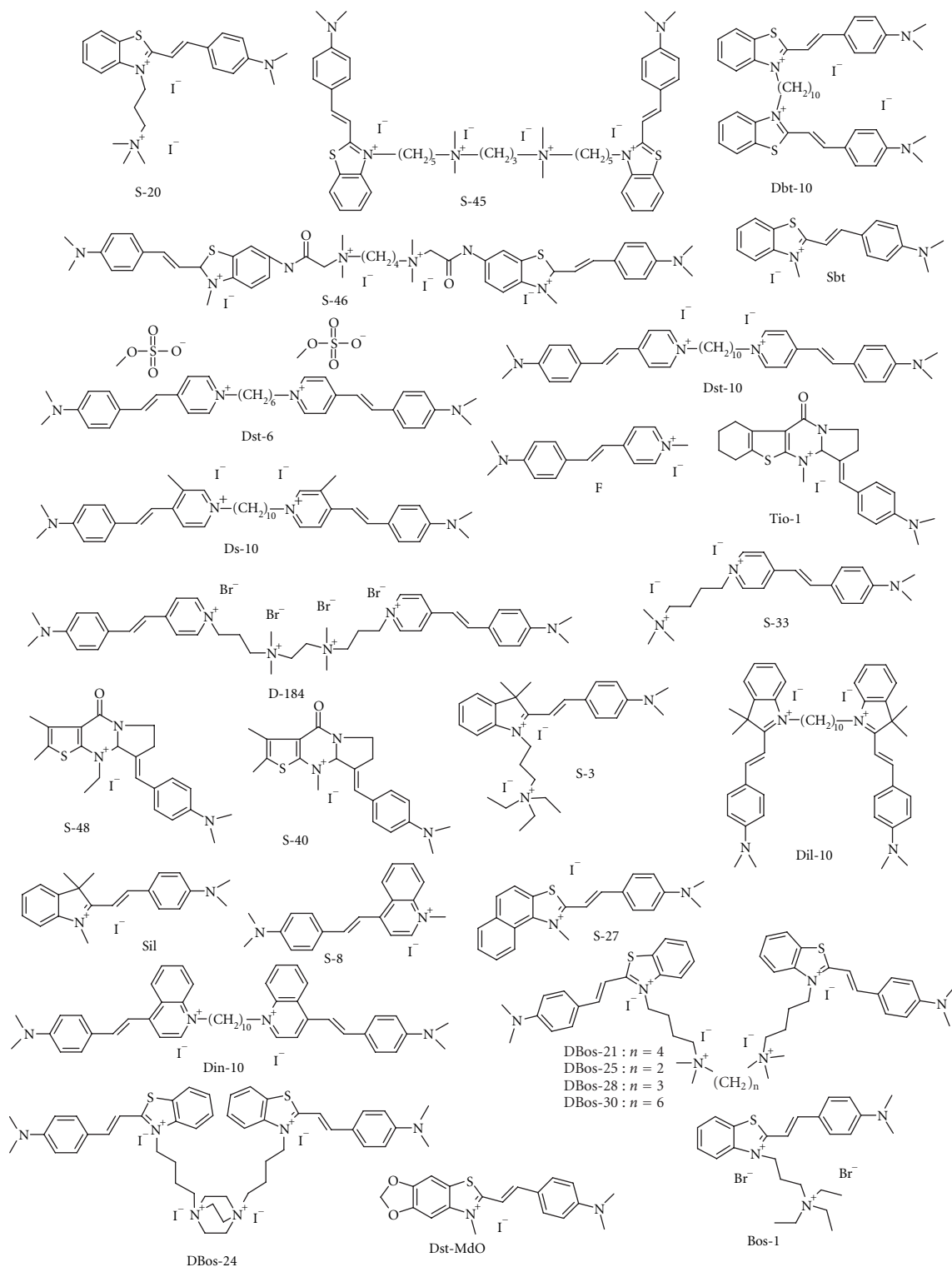


FIGURE 1: Chemical structures of the studied dyes.

The TPE fluorescence measurements of the dyes in DNA presence were performed by using the 1064 nm irradiation of the 20 nanoseconds pulsed YAG: Nd³⁺ laser as the excitation source. Experimental setup was used and two-photon

absorption cross-section values calculation performed as described in [19].

During the TPE fluorescence measurements at wavelength 840 nm, a Ti:Sapphire laser (Mira Optima 900-E,

Coherent Inc (Santa Clara, Calif, USA) pumped up with the cw Nd:YVO₄ laser (Coherent) and generating 90 fs cosec²-shaped pulses with repetition rate 76 MHz was used. Parameters of laser were monitored by autocorrelator (APE Autocorrelator mini) and power meter (Field Master GS, LM-10, Coherent). The fluorescence light was detected at right angle as it passed the telecentric system of two lenses and the entrance slit (100 μ) of the spectrograph (500 mm Imaging Spectrograph SP-2558, Princeton Instruments - Acton (Acton, Mass, USA)). A CCD camera (CCD-Spec-10:256E/TEPLUS 1024 × 256 Open-electrode, Marconi CCD 30-11) was used as a detector of TPE-fluorescence.

3. RESULTS AND DISCUSSION

3.1. The study of SPE and TPE fluorescence of dyes and dye-DNA complexes

Styryl dyes are known to be efficiently excited via the TPE [2, 16, 17]. Thus, the study of the styryl dyes as possible fluorescent probes for the DNA was performed by us as follows. First, wide series of styryl dyes based on different heterocyclic residues were synthesized and studied as the SPE fluorescent probes for DNA detection. Second, the dyes demonstrating both high value of fluorescence intensity in DNA presence and sharp emission intensity increase upon binding to DNA were studied in the TPE experiment.

Recently, the series of novel monomer and homodimer styrylcyanine dyes based on benzothiazole, naphthathiazole, benzoimidazole, pyridinium, quinoline, and 4-oxo-thieno (2,3-d) pyrimidinium heterocyclic residues (Figure 1) was elaborated, synthesized, studied, and partly reported [18, 20, 21]. The dyes demonstrated high DNA sensitivity, namely, fluorescence intensity of dyes upon SPE enhanced up to thousand times upon binding with DNA (Figure 2). The study of the dyes absorption and fluorescence spectra at room temperature in water buffer solution as well as in the DNA presence revealed that the spectra of majority of the studied dyes are connected with the absorption and fluorescence of the separate styryl chromophores. Meanwhile, for the styryl homodimer dyes containing the spermine-like linker (DBos-21, DBos-24, DBos-25, DBos-28, DBos-30, S-45, and S-46) the band corresponding to the aggregate of the styryl chromophores is dominating in the absorption spectrum of the free dyes, while the addition of the DNA to the solution leads to the decrease of the aggregate band and growth of the monomer ones. At the same time, the mentioned aggregates were found to be nonfluorescent at room temperature, thus the fluorescence spectra of the mentioned dimers, as well as of all the studied dyes (both free and bound to DNA), correspond to the emission of the separate styryl chromophores [19]. Hence, the strongly enhanced fluorescence of the studied styryls in DNA presence is the emission of the styryl chromophores, bound to the DNA molecule. The fixation of the separate chromophore on DNA (via either intercalation or groove-binding) leads to the decrease in the rate constant of the nonfluorescent deactivation of the singlet electronic excitation of the dye,

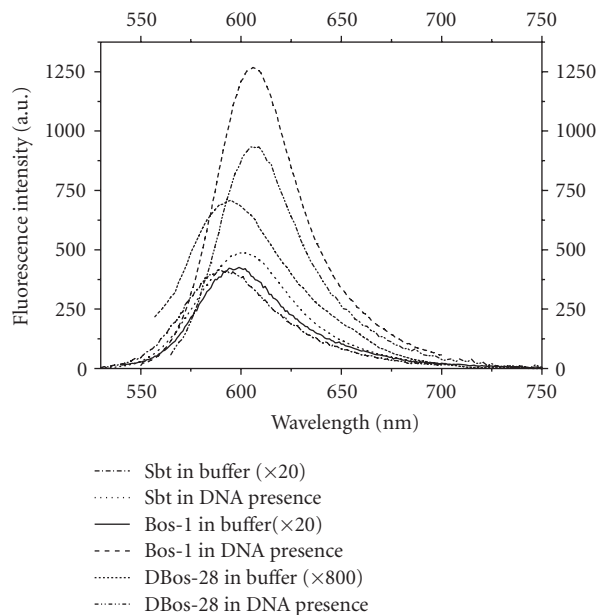


FIGURE 2: SPE fluorescence spectra of dyes in free state and in DNA presence.

and thus to the increase of the dye fluorescence quantum yield [22].

In order to enhance the dye-to-DNA affinity, some of the studied dyes contained the spermine-like tail or linking group. It was shown by us earlier [23] that the spermine-like tail group enhances the constant of dye to DNA binding equilibrium (K_b) in about three times ($1.8 \times 10^4 \text{ M}^{-1}$ for Sbt and about $6 \times 10^4 \text{ M}^{-1}$ for S-20). We believe this enhancement to be connected with the additional interaction of the charged spermine tail group with the DNA. It should be mentioned that the cyanine dyes sensitive to DNA possess the K_b values of the same order of magnitude as the benzothiazole styryl dyes Sbt and S-20 [24], though for some of the cyanines (e.g., TO) the value of K_b was reported to be about 10^6 M^{-1} [25].

3.2. The effect of dyes aggregations on their phosphorescent properties

Phosphorescence excitation and emission spectra of benzothiazole homodimer dyes solutions were measured (Figure 3). The energy of the lowest triplet level of dyes is about 1.85 eV (14900 cm^{-1}). This value is less than the value of the lowest triplet level among DNA bases thus the triplet electron excitation energy transfer from DNA to the dye can take place and is still under study. The phosphorescence lifetime was evaluated and amounted about 20 milliseconds.

Fluorescence excitation and emission spectra of benzothiazole homodimer dyes solutions at liquid nitrogen temperature were obtained. Also fluorescence of dyes' aggregates at liquid nitrogen temperature was registered while at room temperature these aggregates are virtually nonfluorescent. As far as fluorescence excitation spectra of aggregates coincide with phosphorescence excitation spectra of dyes, it was

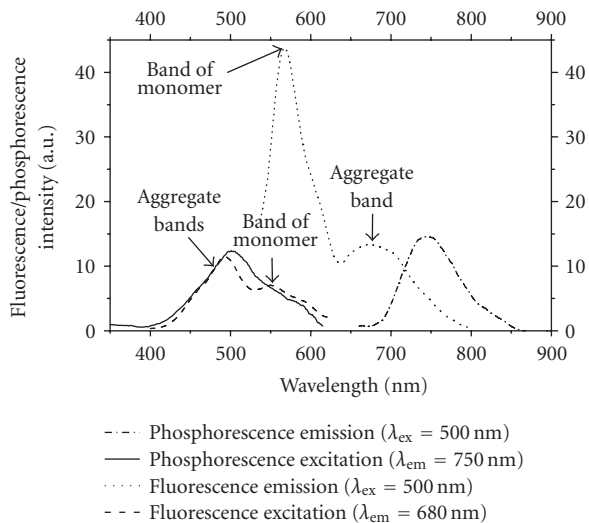


FIGURE 3: Fluorescence and phosphorescence emission and excitation spectra of DBos-30 water solution at liquid nitrogen temperature ($C = 10^{-4}$ M).

concluded that, namely, aggregates are mainly responsible for the phosphorescence (Figure 3). In order to exclude the interaction between the dye-DNA complex and the molecular oxygen in the water solution the studying of the dyes emission in vacuum is under research now.

3.3. TPE fluorescence of dyes and dye-DNA complexes

The TPE study of the fluorescent properties of the mentioned styryl dyes in the presence of DNA was performed.

The dye-DNA complexes revealed intensive emission upon two-photon excitation (TPE) at wavelength 1064 nm with the 20 nanoseconds pulsed YAG:Nd³⁺ laser. Here the numerical results of dyes' studying upon the TPE in complexes with DNA are presented. The values of dyes' two-photon absorption (TPA) cross section δ were evaluated (see Table 1). The calculations of δ were performed using the respective value for Rhodamine 6G [26]. As it is seen from Table 1, the δ values of dye-DNA complexes are about 10^{-50} cm⁴ s.

Dyes from the series with each type of chromophore in complexes with DNA demonstrated emission upon TPE at 840 nm with the 90 femtosecond pulsed Ti:sapphire laser (see Figure 4). TPA cross sections δ at wavelength 840 nm are under evaluation now.

The possibility of the dye DBos-21 application for the TPE fluorescent cell staining was studied. HeLa cells were incubated for 1 hour with DBos-21 (5 μ M) and imaged using 880 nm excitation of the femtosecond pulsed Ti:Sapphire laser (Tsunami, Spectra Physics). TPE fluorescent image of the cells stained with DBos-21 is shown in Figure 5.

The TPE fluorescent imaging study shows that the styrylcyanine dimer dye DBos-21 containing the spermine-like linking group successfully permeates through the living cell membrane. Besides, this dye demonstrated mostly mitochondria staining, possibly because of high positive charge of the dye.

TABLE 1: The values of TPA cross section δ of dyes in DNA presence upon excitation at wavelength 1064 nm.

Dye	$\delta, 10^{-50}$ cm ⁴ · s	Dye	$\delta, 10^{-50}$ cm ⁴ · s
S-20	2.3	S33	1.1
Bos-1	2.2	D-184	1.1
DBos-21	1.7	S40	0.2
DBos-24	1.4	S48	0.2
DBos-25	1.7	Tio1	0.2
DBos-28	2.1	Sil	1.7
DBos-30	1.8	Dil-10	1.0
S45	1.4	S3	0.9
S46	0.3	S8	0.4
Sbt	1.7	Din-10	0.4
Dbt10	0.3	S27	0.8
F	0.04	Rhodamine 6G	5.5
Dst-6	0.6		
Dst-10	0.6		
Ds-10	0.4		

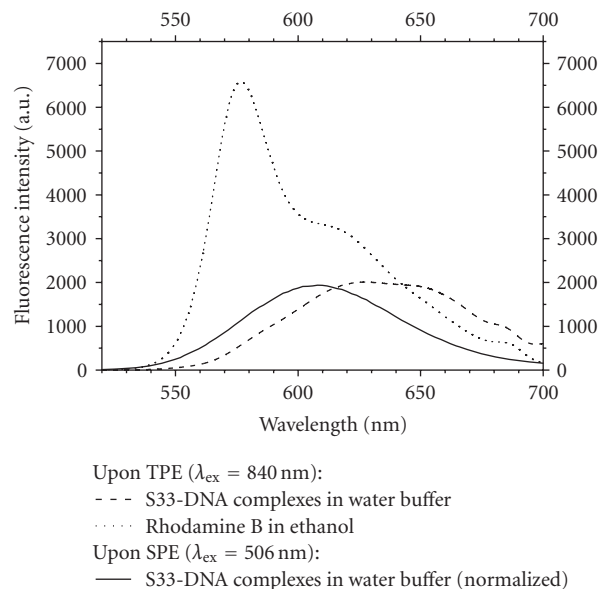


FIGURE 4: Fluorescence emission spectra of dye-DNA water buffer solution and Rhodamine B ethanol solution upon SPE and TPE (concentration of dyes $C = 1.5 \times 10^{-5}$ M).

Thus, the styrylcyanine dimmer dyes containing the spermine-like linking group could be successfully applied for the TPE fluorescent imaging of the living cells.

3.4. The study of dyes phototoxicity and photostability

3.4.1. The first excited singlet and triplet levels of dyes

For the use of the dyes as biomedical sensors for the DNA (or RNA) detection and imaging in the study of the living objects the phototoxic influence of these dyes realized via

TABLE 2: Positions of singlet (S) and triplet (T) levels of the dyes in presence of the DNA, cm^{-1} .

Compound	Bos-1	DBos-21	DBos-24	DBos-25	DBos-28	DBos-30
S (293 K)	18250	18180	18120	18120	18280	17940
S (77 K)	19100	18800	19530	19160	18680	19110
T (77 K)	14790	14820	14240	14730	14750	14890

TABLE 3: Positions of singlet (S_1) and triplet (T_1) levels of the nucleotides, cm^{-1} .

Compound	dCMP	dGMP	dTMP	dAMP
S_1	33090	33030	33530	34490
T_1	26630	26320	26160	25950

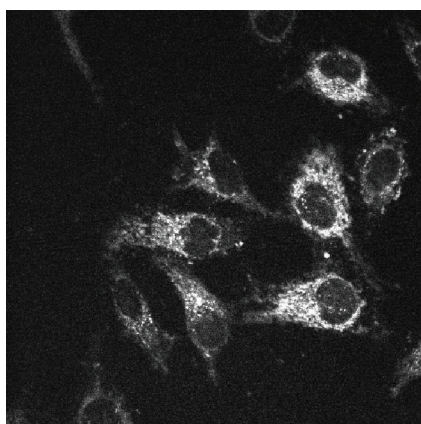


FIGURE 5: TPE fluorescent image of the HeLa cells stained with the dye DBos-21. Fluorescent emission excited with the femtosecond pulsed Ti:Sapphire laser, excitation wavelength 880 nm.

the excitation energy transfer from the dye to the DNA has to be absent. To avoid these processes the first excited singlet and triplet levels of dyes must be situated lower than correspondent levels of any nucleotide. To check this the optical absorption, fluorescence, and phosphorescence spectra of the investigated dyes Bos-1, DBos-21, DBos-24, DBos-25, DBos-28, and DBos-30 as well as correspondent dye+DNA systems were studied. Some of these spectra (namely, for Bos-1, DBos-24 and DBos-30 dyes) are given in Figure 6.

The absorption spectra of the dye Bos-1 both in the presence and the absence of the DNA in visible spectral region consist of the single band with the maxima near 17540 and 18470 cm^{-1} , respectively (Figure 6(a); curves 1,2). Since this band is the most long-wave band in the visible spectral region and the corresponding fluorescence spectrum (Figure 6(a); curves 3,4) obeys the mirror symmetry rule respectively to this absorption band, the latter should be attributed to the absorption transition to the first excited singlet level of the dye molecule. The shift between the maxima of the free dye and the DNA+dye system spectra points to the dye interaction with the DNA. In the absorption spectra of the dimer dyes DBos-24 and DBos-30 in presence of the

DNA the same band with the maximum near 18000 cm^{-1} (Figure 6(b); curve 2) and 17750 cm^{-1} (Figure 6(c); curve 2), respectively, could be observed. At the same time, the spectrum of DBos-24 in the DNA presence contains one more band with the maximum at 22500 cm^{-1} shifted to the short-wavelength region relatively to the main band. This short-wavelength band with the maxima at 22200 and 20800 cm^{-1} , respectively, dominates in absorption spectra of both DBos-24 and DBos-30 in absence of the DNA (Figures 6(b); curve 1, and 6(c); curve 1). Taking into account all the above-mentioned results, the short-wavelength band could be attributed to the aggregates of the styryl chromophore. Since for the dimer dyes the tendency to form aggregates is much higher than for corresponding monomers [27], the short-wavelength band is present in the spectra of DBos-24 and DBos-30 in free state, but is absent in the spectrum of Bos-1 containing the same chromophore. At the same time, interaction of dimer dyes with the DNA at low dye to the DNA concentrations ratio generally leads to the fixation of separate chromophores on the DNA molecule, thus resulting in decrease in the aggregates concentration in solution [27]. This explains the decrease in the short-wavelength band contribution to the absorption spectrum of DBos-24 in presence of the DNA, as well as the disappearance of this band in the same spectrum of DBos-30.

The fluorescence of the dyes Bos-1, DBos-24, and DBos-30, both in free form and in DNA presence, at the room temperature was measured in [19]. The maximum of these spectra was situated near 17000 cm^{-1} similarly to the spectra presented at Figures 6(a), 6(b), 6(c) (curves 3,4). It was shown in [19] with the help of fluorescence excitation spectra that the fluorescence band with the maximum near 17000 cm^{-1} belongs to the emission of the single styryl chromophores. Thus, the absorption and fluorescence spectra of the dyes Bos-1, DBos-24, and DBos-30 in DNA presence could be used for the calculation of the position of the singlet electronic excited energy level of the nonaggregated chromophore of these dyes, bound to DNA.

The positions of the first excited singlet level of the investigated dyes in nonaggregated form in the presence of the DNA were obtained by intersection of the absorption and fluorescence spectra curves and given in Table 2.

The values of singlet and triplet energy levels of the nucleotides obtained by us in [28, 29] are presented in Table 3. The comparison of these data with data given in Table 2 removes all doubts that even the triplet level of any nucleotide is situated much upper than the singlet level of any investigated dye. That is why the irradiation of the dye in the visual spectral region exciting the first singlet electronic

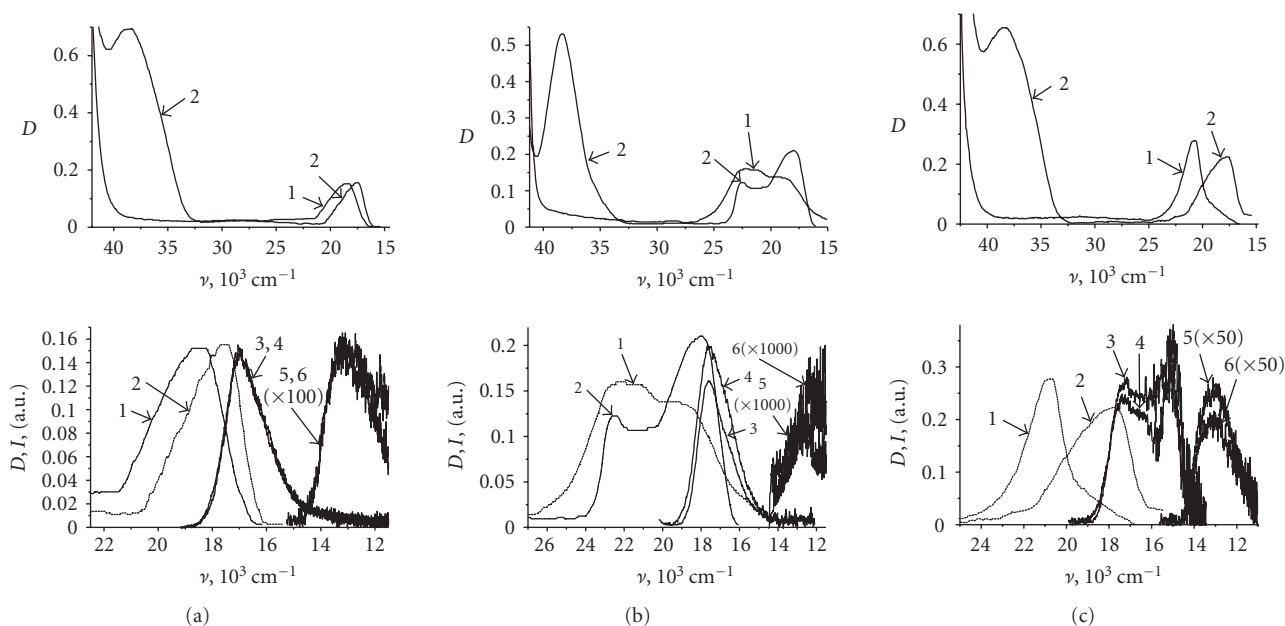


FIGURE 6: The absorption (1,2), fluorescence (3,4), and phosphorescence (5,6) spectra (3–6 at $T = 77 \text{ K}$) of free styryl dyes (1,3,5) and correspondent systems DNA+dye (2,4,6) of: (a) styryl monomer Bos-1, (b) dimer DBos-24, and (c) dimer DBos-30.

level of the dye cannot be resulted in the excitation energy transfer from the dye to the DNA.

3.4.2. Effect of irradiation of dyes and the DNA+dye systems on their optical properties

It is known that the phototoxic influence of a luminescent dye probe on the DNA results in the spectral response of the DNA+dye system. This response is connected with the DNA macromolecule damage and is observed as the change of the optical density of the DNA absorption band (i.e., situated at 260 nm and corresponds to the $S_0 \rightarrow S_1$ electronic transition) in the DNA+dye system under excitation in the dye absorption band (i.e., situated at 400–500 nm and corresponds to its $S_0 \rightarrow S_1$ transition). Besides, the investigation of the optical density changes of the dye band under the free dye excitation at the wavelength of the same band is the way to study the dye photostability. The fact that the DNA absorption band connected with $S_0 \rightarrow S_1$ transition is located far from the same band of majority of dyes and the value of optical density of the absorption band connected with the dye $S_0 \rightarrow S_2$ transition (located near 260 nm) is much less than corresponding value of the DNA band gives the ground to study the dynamics of the absorption bands optical density changes almost independently for a dye and for the DNA. In our paper, the investigations results of the absorption spectra of the elaborated styryls and the respective DNA+dye complexes (that were recorded with the aim to study both the dye photostability and its phototoxicity influence on the DNA) during the irradiation of the investigated compounds solutions by visible light of 1 kW Hg-lamp were described.

As it is shown in Figure 7 the gradual decrease of D of the absorption spectra bands is observed for free

dyes under the irradiation time increase (curve 1). This phenomenon is connected with the damage of dyes π -electron systems under irradiation and is the evidence that Bos-1 and DBos-30 are not photostable in free form. The gradual decrease of D of the dyes absorption spectra bands in the DNA presence takes place too but essentially slower than for free dyes. Moreover, the decrease rate of D of the DNA+DBos-30 system (Figure 7(b); curve 2) is lower than of the system DNA+Bos-1 (Figure 7(a); curve 2). It means that dimer DBos-30 bound to the DNA is more photostable than monomer Bos-1 bound to the DNA. Comparing the dependencies of optical density on irradiation time of investigated styryl dyes with the same dependence of thiazole orange (TO) dye (Figure 7, curve 4), it is shown that both Bos-1 and DBos-30 dyes (bound to the DNA) are more photostable even than TO dye (bound to the DNA). The rise of the dyes photostability under binding to the DNA occurs, in our opinion, because of the formation of the tough spatial fixation of a dye molecule after the intercalation of this dye in the DNA macromolecule. As the result, the DNA macromolecule screens the dye molecule against external influences and decreases the contacts between the dye molecules and dissolved molecules of oxygen. The last is transferred into the singlet excited electronic state under the direct excitation of the dye and becomes an active oxidant [30]. The results obtained in this paper agree with the data obtained in [31] on investigations of the cyanine dyes. Since the constant of binding to the DNA for the dimer is often higher than for the monomer with the same π -electron system [32, 33], the number of dye molecules bound with the DNA is higher for the dimer DBos-30 than for the monomer Bos-1. Thus the DNA macromolecule screens the dimer molecules rather than the monomer molecules that cause the

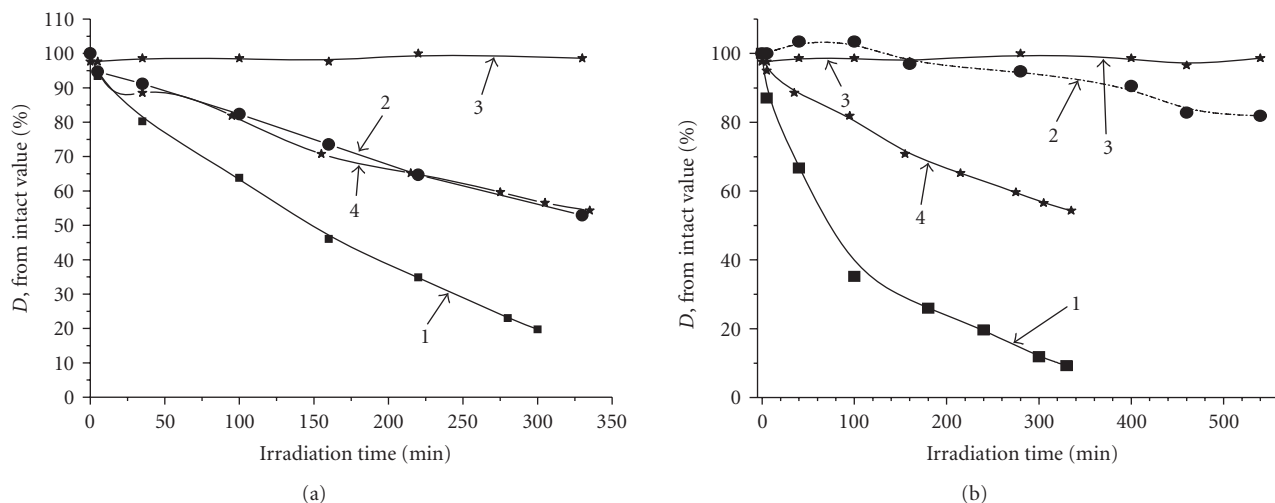


FIGURE 7: The dependence of optical density (obtained from optical absorption spectra) on irradiation time of dyes: (a) Bos-1 and (b) DBos-30 (1—free dye, 2—DNA+dye, 3—the DNA maximum 260 nm, 4—TO with the DNA).

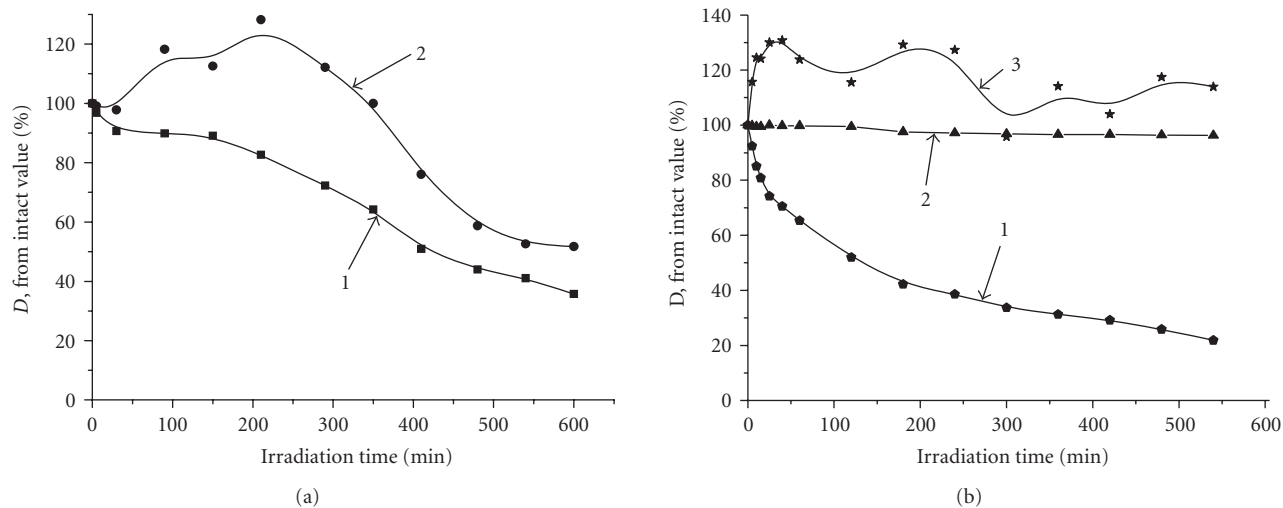


FIGURE 8: The dependence of optical density (obtained from optical absorption spectra) on irradiation time of dimer dye DBos-24: (a) free dye, (b) bond to the DNA (1—at 23100 cm⁻¹, 2—at 18500 cm⁻¹, 3—the DNA maximum at 260 nm).

difference in Bos-1 and DBos-30 photostability in the DNA presence.

The dependencies of the DNA band maximum optical density D on time of dye irradiation (Figure 7; curve 3) for the DNA+Bos-1 and DNA+DBos-30 systems were investigated with the aim to study phototoxic influence of the investigated dyes on the DNA. According to our experimental data the value of the optical density D of the investigated dyes absorption band connected with the $S_0 \rightarrow S_2$ transition is changed negligible during all the time of irradiation. As it is shown in Figure 7 the value of D is changed within 3% at 260 nm out of its intact value that may be connected with these negligible changes of the dyes $S_0 \rightarrow S_2$ band and experimental errors. It is known that the DNA destruction is either the double strand untwisting or the strand cutting that is reverse to the hypochromic effect, the complete untwisting

resulting in the 37% increase in D value at 260 nm [34]. That is why the 3%-changes obtained by us cannot be connected with the significant DNA damage and can be included in experimental errors.

So, Bos-1 and DBos-30 dyes are nonphototoxic for the DNA as the first approximation and can be used as the optical biomedical sensors for the DNA detection and imaging. On the other hand, the DNA protects these dyes against the photodamage.

As is shown in Figure 6(b), the dimer DBos-24 absorption band consists of two bands. Comparing Figures 6(a) and 6(b) it can be seen that the long-wavelength band (18500 cm⁻¹) is located close to the monomer Bos-1 band and corresponds to nonaggregated state. The short-wave band (23100 cm⁻¹), in our opinion, is connected with aggregates (the similar case was observed for cyanine dyes

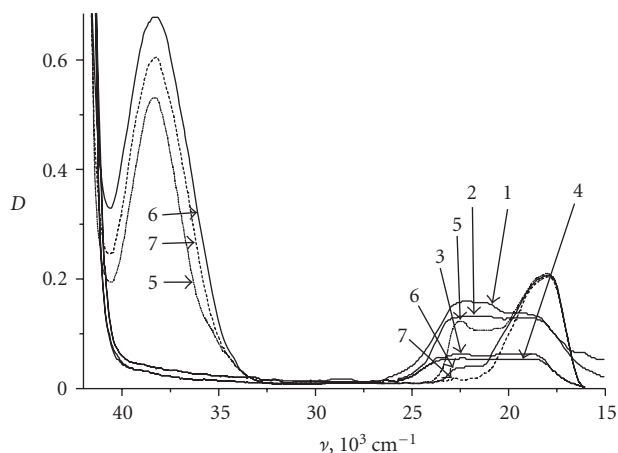


FIGURE 9: The absorption spectra of dimer DBos-24 during irradiation (free dye: 1—intact, 2—210 minutes, 3—540 minutes, 4—600 minutes; dye with DNA: 5—intact, 6—240 minutes, 7—540 minutes).

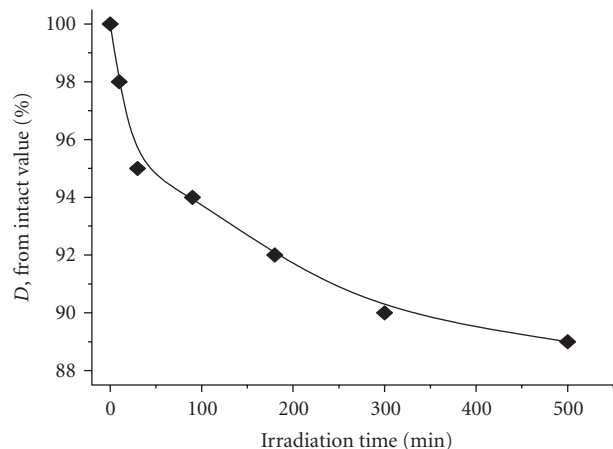


FIGURE 10: The dependence of optical density of the DNA maximum in the DNA+Dst-MdO system.

[35, 36]). Using optical absorption spectra of DBos-24 dye and the DNA+DBos-24 system, the dependencies of the optical density D on irradiation time for these molecular systems are obtained (Figures 8(a), 8(b)). The aggregates band of the free dye decreased gradually during all the irradiation time while the nonaggregated dyes band increased slightly at first (Figure 9). In our opinion, it is connected with the fact that aggregates are damaged and turned into nonaggregated state. Since the D value of dye DBos-24 decreases by 40–50% after 600 minutes of irradiation, this dye is more photostable than Bos-1 and DBos-30.

For the DNA+DBos-24 system, the optical density of aggregate band (Figure 9) decreases gradually with the irradiation time increasing but D of nonaggregated dyes band (in presence of the DNA) remains constant. In our opinion, it is connected with the fact that nonaggregated dyes intercalate into the DNA macromolecule while aggregates bind outside the DNA chain. As it was mentioned above,

during the irradiation the molecules of environmental oxygen are transferred in the singlet excited electronic state and become an active oxidant [30]. Generated singlet oxygen damages the aggregated dyes that are outside the DNA chain. The DNA screens nonaggregated dyes that are intercalated in the DNA macromolecule (between the DNA strands) and protect them from the influence of singlet oxygen and, therefore, the dyes molecules are not damaged.

As it is shown (Figure 8(b); curve 3), the increase (up to by 30%) of D of the DNA absorption spectra bands is observed for the DNA+DBos-24 system under the irradiation time increase. In our opinion, this phenomenon is caused by the untwisting or cutting of the strands of the DNA macromolecule which contacts with the molecules of DBos-24 (this phenomenon is reverse to the hypochromic effect). These results agree with 37% increase for the complete DNA untwisting [34]. Thus the presence of DBos-24 dye causes the DNA damage, that is, DBos-24 showed phototoxic influence on the DNA. But dyes phototoxicity appears not only in the untwisting or cutting of the DNA strands. For the DNA+Dst-MdO system, the value of optical density of the DNA absorption band decreases by 10% (Figure 10). We suppose it is connected with the direct DNA π -electron systems damage that is caused by Dst-MdO molecules.

So, DBos-24 and Dst-MdO dyes could be possibly used in the photodynamic therapy for the DNA damage.

4. CONCLUSIONS

Novel monomer and homodimer styrylcyanine dyes based on benzothiazole, naphthathiazole, benzoimidazole, pyridinium, quinoline, and 4-oxo-thieno[2,3-d]pyrimidinium heterocyclic residues were elaborated, synthesized, and studied. The dyes demonstrated rather high sensitivity to DNA.

Monomer and homodimer styrylcyanine dyes demonstrated fluorescence emission of high intensity upon TPE at wavelength of 840 nm and 1064 nm. TPA cross sections of dyes at the wavelength 1064 nm are of the $10^{-50} \text{ cm}^4 \text{ s}$ order. The dyes based on benzothiazole and benzoimidazole heterocycle generally demonstrate higher TPA cross sections values as compared to the other studied dyes.

Dyes with spermine-like linkage/tail groups demonstrated higher sensitivity to DNA and have higher TPA cross sections than dyes with the same chromophore but without respective groups.

We can conclude that the studied dyes can be used for SPE and TPE fluorescent DNA detection.

The developed dyes are rather photostable and mainly photochemically safe. The DBos-24 is most photostable but manifests some phototoxicity. The dye Dst-MdO is rather phototoxic; both these dyes could be possibly used in the photodynamic therapy.

ACKNOWLEDGMENTS

The authors are thankful to Dr. Tymish Y. Ohulchanskyy (Department of Chemistry and Institute for Lasers, Photonics and Biophotonics, SUNY at Buffalo, Buffalo, New York) for performing the fluorescence microscopy

experiment. They are grateful to The National Academy of Science of Ukraine Center for Collective Use of "LASER FEMTOSECOND COMPLEX" attached to NASU Institute of Physics. The work was supported by the Science and Technology Center of Ukraine (grant no. U3104k).

REFERENCES

- [1] R. P. Haugland, *Handbook of Fluorescent Probes and Research Products*, Molecular Probes, Eugene, Ore, USA, 9th edition, 2002.
- [2] M. Albota, D. Beljonne, J.-L. Brédas, et al., "Design of organic molecules with large two-photon absorption cross sections," *Science*, vol. 281, no. 5383, pp. 1653–1656, 1998.
- [3] D. J. S. Birch, "Multiphoton excited fluorescence spectroscopy of biomolecular systems," *Spectrochimica Acta Part A*, vol. 57, no. 11, pp. 2313–2336, 2001.
- [4] D. Ramaiah, I. Eckert, K. T. Arun, L. Weidenfeller, and B. Epe, "Squaraine dyes for photodynamic therapy: mechanism of cytotoxicity and DNA damage induced by halogenated squaraine dyes plus light (>600 nm)," *Photochemistry and Photobiology*, vol. 79, no. 1, pp. 99–104, 2004.
- [5] J. A. Woods, N. J. Traynor, L. Brancalion, and H. Moseley, "The effect of photofrin on DNA strand breaks and base oxidation in HaCaT keratinocytes: a comet assay study," *Photochemistry and Photobiology*, vol. 79, no. 1, pp. 105–113, 2004.
- [6] R. Bersohn and I. Isenberg, "Phosphorescence in nucleotides and nucleic acids," *The Journal of Chemical Physics*, vol. 40, no. 11, pp. 3175–3180, 1964.
- [7] D. Dee and M. E. Baur, "Charge and excitation migration in DNA chains," *The Journal of Chemical Physics*, vol. 60, no. 2, pp. 541–560, 1974.
- [8] Yu. A. Vladimirov and V. N. Glagolev, "The study of the energy migration from the DNA on the acrydine orange dye," in *Molecular Biophysics*, G. M. Frank, Ed., Nauka, Moscow, Russia, 1965.
- [9] R. G. Shulman and R. O. Rahn, "Electron spin resonance of the excited triplet states of pyrimidines and purines," *The Journal of Chemical Physics*, vol. 45, no. 8, pp. 2940–2946, 1966.
- [10] R. O. Rahn, T. Yamane, J. Eisinger, J. W. Longworth, and R. G. Shulman, "Luminescence and electron spin resonance studies of adenine in various polynucleotides," *The Journal of Chemical Physics*, vol. 45, no. 8, pp. 2947–2954, 1966.
- [11] W. Rhodes, "Hypochromism and other spectral properties of helical polynucleotides," *Journal of the American Chemical Society*, vol. 83, no. 17, pp. 3609–3617, 1961.
- [12] J. W. Longworth, R. O. Rahn, and R. G. Shulman, "Luminescence of pyrimidines, purines, nucleosides, and nucleotides at 77°K. The effect of ionization and tautomerization," *The Journal of Chemical Physics*, vol. 45, no. 8, pp. 2930–2939, 1966.
- [13] A. A. Lamola, M. Guéron, T. Yamane, J. Eisinger, and R. G. Shulman, "Triplet state of DNA," *The Journal of Chemical Physics*, vol. 47, no. 7, pp. 2210–2217, 1967.
- [14] M. Guéron, J. Eisinger, and R. G. Shulman, "Excited states of nucleotides and singlet energy transfer in polynucleotides," *The Journal of Chemical Physics*, vol. 47, no. 10, pp. 4077–4091, 1967.
- [15] R. O. Rahn, R. G. Shulman, and J. W. Longworth, "Phosphorescence and electron spin resonance studies of the uv-excited triplet state of DNA," *The Journal of Chemical Physics*, vol. 45, no. 8, pp. 2955–2965, 1966.
- [16] H. Fujita, M. Nakano, M. Takahata, and K. Yamaguchi, "A new strategy of enhancing two-photon absorption in conjugated molecules: introduction of charged defects," *Chemical Physics Letters*, vol. 358, no. 5-6, pp. 435–441, 2002.
- [17] L.-Z. Wu, X.-J. Tang, M.-H. Jiang, and C.-H. Tung, "Two-photon induced fluorescence of novel dyes," *Chemical Physics Letters*, vol. 315, no. 5-6, pp. 379–382, 1999.
- [18] V. B. Kovalska, D. V. Kryvorotenko, A. O. Balanda, M. Yu. Losytskyy, V. P. Tokar, and S. M. Yarmoluk, "Fluorescent homodimer styrylcyanines: synthesis and spectral-luminescent studies in nucleic acids and protein complexes," *Dyes and Pigments*, vol. 67, no. 1, pp. 47–54, 2005.
- [19] V. P. Tokar, M. Yu. Losytskyy, V. B. Kovalska, et al., "Fluorescence of styryl dyes-DNA complexes induced by single- and two-photon excitation," *Journal of Fluorescence*, vol. 16, no. 6, pp. 783–791, 2006.
- [20] A. O. Balanda, K. D. Volkova, V. B. Kovalska, et al., "Synthesis and spectral-luminescent studies of novel 4-oxo-4,6,7,8-tetrahydropyrrolo[1,2-a]thieno[2,3-d]pyrimidinium styryls as fluorescent dyes for biomolecules detection," *Dyes and Pigments*, vol. 75, no. 1, pp. 25–31, 2007.
- [21] A. O. Balanda, K. D. Volkova, V. B. Kovalska, M. Yu. Losytskyy, S. S. Lukashov, and S. M. Yarmoluk, "Novel styrylcyanines and their dimers as fluorescent dyes for nucleic acids detection: synthesis and spectral-luminescent studies," *Ukrainica Bioorganica Acta*, vol. 4, no. 1, pp. 17–29, 2006 (Ukrainian).
- [22] S. M. Yarmoluk, M. Yu. Losytskyy, and V. M. Yashchuk, "Nonradiative deactivation of the electronic excitation energy in cyanine dyes: influence of binding to DNA," *Journal of Photochemistry and Photobiology B*, vol. 67, no. 1, pp. 57–63, 2002.
- [23] M. Yu. Losytskyy, N. Akbay, V. B. Kovalska, A. O. Balanda, and S. M. Yarmoluk, "Study of styryl dyes-dsDNA binding equilibrium," in *Proceedings of the 1st Asian Spectroscopy Conference and Asian Biospectroscopy Conference*, Book of Abstracts, pp. 206–207, Bangalore, India, January-February 2007.
- [24] S. M. Yarmoluk, S. S. Lukashov, M. Yu. Losytskyy, B. Akerman, and O. S. Korniyushyna, "Interaction of cyanine dyes with nucleic acids: XXVI. Intercalation of the trimethine cyanine dye Cyan 2 into double-stranded DNA: study by spectral luminescence methods," *Spectrochimica Acta Part A*, vol. 58, no. 14, pp. 3223–3232, 2002.
- [25] H. S. Rye, M. A. Quesada, K. Peck, R. A. Mathies, and A. N. Glazer, "High-sensitivity two-color detection of double-stranded DNA with a confocal fluorescence gel scanner using ethidium homodimer and thiazole orange," *Nucleic Acids Research*, vol. 19, no. 2, pp. 327–333, 1991.
- [26] D. J. Bradley, M. H. R. Hutchinson, and H. Koetser, "Interactions of picosecond laser pulses with organic molecules. II. Two-photon absorption cross-section," *Proceedings of the Royal Society of London. Series A*, vol. 329, no. 1576, pp. 105–119, 1972.
- [27] T. Yu. Ogul'chansky, V. M. Yashchuk, M. Yu. Losytskyy, I. O. Kocheshev, and S. M. Yarmoluk, "Interaction of cyanine dyes with nucleic acids. XVII. Towards an aggregation of cyanine dyes in solutions as a factor facilitating nucleic acid detection," *Spectrochimica Acta Part A*, vol. 56, no. 4, pp. 805–814, 2000.
- [28] V. Yashchuk, V. Kudrya, M. Losytskyy, H. Suga, and T. Yu. Ohul'chansky, "The nature of the electronic excitations capturing centres in the DNA," *Journal of Molecular Liquids*, vol. 127, no. 1–3, pp. 79–83, 2006.
- [29] V. M. Yashchuk, V. Yu. Kudrya, M. Yu. Losytskyy, et al., "The effect of triplet-triplet excitation energy transfer on the DNA

- self-protection mechanism,” *The Scientific Notes of NaUKMA: Physics*, vol. 51, pp. 48–56, 2006.
- [30] D. G. Knorre, O. S. Fedorova, and E. I. Frolova, “The oxidation degradation of nucleic acids,” *Chemical Progress*, vol. 62, no. 1, pp. 70–91, 1993 (Russian).
- [31] A. A. Ishchenko, *The Structure and Spectral Luminescent Properties of Polymethine Dyes*, Naukova Dumka, Kyiv, Ukraine, 1994.
- [32] H. S. Rye, S. Yue, D. E. Wemmer, et al., “Stable fluorescent complexes of double-stranded DNA with bis-intercalating asymmetric cyanine dyes: properties and applications,” *Nucleic Acids Research*, vol. 20, no. 11, pp. 2803–2812, 1992.
- [33] H. S. Rye and A. N. Glazer, “Interaction of dimeric intercalating dyes with single-stranded DNA,” *Nucleic Acids Research*, vol. 23, no. 7, pp. 1215–1222, 1995.
- [34] D. Freifelder, *Physical Biochemistry. Applications to Biochemistry and Molecular Biology*, W.H. Freeman, San Francisco, Calif, USA, 1976.
- [35] T. Yu. Ogul’chansky, M. Yu. Losytskyy, V. B. Kovalska, V. M. Yashchuk, and S. M. Yarmoluk, “Interactions of cyanine dyes with nucleic acids. XXIV. Aggregation of monomethine cyanine dyes in presence of DNA and its manifestation in absorption and fluorescence spectra,” *Spectrochimica Acta Part A*, vol. 57, no. 7, pp. 1525–1532, 2001.
- [36] W. West and S. Pearce, “The dimeric state of cyanine dyes,” *Journal of Physical Chemistry*, vol. 69, no. 6, pp. 1894–1903, 1965.

Research Article

Sensitive Label-Free Biomolecular Detection Using Thin Silicon Waveguides

A. Densmore,¹ D.-X. Xu,¹ S. Janz,¹ P. Waldron,¹ J. Lapointe,¹ T. Mischki,² G. Lopinski,² A. Delâge,¹ J. H. Schmid,¹ and P. Cheben¹

¹*Institute for Microstructural Sciences, National Research Council Canada, Ottawa, ON, Canada K1A 0R6*

²*Steele Institute for Molecular Science, National Research Council Canada, Ottawa, ON, Canada K1A 0R6*

Correspondence should be addressed to A. Densmore, adam.densmore@nrc.ca

Received 6 March 2008; Accepted 30 April 2008

Recommended by Stoyan Tanev

We review our work developing optical waveguide-based evanescent field sensors for the label-free, specific detection of biological molecules. Using high-index-contrast silicon photonic wire waveguides of submicrometer dimension, we demonstrate ultracompact and highly sensitive molecular sensors compatible with commercial spotting apparatus and microfluidic-based analyte delivery systems. We show that silicon photonic wire waveguides support optical modes with strong evanescent field at the waveguide surface, leading to strong interaction with surface bound molecules for sensitive response. Furthermore, we present new sensor geometries benefiting from the very small bend radii achievable with these high-index-contrast waveguides to extend the sensing path length, while maintaining compact size. We experimentally demonstrate the sensor performance by monitoring the adsorption of protein molecules on the waveguide surface and by tracking small refractive index changes of bulk solutions.

Copyright © 2008 A. Densmore et al. This is an open access article distributed under the Creative Commons Attribution License, which permits unrestricted use, distribution, and reproduction in any medium, provided the original work is properly cited.

1. INTRODUCTION

Sensing techniques employing fluorescent labeling of molecules are commonly used for simple binding event detection to determine the presence or absence of molecular targets in solution. However, there are few tools available that are capable of providing quantitative, label-free, and real-time monitoring of molecular interactions. There has been extensive activity in both the academic and commercial sectors to develop new sensing technologies that offer these capabilities, allowing important information such as molecular concentrations, binding affinities, and rate constants to be obtained. There have been numerous proposed solutions using planar waveguide optics such as surface plasmon resonance (SPR) [1], ridge waveguide evanescent field sensors [2–6], waveguide-based microcantilevers [7, 8], porous silicon resonant structures [9], optofluidic waveguides [10] as well as many others. The two methods that have been the most widely studied are the SPR sensors and the ridge waveguide evanescent field sensors. These methods employ a waveguide structure as the transducer and surface functionalization chemistry to immobilize receptor molecules on

the sensor surface. The receptors capture target molecules thereby accumulating material on the waveguide surface, which serves to induce a phase shift of the propagating optical field. In the case of SPR sensors, the optical field is the surface plasmon mode which propagates along the metal-analyte interface, whereas for the planar waveguide evanescent field sensor it is the evanescent tail of the optical waveguide mode. The induced phase shift of these devices can be monitored in real time to determine the density of molecules attached to the waveguide surface.

Although only SPR sensors have become widely commercially available, there is significant interest in developing planar waveguide evanescent field sensors due to the potential advantages offered by this technology. For example, these sensors are expected to provide increased sensitivity over SPR due to the much lower optical transmission losses [1]. It is possible for light to propagate through planar optical waveguides for distances of several centimeters with little loss, whereas for the surface plasmon devices the field is effectively extinguished after propagating a few tens of micrometers. This allows a much larger interaction length of the light with the biomolecules to be achieved, thereby

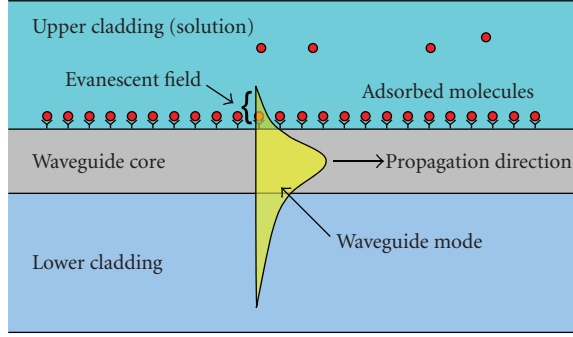


FIGURE 1: Illustration of a waveguide evanescent field sensor. Molecular targets are captured by receptor molecules at the waveguide surface thereby changing the waveguide mode effective index. This creates a phase shift of the propagating optical mode.

allowing a larger phase shift to be observed in the sensor output. In addition, the planar waveguide evanescent field sensor is well suited for arraying permitting the development of high density, waveguide-based microarray biochips for multianalyte monitoring.

Ridge waveguide evanescent field sensors have been demonstrated in many planar material systems such as silica [2], polymer [3], and silicon nitride [4, 5] as well as nonplanar systems including optical fibers [11]. The planar devices offer many well-known advantages over the nonplanar approaches including the possibility of creating arrays of sensors on a compact chip, the ability to integrate additional optical and electrical components on chip thereby increasing functionality, the capability for mass production using high volume semiconductor manufacturing techniques, and the possibility to integrate microfluidic systems on chip permitting convenient analyte delivery and reduced consumed sample volumes. Waveguide evanescent field sensors have been demonstrated using various waveguide circuit configurations including grating couplers [12], Mach-Zehnder interferometers [2, 3, 5], ring resonators [4, 6], and microdisks [13, 14]. It has been shown that the sensitivity achievable with these devices improves with increasing refractive index contrast between the waveguide core and the surrounding cladding materials [15, 16]. Motivated by these predictions, as well as other important advantages that will be discussed, we have developed evanescent field sensors using the silicon-on-insulator (SOI) material platform. The SOI material system consists of a top silicon waveguide core layer positioned on a silicon dioxide lower cladding layer grown on a silicon substrate [17] and has the highest refractive index contrast of all commonly available planar waveguide systems.

In this manuscript, we review our work developing evanescent field sensors in SOI. We show that silicon nanophotonic waveguides with dimensions smaller than the wavelength of light they guide have a strong evanescent field at the waveguide surface for the transverse magnetic (TM) polarized waveguide mode. This results in increased interaction with surface bound molecules, which leads to larger response compared to waveguide sensors fabricated on

traditional low-index-contrast material platforms [16, 18]. Furthermore, we show that using submicrometer dimension silicon waveguides with rectangular cross section, known as silicon photonic wires, allows extremely compact devices to be realized using well-established silicon fabrication technology. The compact footprint of these sensors allows two-dimensional sensor arrays to be fabricated allowing both spotter-based functionalization and microfluidic delivery systems to be used. We present experimental results demonstrating the performance of these devices using two different waveguide configurations: the Mach-Zehnder interferometer (MZI) and the ring resonator. We illustrate the performance of these sensors to track homogeneous refractive index change of bulk solutions and to monitor the formation of thin molecular layers on the waveguide surface.

2. THEORY: HIGH-INDEX-CONTRAST WAVEGUIDES FOR EVANESCENT FIELD SENSING

A schematic of a planar waveguide evanescent field sensor is shown in Figure 1, where specific target molecules are captured by receptor molecules on the waveguide surface. This induces an effective index change of the propagating optical mode, causing a phase shift to be observed at the device output. A primary goal in the design of these devices is to maximize their sensitivity for the application of interest. These applications can be divided into two categories including homogeneous sensing, which involves a uniformly distributed analyte extending over a distance well exceeding the evanescent field penetration depth, and surface sensing in which the analyte is bound to the waveguide surface in a layer that is usually much thinner than the evanescent field penetration. The intrinsic sensitivity of the devices is determined by the overlap of the squared waveguide mode field with the analyte. For homogeneous sensing, the intrinsic sensitivity is defined as the change of effective index ∂N_{eff} of the waveguide mode relative to homogeneous refractive index change of the bulk solution ∂n_c : $\partial N_{\text{eff}}/\partial n_c$. For the case of surface sensing, it is defined as the effective index change relative to the variation of thickness d of an adsorbed molecular layer with a given refractive index: $\partial N_{\text{eff}}/\partial d$ [12]. These sensitivity constants are independent of waveguide length and are used to compare waveguides of different cross-sectional geometries and refractive index profiles.

From the variational theorem of waveguides [19], ∂N_{eff} caused by a local change of dielectric constant $\Delta\epsilon(x, y)$ can be expressed as

$$\partial N_{\text{eff}} = c \int \Delta\epsilon E \cdot E^* dx dy, \quad (1)$$

where $E(x, y)$ is the normalized modal electric field vector. The sensitivity of the device thus scales with the squared amplitude of the electric field within the perturbation, and therefore with the fraction of the modal power contained in the surface volume where the dielectric constant is modified by the analyte. This fraction can be increased by reducing the waveguide core layer thickness to a point where the mode becomes less confined and expands from the core,

raising the field magnitude at the interface. Furthermore, given the boundary condition that the normal component of the electric displacement vector $\mathbf{D} = \epsilon\mathbf{E}$ must be continuous across the interface, the field amplitude above the surface is increased by using a high-index-contrast waveguide and the TM mode, for which the dominant field component is polarized normal to the sensing surface. This results in a discontinuity of the normal component of \mathbf{E} at the surface, which serves to enhance the field at the analyte side of the interface relative to that on the core side by a factor of the ratio of the respective dielectric constants. This enhancement factor thereby increases with index contrast.

For surface sensing, it is important that the evanescent tail of the waveguide mode is localized near the waveguide surface where the biomolecules are located and not extend too far into the analyte solution. The penetration depth of the waveguide mode into the cladding material of refractive index n_c is given by [20]

$$\gamma = \frac{\lambda}{2\pi\sqrt{N_{\text{eff}}^2 - n_c^2}}. \quad (2)$$

From (2), it follows that as the index contrast increases (which raises N_{eff}) the evanescent field becomes more localized near the waveguide surface.

Finally, it is important to maximize the proportion of the evanescent field on the analyte side of the waveguide core relative to that on the substrate (lower cladding) side. In most practical sensing applications where the lower cladding refractive index is greater than the analyte medium index, the sensitivity can be shown to be an increasing function of the waveguide symmetry [15]. The use of high refractive index core materials on low refractive index cladding materials increases the effective waveguide index symmetry, and the fraction of the optical power traveling through the lower cladding can be minimized.

3. WAVEGUIDE OPTIMIZATION AND SENSING CONFIGURATIONS

3.1. Waveguide design

The above arguments suggest that a high refractive index, thin waveguide core layer on a low refractive index lower cladding is an ideal choice for evanescent field sensors. Submicron dimension waveguides fabricated on the SOI material platform strongly meet these requirements. To optimize the SOI waveguide parameters and to examine how the thickness of the silicon waveguide core layer influences the evanescent field interaction with molecules located at the waveguide surface, we performed transfer-matrix-based waveguide simulations using a simple step-index, one-dimensional slab waveguide model. This model was used to calculate the effective index change induced by the adsorption of a thin biomolecular layer on the silicon waveguide core layer. An aqueous upper waveguide cladding and a silica lower cladding were assumed, and the signal wavelength was taken as 1550 nm. Working at this optical wavelength allows low cost and widely available optical test

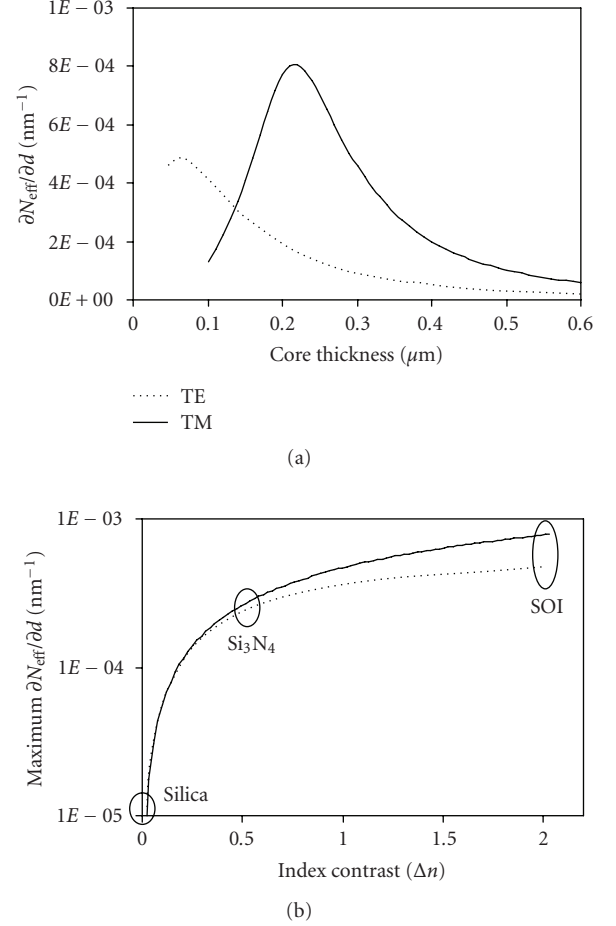


FIGURE 2: (a) Calculated sensitivity constants for a SOI slab waveguide as a function of waveguide core thickness. (b) Calculated maximum $\partial N_{\text{eff}}/\partial d$ obtained for slab waveguides with varying refractive index contrast.

equipment developed for the telecommunications industry to be used. The calculations were performed for varying silicon waveguide thickness for both the transverse electric (TE) and TM polarization modes and are shown in Figure 2(a). As seen, the sensitivity has a clear maximum at a specific silicon waveguide thickness, which is $0.06 \mu\text{m}$ for TE polarization and $0.22 \mu\text{m}$ for TM polarization. Advantageously, the optimum silicon thickness value of $\sim 0.2 \mu\text{m}$ for the more sensitive TM polarization is a commonly used SOI wafer structure and is readily available from commercial suppliers.

Similar calculations were performed for waveguide systems with varying refractive index contrast (Δn) to confirm the sensitivity arguments discussed in Section 2. For consistency, all calculations were performed for a signal wavelength of 1550 nm, and an aqueous upper cladding and a silica lower cladding were assumed. The maximum achievable sensitivity is plotted in Figure 2(b). For the lower-index contrast systems ($\Delta n \leq 0.16$), a minor increase in sensitivity is obtained for the TE polarized mode compared with the TM mode. For larger index contrast platforms, the sensitivity is higher for the TM mode as expected from the

electric field boundary conditions discussed above. From Figure 2(b), the sensitivity advantage of using high-index-contrast waveguides such as SOI is clearly seen.

For a practical sensor, the waveguide should provide confinement in two dimensions and support only a single optical mode. The latter is required to obtain a well-defined spectral transmission function that can be easily analyzed. For single mode operation near the optimum silicon core thickness, silicon photonic wire waveguides, with the silicon etched fully down to the buried oxide, are a natural choice. The calculated TM mode field is shown in Figure 3 for the $0.26 \mu\text{m} \times 0.45 \mu\text{m}$ photonic wire waveguide used in our experiments. A large surface field magnitude is obtained along the top of the waveguide, which is localized within $\sim 120 \text{ nm}$ of the waveguide surface for strong interaction with surface bound molecules.

3.2. Fiber-to-waveguide optical coupling

A major challenge with the use of photonic wire waveguides is the difficulty of coupling light from an optical fiber with a mode size diameter of several μm to these waveguides with a submicron mode size. Due to the large mismatch, coupling losses exceeding 15 dB are common with such structures. To overcome this problem, we have developed optical mode transformers using inversely tapered waveguides covered with a 2- μm -thick SU-8 photoresist upper cladding layer. The sensor waveguide (nominal width of $0.45 \mu\text{m}$) is adiabatically tapered to a $0.15 \mu\text{m}$ wide coupling section at the device facet, as shown in Figure 4. At this narrow width, the mode becomes weakly confined in the core layer, thereby increasing its size in both the horizontal and vertical directions for greater overlap with the light emerging from the optical fiber. The mode transformers utilize a similar principle to the design reported in [21] and were developed for use with a lensed single-mode fiber. Using such a design, we have achieved less than 3 dB fiber-to-waveguide coupling loss, thus significantly improving the signal-to-noise ratio of our measurements compared to devices without mode transformers. Furthermore, since a large fraction of the optical field is traveling through the cladding materials in the tapered section near the device facet, the mode effective index is reduced. This minimizes reflection loss and Fabry-Pérot cavity effects, which cause instability of the fiber coupling due to mechanical vibration.

3.3. The Mach-Zehnder interferometer sensor

An evanescent field sensor relies on the perturbation of waveguide mode effective index that induces a phase shift of the propagating optical signal. This phase shift is not easily monitored directly and various interferometric waveguide circuits can be used to transform it to a more easily detectable intensity change. A simple and effective waveguide device for this purpose is the Mach-Zehnder interferometer (MZI), which is illustrated in Figure 5(a). In a typical configuration, light of wavelength λ (in vacuum) and intensity I_0 is split into two paths: a sensing path that is exposed to the analyte and an isolated reference path. These waveguide paths are

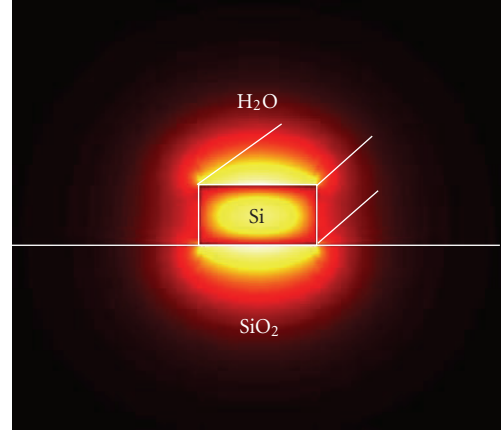


FIGURE 3: The electric field distribution for the TM polarization of a $0.26 \mu\text{m} \times 0.45 \mu\text{m}$ silicon photonic wire waveguide covered with an aqueous cladding. As seen, large electric field magnitude is obtained at the waveguide surface.

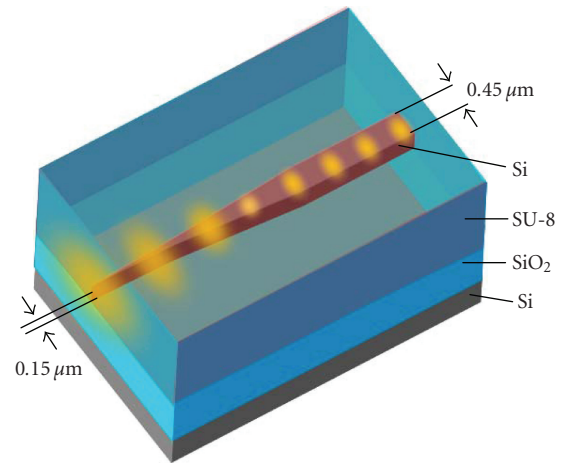


FIGURE 4: Schematic of the inversely tapered mode transformer used for improved fiber-to-waveguide coupling. The nominal $0.45 \mu\text{m}$ wide photonic wire sensor waveguide is laterally tapered down to $0.15 \mu\text{m}$ for adiabatic expansion of the waveguide mode near the device facet.

then recombined causing the signals from the two arms to interfere producing a phase dependent intensity I , to be observed at the MZI output. The transfer function of the MZI is

$$I = \frac{I_0}{2} \left[1 + \cos\left(\frac{2\pi}{\lambda} (N_{\text{eff},s}L_s - N_{\text{eff},r}L_r)\right) \right], \quad (3)$$

where $N_{\text{eff},s}$ and L_s are the effective refractive index and length of the sensing waveguide, and $N_{\text{eff},r}$ and L_r are the effective refractive index and length of the reference waveguide. The phase difference between the two arms is given by the argument of the cosine function in (3). By differentiating this

quantity, the sensitivity of the phase ϕ to homogeneous and surface sensing can be expressed as

$$\begin{aligned} \frac{\partial\phi}{\partial n_c} &= \frac{2\pi L_s}{\lambda} \frac{\partial N_{\text{eff},s}}{\partial n_c} \quad (\text{homogeneous sensing}), \\ \frac{\partial\phi}{\partial d} &= \frac{2\pi L_s}{\lambda} \frac{\partial N_{\text{eff},s}}{\partial d} \quad (\text{surface sensing}). \end{aligned} \quad (4)$$

It is seen that the phase sensitivity scales with sensing waveguide length L_s and with the waveguide sensitivity constants: $\partial N_{\text{eff}}/\partial n_c$ or $\partial N_{\text{eff}}/\partial d$. MZI devices provide important practical advantages over other waveguide circuit designs. Since the intensity change is monitored, they can be used with a low cost, fixed wavelength laser source and by tracking the sinusoidal output variations they can function over a large dynamic range of surface loading conditions. Furthermore, by balancing the optical path lengths of the sensor and reference arms the MZI can be designed to function independently of temperature and signal wavelength. This reduces the requirements for temperature stability of the chip and wavelength stability of the laser source, thereby reducing potential instrumentation costs associated with this technology.

3.4. The ring resonator sensor

The high lateral index contrast provided by silicon photonic wire waveguides allows waveguide bends to be fabricated with a radius of curvature of only a few micrometers with little excess loss. This has led to the development of ultracompact ring resonator structures, which have been used for many applications, including optical add/drop filtering [22], sensing [18], optical logic [23], nonlinear optics [24], and optical modulation [25].

In the simplest form, a ring resonator contains a straight bus waveguide evanescently coupled to a ring cavity using a directional coupler, as illustrated in Figure 5(b). Light of specific wavelengths couples from the bus waveguide to the ring waveguide and circulates, making many round trips and building up intensity within the ring cavity. At these resonant wavelengths, a sharp dip is observed in the transmission spectrum of the bus waveguide. The sharpness of the resonance dip is described by the quality factor Q of the ring [26]:

$$Q \equiv \frac{\lambda}{\Delta\lambda_{\text{FWHM}}} \cong \frac{\pi n_g L}{\lambda} \frac{\sqrt{\alpha t}}{1 - \alpha t}, \quad (5)$$

where $\Delta\lambda_{\text{FWHM}}$ is the full width at half maximum of the resonance, L is the ring cavity length, n_g is the ring waveguide group index, t is the through coupling coefficient between the bus and ring waveguides, and α is the total resonator loss including the coupler loss and the round trip propagation loss in the ring.

An undesirable characteristic of conventional ring resonators with a directional coupler is the inherent wavelength dependence of the coupling between the bus and ring waveguides. This causes a slowly varying modulation of the resonance depths in the output spectrum, limiting the

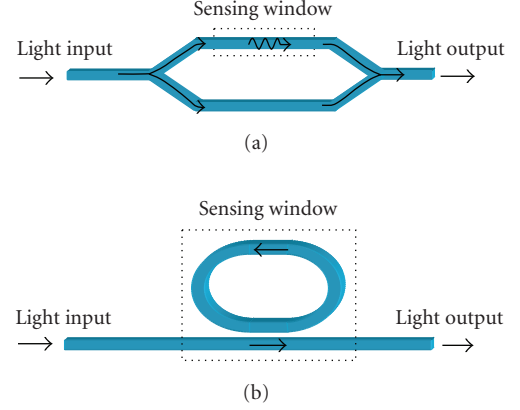


FIGURE 5: (a) Schematic of an MZI evanescent field sensor. The input waveguide is split into two paths where one is exposed to the analyte and the other is isolated from the analyte. The paths are recombined and the signals interfere causing a sinusoidal phase dependent intensity signal to be transmitted through the output waveguide. (b) A conventional ring resonator design employing a directional coupler between the straight bus waveguide and the ring cavity. The dashed lines indicate the positions of the sensor windows where the upper SU-8 isolation layer is removed.

useable wavelength range over which a uniform transmission spectrum is obtained. To overcome this limitation, we have designed a new ring resonator structure in SOI that utilizes a multimode-interference coupler (MMI) between the bus and ring waveguides [26]. The MMI significantly reduces the wavelength dependence of the coupling, producing a more uniform resonance spectrum over a broad range of wavelengths. In addition, the MMI structure improves the fabrication tolerance by eliminating the narrow gap of the directional coupler.

As molecules bind to the ring surface (or if the bulk refractive index of the analyte solution changes) a phase shift of the optical mode is induced, resulting in a wavelength shift of the resonances. This wavelength shift scales with the number of adsorbed molecules to the ring waveguide (or with the refractive index change of a bulk solution) and is typically the parameter being measured in this type of sensor. Alternatively, it is also possible to track the intensity change at a fixed wavelength over a single resonance peak. In this case, the dynamic range is limited and the sensor can only be used to track comparatively low analyte concentrations or low refractive index changes of bulk solutions since the peak position may shift away from the input wavelength. However, active tuning of the resonance through temperature or other means may provide a solution to this tradeoff at the price of increased complexity.

Ring resonators have very sharp resonances and may provide higher sensitivity compared to other waveguide circuit configurations such as the MZI. Since light at the resonance wavelengths circulates around the ring cavity, it has numerous interactions with the same molecules amplifying the measured response. They also offer a more compact geometry desirable for the fabrication of high-density sensor arrays. However, when the resonance wavelengths are

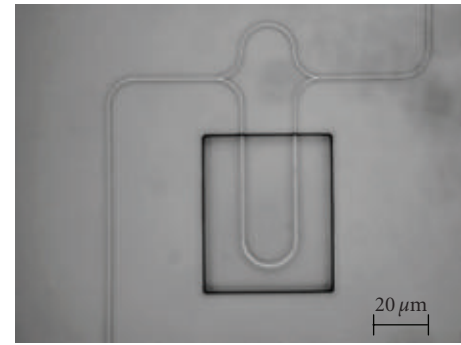
monitored, ring resonators require either a tunable laser source or a broadband optical source and a means to monitor the output wavelengths. In either case, this increases the potential instrumentation costs for this technology. Ring resonators also do not provide for internal referencing for temperature or wavelength drifts and therefore require either precise temperature control of the sensor and optical source, or they require a second reference device.

Due to the different characteristics of the ring resonator and the MZI, we are currently developing both types of sensors where we believe that the optimal circuit choice will depend on the sensitivity and cost requirements of the particular application.

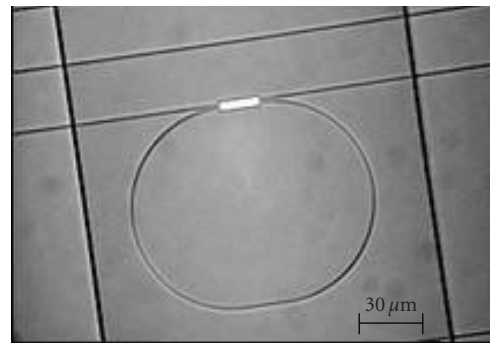
4. DESIGN AND FABRICATION

MZI sensors and ring resonators were designed having $0.26\ \mu\text{m} \times 0.45\ \mu\text{m}$ photonic wire sensing waveguides. The waveguide height was chosen to be near the optimum sensitivity point of Figure 2(a) for TM polarization. The waveguide width was designed to be narrow enough to provide single mode operation, while being wide enough to permit sharp bends of the waveguide with a radius of curvature of a few microns. Optical mode transformers having a $0.26\ \mu\text{m} \times 0.15\ \mu\text{m}$ cross section were integrated at both waveguide facets for improved input and output coupling. Our early designs used conventional waveguide layout geometries for the ring and MZI sensors and are shown in Figure 6. We have demonstrated sensitive evanescent field sensors using these devices, capable of detecting less than 1% of a monolayer of streptavidin molecules adsorbed to the biotinylated waveguide surface [18].

Here, we will focus on our more recent sensor designs that further exploit the high lateral index contrast of the silicon photonic wire waveguide, which allows very sharp waveguide bends to be achieved. As mentioned above, the phase sensitivity of evanescent field sensors is determined by both the intrinsic waveguide sensitivity constants ($\partial N_{\text{eff}}/\partial n_c$ or $\partial N_{\text{eff}}/\partial d$) and the waveguide length. By increasing the waveguide length, a larger number of molecules will be captured on the waveguide surface for a given analyte concentration and interaction time, thereby inducing a larger phase shift (see (4)). However, long straight waveguides are not desirable for two-dimensional arraying purposes and are not suited for common functionalization techniques using commercial spotting apparatus. To address these issues, we have designed coiled waveguide sensing structures as shown in Figure 7. For the MZI devices, several mm of sensing path length have been designed in a circular area of $150\ \mu\text{m}$ diameter, comparable to the drop size employed by modern spotting tools. Spiral ring cavities with 1.3 mm length have also been designed with similar dimensions. The additional length over conventional circular/oval cavities leads to improvement of the quality factor of the resonance allowing increased measurement accuracy of the resonance wavelengths. Both the spiral MZI and ring designs offer the high sensitivity of a long waveguide without sacrificing



(a)



(b)

FIGURE 6: Scanning electron microscope images of our early sensor designs employing silicon photonic wire waveguides arranged in: (a) a conventional MZI structure and (b) a ring cavity containing a MMI coupler.

size, and their increased surface areas provide more efficient molecular capture.

The devices in Figure 7 were fabricated on SOI wafers having a $0.26\text{-}\mu\text{m}$ -thick silicon layer on a $2\text{-}\mu\text{m}$ -thick buried oxide layer. Waveguides were patterned by electron beam lithography and etched in an inductively coupled plasma reactive ion etching system. To isolate the optical mode of the nonsensing portions of the device from the environment, a $2\text{-}\mu\text{m}$ -thick layer of SU-8 photoresist was spun on the wafer and windows were opened over the active sensing area using optical contact lithography. The devices were then baked to cure the SU-8 film. Finally, samples were exposed to an O_2 plasma to remove any residual photoresist in the sensor windows as well as to increase the thickness of the native oxide layer (used later for functionalization). The sensors were then diced into individual chips and some were then used for homogeneous solution sensing experiments as described in Section 5.

For surface sensing experiments, the sensors were functionalized by immobilizing biotin on the chip surface in order to monitor the affinity reaction between the vitamin biotin and the protein streptavidin. The oxide on the silicon waveguide surface, measured to be $2.7 \pm 0.2\ \text{nm}$ thick by ellipsometry, was left intact so that standard glass-based functionalization procedures to attach biotin to the surface

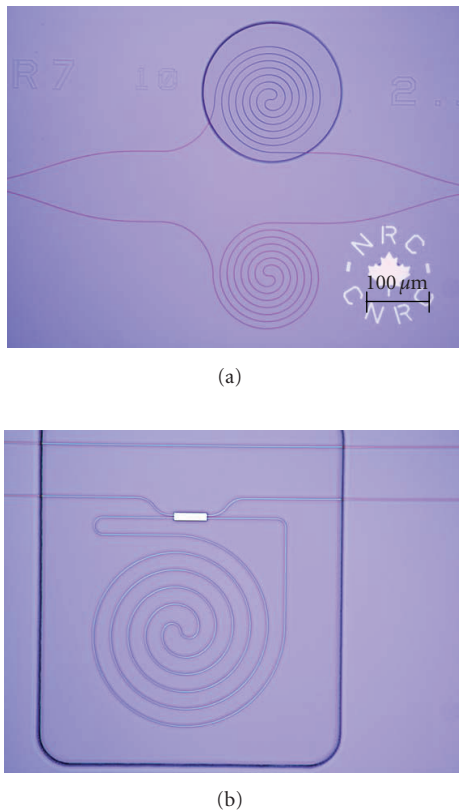


FIGURE 7: Sensor designs with double spiral waveguide geometries providing increased sensing path length while maintaining a compact sensor footprint. (a) MZI sensor with 2 mm sensing path length contained within a circular 150 μm diameter area. (b) Spiral cavity ring resonator design with 1.3 mm sensor length contained within a circular 110 μm diameter area.

could be used. The functionalization procedure began with a cleaning step where the sample was rinsed with ethanol and then cleaned and activated with nitric acid for 5 minutes. The samples were then rinsed with deionized water and ethanol and dried under nitrogen. Surfaces were then silanized with 3-aminopropyltriethoxysilane (APTES) vapor. The surfaces were rinsed with ethanol, dried and biotinylated by coating the surface in a solution of 1 mg/mL of N-hydroxysuccinimide (NHS) activated biotin in dimethylformamide (DMF) for 1 hour, followed by rinsing with DMF and ethanol. The incremental thickness change induced by adsorption of streptavidin to the sensor surface was assessed using a functionalized silicon wafer, which was immersed in a streptavidin solution for 1 hour followed by rinsing with phosphate buffered saline (PBS). Based on ellipsometry measurements, we estimate a surface mass coverage of 2.2 ng/mm² of streptavidin, following Elwing [27]. The above process was performed on the entire sensing chip. Future experiments will attempt to functionalize individual sensor elements using a microarray spotter for multianalyte detection.

Analyte was delivered to the sensor through a microfluidic component fabricated in polydimethylsiloxane (PDMS).

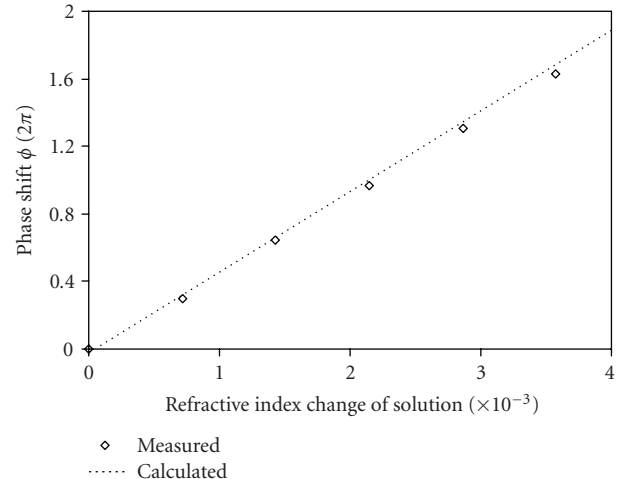


FIGURE 8: MZI sensor response to homogeneous solution refractive index change. The calculated phase shift values are shown by the dotted line.

Channels with a width of 200 μm were defined in the PDMS by using a surface relief mold fabricated using 50 μm thick SU-8 resist tracks defined on a silicon wafer. The PDMS component was subsequently aligned and fixed to the sensor chip, and a syringe pump was used to drive solutions through the microfluidic channels.

5. EXPERIMENTAL DEMONSTRATION

Using a tapered optical input fiber, a tunable laser source, and an InGaAs photodetector, the propagation loss of the fabricated waveguides was assessed by the Fabry-Pérot technique. Several waveguides were measured with loss values varying between 0.3-0.4 dB/mm. The optical coupling loss from a tapered optical fiber was found to be less than 3 dB per facet using the inversely tapered mode converters.

The response of an MZI sensor with a 2-mm-long spiral sensing arm, to homogeneous refractive index change of the analyte solution, was then evaluated by passing sucrose solutions of varying concentration through the microfluidic channel. The solutions were drawn over the exposed sensor arm at a rate of 2 mL/hour, and the transmission of the sensor was measured for each solution. The corresponding phase shift values are shown in Figure 8 as a function of sucrose solution refractive index change (with respect to water). At a signal wavelength of 1550 nm, these phase shift values correspond to a large intrinsic sensitivity constant of $\partial N_{\text{eff}}/\partial n_c = 0.35$, which is only approximately three times less than that achievable using a free-space beam passing through a bulk solution cell. These results agree to within 5% of the calculated phase shift values from the effective indices obtained in mode expansion-based waveguide simulations.

Using the biotin-streptavidin binding system, the response of an MZI with a 2-mm-long spiral sensing arm and a ring resonator sensor with a 1.3-mm-spiral cavity length to the adsorption of a thin protein monolayer was then examined. The intensity change at the MZI output was

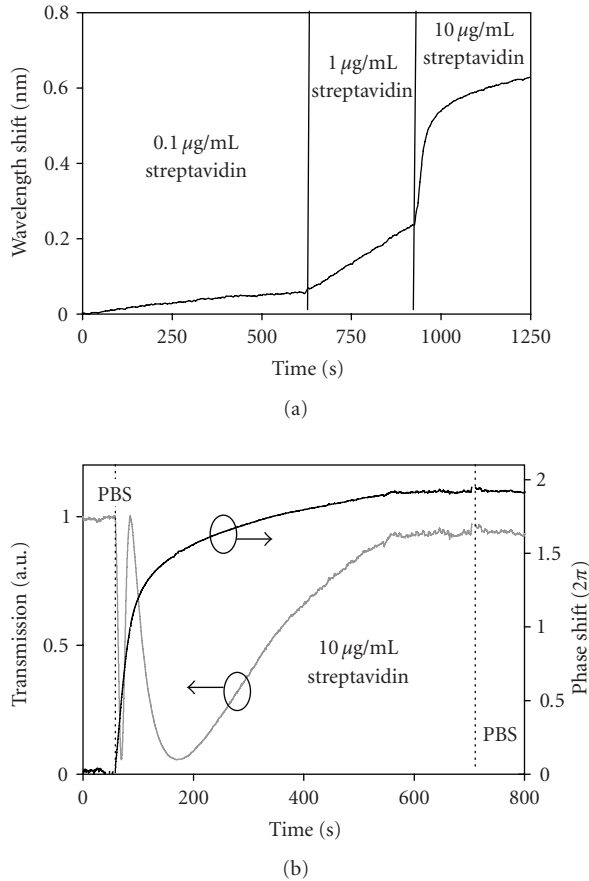


FIGURE 9: Surface adsorption measurements using the sensors to monitor the affinity reaction between streptavidin and the biotinylated waveguide surface. (a) Measured shift in the resonance wavelength for a ~ 1.3 -mm-long double spiral ring resonator sensor. (b) Measured intensity change (grey) and phase shift (black) of an MZI sensor with a 2-mm-long double spiral sensing arm.

monitored at a constant signal wavelength of ~ 1550 nm, whereas the wavelength shift of the ring resonator resonance was monitored during the experiment by sweeping a tunable laser and recording the transmission spectrum. The results of the measurements are shown in Figure 9(a) for the ring resonator sensor and Figure 9(b) for the MZI sensor.

For the ring resonator, the first analyte solution consisted of $0.1 \mu\text{g/mL}$ of streptavidin in PBS. It was passed through the microfluidic channel over the ring cavity, and the transmission spectrum of the ring was recorded every 5 seconds over a 3-nm-wavelength range. Molecular binding is observed by the wavelength shift in the ring resonator response as shown in Figure 9(a). The streptavidin concentration was then increased to $1 \mu\text{g/mL}$ and then to $10 \mu\text{g/mL}$, where successively increased binding rates are observed. For the MZI device, a constant wavelength laser source was used, and the transmitted power was recorded as solutions were drawn over the sensing arm. The results of the experiment are shown in Figure 9(b) for both the raw transmitted intensity signal and the corresponding phase change. The experiment began by flowing PBS solution through the microfluidic

channel for 60 seconds. The solution was then switched to a $10 \mu\text{g/mL}$ streptavidin solution, followed by a PBS solution to rinse nonspecifically bound molecules from the waveguide surface. A typical high-affinity binding curve is obtained. Taking the RMS noise levels in Figure 9 as the minimum detectable phase change or wavelength shift, we estimate that the MZI sensor is capable of detecting $\sim 0.3\%$ of a protein monolayer, while the ring resonator demonstrates a resolution of $\sim 0.2\%$ of a monolayer. These values correspond to a minimum detectable surface coverage of $\sim 6 \text{ pg/mm}^2$ for the MZI sensor and $\sim 4 \text{ pg/mm}^2$ for the ring resonator, which are comparable to the sensitivities reported for state-of-the-art SPR sensors. We have established that the sensor performance is currently limited by intensity noise resulting from Fabry-Pérot cavity effects between the fiber tip and the device facet. These effects are lessened with the inverse tapered mode transformers and can be further reduced by depositing an antireflection coating on the input waveguide facet. Furthermore, for applications where a larger sensor area is permitted the waveguide length can be increased for improved performance. With further optimization of the sensor design and with improvement of the experimental setup to reduce the measurement noise, we expect that minimum detectable surface coverage values well below 1 pg/mm^2 are attainable.

6. SUMMARY

We have reviewed our work developing biological sensors based on silicon photonic wire waveguides arranged in an MZI and ring resonator configuration. We have shown that high-index-contrast SOI waveguides provide a large and localized evanescent field for the TM polarized waveguide mode, resulting in high surface sensitivity. We have also used the high lateral index contrast of silicon photonic wires to make densely coiled sensor waveguide structures that provide the advantages of long sensing path length without compromising the sensor footprint. Due to their compact size, these sensors are compatible with spotter functionalization, microfluidic sample delivery, and the fabrication of two-dimensional arrays. Our future work will focus on the development of an evanescent field-based microarray biochip for multianalyte monitoring that exploits the benefits offered by this technology.

ACKNOWLEDGMENT

This work is supported by the National Research Council Canada's Genomics and Health Initiative Program.

REFERENCES

- [1] W. Lukosz, "Principles and sensitivities of integrated optical and surface plasmon sensors for direct affinity sensing and immunosensing," *Biosensors and Bioelectronics*, vol. 6, no. 3, pp. 215–225, 1991.
- [2] B. J. Luff, J. S. Wilkinson, J. Piehler, U. Hollenbach, J. Ingenhoff, and N. Fabricius, "Integrated optical Mach-Zehnder biosensor," *Journal of Lightwave Technology*, vol. 16, no. 4, pp. 583–592, 1998.

- [3] B. Y. Shew, C. H. Kuo, Y. C. Huang, and Y. H. Tsai, "UV-LIGA interferometer biosensor based on the SU-8 optical waveguide," *Sensors and Actuators A*, vol. 120, no. 2, pp. 383–389, 2005.
- [4] A. Ksendzov and Y. Lin, "Integrated optics ring-resonator sensors for protein detection," *Optics Letters*, vol. 30, no. 24, pp. 3344–3346, 2005.
- [5] F. Prieto, B. Sepúlveda, A. Calle, et al., "An integrated optical interferometric nanodevice based on silicon technology for biosensor applications," *Nanotechnology*, vol. 14, no. 8, pp. 907–912, 2003.
- [6] A. Yalçın, K. C. Popat, J. C. Aldridge, et al., "Optical sensing of biomolecules using microring resonators," *IEEE Journal on Selected Topics in Quantum Electronics*, vol. 12, no. 1, pp. 148–155, 2006.
- [7] G. P. Nordin, S. Kim, Y. Qian, J. W. Noh, and J. Jiang, "In-plane photonic transduction of SOI microcantilever sensors," in *Proceedings of the 3rd IEEE International Conference on Group IV Photonics (GFP '06)*, pp. 4–6, Ottawa, Canada, September 2006.
- [8] L. G. Carrascosa, M. Moreno, M. Álvarez, and L. M. Lechuga, "Nanomechanical biosensors: a new sensing tool," *Trends in Analytical Chemistry*, vol. 25, no. 3, pp. 196–206, 2006.
- [9] J. J. Saarinen, S. M. Weiss, P. M. Fauchet, and J. E. Sipe, "Optical sensor based on resonant porous silicon structures," *Optics Express*, vol. 13, no. 10, pp. 3754–3764, 2005.
- [10] D. Yin, D. W. Deamer, H. Schmidt, J. P. Barber, and A. R. Hawkins, "Integrated optical waveguides with liquid cores," *Applied Physics Letters*, vol. 85, no. 16, pp. 3477–3479, 2004.
- [11] G. P. Anderson, J. P. Golden, and F. S. Ligler, "A fiber optic biosensor: combination tapered fibers designed for improved signal acquisition," *Biosensors and Bioelectronics*, vol. 8, no. 5, pp. 249–256, 1993.
- [12] K. Tiefenthaler and W. Lukosz, "Sensitivity of grating couplers as integrated-optical chemical sensors," *Journal of the Optical Society of America B*, vol. 6, no. 2, pp. 209–220, 1989.
- [13] A. M. Armani, R. P. Kulkarni, S. E. Fraser, R. C. Flagan, and K. J. Vahala, "Label-free, single-molecule detection with optical microcavities," *Science*, vol. 317, no. 5839, pp. 783–787, 2007.
- [14] R. W. Boyd and J. E. Heebner, "Sensitive disk resonator photonic biosensor," *Applied Optics*, vol. 40, no. 31, pp. 5742–5747, 2001.
- [15] O. Parriaux and G. J. Veldhuis, "Normalized analysis for the sensitivity optimization of integrated optical evanescent-wave sensors," *Journal of Lightwave Technology*, vol. 16, no. 4, pp. 573–582, 1998.
- [16] A. Densmore, D.-X. Xu, P. Waldron, et al., "A silicon-on-insulator photonic wire based evanescent field sensor," *IEEE Photonics Technology Letters*, vol. 18, no. 23, pp. 2520–2522, 2006.
- [17] G. T. Reed and A. P. Knights, *Silicon Photonics: An Introduction*, John Wiley & Sons, Hoboken, NJ, USA, 2004.
- [18] A. Densmore, D.-X. Xu, P. Waldron, et al., "Thin silicon waveguides for biological and chemical sensing," in *Silicon Photonics II*, vol. 6477 of *Proceedings of SPIE*, pp. 1–10, San Jose, Calif, USA, January 2007.
- [19] H. Kogelnik, "Theory of optical waveguides," in *Guided Wave Optoelectronics*, T. Tamir, Ed., pp. 7–87, Springer, Berlin, Germany, 2nd edition, 1990.
- [20] R. G. Hunsperger, *Integrated Optics: Theory and Technology*, Springer, Berlin, Germany, 3rd edition, 1991.
- [21] V. R. Almeida, R. R. Panepucci, and M. Lipson, "Nanotaper for compact mode conversion," *Optics Letters*, vol. 28, no. 15, pp. 1302–1304, 2003.
- [22] B. E. Little, S. T. Chu, H. A. Haus, J. Foresi, and J.-P. Laine, "Microring resonator channel dropping filters," *Journal of Lightwave Technology*, vol. 15, no. 6, pp. 998–1005, 1997.
- [23] Q. Xu and M. Lipson, "All-optical logic based on silicon micro-ring resonators," *Optics Express*, vol. 15, no. 3, pp. 924–929, 2007.
- [24] S. Blair, J. E. Heebner, and R. W. Boyd, "Beyond the absorption-limited nonlinear phase shift with microring resonators," *Optics Letters*, vol. 27, no. 5, pp. 357–359, 2002.
- [25] Q. Xu, B. Schmidt, S. Pradhan, and M. Lipson, "Micrometre-scale silicon electro-optic modulator," *Nature*, vol. 435, no. 7040, pp. 325–327, 2005.
- [26] D.-X. Xu, A. Densmore, P. Waldron, et al., "High bandwidth SOI photonic wire ring resonators using MMI couplers," *Optics Express*, vol. 15, no. 6, pp. 3149–3155, 2007.
- [27] H. Elwing, "Protein absorption and ellipsometry in biomaterial research," *Biomaterials*, vol. 19, no. 4-5, pp. 397–406, 1998.

Research Article

Nanotomography of Cell Surfaces with Evanescent Fields

Michael Wagner,¹ Petra Weber,¹ Wolfgang S. L. Strauss,² Henri-Pierre Lassalle,^{1,3}
and Herbert Schneckenburger^{1,2}

¹ Institute of Applied Research, Hochschule Aalen, Anton-Huber-Street 1, 73430 Aalen, Germany

² Institute of Laser Technologies in Medicine and Metrology, Ulm University, Helmholtzstr. 12, 89081 Ulm, Germany

³ Centre de Recherche en Automatique de Nancy, Nancy Université, CNRS, Centre Alexis Vautrin, Avenue de Bourgoigne, 54511 Vandoeuvre les Nancy, France

Correspondence should be addressed to Herbert Schneckenburger, herbert.schneckenburger@htw-aalen.de

Received 13 March 2008; Accepted 29 April 2008

Recommended by Stoyan Tanev

The technique of variable-angle total internal reflection fluorescence microscopy (TIRFM) and its application to nanotomography of cell surfaces are described. Present applications include (1) 3D imaging of chromosomes in their metaphase to demonstrate axial resolution in the nanometre range, (2) measurements of cell-substrate topology, which upon cholesterol depletion shows some loosening of cell-substrate contacts, and (3) measurements of cell topology upon photodynamic therapy (PDT), which demonstrate cell swelling and maintenance of focal contacts. The potential of the method for in vitro diagnostics, but also some requirements and limitations are discussed.

Copyright © 2008 Michael Wagner et al. This is an open access article distributed under the Creative Commons Attribution License, which permits unrestricted use, distribution, and reproduction in any medium, provided the original work is properly cited.

1. INTRODUCTION

Microscopy with subwavelength resolution has been a challenge for many years. While lateral resolution has been increased continuously to about 60 nm [1] in far-field microscopy and to even less in optical near-field microscopy, axial resolution has remained in a range above 100 nm. However, in close vicinity to a surface (e.g., cell-substrate interface), further improvement in axial resolution may be achieved by total internal reflection (TIR) techniques. Total internal reflection fluorescence microscopy (TIRFM) has first been described in 1981 [2], and since that time has been used increasingly for measuring cell-substrate contacts [3–5], membrane or protein dynamics [6, 7], membrane proximal ion fluxes [8] as well as endocytosis or exocytosis [9–11]. TIRFM is based on total internal reflection of a light beam propagating through a medium of refractive index n_1 (e.g., glass substrate) and meeting a second medium of refractive index $n_2 < n_1$ (e.g., cell). Despite being totally reflected at all angles $\Theta \geq \Theta_c = \arcsin(n_2/n_1)$, the incident beam establishes an evanescent electromagnetic field E_{ev} that penetrates into the second medium and decays exponentially

with the distance z from the interface. According to the relation

$$d = \left(\frac{\lambda}{4\pi} \right) (n_1^2 \sin^2 \Theta - n_2^2)^{-1/2}, \quad (1)$$

penetration depths d between about 60 nm and more than 200 nm are attained for its intensity $I_{ev} \sim E_{ev}^2$, depending on the wavelength λ and the angle of incidence Θ . Therefore, fluorescent dyes located within or close to the plasma membrane can be examined almost selectively in living cells. In addition, upon variation of Θ , the relation

$$I_F(\Theta) = AcT(\Theta)te^{-\Delta/d(\Theta)} \quad (2)$$

between fluorescence intensity $I_F(\Theta)$, penetration depth $d(\Theta)$, and cell-substrate distance Δ has been established for fluorescent dyes (of constant quantum yield) distributed within a thin layer of thickness t [4] with A corresponding to an experimental constant, c to the local concentration of the fluorophore, and $T(\Theta) = 4\cos^2\Theta/[1 - (n_2/n_1)^2]$ to the transmission factor of incident light through the cell-substrate interface (on the condition that light is

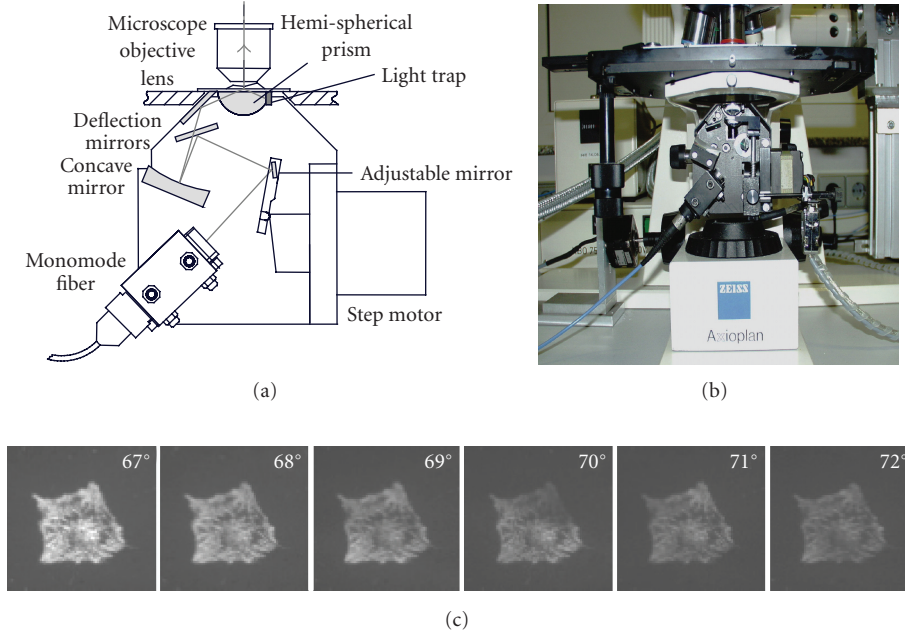


FIGURE 1: Illumination device (microscope condenser) for variable-angle TIRFM with an additional option for transillumination and phase contrast microscopy (a) scheme, (b) experimental setup, and (c) fluorescence images of the cytoplasm marker calcein in a U373MG glioblastoma cell upon variable-angle illumination.

polarized perpendicular to the plane of incidence). Similarly, a relation

$$I_F = AcT(\Theta)d(\Theta)e^{-\Delta/d(\Theta)} \quad (3)$$

has been established for fluorescent dyes distributed homogeneously at distances larger than Δ [4], again assuming a constant fluorescence quantum yield over the samples.

On the basis of (2) fluorescence images of a membrane marker recorded at different angles of incidence Θ can be used to calculate the cell-substrate distance Δ with nanometre precision, when $\ln[I_F(\Theta)/T(\Theta)]$ is evaluated as a function of $d^{-1}(\Theta)$. Similarly, fluorescence images of a cytoplasm marker can be used for calculation of Δ , when $\ln[I_F(\Theta)/T(\Theta)d(\Theta)]$ is evaluated as a function of $d^{-1}(\Theta)$ according to (3). In both cases, Δ results from the slope of a straight line, which can be calculated for each pixel of a fluorescence image.

In the present paper, three examples of nanotomography with variable-angle TIRFM are given.

- (1) Chromosomes in metaphase stained with the fluorescence marker DAPI are used to show the potential of 3D tomography.
- (2) Human glioblastoma cells incubated with the membrane marker laurdan are used to visualize changes of cell-substrate topology upon depletion of cholesterol.
- (3) Human glioblastoma cells loaded with 5-aminolevulinic acid induced protoporphyrin IX are shown to change their membrane topology upon photodynamic therapy (PDT) [12].

2. MATERIALS AND METHODS

All TIRFM measurements were carried out with either chromosomes or cultivated cells. Chromosomes from Chinese hamster ovary (CHO) cells stained with the DNA marker DAPI were stopped in the metaphase of mitosis by colchicine and prepared on microscope object slides. Their typical length was about $5 \mu\text{m}$ and their diameter around 500 nm .

U373MG human glioblastoma cells obtained from the European Collection of Cell Cultures (ECACC no. 89081403) were routinely grown in RPMI 1640 medium supplemented with 10% fetal calf serum and antibiotics at 37°C and 5% CO_2 . After seeding of $150 \text{ cells}/\text{mm}^2$, cells were grown on microscope object slides for 48 hours prior to rinsing with Earl's balanced salt solution (EBSS) and incubation for 1 hour with either the fluorescent membrane marker laurdan ($8 \mu\text{M}$) or coinubation with laurdan ($8 \mu\text{M}$) and methyl- β -cyclodextrin ($\text{M}\beta\text{CD}$; 1 mM or 4 mM) diluted in culture medium without serum. Cholesterol depletion after application of $\text{M}\beta\text{CD}$ is well documented in the literature [13], and preliminary experiments proved that its intracellular amount is reduced by about 30% (at 1 mM $\text{M}\beta\text{CD}$) or 50% (at 4 mM $\text{M}\beta\text{CD}$). After incubation for 60 minutes, cells were again rinsed with EBSS and examined in the fluorescence microscope at room temperature.

In a further experiment U373MG cells cultivated under the same conditions were incubated for 6 hours at $\text{pH} = 7.2$ with 10^{-3} M 5-aminolevulinic acid (5-ALA; Medac Wedel, Germany), an intermediate in porphyrin biosynthesis, and rinsed with EBSS prior to TIRFM measurements. Part of the cells was transiently transfected with the plasmid encoding for the yellow fluorescent protein (YFP)-focal

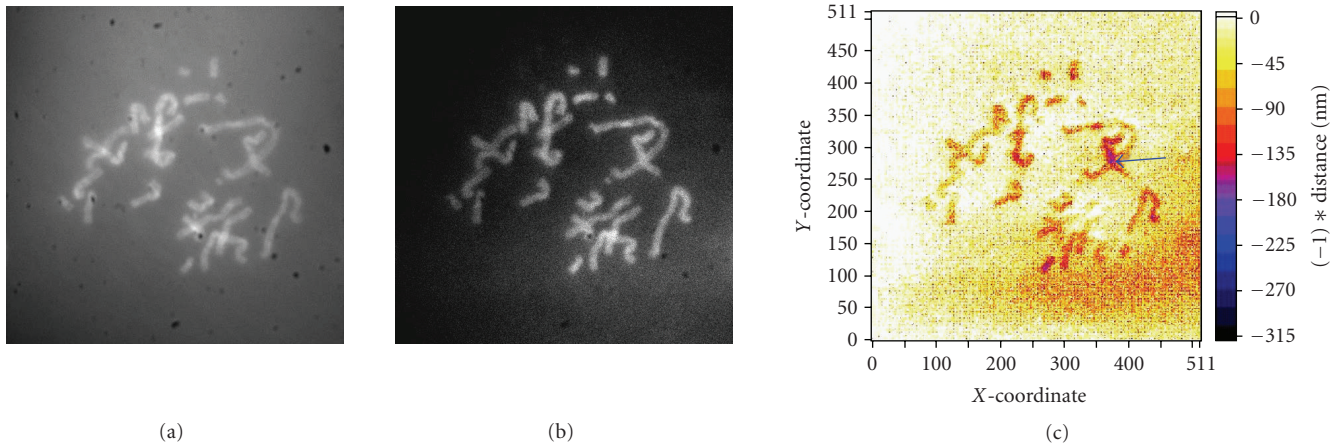


FIGURE 2: Fluorescence images of chromosomes from T47D breast cancer cells stained with DAPI in metaphase. (a) Conventional fluorescence microscopy, (b) TIRFM at $\Theta = 72.5^\circ$, and (c) tomographic imaging of chromosome-substrate distances (fluorescence excited at 391 nm and detected at $\lambda \geq 415$ nm; image size: $55 \mu\text{m} \times 55 \mu\text{m}$). The arrow marks overlapping chromosomes.

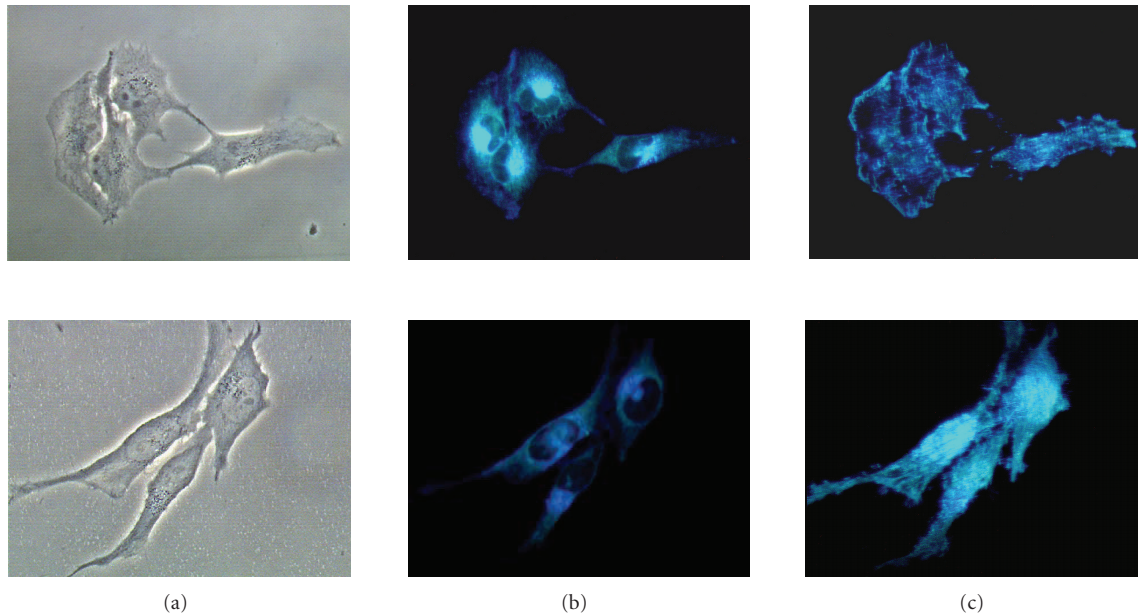


FIGURE 3: (a) Phase contrast, (b) whole cell fluorescence, and (c) TIRFM images of U373MG glioblastoma cells upon incubation with laurdan either without further treatment (upper series) or with 30% cholesterol depletion (by 1 mM $M\beta CD$; lower series). Fluorescence excited at 391 nm and detected at $\lambda \geq 415$ nm; image size: $200 \mu\text{m} \times 150 \mu\text{m}$. Real colour images recorded with a 3-chip CCD camera.

adhesion kinase (FAK) fusion protein [14] by lipofection (FuGene 6 Transfection Reagent, Roche Diagnostics GmbH, Mannheim, Germany) in order to visualize focal adhesions. The YFP-FAK vector was kindly provided by A.R. Horwitz, University of Virginia, USA.

For TIR illumination of cultivated cells a UV-laser diode (LDH 400 with driver PDL 800-B, Picoquant, Berlin, Germany; wavelength: 391 nm, pulse energy: 12 pJ, repetition rate 40 MHz, average power: 0.5 mW) was adapted to a fluorescence microscope (Axioplan 1, Carl Zeiss Jena, Germany) by single mode fibre optics (Point Source, kineFlex-p-3-S-395, Southampton, UK). For measurements of DAPI stained chromosomes, the 391 nm laser diode was replaced by a

diode of the same type, but emitting light at 375 nm. EYFP-FAK was illuminated by the 514 nm line of an argon ion laser operated at 10 mW (Innova 90, Coherent, Santa Clara, USA). TIR illumination was carried out with a custom made device [4] permitting to vary the angle of incidence in steps of 0.5° with a resolution of 0.15° . Angles were varied either between 66° and 72° (U373MG cells) or between 70° and 76° (chromosomes). Assuming refractive indices $n_1 = 1.515$ (glass substrate) and $n_2 = 1.37$ (cytoplasm), penetration depths of the evanescent electromagnetic field within cells varied between about 160 nm and 70 nm according to (1). Fluorescence images were recorded with an electron multiplying (EM-) CCD camera with Peltier cooling and

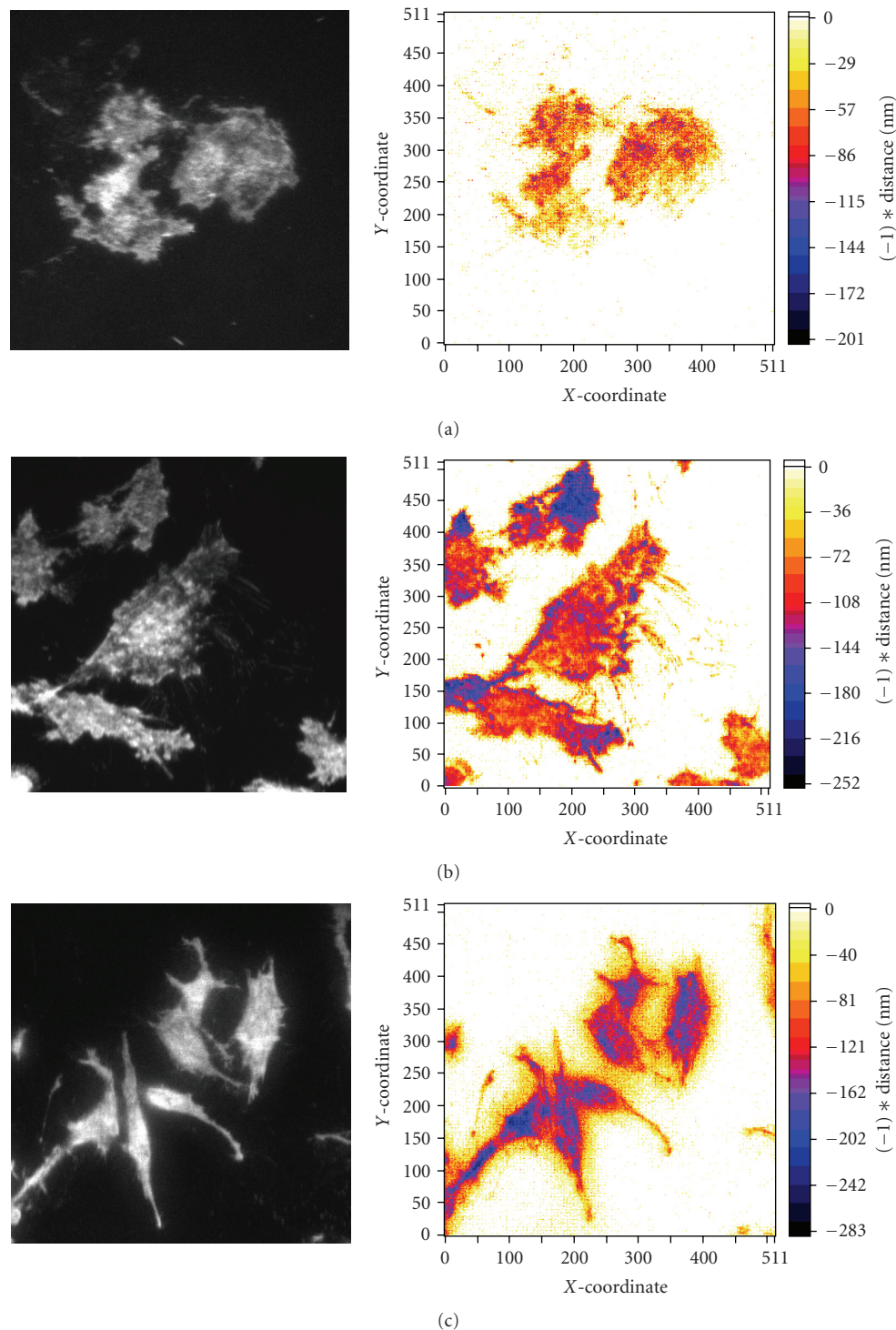


FIGURE 4: TIRFM images recorded at $\Theta = 66^\circ$ (left) and cell-substrate topology (right) of U373MG glioblastoma cells upon incubation with laurdan either (a) without further treatment or 30% cholesterol depletion (by 1 mM $M\beta CD$; (b) or (c) 50% cholesterol depletion (by 4 mM $M\beta CD$). Fluorescence excited at 391 nm and detected at $\lambda \geq 415$ nm; image size: $210 \mu\text{m} \times 210 \mu\text{m}$).

a sensitivity below 10^{-17} W/Pixel (DV887DC-BV, ANDOR Technology, Belfast, UK). In one case, this camera was replaced by a Sony 3CCD Colour Camera (Model MC-3254, AVT Horn, Aalen, Germany, in combination with the software AxioVision, Carl Zeiss Jena, Germany). A long pass

filter for $\lambda \geq 415$ nm was used for detection of DAPI stained chromosomes as well as for laurdan, whereas a long-pass filter for $\lambda \geq 590$ nm was used for detection of 5-ALA induced protoporphyrin IX (PP IX), and a bandpass filter for 529 ± 20 nm (in combination with a notch filter at 514 nm)

was used for YFP-FAK. For experiments on photodynamic therapy sublethal light doses of 4 J/cm^2 at 633 nm (resulting from a 25 mW helium-neon laser; Stabilite 124B, Spectra Physics, Mountain View, USA) were applied under epi-illumination, and recording of TIRFM images was repeated immediately afterwards.

Cell-substrate distances were calculated according to (2) or (3) with a custom made computer program from a series of 8–12 TIRFM images each. For each image, the background of the camera system was subtracted. Cell-substrate distances (or chromosome-substrate distances) were evaluated for all pixels, where fluorescence intensity exceeded this background level. The scheme and the experimental setup of the TIR illumination device are depicted in Figure 1 together with a series of variable-angle TIRFM images of U373MG cells loaded with the cytoplasm marker calcein.

3. RESULTS AND DISCUSSION

3.1. 3D topology of chromosomes

Fluorescence images of DAPI stained chromosomes on a microscope slide are depicted in Figure 2 upon epi-illumination (conventional fluorescence microscopy) and TIR illumination at $\Theta = 72.5^\circ$. Upon TIR illumination, a pronounced increase of the signal-to-background ratio occurs. Figure 2 also shows a topographic image calculated according to (3) from variable-angle TIRFM images (since the fluorescent dye is distributed over the whole chromosomes, the same fitting algorithm as for a cytoplasm marker is used). According to this topographic image, the distance between the chromosomes and the glass surface varies between 0 nm and 150 nm . Only when chromosomes are overlapping (marked by an arrow) larger distances are observed. In Figure 2, the axial resolution is far below 100 nm and typically reaches values around $10\text{--}20 \text{ nm}$.

3.2. Impact of cholesterol on cell-substrate topology

The fluorescence marker 6-dodecanoyl-2-dimethylaminonaphthalene (laurdan) is described in the literature as a polarity-sensitive probe, whose optical spectra depend on membrane stiffness and fluidity [15, 16]. Its fluorescence spectrum is composed by two emission bands with maxima around 440 nm and 490 nm , respectively. It is well documented that with decreasing membrane stiffness the long-wave 490 nm band becomes more pronounced compared to the short-wave 440 nm band, for example, upon temperature increase or cholesterol depletion [17]. The effect of cholesterol depletion on laurdan fluorescence in whole cells and plasma membranes is documented in Figure 3 upon (b) epi-illumination and (c) TIR illumination by real colour imaging. For a comparison, (a) phase contrast images of these cells are added. Upon incubation of the cells with laurdan (without any further treatment) the fluorescence images appear dark blue, since they are dominated by the 440 nm band, whereas upon coincubation with laurdan and $M\beta CD$ (30% cholesterol depletion) whole cells still appear

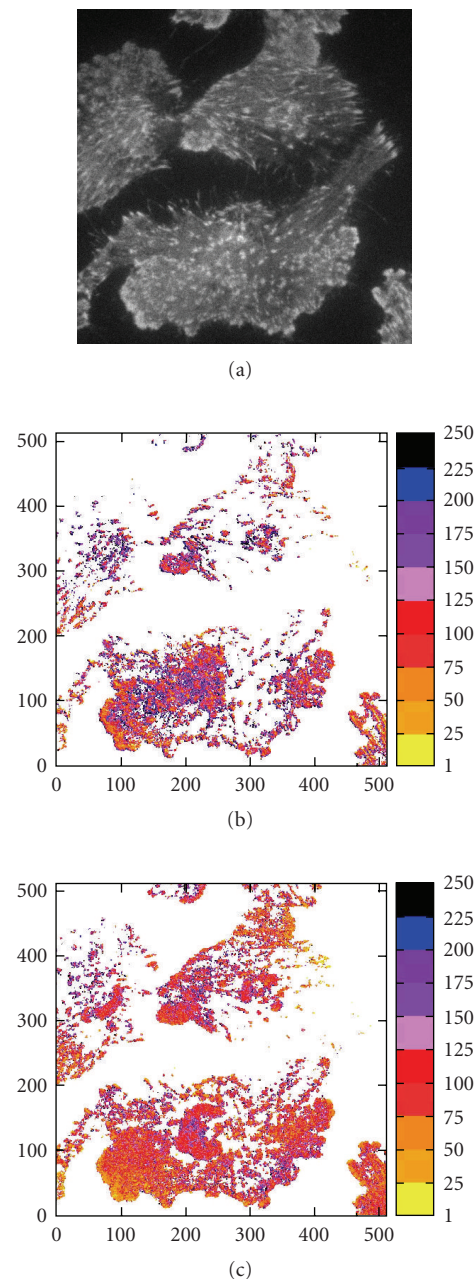


FIGURE 5: TIRF image of 5-ALA induced PP IX (A, $\Theta = 66^\circ$) as well as (b) cell-substrate topology prior and (c) after PDT (633 nm ; 4 J/cm^2). Fluorescence excited at 391 nm and detected at $\lambda \geq 590 \text{ nm}$; image size: $140 \mu\text{m} \times 140 \mu\text{m}$; cell-substrate distances (colour scale) given in nanometres. Reproduced from [5] with modifications.

dark blue, whereas the plasma membranes appear blue-green due to an increasing contribution of the 490 nm band at decreasing membrane stiffness.

The question now arises how cell-substrate topology is affected by cholesterol depletion. This effect is well illustrated in Figure 4. First, upon incubation with laurdan but without any further treatment, cell-substrate distances vary between about 20 nm and 120 nm . Upon application of $1 \text{ mM } M\beta CD$

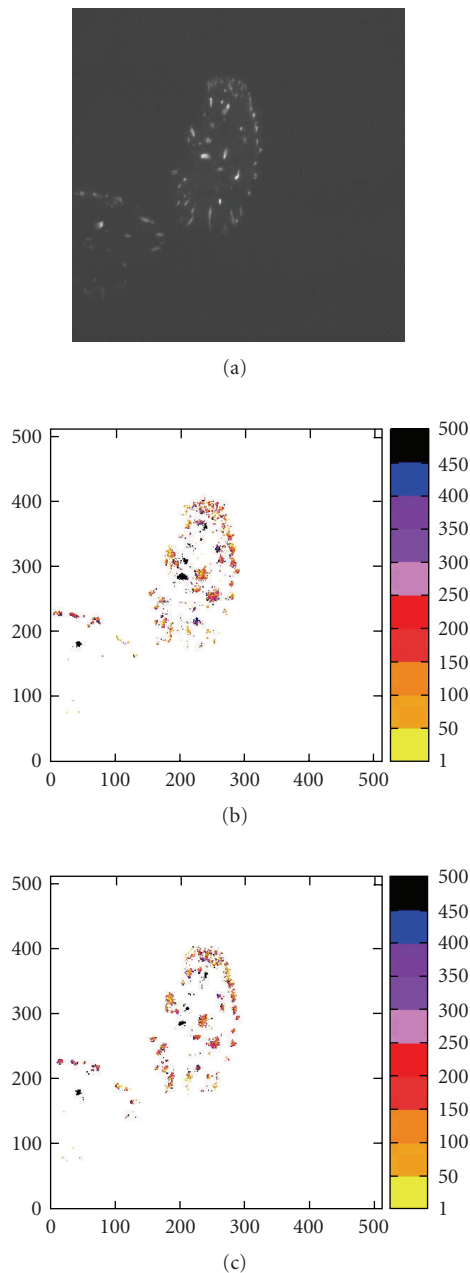


FIGURE 6: TIRF image of YFP-FAK (A , $\Theta = 66^\circ$) as well as (b) topology of focal adhesions prior and (c) after PDT with ALA-induced PP IX (633 nm; 4 J/cm^2). Fluorescence excited at 514 nm and detected at 520–550 nm; image size: $140 \mu\text{m} \times 140 \mu\text{m}$; cell-substrate distances (colour scale) given in nanometres.

(30% cholesterol depletion) cell-substrate distances generally increase, and upon application of 4 mM M β CD (50% cholesterol depletion), these distances are above 200 nm in the central parts of the cells, whereas on the cell edges the smaller distances are maintained. This proves that cell-substrate contacts are loosened in the central parts of the cells, which finally may lead to dissolution of the cells.

3.3. Cell-substrate topology upon photodynamic therapy

Adhesion of tumour cells upon photodynamic therapy (PDT) [18, 19] is an important question with regard to a possible formation of metastases. Therefore, variable-angle TIRFM appears very promising for investigation of cell-substrate topology and focal adhesions. Since 5-ALA induced protoporphyrin IX (PP IX) is partly located in the plasma membrane, it can be used as a photosensitizer as well as a membrane marker permitting to calculate cell-substrate distances according to (2). While Figure 5(a) shows a TIRFM image ($\Theta = 66^\circ$) of U373MG glioblastoma cells incubated with 5-ALA, Figure 5(b) shows cell-membrane topology before, and Figure 5(c) after application of a nonlethal light dose of 4 J/cm^2 (633 nm). While cell-substrate distances between 100 nm and 150 nm are the most frequent ones before PDT, these distances are decreasing after PDT, probably due to an increase of the cell volume upon swelling. If, instead of the plasma membrane, focal adhesions are visualized by YFP-FAK, it becomes evident from Figure 6 that these focal adhesions are maintained upon PDT. While Figure 6(a) shows a TIRFM image of focal adhesions, Figures 6(b) and 6(c) show their topologies prior and after PDT, which obviously are almost equal. Results described for PP IX and YFP-FAK have recently been verified with a larger number of U373MG glioblastoma cells and HeLa cervix cancer cells [5], proving that detachment of these cells from their substrate upon photodynamic therapy is unlikely to occur.

4. CONCLUSION

The potential of cell-substrate tomography with nanometre resolution has been demonstrated for 3 examples. Variable-angle TIRFM seems to be an ideal method, if a fluorescent dye is distributed rather homogeneously either within a thin layer (e.g., cell membrane) or on top of a layer (e.g., within the cytoplasm or an isolated chromosome). A user-friendly two-layer model was applied for all calculations reported above, although up to 4 layers (glass substrate, buffer solution, cell membrane, cytoplasm) may interfere. However, for thin cell membranes, and cell-substrate distances which are smaller than the laser wavelength, the two-layer model still holds with only few percent of error [20]. Similarly, the error resulting from an inhomogeneous spot of incident light may become negligible, if this spot is large compared to the object field [4]. Further requirements for calculation of tomographic images are a stationary spot of illumination (upon variation of the angle Θ), a constant fluorescence quantum yield over the measured parts of the sample (as deduced in the case of laurdan from the homogeneous distribution of fluorescence lifetimes) and a high signal-to-noise ratio. Since TIRFM images are usually about 100 times weaker than conventional fluorescence images, a high sensitivity of the detection system, for example, of an EM-CCD camera, is needed. This kind of detection system also permits the use of very low illumination doses (far below 1 J/cm^2 for 10–12 TIRFM images), which may assure

cell survival in high-resolution microscopy and in vitro diagnostics.

ACKNOWLEDGMENTS

This project was funded by the Bundesministerium für Bildung und Forschung (BMBF; Grant no. 1701B04). Technical assistance by Claudia Hintze is gratefully acknowledged.

REFERENCES

- [1] K. I. Willig, B. Harke, R. Medda, and S. W. Hell, "STED microscopy with continuous wave beams," *Nature Methods*, vol. 4, no. 11, pp. 915–918, 2007.
- [2] D. Axelrod, "Cell-substrate contacts illuminated by total internal reflection fluorescence," *The Journal of Cell Biology*, vol. 89, no. 1, pp. 141–145, 1981.
- [3] G. A. Truskey, J. S. Burmeister, E. Grapa, and M. W. Reichert, "Total internal reflection fluorescence microscopy (TIRFM). II. Topographical mapping of relative cell/substratum separation distances," *Journal of Cell Science*, vol. 103, no. 2, pp. 491–499, 1992.
- [4] K. Stock, R. Sailer, W. S. L. Strauss, M. Lyttek, R. Steiner, and H. Schneckenburger, "Variable-angle total internal reflection fluorescence microscopy (VA-TIRFM): realization and application of a compact illumination device," *Journal of Microscopy*, vol. 211, no. 1, pp. 19–29, 2003.
- [5] H.-P. Lassalle, H. Baumann, W. S. L. Strauss, and H. Schneckenburger, "Cell-substrate topology upon ALA-PDT using variable-angle total internal reflection fluorescence microscopy (VA-TIRFM)," *Journal of Environmental Pathology, Toxicology and Oncology*, vol. 26, no. 2, pp. 83–88, 2007.
- [6] N. L. Thompson, A. W. Drake, L. Chen, and W. Vanden Broek, "Equilibrium, kinetics, diffusion and self-association of proteins at membrane surfaces: measurement by total internal reflection fluorescence microscopy," *Photochemistry and Photobiology*, vol. 65, no. 1, pp. 39–46, 1997.
- [7] S. E. Sund and D. Axelrod, "Actin dynamics at the living cell submembrane imaged by total internal reflection fluorescence photobleaching," *Biophysical Journal*, vol. 79, no. 3, pp. 1655–1669, 2000.
- [8] A. Demuro and I. Parker, "Imaging the activity and localization of single voltage-gated Ca^{2+} channels by total internal reflection fluorescence microscopy," *Biophysical Journal*, vol. 86, no. 5, pp. 3250–3259, 2004.
- [9] W. J. Betz, F. Mao, and C. B. Smith, "Imaging exocytosis and endocytosis," *Current Opinion in Neurobiology*, vol. 6, no. 3, pp. 365–371, 1996.
- [10] M. Oheim, D. Loerke, W. Stühmer, and R. H. Chow, "The last few milliseconds in the life of a secretory granule. Docking, dynamics and fusion visualized by total internal reflection fluorescence microscopy (TIRFM)," *European Biophysics Journal*, vol. 27, no. 2, pp. 83–98, 1998.
- [11] S. S. Licht, A. Sonnleitner, S. Weiss, and P. G. Schultz, "A rugged energy landscape mechanism for trapping of transmembrane receptors during endocytosis," *Biochemistry*, vol. 42, no. 10, pp. 2916–2925, 2003.
- [12] T. J. Dougherty, "Photosensitizers: therapy and detection of malignant tumors," *Photochemistry and Photobiology*, vol. 45, no. 6, pp. 879–889, 1987.
- [13] A. E. Christian, M. P. Haynes, M. C. Phillips, and G. H. Rothblat, "Use of cyclodextrins for manipulating cellular cholesterol content," *Journal of Lipid Research*, vol. 38, no. 11, pp. 2264–2272, 1997.
- [14] D. J. Webb, K. Donais, L. A. Whitmore, et al., "FAK-Src signalling through paxillin, ERK and MLCK regulates adhesion disassembly," *Nature Cell Biology*, vol. 6, no. 2, pp. 154–161, 2004.
- [15] T. Parasassi, E. K. Krasnowska, L. A. Bagatolli, and E. Gratton, "Laurdan and prodan as polarity-sensitive fluorescent membrane probes," *Journal of Fluorescence*, vol. 8, no. 4, pp. 365–373, 1998.
- [16] L. A. Bagatolli, T. Parasassi, G. D. Fidelio, and E. Gratton, "A model for the interaction of 6-lauroyl-2-(N,N-dimethylamino)naphthalene with lipid environments: implications for spectral properties," *Photochemistry and Photobiology*, vol. 70, no. 4, pp. 557–564, 1999.
- [17] P. Weber, M. Wagner, and H. Schneckenburger, "Microfluorometry of cell membrane dynamics," *Cytometry Part A*, vol. 69, no. 3, pp. 185–188, 2006.
- [18] N. Rousset, V. Vonarx, S. Eléouet, et al., "Effects of photodynamic therapy on adhesion molecules and metastasis," *Journal of Photochemistry and Photobiology B*, vol. 52, no. 1–3, pp. 65–73, 1999.
- [19] A. Uzdensky, E. Kolpakova, A. Juzeniene, P. Juzenas, and J. Moan, "The effect of sub-lethal ALA-PDT on the cytoskeleton and adhesion of cultured human cancer cells," *Biochimica et Biophysica Acta*, vol. 1722, no. 1, pp. 43–50, 2005.
- [20] W. M. Reichert and G. A. Truskey, "Total internal reflection fluorescence (TIRF) microscopy. I. Modelling cell contact region fluorescence," *Journal of Cell Science*, vol. 96, no. 2, pp. 219–230, 1990.

Research Article

A Proposed Method for Thermal Specific Bioimaging and Therapy Technique for Diagnosis and Treatment of Malignant Tumors by Using Magnetic Nanoparticles

Iddo M. Gescheit, Moshe Ben-David, and Israel Gannot

Department of Biomedical Engineering, Faculty of Engineering, Tel-Aviv University, Tel-Aviv 69978, Israel

Correspondence should be addressed to Israel Gannot, iddog@medingo.com

Received 25 February 2008; Accepted 9 April 2008

Recommended by Stoyan Tanev

The objective of this research program is to develop a novel, noninvasive, low-cost infrared (8–12 μm spectral range) imaging technique that would improve upon current methods using nanostructured core/shell magnetic/noble metal-based imaging and therapies. The biocompatible magnetic nanoparticles are able to produce heat under AC magnetic field. This thermal radiation propagates along the tissue by thermal conduction reaching the medium's (tissue's) surface. The surface temperature distribution is acquired by a thermal camera and can be analyzed to retrieve and reconstruct nanoparticles' temperature and location within the tissue. The technique may function as a diagnostic tool thanks to the ability of specific bioconjugation of these nanoparticles to tumor's outer surface markers. Hence, by applying a magnetic field, we could cause a selective elevation of temperature of the targeted nanoparticles up to 5°C, which detects the tumor. Furthermore, elevating the temperature over 65°C and up to 100°C stimulates a thermo ablating interaction which causes a localized irreversible damage to the cancerous site with no harm to the surrounding tissue. While functioning as a diagnostic tool, this procedure may serve as a targeted therapeutic tool under thermal feedback control as well.

Copyright © 2008 Iddo M. Gescheit et al. This is an open access article distributed under the Creative Commons Attribution License, which permits unrestricted use, distribution, and reproduction in any medium, provided the original work is properly cited.

1. INTRODUCTION

Cancer is a very prevalent disease with no satisfying cure and/or treatment. American Cancer Society statistics shows that about 1 399 790 new cancer cases were diagnosed in 2006. This number does not include carcinoma in situ (noninvasive cancer) or any site except urinary bladder, and does not include basal and squamous cell skin cancer. More than 1 million cases of basal and squamous cell skin cancers were diagnosed in 2006. In the same year, about 564 830 Americans died of cancer, more than 1 500 people a day. Cancer is the second most common cause of death in the US, exceeded only by heart disease. In the US, cancer accounts for 1 out of every 4 deaths. The National Institute of Health (NIH) estimates overall costs for cancer in 2005 with \$209.9 billion [1–3].

Conventional (anatomical, structural) imaging is insensitive to the presence of cancer, often failing to yield the very information needed for accurate diagnosis and staging, for

proper treatment selection and monitoring or for effective followup after treatment. For example, small primary tumors go undetected. For many cancers, an internal, aggressive, noncalcified tumor under containing fewer than 500 000 cells (i.e., under 2 mm wide) is likely to pass undetected through most body-region scans, including CT, MRI, ultrasound, radionuclide, and metabolic PET. At this size, a tumor has effectively undergone 19 cell doublings about halfway through doubling toward a predicted lethal load of 10^{10} – 10^{12} cells and is likely to be sufficiently repleted with gene defects so that it will undergo continued and uninterrupted growth if not treated [4].

While cancer may be suspected for a variety of reasons, the definitive diagnosis of most malignancies must be confirmed by histological examination of the cancerous cells by a pathologist. After obtaining tissue sample by a biopsy or surgery, the tissue diagnosis indicates the type of cell that is proliferating, its histological grade and other features of the tumor. Together, this information is useful

to evaluate the prognosis of this patient and choose the best treatment. However, current therapy techniques (e.g., surgery, chemotherapy, radiation) still show poor results and therefore, unfortunately, the standard of care is to blindly treat with chemotherapy selected by convention using prior retrospective studies. A treatment is considered a success or failure only in retrospect (i.e., success is when a patient survives 5 years, and failure is when a relapse occurs).

Hence, the majority of diagnosis and therapy modalities is not capable of distinguishing between malignant cells and healthy tissue (especially in early stages) and does not provide the physician with adequate precision and specificity. Moreover, there is no real-time control referring to the physiological margins distinguishing the malignant and benign tissue. The implications of the latter are, for example, in surgery: if the surgeon does not remove all the malignant cells, the progression or recurrence of the disease is almost without doubt. On the other hand, if the surgeon removes more than necessary, the “extra” tissue being removed is a healthy tissue and may be vital for the organ-life cycle or patient’s life.

2. MATERIALS AND METHODS

2.1. The system

The suggested system and method are schematically depicted in Figure 1. After the insertion of magnetic nanoparticles into a patient’s body (either locally to a suspected tissue or systematically to the blood stream by IV injection), the nanoparticles arrive in short proximity to the tumor and a process of bioconjugation occurs in compliance with a pharmacokinetic profile. Thus, the tumor’s outer surface is bound with nanoparticles by virtue of strong chemical bonds configured as antigen-antibody complex. Since the biocompatible magnetic nanoparticles are able to produce heat under AC magnetic field, the region of interest (ROI) is placed under a suitable field. This emitted thermal radiation propagates along the tissue by thermal conduction reaching medium’s (tissue’s) surface. The surface temperature distribution is acquired by a thermal camera and could be analyzed to retrieve and reconstruct nanoparticles’ temperature and location within the tissue. In future minimal invasive applications, the IR radiation can be “guided” from internal compartments of the body to the outside by waveguides and dedicated optical fibers, for example, thermal imaging bundles shown by Gannot et al. [5–8].

By elevating the temperature of the conjugated nanoparticles up to $\sim 5^\circ\text{C}$, diagnosis is enabled while elevation of local temperature over 65°C allows “clean treatment,” that is, localized irreversible damage to the cancerous site almost without harming the surrounding tissue.

2.2. Bioconjugation

A fundamental issue lying on the basis of this system is the fact that the magnetic nanoparticles are localized specifically and functions as mediators situated on the periphery of the tumor. In order to target the tumor

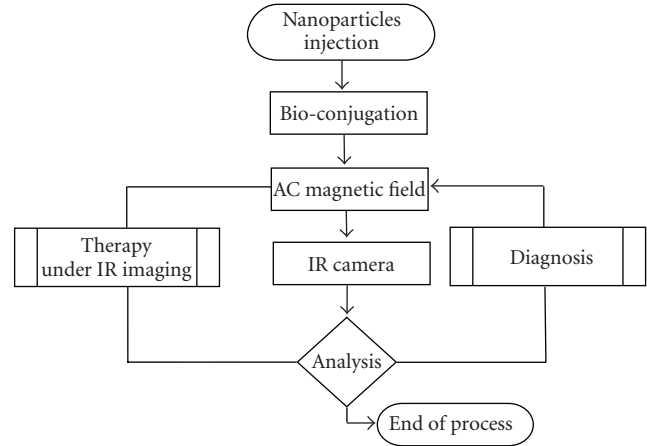


FIGURE 1: Schematic description of the system employing a targeted imaging technique and a closed-loop system for therapy under real-time feedback.

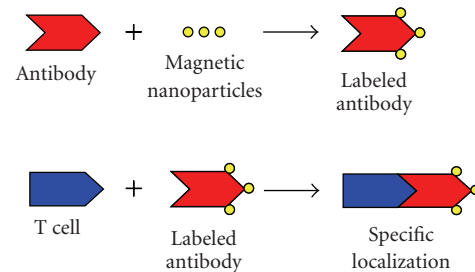


FIGURE 2: Bioconjugation of magnetic nanoparticles by using the natural immune system.

and deliver the nanoparticles reliably and specifically, the suggested transportation leans on human’s immune system. The malignant tumor tends to present specific antigens on its outer surface. These antigens are able to communicate with corresponding agents of the immune system (e.g., antibodies) to establish antigen-antibody complexes which are characterized in strong chemical bonds. For instance, we can bind the magnetic nanoparticles’ surface to the antibodies via adhering polymers (e.g., PEG) so that antibodies transfer them towards the tumor being delivered by immune agents (T-cell), and conjugate them to the tumor, retaining them along the tumor’s outer surface (Figures 2 and 3).

This bioconjugation is analogous to that made with fluorophores in research conducted by Fibich et al. [9] and Gannot et al. [10].

2.3. Heat generation

There exist at least three different mechanisms by which magnetic materials can generate heat in an alternating field [11]:

- (i) generation of eddy currents in bulk magnetic materials;

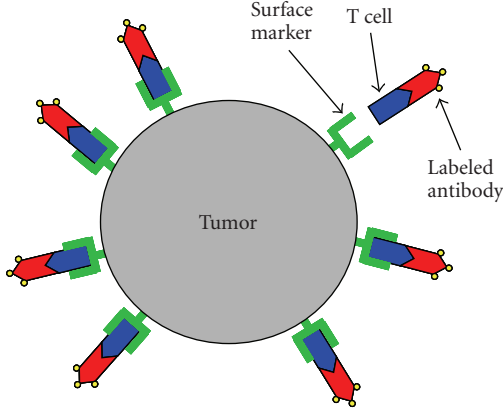


FIGURE 3: Magnetic nanoparticles schematic siting along the tumor surface.

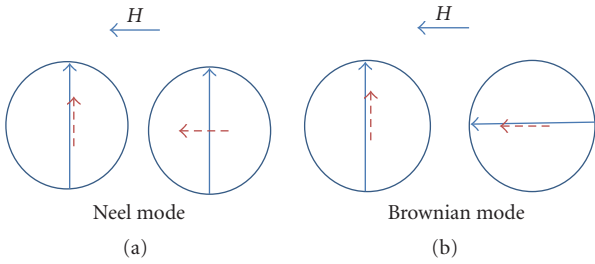


FIGURE 4: Relaxational losses leading to heating in an alternating magnetic field (H).

- (ii) hysteresis losses in bulk and multidomain magnetic materials
- (iii) relaxation losses in “superparamagnetic” single-domain magnetic materials.

In this technique, we use single-domain particles in which mechanism (i) and (ii) contribute very little to the heating of these particles (if at all) [12], while the significant mechanism in contribution with heating is the relaxation mechanism (iii) [13, 14].

Relaxation losses in single-domain magnetic nanoparticles fall into two modes: (a) rotational (Brownian) mode and (b) Néel mode [13, 15]. The principle of heat generation due to each individual mode is shown in Figure 4.

In the Néel mode (Figure 4(a)), the magnetic moment (dotted arrow) originally locked along the crystal easy axis (solid arrow) rotates away from the crystal axis towards the external field (H). The Néel mechanism is analogous to the hysteresis loss in multidomain magnetic particles whereby there is an “internal friction” due to the movement of the magnetic moment in an external field that results in heat generation.

In the Brownian mode (Figure 4(b)), the whole particle oscillates towards the field with the moment locked along the crystal axis under the effect of a thermal force against a viscous drag in a suspending medium. This mechanism essentially represents the mechanical friction component in a given suspending medium [16].

Each of the relaxation modes that lead to heat generation is characterized by a time constant. τ_N is the Néel time constant given by

$$\tau_N = \tau_0 \exp\left(\frac{E_B}{k_B T}\right), \quad (1)$$

where $E_B = K_u V$ is analogous to an activation energy that has to be overcome by the thermal energy $k_B T$ to overcome the inherent magnetic anisotropy energy.

The energy barrier E_B is represented by the constant K_u , which is a material property and is the anisotropy constant, multiplied by V , which is the volume of the magnetic nanoparticle. The thermal energy is represented by the constant k_B , named by Stephan Boltzmann, and multiplied by the absolute temperature T . The constant τ_0 is of the order of 10^{-9} seconds [13].

The Brownian time constant represented by τ_B is given by

$$\tau_B = \frac{3\eta V_H}{k_B T}, \quad (2)$$

where V_H is the hydrodynamic volume of the magnetic nanoparticle which is the effective volume (including that of the nanoparticle and coating or surfactant attached to the nanoparticle), η is the viscosity of the liquid carrier, and $k_B T$ is the thermal energy.

The resultant power generation is a strong function of the effective time constant, and the field parameters and is given by

$$P_{SPM} = \pi\mu_0\chi_0 H_0^2 f \frac{2\pi f \tau}{1 + (2\pi f \tau)^2}, \quad (3)$$

where H_0 and f are the amplitude and frequency of the applied alternating magnetic field, respectively, χ_0 is the magnetic susceptibility, μ_0 is the permeability of free space, and τ is the effective time constant given by $1/\tau = (1/\tau_N) + (1/\tau_B)$ [11, 13].

2.4. Affecting parameters

There are numerous parameters affecting the heat generation, which is produced by magnetic nanoparticles excited by a magnetic field. A few examples for some crucial parameters are given below which one should take into consideration when heating with magnetic nanoparticles.

2.4.1. Field parameters

According to (3), it is obvious that field strength and frequency are controllable parameters that directly affect the power produced by the nanoparticles when alternative magnetic field is applied. It should be understood that the of field parameter is not simply proportional to the generated power but more complex, and depends on additional parameters such as the nanoparticles’ material properties [17].

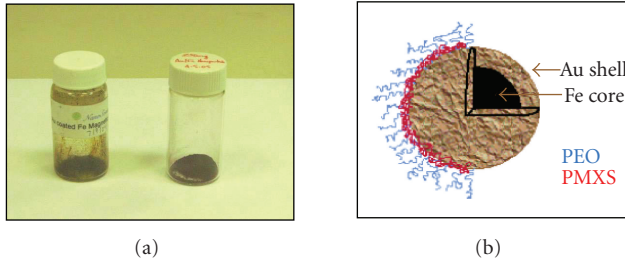


FIGURE 5: Fe Nanoparticles produced by Nanosonics Inc. (a) Magnetic nanoparticles in different particle size configured as powder. (b) Schematic illustration of a single Fe-Au nanoparticle.

2.4.2. Material properties

An interesting class of magnetic materials that are common for this purpose is iron oxides such as Fe_3O_4 , $\gamma\text{-Fe}_2\text{O}_3$ and $\text{MO}\cdot\text{Fe}_2\text{O}_3$ (where M is Mn, Co, Ni, Cu) [18], because they display ferrimagnetism. Magnetite (Fe_3O_4), meghemite ($\gamma\text{-Fe}_2\text{O}_3$), and hematite ($\alpha\text{-Fe}_2\text{O}_3$) are the most common iron oxides and they are discussed below.

Another alternative is the magnetic nanoshells which were designed and characterized by Nanosonic Inc. (Figure 5(a)). The nanoshells are comprised of an iron core with diameter of 8 nm coated with a layer of gold. The gold coatings are made in order to prevent oxidation, hence demagnetization; ultrathin noble metal coatings of Au (~ 2 nm) were prepared to provide long-term stability and biocompatibility for the Fe core. The Fe core was coated with a series of block copolymer stabilizers that are compatible with analgesics to prevent flocculation in the arterial system in vivo (see Figure 5(b)). In addition, the block copolymers assist in preventing agglomeration.

Other materials are also being investigated including platinumium compounds, vanadium oxides, cobalt, nickel, lanthanum, and manganese [19, 20].

2.4.3. Size dependence

The size of the nanoparticles is a fundamental characteristic in this field. Ma et al. [21] investigated the specific absorption rate (SAR) values of aqueous suspensions of magnetite particles with different diameters varying from 7.5 to 416 nm by measuring the time-independent temperature curves in an external altering magnetic field

(80 kHz, 32.5 kA/m). Results indicate that the SAR values of magnetite particles are strongly size dependent. For magnetite larger than 46 nm, the SAR values increase as the particle size decreases where hysteresis loss is the main contribution mechanism. For magnetite particles of 7.5 and 13 nm which are superparamagnetic, hysteresis loss decreases to zero and, instead relaxation losses (Néel loss and Brownian rotation loss) dominate.

The dividing line between the two cases depicted above is given by the ferromagnetic exchange length $d_{ex} \cong \sqrt{A/K}$ using the material parameters of magnetite ($K = 1.35 \times 10^4 \text{ J/m}^3$, $A = 10^{-11} \text{ J/m}$), the exchange length is estimated as $d_{ex} \cong 27 \text{ nm}$.

Therefore, when the particle size is larger than d_{ex} , the hysteresis loss increases as the particle size decreases. However, once the particle size is less than d_{ex} , hysteresis loss will vanish and the main contribution will be of relaxation losses, as shown, for example, by Ma et al. [21]. In addition, Hergt et al. show that in the critical particles size region where hysteresis losses vanish, Néel losses grow as a new loss mechanism which, roughly speaking, extends the loss region toward even smaller particle sizes [12].

2.4.4. Other parameters

The parameters discussed above are merely a few examples for a larger collection of affecting parameters. Some of them have been investigated and some are probably yet unknown. Amongst them is the concentration of the nanoparticle inserted into the body [11]. The concentration should be large enough to effectively produce heat, but yet in an amount that will not be toxic for the human body. One also needs to be aware of the evacuation of those particles once their job is done. (We are not dealing with toxicity and pharmacokinetics issues in this paper.) The coating of nanoparticles (e.g., derivatives of dextran, polyethylene glycol (PEG), polyethylene oxide (PEO), and poloxamers and polyoxamines) and suspending medium also affect the heat generation [11, 16, 22]. The period of time of excitation filed application and profile (e.g., continuous, pulsatile) deeply affects the SAR which is proportional to the power dissipated [23]. Another affecting parameter under investigation is the presence of nanoparticles' agglomeration in comparison with the heat generated in single or dispersed nanoparticles [24].

2.5. Thermal analysis

Upon the heating of the bioconjugated nanoparticles, we generate a heat source within the body. The heat source, namely the tumor, and in particular the tumor's surface, is actively heated by external and controlled magnetic fields. Based on a two dimensional thermal image acquired from the tissue surface, we seek to derive two fundamental characteristics: the *depth* of the tumor and the *temperature* of the tumor and its surroundings. Knowing the temperature in real-time is crucial in order to avoid any damage to all tissues in the diagnostic mode on one hand, and on the other hand, operating in therapeutic mode, we expect to damage only the malignant tissue leaving the healthy surrounding tissue with minimal damage. There are various techniques for analyzing the thermal data such as, for example, automatic segmentation approaches, and feature extraction and classification as shown by Qi and Diakides [25].

2.6. Setup

The main building blocks of the suggested system are comprised of means for (shown in Figure 6):

- (i) heat generation;
- (ii) thermal image acquisition;
- (iii) thermal image analysis;
- (iv) heat generation.

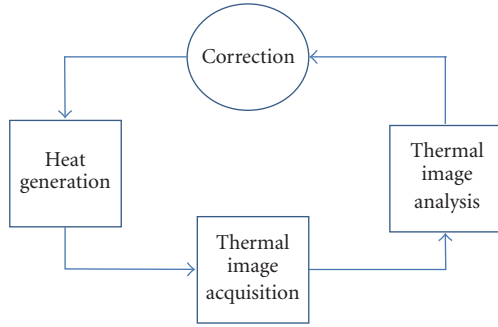


FIGURE 6: Schematic description of the system.

Heat generation is conceptually comprised of two parts:

- (i) magnetic nanoparticles (for “heat emission”);
- (ii) magnetic field (for nanoparticles’ excitation).

The magnetic field is generated by a magnetic system usually comprised of the following:

- (i) antenna (e.g., coils)
- (ii) AC current generator.

The design of the magnetic system is implemented bottom-to-up, that is, after choosing the desirable field parameters (e.g., field strength, frequency), we are capable of designing the system itself (e.g., coils, circuitry). Determination of the desirable parameters is not trivial since the system is characterized by a large number of degrees-of-freedom.

Previous research works investigated various fields: Kalambur et al. used a 1 kW generator and 4 turn RF coils to produce field strength of $H_0 = 14$ [kA/m] and frequency $f = 175$ [kHz]; Giri et al. examined the fields (10–45[kA/m], 300 [kHz]);

Ma et al. used a 15 kW RF generator to produce the field (32.5 [kA/m], 80 [kHz]); Hergt et al. (2004) showed losses under the AC field (11 [kA/m], 410 [kHz]); Pankhurst et al. investigated nanoparticles under the extensive field region of (0–15 [kA/m], 0.05–1.2 [MHz]) and Kim et al. examined the influence of fields of (110 [kA/m], 0.1–15 [MHz]).

The two principle parameters of the externally applied magnetic field, that is, the frequency and strength, are limited by deleterious physiological responses to high-frequency magnetic fields [26, 27]: stimulation of peripheral and skeletal muscles, possible cardiac stimulation and arrhythmia, and nonspecific inductive heating of tissue. Generally, the useable range of frequencies and amplitudes is considered to be $f = 0.05$ –1.2 MHz and $H = 0$ –15 kA/m.

Experimental data on exposure to much higher frequency fields come from groups such as Oleson et al. [28] who developed a hyperthermia system based on inductive of tissue, and Atkinson et al. who developed a treatment system based on eddy current heating of implantable metal thermoseeds. Atkinson et al. [29] concluded that exposure

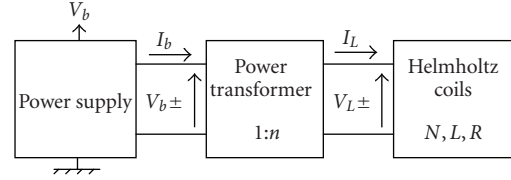


FIGURE 7: System’s block scheme.

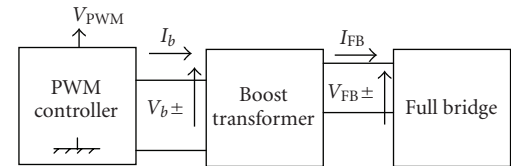


FIGURE 8: The power generator’s block scheme.

to fields where the product $H \cdot f$ does not exceed 4.85×10^8 , $\text{kA}/(\text{m} \cdot \text{s})^{-1}$ is safe and tolerable [30].

Hence, following the physiological constraints shown above and based on previous research results such as those mentioned above, the desirable averaged working point was chosen to be $H_0 \approx 10$ [kA/m]; $f \approx 100$ [kHz].

Trying to meet with the fundamental objectives of the suggested system, particularly cost effectiveness and bedside capability, we seek an alternative technology for the commonly used giant and expensive RF generators of several kilowatts and up, since they cost about 10 k–100 k of dollars and are not comfortable to be located near the patient’s bed or at the clinic. Most of research works in this field are using a single RF coil with a few turns, for example, 3–4 turns. A major drawback of the coil configuration is that there is no accessibility for any imaging element, such as an IR camera. If we had desired to use that kind of solenoid coil, it would have been characterized with a very large diameter, and the camera would have been exposed to the AC field. Hence, this configuration is not applicable and does not apply to our needs.

An alternative preferred method relies on a Helmholtz coil configuration. The fundamental premise of this configuration is that it produces a uniform (homogeneous) magnetic field between the coils with the primary field component parallel to the axes of the two coils. The Helmholtz configuration further enables an open workspace for sample (tissue) handling and imaging device accessibility, that is, an easy and safe path for placing the IR camera, and further enables the change of the distance between the two coils, that is, adjustable workspace.

In order to produce a desired high voltage over the coils, the system design includes power transformer for voltage elevation, as shown in Figure 7.

The power supply of the system is composed of an oscillator (PMW controller) with a tunable frequency, boost transformer, and a push-pull full bridge inverter (H-bridge), as shown in Figure 8. The full bridge is mainly composed of four FETs to allow the alternate current.

The thermal imaging is carried out by an IR camera (FLIR A40M), which detect the infrared emission which is

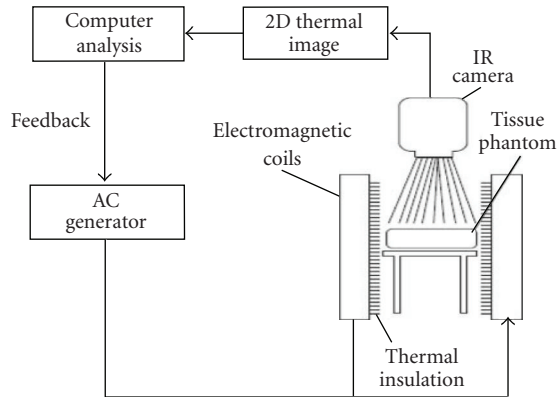


FIGURE 9: Schematic description of the closed-loop system.

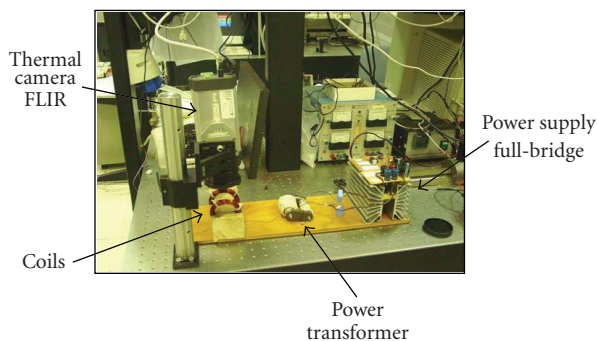


FIGURE 10: Laboratory system.

emitted from the examined object's surface (e.g., phantom).

The IR camera is positioned perpendicularly above the object, which is situated within the magnetic field induced between the two coils. When the magnetic field is applied, the nanoparticles generate heat which can be detected by the IR camera.

Integrating the main building blocks of the required system mentioned above comprises the system as shown in Figure 9. The system should preferably include a closed-loop feedback to allow the adjustment of the field parameters (generated by the coils) according to the temperature readings (acquired via the IR camera).

Obviously, interruption by the user (e.g., physicist) is possible, such as the tuning of magnetic field when changing its mode of operation (e.g., achieving therapy requires a substantial increase of the temperature within the treated tissue).

3. CONCLUSIONS

This system is dedicated to the detection of malignant tumors and for the treatment of those tumors based on the physical principle of heat generation for both diagnosis and therapy. The heat generation and its amplification above the body's normal temperature level are achieved by biocompatible magnetic nanoparticles which are bioconjugated to the

tumor and their stimulation by a suitable external magnetic field.

This procedure is specifically targeted to the tumor since it relies on the capability of the immune system and its detectability, that is, the body knows best how to locate the malignant cells. Hence, the bioconjugation of the nanoparticles to the antigen-antibody complex is probably the most accurate method to reach the real malignancies.

The preferable configuration for the generation of the AC magnetic field in our view is the Helmholtz configuration, however the characteristics of the current generator and coils should still be evaluated.

In conclusion, this research work may serve as a novel fundamental concept for having both diagnosis and therapy in a single device, where the transfer between the two modes is merely a simple alteration of field parameters. The minimally invasive method is selective and has the potential of being very accurate, reliable, and friendly both to the operator (e.g., physician) and to the patient. It incorporates various field of research and we believe and hope that it can be developed into a bedside, cost effective, and applicable device that may assist in a better and improved detection and treatment of one of the prevalence diseases that the medical industry currently has to deal with.

4. FUTURE WORK

This research shows a fundamental design of the system which is meant to pursue thermal diagnosis and therapy in one single device which is still not bulky and can operate near the patient's bed, be accurate, reliable, and cost effective. The concept and modularly design that were described in this research work are the basis for such a system. The system comprises several main modules: heat generation (including nanoparticles and the external field generation), thermal imaging, analysis and feedback. This multidisciplinary system incorporates various scientific and technological fields. Furthermore, each module may be investigated and improved independently with no direct relation to the other modules.

Producing the required external magnetic field should be designed to generate a higher magnetic field, preferably with adjusted parameters, for example, magnitude, frequency, distance between the coils. One of the goals in our view is to increase the efficiency of this module and to enable the use of standard voltage and current one of a domestic electrical infrastructure.

The analysis module is based on the acquired raw thermal image and includes the processing for improving the data quality and derivation of desired parameters. This module may be approached by various methods implementing different mathematical models, computational algorithms, and so forth. It is desirable to try and derive additional parameters (other than tumor's depth and tumor's temperature) such as 3D geometrical boundaries of the tumor.

The current model is a basic model that relies on ideal assumptions (e.g., homogeneous tissue, steady state). Furthermore, the inverse model assumes a point source which is merely an ideal approximation for much more

complicated scenarios that involve undefined tumor boundaries, noise signals, physiological, anatomical abnormalities, and so forth.

The closed-loop feedback that allows control on the external magnetic field's parameters (e.g., magnitude and frequency) can be automatically adjusted based on the thermal imaging to maintain appropriate contrast and to achieve control on the heat expansion within the tissue in real time in order not to harm surrounding healthy tissue. This can be carried out by a LabView dedicated program.

REFERENCES

- [1] F. Bretagnol and L. de Calan, "Surgery treatment of rectal cancer," *Journal de Chirurgie*, vol. 143, no. 6, pp. 366–372, 2006.
- [2] Cancer Facts and Figures, 2006.
- [3] L. J. Kleinsmith, D. Kerrigan, J. Kelly, and B. Hollen, "Understanding Cancer and Related Topics Understanding Cancer," National Cancer Institute, 2007.
- [4] D. A. Benaron, "The future of cancer imaging," *Cancer and Metastasis Reviews*, vol. 21, no. 1, pp. 45–78, 2002.
- [5] M. Ben-David, A. Inberg, I. Gannot, and N. Croitoru, "The effect of scattering on the transmission of infrared radiation through hollow waveguides," *Journal of Optoelectronics and Advanced Materials*, vol. 1, no. 3, pp. 23–30, 1999.
- [6] I. Gannot, M. Ben-David, A. Inberg, and N. Croitoru, "Broadband omnidirectional IR flexible waveguides," *Journal of Optoelectronics and Advanced Materials*, vol. 3, no. 4, pp. 933–935, 2001.
- [7] I. Gannot, M. Ben-David, A. Inberg, N. Croitoru, and R. W. Waynant, "Beam shape analysis of waveguide delivered infrared lasers," *Optical Engineering*, vol. 41, no. 1, pp. 244–250, 2002.
- [8] N. Croitoru, A. Inberg, M. Ben-David, and I. Gannot, "Broad band and low loss mid-IR flexible hollow waveguides," *Optics Express*, vol. 12, no. 7, pp. 1341–1352, 2004.
- [9] G. Fibich, A. Hammer, G. Gannot, A. Gandjbakhche, and I. Gannot, "Modeling and simulations of the pharmacokinetics of fluorophore conjugated antibodies in tumor vicinity for the optimization of fluorescence-based optical imaging," *Lasers in Surgery and Medicine*, vol. 37, no. 2, pp. 155–160, 2005.
- [10] I. Gannot, A. Garashi, G. Gannot, V. Chernomordik, and A. Gandjbakhche, "In vivo quantitative three-dimensional localization of tumor labeled with exogenous specific fluorescence markers," *Applied Optics*, vol. 42, no. 16, pp. 3073–3080, 2003.
- [11] V. S. Kalambur, B. Han, B. E. Hammer, T. W. Shield, and J. C. Bischof, "In vitro characterization of movement, heating and visualization of magnetic nanoparticles for biomedical applications," *Nanotechnology*, vol. 16, no. 8, pp. 1221–1233, 2005.
- [12] R. Hergt, W. Andrae, C. G. d'Ambly, et al., "Physical limits of hyperthermia using magnetite fine particles," *IEEE Transactions on Magnetism*, vol. 34, no. 5, part 2, pp. 3745–3754, 1998.
- [13] R. E. Rosensweig, "Heating magnetic fluid with alternating magnetic field," *Journal of Magnetism and Magnetic Materials*, vol. 252, no. 1–3, pp. 370–374, 2002.
- [14] A. Jordan, P. Wust, H. Fahling, W. John, A. Hinz, and R. Felix, "Inductive heating of ferrimagnetic particles and magnetic fluids: physical evaluation of their potential for hyperthermia," *International Journal of Hyperthermia*, vol. 9, no. 1, pp. 51–68, 1993.
- [15] P. C. Fannin and S. W. Charles, "Study of a ferrofluid exhibiting both Brownian and Neel relaxation," *Journal of Physics D*, vol. 22, no. 1, pp. 187–191, 1989.
- [16] C. C. Berry and A. S. G. Curtis, "Functionalisation of magnetic nanoparticles for applications in biomedicine," *Journal of Physics D*, vol. 36, no. 13, pp. R198–R206, 2003.
- [17] G. Glöckl, R. Hergt, M. Zeisberger, S. Dutz, S. Nagel, and W. Weitschies, "The effect of field parameters, nanoparticle properties and immobilization on the specific heating power in magnetic particle hyperthermia," *Journal of Physics: Condensed Matter*, vol. 18, no. 38, pp. S2935–S2949, 2006.
- [18] R. M. Cornell and U. Schwertmann, *The Iron Oxides: Structure, Properties, Reactions, Occurrence and Uses*, John Wiley & Sons, New York, NY, USA, 1996.
- [19] S. Vasseur, E. Duguet, J. Portier, et al., "Lanthanum manganese perovskite nanoparticles as possible in vivo mediators for magnetic hyperthermia," *Journal of Magnetism and Magnetic Materials*, vol. 302, no. 2, pp. 315–320, 2006.
- [20] D. Bahadur, J. Giri, B. B. Nayak, et al., "Processing, properties and some novel applications of magnetic nanoparticles," *Pramana*, vol. 65, no. 4, pp. 663–679, 2005.
- [21] M. Ma, Y. Wu, J. Zhou, Y. Sun, Y. Zhang, and N. Gu, "Size dependence of specific power absorption of Fe₃O₄ particles in AC magnetic field," *Journal of Magnetism and Magnetic Materials*, vol. 268, no. 1–2, pp. 33–39, 2004.
- [22] H. Yin, H. P. Too, and G. M. Chow, "The effects of particle size and surface coating on the cytotoxicity of nickel ferrite," *Biomaterials*, vol. 26, no. 29, pp. 5818–5826, 2005.
- [23] I. Baker, Q. Zeng, W. Li, and C. R. Sullivan, "Heat deposition in iron oxide and iron nanoparticles for localized hyperthermia," *Journal of Applied Physics*, vol. 99, no. 8, Article ID 08H106, 3 pages, 2006.
- [24] P. Keblinski, D. G. Cahill, A. Bodapati, C. R. Sullivan, and T. A. Taton, "Limits of localized heating by electromagnetically excited nanoparticles," *Journal of Applied Physics*, vol. 100, no. 5, Article ID 054305, 5 pages, 2006.
- [25] H. Qi and N. A. Diakides, "Thermography," in *Encyclopedia of Medical Devices and Instrumentation*, J. G. Webster, Ed., John Wiley & Sons, New York, NY, USA, 2nd edition, 2006.
- [26] J. R. Oleson, T. C. Cetas, and P. M. Corry, "Hyperthermia by magnetic induction: experimental and theoretical results for coaxial coil pairs," *Radiation Research*, vol. 95, no. 1, pp. 175–186, 1983.
- [27] J. P. Reilly, "Principle of nerve and heart excitation by time-varying magnetic fields," *Annals of the New York Academy of Sciences*, vol. 649, pp. 96–117, 1992.
- [28] J. R. Oleson, R. S. Heusinkveld, and M. R. Manning, "Hyperthermia by magnetic induction: II. Clinical experience with concentric electrodes," *International Journal of Radiation Oncology Biology Physics*, vol. 9, no. 4, pp. 549–556, 1983.
- [29] W. J. Atkinson, I. A. Brezovich, and D. P. Chakraborty, "Usable frequencies in hyperthermia with thermal seeds," *IEEE Transactions on Biomedical Engineering*, vol. 31, no. 1, pp. 70–75, 1984.
- [30] Q. A. Pankhurst, J. Connolly, S. K. Jones, and J. Dobson, "Applications of magnetic nanoparticles in biomedicine," *Journal of Physics D*, vol. 36, no. 13, pp. R167–R181, 2003.

Research Article

Ultrashort Laser Pulse Heating of Nanoparticles: Comparison of Theoretical Approaches

Renat R. Letfullin,¹ Thomas F. George,² Galen C. Duree,¹ and Brett M. Bollinger¹

¹Department of Physics and Optical Engineering, Rose-Hulman Institute of Technology, 5500 Wabash Avenue, Terre Haute, IN 47803, USA

²Office of the Chancellor and Center for Nanoscience, Department of Chemistry and Biochemistry and Department of Physics and Astronomy, University of Missouri—St. Louis, One University Boulevard, St. Louis, MO 63121, USA

Correspondence should be addressed to Renat R. Letfullin, letfullin@rose-hulman.edu

Received 28 January 2008; Accepted 11 March 2008

Recommended by Stoyan Tanev

The interaction between nanoparticles and ultrashort laser pulses holds great interest in laser nanomedicine, introducing such possibilities as selective cell targeting to create highly localized cell damage. Two models are studied to describe the laser pulse interaction with nanoparticles in the femtosecond, picosecond, and nanosecond regimes. The first is a two-temperature model using two coupled diffusion equations: one describing the heat conduction of electrons, and the other that of the lattice. The second model is a one-temperature model utilizing a heat diffusion equation for the phonon subsystem and applying a uniform heating approximation throughout the particle volume. A comparison of the two modeling strategies shows that the two-temperature model gives a good approximation for the femtosecond mode, but fails to accurately describe the laser heating for longer pulses. On the contrary, the simpler one-temperature model provides an adequate description of the laser heating of nanoparticles in the femtosecond, picosecond, and nanosecond modes.

Copyright © 2008 Renat R. Letfullin et al. This is an open access article distributed under the Creative Commons Attribution License, which permits unrestricted use, distribution, and reproduction in any medium, provided the original work is properly cited.

1. INTRODUCTION

The application of ultrashort laser pulse thermal-based killing of abnormal cells (e.g., cancer cells) targeted with absorbing nanoparticles (e.g., solid gold nanospheres, nanoshells, or nanorods) is becoming an extensive area of research [1–3]. High laser energies in ultrashort pulses can be concentrated on an extremely small biological mass infused with metallic nanoparticles, and the heat gained by the particles used as a protein denaturing agent in targeted cells. Photons emitted from the ultrashort laser pulse are absorbed by free electrons within the metal via inverse Bremsstrahlung and transferred to the lattice subsystem, and then to the surrounding medium. Injected into biological media, nanoparticles provide a highly selective method for ablating target cells when coupled with appropriate laser pulse duration.

Traditional knowledge of laser-nanoparticle interactions has necessitated specialized models for each case, dependent upon the laser pulse duration. Previous research has recognized the existence of these conditions and dual-

temperature models for the ultrashort laser pulse mode calculating electron, and lattice subsystem temperatures are readily available (see, e.g., [4, 5]). Pulses of longer duration are modeled using a uniform heating model [6–9], an appropriate approximation for pulse durations greatly exceeding the electron-phonon coupling time. On a dimensional scale, this approximation is reasonable for particles sizes not much larger than a laser wavelength, which is completely applicable for the heating of nanoparticles.

Ultrashort pulses, specifically those in the femtosecond and picosecond ranges, impose several challenges in modeling material response. Free electrons with minimal capacity for heat are the first to absorb energy, rapidly attaining high temperatures, and transferring thermal energy to the material lattice. These processes do not occur instantaneously: time must be allowed for the cooling of the electrons and the heating of the lattice. In our work, electron cooling and lattice heating have time delays on the order of femtoseconds and picoseconds, respectively. Ultrashort laser pulses end before the transfer of energy to the lattice is complete, requiring two-temperature models in order to describe the

further conversion of energy from electron excitation to heat within the lattice system.

In the present paper, we demonstrate that a simpler, one-temperature model (OTM) utilizing the uniform heating approximation is appropriate for understanding ultrashort laser pulse interactions with metal nanoparticles. The approximation may be used in this situation due to the extremely small size of nanoparticles in comparison to the wavelength of laser radiation. Using this idea, the time delay between the electron and lattice interactions will be bypassed, and the simpler model will ultimately yield results similar to the two-temperature model (TTM). Comparative simulations of the two modeling approaches are performed in this paper to confirm OTM as an appropriate approximation for nanoparticle heating in the femtosecond, picosecond, and nanosecond regimes, thus providing an effective modeling method for further nanomedicine research to explore.

2. THEORETICAL BACKGROUND

2.1. One-temperature model

During the interaction of a laser pulse of intensity I_0 and pulse duration τ_L with a metal nanoparticle of radius r_0 , the laser energy is absorbed by free electrons due to the inverse Bremsstrahlung, and then transferred from the electron gas into the lattice. In OTM, it is assumed that the electron heat transfer into phonon subsystem is very fast, that is, the electron and lattice temperatures are equal $T_e = T_s$ at any moment of the time. In this approximation, we can limit our description to only one lattice temperature distribution, $T_s(t, r)$, which could be found by numerical solution of a heat-mass transfer equation between the particle and the surrounding medium:

$$\begin{aligned} & \frac{dT_s(t, r)}{dt} \\ &= \frac{\mu_s(T_s)}{\rho_s C_s(T_s)} \Delta T_s(t, r) + \frac{Q(t, r)}{\rho_s C_s(T_s)} - j_D(T_s) S_0 + \frac{3L}{r_0 C_s(T_s)} \frac{dr_0}{dt}, \end{aligned} \quad (1)$$

where $\Delta = \partial^2/\partial x^2 + \partial^2/\partial y^2 + \partial^2/\partial z^2$ is a Laplace operator; $\mu_s(T_s)$, $C(T_s)$, L , ρ_s , and r_0 are, respectively, the heat conductivity, specific heat, evaporation heat, density, and radius of the nanoparticle; $Q(t, r)$ is a heat source; $j_D(T_s)$ is the heat lost from the surface of the nanoparticle into the surrounding medium; $S_0 = 4\pi r_0^2$ is the particle surface area.

The power density of energy generation in the particle $Q(t, r)$ due to radiation energy absorption is generally nonuniform throughout the particle volume, with the nonuniformity being dependent on the size and optical constants of the particle. Since for nanoparticles $2\pi r_0/\lambda < 1$, we can assume that $Q(t, r)$ is uniform throughout the particle volume [6–9], and it can be described by the equation

$$Q(t, r_0) = \frac{3K_{\text{abs}}(r_0, \lambda) I_0 f(t)}{4r_0}, \quad (2)$$

where $K_{\text{abs}}(r_0, \lambda)$ is the absorption efficiency of the nanoparticle as a function of laser wavelength λ and particle radius r_0 , and $f(t)$ is a time profile of a laser pulse.

Heat exchange between the nanoparticle surface and the surrounding medium is rapid, and heat loss becomes substantial for relatively long laser pulses. Assuming that the heat lost from the surface of nanoparticle occurs only due to heat diffusion into surrounding medium, the energy flux density $j_D(T_s)$ removed from the particle surface can be expressed as a nonlinear function of temperature [7–9]:

$$j_D(T_s) = \frac{\mu_\infty T_s}{(s+1)r_0^2 C_s(T_s) \rho_s} \left[\left(\frac{T_s}{T_\infty} \right)^{s+1} - 1 \right], \quad (3)$$

where μ_∞ is the heat conductivity of the surrounding medium at normal temperature T_∞ , and the power exponent $s = \text{const}$ depends on the thermal properties of the surrounding medium.

After integration over the volume for the spherically symmetric case and transition to a uniform temperature over the particle volume, the equation which describes the kinetics of laser heating of the nanoparticle and results from (1) takes the following form [7–9]:

$$\begin{aligned} \frac{dT_s}{dt} &= \frac{3K_{\text{abs}} I_0 f(t)}{4r_0 C_s(T_s) \rho_s} - \frac{\mu_\infty T_s}{(s+1)r_0^2 C_s(T_s) \rho_s} \left[\left(\frac{T_s}{T_\infty} \right)^{s+1} - 1 \right] \\ &+ \frac{3L}{r_0 C_s(T_s)} \frac{dr_0}{dt}. \end{aligned} \quad (4)$$

Here, the first term on the right side of the equation describes the heat generation into the spherical volume due to laser energy absorption by the nanoparticle. The second term describes the energy losses from the surface of the particle into the surrounding medium due to the heat diffusion process. The last term describes the energy losses due to the evaporation of the particle. This evaporation depends on the laser pulse characteristics and particle properties, and it can be realized in five different regimes (see, e.g., [8, 9]): free-molecular, convective, diffusive, gas-dynamic, and explosive [3] modes of evaporation. For example, within the approximation of free-molecular flow, the evaporation term in (4) can be written as

$$4\pi r_0^2 \frac{dr_0}{dt} \rho_s = -\eta 4\pi r_0^2 V_s(T_s) \rho_v(T_s), \quad (5)$$

where η is the accommodation coefficient, and $V_s(T_s)$ and $\rho_s(T_s)$ are, respectively, the average velocity and density of the vapor at temperature T_s . If the heating of the nanoparticle occurs below the temperature of phase transition in the particle material, the third term on the right side of (4) can be neglected.

2.2. Two-temperature model

In TTM, the temperature relaxation in time and sample depth can be modeled by two-coupled diffusion equations: one describing the heat conduction of electrons and the

other than in the lattice. Both equations are connected by a term that is proportional to the electron-phonon coupling constant γ and to the temperature difference between electrons and lattice, originally proposed by Anisimov et al. [10]. We modify this original set of equations, adding a heat exchange term between the surface of the particle and the surrounding medium. Also, we are taking into account the dependence of the thermophysical parameters of electrons, particle, and surrounding medium on temperature during the laser treatment, as presented in Table 1. The modified set of equations describing the heating of electron and lattice subsystems and the energy transfer between particle and surrounding medium has the form

$$C_e(T_e) \frac{\partial T_e}{\partial t} = -\frac{\partial Q(z)}{\partial z} - \gamma(T_e - T_s) + S,$$

$$C_i(T_s) \frac{\partial T_s}{\partial t} = \gamma(T_e - T_s) - \frac{\mu_\infty T_s}{(s+1)r_0^2 C_s(T_s) \rho_s} \left[\left(\frac{T_s}{T_\infty} \right)^{s+1} - 1 \right], \quad (6)$$

where $Q(z) = -k_e(\partial T_e/\partial z)$ is the heat flux; z is the direction perpendicular to the target surface; k_e is the electron thermal conductivity; $S = I_0 f(t) \alpha \exp(-\alpha z)$ is the laser heating source term; α is the material absorption coefficient; $C_e(T_e)$ and $C_i(T_s)$ are the temperature-dependent heat capacities (per unit volume) of the electron and lattice subsystems. The expressions for the temperature dependence of the heat capacities, as well as the values for the electron-phonon coupling constant γ and material data, are listed in Table 1.

3. RESULTS AND DISCUSSION

Comparative simulations using the models described above have been performed for the laser heating of a gold nanoparticle with radius $r_0 = 20$ nm in a surrounding medium of water. The same set of input data presented in Table 1 was used for the calculations in both models. The temperature dependences of the electron heat capacity for the gold, specific heat, and thermal conductivity for the water were obtained by interpolating the experimental data available in the literature (references are listed in Table 1). As can be seen from the table, the electron heat capacity is much less than the lattice heat capacity, and therefore electrons can be heated to very high transient temperatures. Then, the evolution of the electron temperature involves energy transfer to the lattice and energy losses due to the electron heat transport into the target. The electron-phonon coupling process has several characteristic time scales: electron thermalization time τ_e , electron cooling time τ_c , lattice heating time τ_i , and duration of the laser pulse τ_L . The relationship between them defines three different regimes of the laser-metal interaction—femtosecond, picosecond, and nanosecond modes of heating.

3.1. Femtosecond pulses

TTM and OTM have been solved numerically to predict the time dependence of the electron and lattice temperatures

in the femtosecond mode when the laser pulse duration is shorter than the electron thermalization and cooling times, $\tau_L \ll \tau_e, \tau_c$. The calculations were performed for a laser pulse energy density of $E = 1.0$ mJ/cm² and pulse duration of $\tau_L = 60$ femtoseconds. The time profile of the femtosecond laser pulse given in Table 1 and shown in Figure 1(b) (solid curve) corresponds to the experimentally observed output from an amplified Ti: sapphire laser (Legend-HE from Coherent Inc., Santa Clara, Calif, USA). The laser flux is chosen at the level 1.0 mJ/cm² to provide the cell lethality during a single laser pulse. The results of the simulations for the heating of a gold nanoparticle by a femtosecond laser pulse are shown in Figures 1 and 2. Figure 1(b) displays the results obtained by TTM, and Figure 1(b) presents the results of OTM simulations. A comparison of these two models is shown in Figure 2.

As follows from Figure 1(a), thermal equilibrium among the excited electrons with equilibrium temperature $T_e \approx 3300$ K for a given laser fluence is established within 175 femtoseconds. We should note that the equilibrium temperature for electrons is reached long after the end of a laser pulse, which had a duration of 60 femtoseconds. The electrons remain in the thermal equilibrium state from several hundred femtoseconds up to 1 picosecond (see Figure 3(a)). Then, the electrons cool exclusively by coupling to the lattice, resulting in a linear decay of the electron temperature during the first 10 picoseconds (Figure 3(a)). Our simulations agreed with the electron relaxation time measured in [15] for femtosecond pulse excitation of a DNA-modified gold nanoparticle.

The slow rate of electron heat diffusion into the phonon subsystem on the femtosecond time scale results in a delay of about 100 femtoseconds in the heating of the bulk sample (dashed curve in Figure 1(a)). Once the electron thermal equilibrium is established, a hot electron bath raises the temperature of the cold lattice up to 1090 K for a given laser energy density $E = 1$ mJ/cm².

The results of heating the gold nanoparticle obtained by OTM are demonstrated in Figure 1(b). This figure also shows the femtosecond laser pulse time profile used in the calculations. Comparative simulations for the evolution of the nanoparticle temperature using both models under the same conditions are presented in Figure 2. It follows from these simulations that both models demonstrate the same scenario in the heating kinetics of a metal nanoparticle by a femtosecond laser pulse. Both models reveal approximately a 100-femtosecond time delay in the heating of the particle, followed by a maximum lattice temperature of around 1090 K within 175 femtoseconds after the end of a laser pulse. Even the maximum values of the particle temperature predicted by both models are the same (see Figure 2). The saturation parts in the lattice temperature curves are explained by negligibly small heat diffusion from the surface of the nanoparticle into the surrounding medium on the femtosecond time scale. A slight difference in the slopes of the temperature curves within the first 100 femtoseconds of heating occurs due to the assumption made in OTM that the electron heat transfer into the lattice subsystem is very fast. Because of this, the particle temperature in OTM promptly

TABLE 1: Input parameters used for simulations in both models.

Parameters	Magnitude and units	Reference
Laser pulse shape	$f(t) = \exp[-(at - b)^2 - (at - c)^2]$, $a, b, c = \text{const}$	
Energy density	$E = 10^{-3} \text{ J/cm}^2$	
Volume density of the gold	$\rho_0 = 0.0193 \text{ kg/cm}^3$	[11]
Electron heat capacity (gold)	$C_e(T_e) = aT_e^4 - bT_e^3 + cT_e^2 - dT_e + e, \left(\frac{\text{J}}{\text{K}^2\text{cm}^3}\right)$ $a = 6.0 \times 10^{-17},$ $b = 3.0 \times 10^{-12},$ $c = 5.07 \times 10^{-8},$ $d = 6.7589 \times 10^{-5},$ $e = 7.207 \times 10^{-2},$	[12]
Electron-phonon coupling constant for gold	$\gamma = 2.27 \times 10^{10} \frac{\text{W}}{\text{K cm}^3}$	[13]
Gold specific heat	$C = 129 \frac{\text{J}}{\text{K kg}}$	
Specific heat of water	$C_w(T_s) = a(1 + b(T_s - 293 \text{ K})), \left(\frac{\text{J}}{\text{K kg}}\right)$ $a = 4182.0,$ $b = 1.016 \times 10^{-4}.$	
Radius of gold nanoparticle	$r_0 = 20 \text{ nm}$	
Absorption efficiency of gold nanoparticle	$K_{\text{abs}} = 4.0195$ ($r_0 = 20$ and $\lambda = 528 \text{ nm}$)	[2, 14]
Absorption coefficient of gold nanoparticle	$\alpha = 8.736 \times 10^5 \text{ cm}^{-1}$ ($r_0 = 20 \text{ nm}$ and $\lambda = 528 \text{ nm}$)	[14]
Power exponent	$s = 1.0$	
Thermal conductivity of water	$\mu_0(T_s) = a(1 + b(T_s - T_\infty)), \left(\frac{\text{W}}{\text{K cm}}\right)$ $a = 0.00597,$ $b = 1.78 \times 10^{-3}.$	

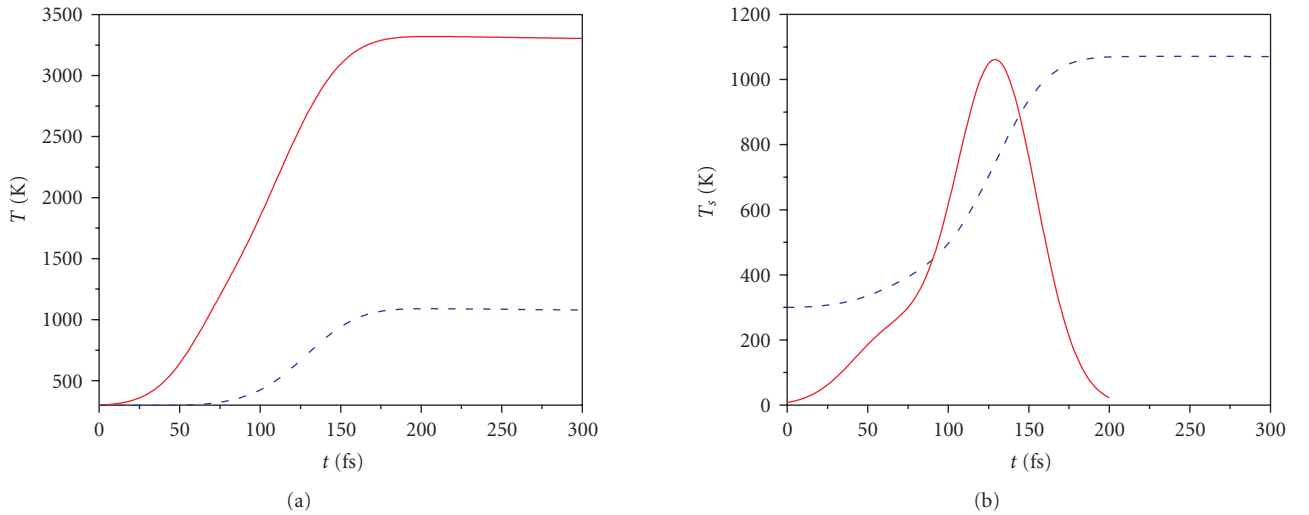


FIGURE 1: (a) Electron (solid curve) and lattice (dashed curve) temperature evolutions on the femtosecond time scale for a gold nanoparticle predicted by TTM. (b) Evolution of the nanoparticle temperature (dashed curve) after the femtosecond laser pulse, predicted by OTM, and laser pulse shape (solid curve).

follows electron thermal behavior. A comparison of these two models shows that the simpler OTM gives the same results as the more precise TTM. Thus, OTM provides an adequate description of the laser heating of nanoparticles in the femtosecond regime.

3.2. Picosecond pulses

In this mode, the constants a , b , and c in the time profile for the laser pulse have been chosen to provide the laser pulse width of 60 picoseconds at FWHM with the same pulse shape

TABLE 2: Thermophysical characteristics of the gold particle and surrounding biological tissue.

Material	Specific heat C (J/K kg)	Interval of T (K)	Thermal conductivity μ_0 (W/m K)	Thermal diffusivity χ (m^2/s)
Gold	129	273–373	318	1.18×10^{-4}
	4181.6–4215.6		0.597–0.682	
Water	$C(T) = 4182(1 + 1.016 \times 10^{-4}(T - 293 \text{ K}))$	273–373	$\mu(T) = 0.597(1 + 1.78 \times 10^{-3}(T - T_\infty))$	1.43×10^{-7}
Human prostate	3740	310	0.529	
Blood	3645–3897	273–373	0.48–0.6	1.6×10^{-7}
Fat	2975	273–373	0.185–0.233	
Tumor	3160	310	0.561	
Skin		273–373	0.210–0.410	

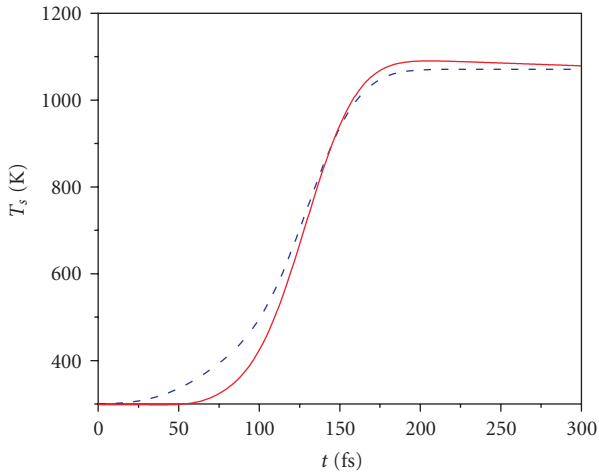


FIGURE 2: Comparison of nanoparticle temperature evolutions after the 60 femtoseconds laser pulse-predicted TTM (solid curve) and one-temperature model (dashed curve).

listed in Table 1 and shown in Figure 1(b). As can be seen from Figures 1(b) and 3(b), in the picosecond regime the electron thermalization time τ_e and electron cooling time τ_c are much less than the duration τ_L of the 60 picoseconds laser pulse. Hence, during the first 10 picoseconds, the electron subsystem has already been completely cooled (Figure 3(a)), and the electron temperature above the ambient no longer exists for the considered picosecond mode of heating. This is confirmed by our calculations presented on Figure 3(b) (dashed curve). Thus, TTM provides a very good approximation for the femtosecond mode as soon as the electron temperature exists, but it fails to describe the laser heating of nanoparticles for longer pulse durations in the picosecond and nanosecond regimes.

Opposite to TTM, OTM describes the picosecond heating kinetics very well. A typical time evolution of the particle temperature predicted by OTM on the picosecond time scale is displayed in Figure 3(b) (solid curve) for the same material constants listed in Table 1. The main feature is the appearance of heat lost from the surface of the nanoparticle into the surrounding medium on the picosecond time scale. After about 200 picoseconds, cooling of the nanoparticle

begins due to heat diffusion into the water. The maximum temperature reached by a 20-nm gold particle for the given laser pulse is 995 K. This temperature is sufficient to initiate any thermal killing mechanisms in cancer cells.

3.3. Nanosecond pulses

For laser heating of metal nanoparticles in the nanosecond regime, the characteristic lattice heating time τ_i is much smaller than the laser pulse duration: $\tau_L \gg \tau_i$. This means that, the temperature inside the nanoparticle is nearly uniform over the whole particle at the time scale of the laser pulse duration τ_L . In this case, the electron and lattice temperatures are equal, $T_e = T_s$, so that the homogeneous heating of the particle and quasisteady heat exchange with the surrounding medium can be described by just OTM. The characteristic lattice heating time τ_i required for the formation of a quasistationary temperature profile across the nanoparticle can be estimated from the formula $\tau_i = r_0^2/4\chi$, where r_0 is the particle radius and χ the thermal diffusivity of the particle material. For gold nanoparticle ($\chi = 1.18 \times 10^{-4} \text{ m}^2/\text{s}$) with radii $r_0 = 20\text{--}30 \text{ nm}$, the lattice heat diffusion time is $\tau_i \sim 2 \times 10^{-12} \text{ s} \ll \tau_L \sim 10^{-8} \text{ s}$.

Sample calculations have been carried out using OTM for gold nanoparticles with radii $r_0 = 30\text{--}35 \text{ nm}$ in different surrounding biomedica for an incident laser pulse of energy $E = 10 \text{ mJ}/\text{cm}^2$ and pulse duration $\tau_L = 8 \text{ nanoseconds}$ with the time profile shown in Figure 1(b). The laser pulse profile and duration 8 nanoseconds have been chosen to be close to those used in previous experiments [2]. The laser flux chosen is ten times higher than in the regimes considered above to provide approximately the same maximum nanoparticle temperature as observed for femtosecond and picosecond laser heating. We should note that $10 \text{ mJ}/\text{cm}^2$ is comparable to the laser fluence currently used in the photothermal therapy of cancer cells [1, 3]. The kinetics of heating and cooling the gold nanoparticle are demonstrated in Figure 4, where (a) illustrates the time dynamics of laser heating of a 30-nm gold particle in different biological media: blood, human prostate, tumor, and fat. The thermophysical characteristics of gold and biological surrounding media for different temperatures are listed in Table 2. Figure 4(b) shows results of thermal calculations for a 35-nm gold particle, which is heated and cooled in water at different heat transfer rates s .

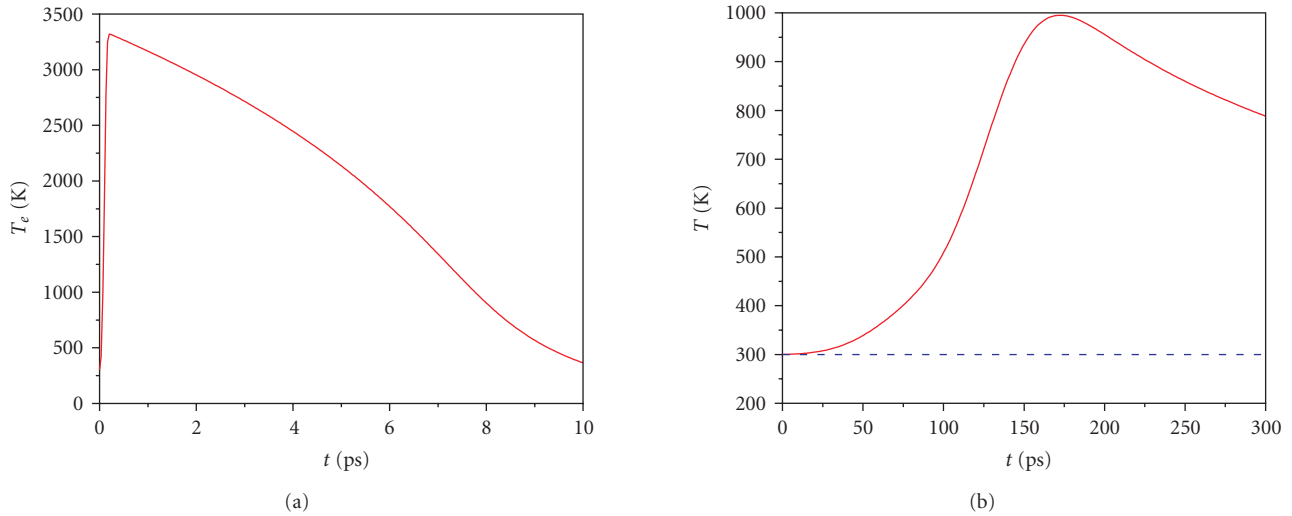


FIGURE 3: (a) Electron temperature relaxation on the picosecond time scale. (b) Temperature time distributions for a gold nanoparticle predicted by OTM (solid curve) and TTM (dashed curve) after the 60 picoseconds laser pulse.

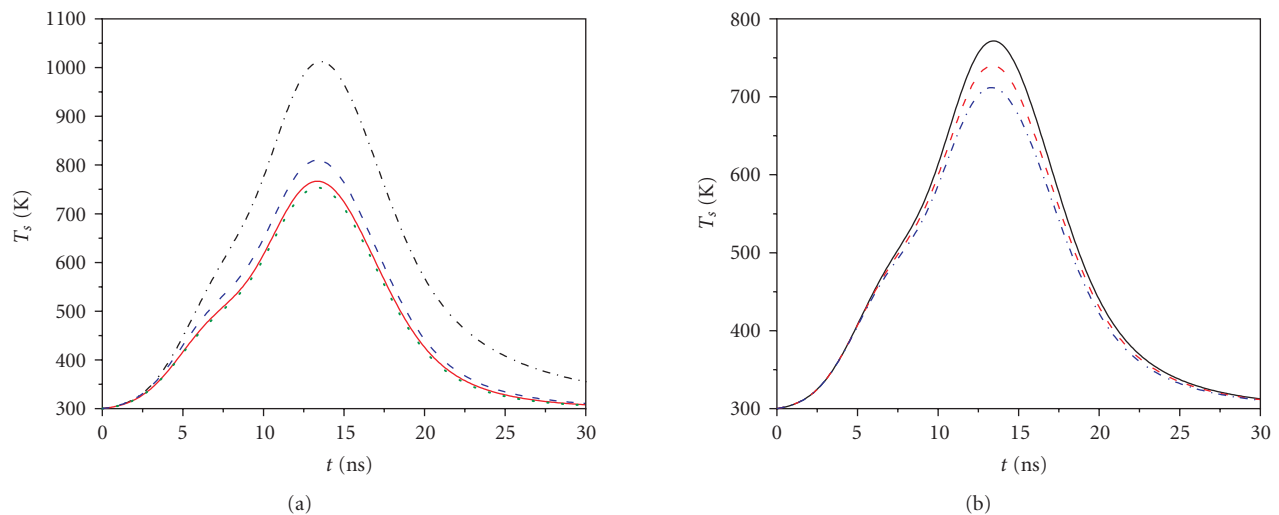


FIGURE 4: Kinetics of heating and cooling of a gold nanoparticle by a nanosecond laser pulse of energy density 10 mJ/cm^2 and duration 8 nanoseconds. Calculations have been made by using OTM. (a) Illustration of the time dynamics of laser heating of a 30-nm gold particle in different biological media: fat (dashed-dotted curve), blood (dashed curve), tumor (solid curve), and prostate (dotted curve). (b) Results of thermal calculations for a 35-nm gold particle: heating and cooling in the water surrounding medium at different heat transfer rates s : $s = 1.0$ (solid curve), $s = 1.25$ (dashed curve), and $s = 1.5$ (dashed-dotted curve).

It follows from these calculations that during the laser pulse duration the transfer of heat from the nanoparticle into the surrounding media is slight, and the particle rapidly reaches a high temperature. The heating rate is about 10^{12} Ks^{-1} . The temperature of the particle continues to rise even after the end of the laser pulse. The highest temperature, 770 K, for a given laser pulse fluence is observed for the heating time of 13.5 nanoseconds, when the laser pulse has already degraded (see Figure 4(a)). After that time, the transfer of heat from the particle to the surrounding medium becomes increasingly important, since the energy source is no longer present in the system. The temperature of the particle and surrounding medium remains high ($\sim 400 \text{ K}$)

up to 20 nanoseconds, exceeding the laser pulse duration by 2.5 times. The total time for one cycle (heating from the initial temperature 300 K to maximum temperature, followed by cooling back to the initial temperature) is about 30 nanoseconds.

We have also examined the effect of different biological surroundings on the laser heating dynamics of 30 nm gold particles. Four biomedias were used: namely, blood, human prostate, tumor, and fat. Results of computer simulations of the time-temperature profiles of gold nanoparticles in various biological media, performed by using OTM, are plotted in Figure 4(a). As follow from our calculations, the laser heating and temperature behavior of the gold

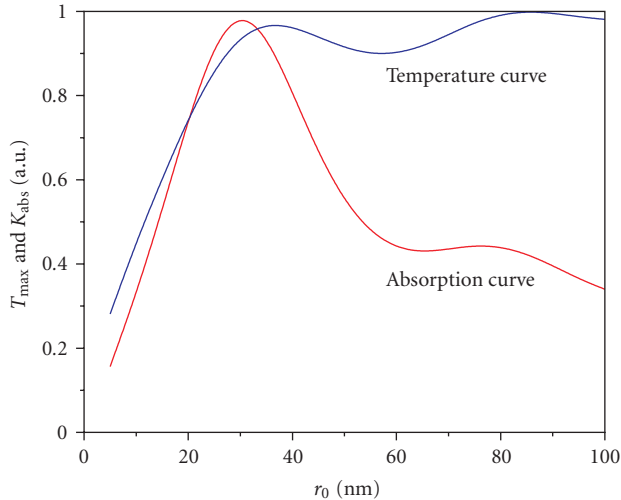


FIGURE 5: Nondimensional (a.u.) absorption efficiency K_{abs} and maximal temperature T_{max} curves as a function of the particle's radius for the gold nanoparticles in blood heated by a laser pulse of energy density 10 mJ/cm^2 and duration 8 nanoseconds.

nanoparticles in blood, prostate, and tumor are comparable to the water surrounding medium case, since the thermodynamic properties of those media are very close to each other (see Table 2). This means that for the thermal calculations of laser heating of biological media, the thermal properties of water can be used if the water content in the media is high. But the heating of a gold nanoparticle in fat is substantially different from the water case, since the fat has low-thermal characteristics. Here, we observe higher overheating of the particle at the same energy level and duration of the laser pulse due to the relatively low-thermal conductivity of fat as compared to other biomedias.

The temperature dynamics of the particle is sensitive to the power exponent s used in the temperature dependence of the heat lost from the surface of the nanoparticle into the surrounding medium, that is, $(j_D(T_s))$ in (3) (see Figure 4(b)). The value of $s = 1$ better corresponds to the real biological surrounding. The power $s > 1$ describes the medium with high thermophysical characteristics, like the cooling liquids and metals. The medium with $s < 1$ has a low thermal conductivity and can be used as a thermal isolator.

It is interesting to investigate the effect of the particle's radius on the temperature dynamics of the nanoparticle heated by the nanosecond laser radiation in the biological surroundings. There are two competitive factors here. On one hand, according to the Mie diffraction theory, the absorption efficiency of the gold nanoparticle drops with the decreasing size of the particle. On the other hand, the heating rate increases for smaller particles as follows from (4). To find which factor has a stronger effect on the effective laser heating of a gold nanoparticle, we have calculated the maximal temperature profile for different nanoparticle radii in blood and compared it to the gold nanoparticle absorption curve. The results of these simulations are performed by using OTM and presented in Figure 5. It follows from this figure that the optical effect is much stronger than the

thermal effect when the radius of nanoparticle is less than 35 nm. In the radii range 1–35 nm, the overheating effect of the particle behaves according to the absorption efficiency. For a radius of 35 nm, the thermal processes dominate over the optical properties. For large radii ($\geq 35 \text{ nm}$), the maximal temperature profile is saturated with oscillations, repeating the maxima and minima of the absorption curve. The saturation of the maximal temperature curve for large particle radii is explained by the balance between heating of the particle due to absorption of laser energy and energy losses from the surface of the particle due to heat diffusion into the surrounding biological medium.

4. CONCLUSIONS AND SUMMARY

The comparative analysis of OTM and TTM for heating of a metal nanoparticle in the femtosecond, picosecond, and nanosecond regimes has shown that

- (i) in the femtosecond mode, the thermal equilibrium among the excited electrons is established within the first 175 femtoseconds, long after the end of the laser pulse duration;
- (ii) the electrons remain in the thermal equilibrium state up to 1 picosecond;
- (iii) both models demonstrate the same scenario in the heating kinetics of a metal nanoparticle by a femtosecond laser pulse: about a 100-femtosecond time delay in the heating of the particle is observed, until reaching a maximum lattice temperature and saturation in temperature curves after 175 femtoseconds;
- (iv) the electron cooling time due to coupling to the lattice is about 10 picoseconds, which imposes an upper time limit for TTM application;
- (v) TTM gives a very good approximation for the femtosecond mode while an electron temperature exists, but it fails to describe the laser heating of nanoparticles for longer pulse durations in the picosecond and nanosecond regimes;
- (vi) OTM shows that the heat lost from the surface of the nanoparticle into the surrounding medium becomes noticeable after 200 picoseconds;
- (vii) the heating of a metal nanoparticle by a nanosecond laser pulse in fat provides higher particle overheating than in blood, prostate, and water as surrounding media due to the thermally isolating property of the fat;
- (viii) the optical properties of the nanoparticle have a much stronger effect on the heating dynamics in the nanosecond mode than the thermal effects when the radius of the particle is less than 35 nm. For larger particles, the thermal processes dominate the optical properties, and the temperature curve is determined by the balance between heating of the nanoparticle and energy losses from the surface of the particle due to heat diffusion into the surrounding biological medium.

Thus, the comparison of the two models shows that OTM provides an adequate description of the laser heating of

nanoparticles in the femtosecond, picosecond, and nanosecond regimes.

ACKNOWLEDGMENT

This work has been supported by the Lilly Foundation Grant AA0000010.

REFERENCES

- [1] C. M. Pitsillides, E. K. Joe, X. Wei, R. R. Anderson, and C. P. Lin, "Selective cell targeting with light-absorbing microparticles and nanoparticles," *Biophysical Journal*, vol. 84, no. 6, pp. 4023–4032, 2003.
- [2] V. P. Zharov, R. R. Letfullin, and E. N. Galitovskaya, "Microbubbles-overlapping mode for laser killing of cancer cells with absorbing nanoparticle clusters," *Journal of Physics D*, vol. 38, no. 15, pp. 2571–2581, 2005.
- [3] R. R. Letfullin, C. Joenathan, T. F. George, and V. P. Zharov, "Cancer cell killing by laser-induced thermal explosion of nanoparticles," *Journal of Nanomedicine*, vol. 1, pp. 473–480, 2006.
- [4] J. L. Wu, C. M. Wang, and G. M. Zhang, "Ultrafast optical response of the Au-BaO thin film stimulated by femtosecond pulse laser," *Journal of Applied Physics*, vol. 83, no. 12, pp. 7855–7859, 1998.
- [5] B. N. Chichkov, C. Momma, S. Nolte, F. von Alvensleben, and A. Tünnermann, "Femtosecond, picosecond and nanosecond laser ablation of solids," *Applied Physics A*, vol. 63, no. 2, pp. 109–115, 1996.
- [6] V. K. Pustovalov, "Theoretical study of heating of spherical nanoparticle in media by short laser pulses," *Chemical Physics*, vol. 308, no. 1-2, pp. 103–108, 2005.
- [7] R. R. Letfullin and V. I. Igoshin, "Multipass optical reactor for laser processing of disperse materials," *Quantum Electronics*, vol. 25, no. 7, pp. 684–689, 1995.
- [8] R. R. Letfullin, "Solid aerosols into the strong laser fields," *Bulletin of the Samara State Technical University. Physical-Mathematical Sciences*, no. 4, pp. 243–263, 1996.
- [9] R. R. Letfullin and V. I. Igoshin, "Theoretical modeling of plasma formation and generation of electromagnetic fields in the gas-dispersed media under the action of laser radiation," *Trudy FIAN*, vol. 217, pp. 112–135, 1993.
- [10] S. I. Anisimov, B. L. Kapeliovich, and T. L. Perel'man, "Electron emission from metal surfaces exposed to ultrashort laser pulses," *Soviet Physics JETP*, vol. 39, pp. 375–377, 1974.
- [11] R. B. Ross, *Metallic Materials Specification Handbook*, Chapman & Hall, London, UK, 4th edition, 1992.
- [12] Z. Lin, L. V. Zhigilei, and V. Celli, "Electron-phonon coupling and electron heat capacity of metals under conditions of strong electron-phonon nonequilibrium," *Physical Review B*, vol. 77, no. 7, Article ID 075133, 17 pages, 2008.
- [13] J. Hohlfeld, S.-S. Wellershoff, J. Güdde, U. Conrad, V. Jahnke, and E. Matthias, "Electron and lattice dynamics following optical excitation of metals," *Chemical Physics*, vol. 251, no. 1–3, pp. 237–258, 2000.
- [14] P. K. Jain, K. S. Lee, I. H. El-Sayed, and M. A. El-Sayed, "Calculated absorption and scattering properties of gold nanoparticles of different size, shape, and composition: applications in biological imaging and biomedicine," *Journal of Physical Chemistry B*, vol. 110, no. 14, pp. 7238–7248, 2006.
- [15] P. K. Jain, W. Qian, and M. A. El-Sayed, "Ultrafast cooling of photoexcited electrons in gold nanoparticle-thiolated DNA

conjugates involves the dissociation of the gold-thiol bond," *Journal of the American Chemical Society*, vol. 128, no. 7, pp. 2426–2433, 2006.

Research Article

A New 3D Simulation Method for the Construction of Optical Phase Contrast Images of Gold Nanoparticle Clusters in Biological Cells

Stoyan Tanev,¹ James Pond,² Paul Paddon,² and Valery V. Tuchin^{3,4}

¹Department of Systems and Computer Engineering, Carleton University, 1125 Colonel By Drive, Ottawa, ON, Canada K1S 5B6

²Lumerical Solutions, Inc., Vancouver, BC, Canada V6B 2Y5

³Research-Educational Institute of Optics and Biophotonics, Saratov State University, 410012 Saratov, Russia

⁴Institute of Precise Mechanics and Control of RAS, 410028 Saratov, Russia

Correspondence should be addressed to Stoyan Tanev, tanev@sce.carleton.ca

Received 5 June 2008; Accepted 30 October 2008

Recommended by Brian Wilson

A new 3D simulation method based on the finite-difference time domain (FDTD) approach in combination with Fourier optic techniques is applied to the modeling of optical phase contrast microscope (OPCM) imaging of gold nanoparticles (NPs) in single biological cells. We consider a realistic size 3D cell model at optical immersion conditions, that is, when the refractive index values of the cytoplasm and of the extracellular medium are equal. For the first time, an FDTD-based OPCM model is applied to visualize the presence of a cluster of gold NPs in the cytoplasm at both resonant and nonresonant conditions. The results demonstrate the capability to model OPCM image enhancement by optically controlling the resonant properties of the NPs. Our research study extends the applicability of the FDTD modeling approach into a new biomedical optics research area.

Copyright © 2008 Stoyan Tanev et al. This is an open access article distributed under the Creative Commons Attribution License, which permits unrestricted use, distribution, and reproduction in any medium, provided the original work is properly cited.

1. INTRODUCTION

One of the growing areas in biomedical optics and photonics [1, 2] is the application of optical software simulation and modeling tools to provide deeper understanding of newly developed optical diagnostics and imaging techniques. There are a number of numerical modeling approaches that can be used for the modeling of the light scattering from biological cells [3] including the finite-difference time domain (FDTD) method [4–9]. Recently, we demonstrated the applicability of the 2D FDTD approach to numerically study the changes in the forward scattered light phase and intensity distributions due to different cell membrane thicknesses and different configurations of gold NPs in the cytoplasm of small size cells using the optical immersion technique (OIT) [7, 8]. The OIT is associated with the so-called “optical clearing” (OC) effect consisting in the increased light transmission through cells or tissues due to the matching of the refractive indices of some of their morphological components to that of the extracellular or interstitial media [10–12]. In this article, we present the first

results of a research study applying a 3D FDTD-based optical phase contrast microscope (OPCM) imaging approach to the modeling of a cluster of gold nanoparticles (NPs) in realistic size single cells. We demonstrate a new simple way of using the FDTD approach for the construction of OPCM images by moving its modeling power from the calculation of phase distribution curves [7] to realistic cell images. We validate our approach by modeling a gold nanoparticle cluster in the cell cytoplasm to provide a valuable design methodology for further studies in optical nano-bioimaging and nanotherapeutics.

2. THE FDTD APPROACH

The FDTD technique is a numerical solution of Maxwell's equations [13]. In most light scattering simulation experiments, one usually uses the so-called total field/scattered field (TF/SF) formulation [8, 13] to excite the magnetic and electric fields and simulate a linearly polarized plane wave propagating in a finite region containing the simulation equivalent of the object under investigation [13].

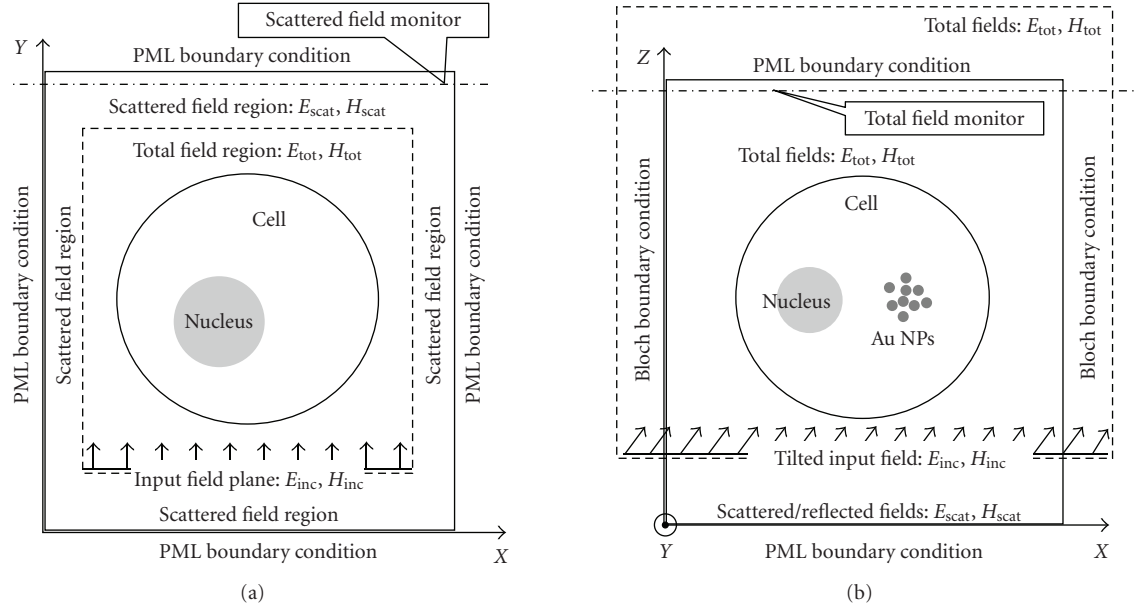


FIGURE 1: Schematic representation of the FDTD computational domain: (a) total field/scattered field 2D formulation; (b) total field/reflected field 3D formulation.

A schematic representation of the 2D FDTD computational domain is shown in Figure 1(a). TFSF sources are used to separate the FDTD computation domain into two distinct regions. The first one is internal to the computational domain and contains the total near fields $E_{\text{tot}} = E_{\text{inc}} + E_{\text{scat}}$ and $H_{\text{tot}} = H_{\text{inc}} + H_{\text{scat}}$, that is, the sum of the incident field and the scattered near field. The second one occupies the rest of the computational domain and contains only the scattered near fields $E_{\text{scat}} = E_{\text{tot}} - E_{\text{inc}}$ and $H_{\text{scat}} = H_{\text{tot}} - H_{\text{inc}}$. The final FDTD simulation results require additional postprocessing computational procedures to transform the real values of the calculated near fields into their complex far field counterparts. The far fields include the transverse distribution of the forward scattered light from the cell which is of high relevance for the modeling of optical phase contrast imaging. At the edges, the entire FDTD computational domain is truncated by the so-called perfectly matched layer (PML) boundary conditions [13].

The 3D case of the TFSF formulation described above follows a similar logic. The 3D simulation results provided here are based on a modified 3D TFSF formulation that could be more appropriately called total field/reflected field (TFRF). The 3D “TFRF” formulation uses a TFSF region which contains the biological cell and extends beyond the limits of the simulation domain (Figure 1(b)). The extension of the transverse dimension of the input field beyond the limits of the computational domain through the PML boundaries would lead to distortions of its ideal plane wave shape and eventually distort the simulation results. To avoid these distortions, one must use Bloch periodic boundary conditions (Figure 1(b)) in the lateral x - and y -directions which are perpendicular to the direction of propagation- z [13]. Bloch boundary conditions are periodic boundary conditions which take into account the phase effects due to

the tilting of the input plane waves incoming at periodic structures, that is, what we are actually modeling is a periodic row of biological cells. The near scattered fields, however, are calculated in the transverse planes located in the close proximity to the cell where the coupling effect due to waves scattered from adjacent cells is negligible. This effect can be further minimized or completely removed by controlling the lateral dimension of computational domain by using a large enough period of the periodic cell structure. The larger is this period, the smaller is the coupling effect. In the 3D TFRF formulation, the location in the computational domain corresponding to the forward scattered light is positioned within the total field region (Figure 1(b)). The OPCM simulation model requires the explicit availability of the forward scattered transverse distribution of the fields. The phase of the scattered field accumulated by a plane wave propagating through a biological cell will be used in the FDTD model of the OPCM that will be described in Section 3.

3. OPTICAL PHASE CONTRAST MICROSCOPE MODEL

3.1. FDTD OPCM principle

Phase contrast microscopy is utilized to produce high-contrast images of transparent specimens such as microorganisms, thin tissue slices, living cells, and subcellular components such as nuclei and organelles. It translates small-phase variations into corresponding changes in amplitude visualized as differences in image contrast. A standard phase contrast microscope design is shown in Figure 2(a), where an image with a strong contrast ratio is created by coherently interfering a reference (R) with a diffracted beam (D) from the specimen (<http://www.microscopyu.com/articles/phase-contrast/phasemicroscopy.html>). Relative to the reference

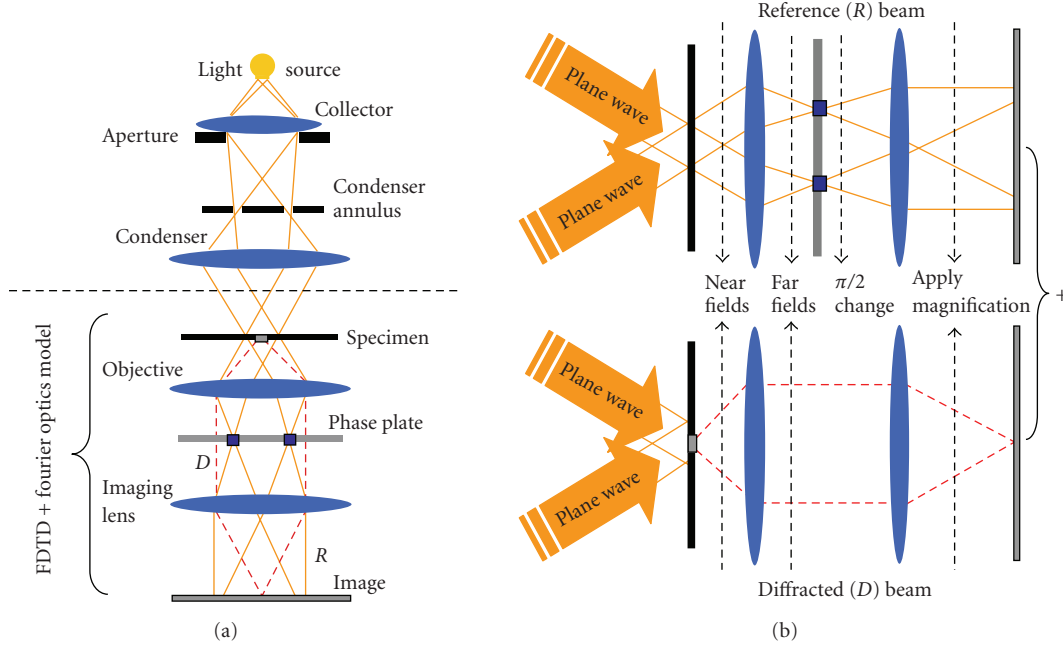


FIGURE 2: (a) Schematic representation of an OPCM. (b) 2D visual representation of the FDTD OPCM model using incoherent illumination by two plane waves at a polar angle of 30 degrees. For each of the two plane waves, the propagation of light is modeled as a combination of two parallel wave phenomena: (i) propagation of the reference (R) beam without the cell, and (ii) propagation of the diffracted (D) beam due to the cell.

beam, the diffracted beam has lower amplitude and is retarded in phase by approximately $\pi/2$ through interaction with the specimen.

The main concept underlying the design of the phase contrast microscope is the spatial separation of the R beam from D wave front emerging from the specimen. In addition, the amplitude of the R beam light must be reduced and the phase should be advanced or retarded by another $\pm\pi/2$ in order to maximize the differences in the intensity between the specimen and the background in the image plane. The mechanism for generating relative phase retardation has two steps: (i) the D beam is being retarded in phase by a quarter wavelength (i.e., $\pi/2$) at the specimen, and (ii) the R beam is advanced (or retarded) in phase by a phase plate positioned in or very near the objective rear focal plane (Figure 2(a)). This two-step process is enabled by a specially designed annular diaphragm—the condenser annulus—which is placed in the condenser front focal plane, is matched in diameter, and optically conjugates to the phase plate residing in the objective rear focal plane. The resulting image, where the total phase difference is translated by interference at the image plane into an amplitude variation, can have a high contrast ratio, particularly if both beams have the same amplitude.

3.2. Excitation and simulation of the FDTD near fields

Figure 2(a) illustrates the part of the microscope that will become the subject of FDTD modeling combined with Fourier optics. Figure 2(b) provides a visual representation

illustrating the major steps in the FDTD OPCM model. The phase contrast microscope uses incoherent annular illumination that could be approximately modeled by adding up the results of eight different simulations using ideal input plane waves incident at a given polar angle (30 degrees), an azimuthal angle (0, 90, 180, or 270 degrees), and a specific light polarization (parallel or perpendicular to the plane of the graph). Every single FDTD simulation provides the near field components in a transverse monitoring plane located right behind the cell (Figure 1(b)).

3.3. Far-field transformation

The far field transformations (Figure 3) use the FDTD calculated near fields right behind the cell and return the three complex components of the electromagnetic fields at 1 meter distance (i.e., long enough) from the location of the near fields, that is, in the far field [13, 14]: $E_r(u_x, u_y)$, $E_\theta(u_x, u_y)$, and $E_\phi(u_x, u_y)$, where (r, θ, Φ) refer to a spherical coordinate system and the variables u_x and u_y are the x and y components of the unit direction vector \mathbf{u} . The unit direction vector is related to the angular variables by $u_x = \sin(\theta) \cos(\Phi)$, $u_y = \sin(\theta) \sin(\Phi)$, $u_z = \cos(\theta)$, with $u_x^2 + u_y^2 + u_z^2 = 1$. The in-plane wave vectors for each plane wave are given by $k_x = ku_x$ and $k_y = ku_y$, where $k = 2\pi/\lambda$. To scale the far field to a different distance, we can recognize that in 3D, the electric field intensity decreases like $1/R^2$: $|E(R)|^2 = |E_0|^2/R^2$, where E_0 is the field at 1 m distance resulting from the far field transformation and R is measured

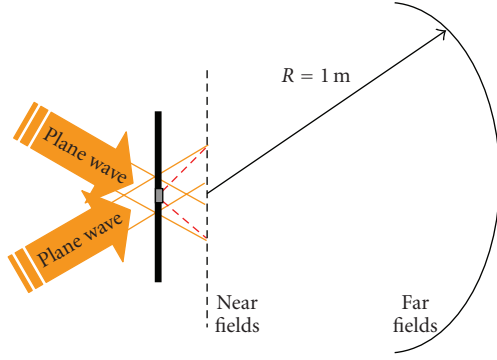


FIGURE 3: Visual representation of the far field transformation procedure within the context of the optical phase contrast microscope schematics presented in Figures 2.

in meters. The specific details of the far field transformation can be found elsewhere [13].

It is important to note that the near-to-far field projection must take into account the Bloch periodic boundary conditions in the lateral dimension and is calculated only at angles that correspond to diffracted orders of the periodic structure as defined by the Bragg conditions. This is done by calculating the direction cosines of all the diffracted orders that meet the Bragg condition, and interpolating the previously far-field distributions onto those specific directions. The near-to-far field projection, therefore, provides the electric field amplitude and phase corresponding to each diffracted order. The zeroth order, that is, the light travelling through the scattering object without any deviation in angle, is the reference beam; and the phase contrast microscope is designed to provide a phase delay to this order.

3.4. Optical magnification

Now that we have the field components $\mathbf{E}(k_x, k_y)$, we can use their amplitudes and phases to determine all the properties of the polarization as well as do Fourier optics for both the scattered and reference beams. We assume an ideal optical lens system that could be characterized by a given magnification factor. This simple model could be easily extended to include the numerical equivalent of the two lenses (Figure 2) together with an additional model to take into account any aberrational effects. The magnification was implemented by modifying the angle of light propagation, that is, by multiplying the direction cosines u_x and u_y by the inverse value of the desired magnification factor M : $U_x = u_x/M$ and $U_y = u_y/M$. In any other circumstances, the modification of the direction cosines would lead to complications because of the vectorial nature of the E field. In our case, however, working in spherical coordinates (E_r , E_θ , and E_Φ) leads to the advantage that the vectorial components do not change when u_x and u_y are modified because they are part of a local coordinate system that is tied to the values of u_x and u_y . The magnification factor $M = 10$ was applied to the far fields before the interference of the diffracted (D) and reference (R) beams at the image plane.

3.5. Numerical aperture

It was also possible to apply the effect of a numerical aperture $NA = 0.8$ which clips any light that has too steep angle and would not be collected by the lens system. This means that all the light with $U_x^2 + U_y^2 > NA^2$ is being clipped. The effect of the aperture is defined by the inequality $U_x^2 + U_y^2 > NA^2$ applied to the corrected aperture angles θ' and Φ' :

$$\begin{aligned}\sin(\Phi') &= \frac{U_y}{U_{xy}}, \\ \cos(\Phi') &= \frac{U_x}{U_{xy}}, \\ \cos(\theta') &= U_z, \\ \sin(\theta') &= U_{xy},\end{aligned}\quad (1)$$

where $U_{xy} = \sqrt{U_x^2 + U_y^2}$, $U_z = \sqrt{1 - U_{xy}^2}$ and the ‘‘sqrt’’ labels a square root mathematical operation. The magnified field components will then have the following form.

Diffracted (D) beam:

$$\begin{aligned}E_{x-D}(k_x, k_y) &= -E_\Phi \sin(\Phi') + E_\theta \cos(\Phi') \cos(\theta'), \\ E_{y-D}(k_x, k_y) &= E_\Phi \cos(\Phi') + E_\theta \sin(\Phi') \cos(\theta'), \\ E_{z-D}(k_x, k_y) &= -E_\theta \sin(\theta').\end{aligned}\quad (2)$$

Reference (R) beam:

$$\begin{aligned}E_{x-R}(k_x, k_y) &= -E_{\Phi-R} \sin(\Phi') + E_{\theta-R} \cos(\Phi') \cos(\theta'), \\ E_{y-R}(k_x, k_y) &= E_{\Phi-R} \cos(\Phi') + E_{\theta-R} \sin(\Phi') \cos(\theta'), \\ E_{z-R}(k_x, k_y) &= -E_{\theta-R} \sin(\theta'),\end{aligned}\quad (3)$$

where $E_{\theta-R}$ and $E_{\Phi-R}$ are the far field components of the reference beam.

3.6. OPCM image construction

The fields given above are then used to calculate back the Fourier inverse transform of the far field transformed fields leading to the distribution of the scattered and the reference beams in the image plane.

Diffracted (D) beam:

$$\begin{aligned}E_{x-D} &= \text{sum}(E_{x-D}(k_x, k_y) \exp(ik_x x + ik_y y + ik_z z)), \\ E_{y-D} &= \text{sum}(E_{y-D}(k_x, k_y) \exp(ik_x x + ik_y y + ik_z z)), \\ E_{z-D} &= \text{sum}(E_{z-D}(k_x, k_y) \exp(ik_x x + ik_y y + ik_z z)).\end{aligned}\quad (4)$$

Reference (R) beam:

$$\begin{aligned}E_{x-R} &= \text{sum}(E_{x-R}(k_x, k_y) \exp(ik_x x + ik_y y + ik_z z)), \\ E_{y-R} &= \text{sum}(E_{y-R}(k_x, k_y) \exp(ik_x x + ik_y y + ik_z z)), \\ E_{z-R} &= \text{sum}(E_{z-R}(k_x, k_y) \exp(ik_x x + ik_y y + ik_z z)),\end{aligned}\quad (5)$$

where the summation is over all angles.

The OPCM images at the image plane are calculated by adding up the scattered and the reference beam at any desired phase offset Ψ :

$$I = \text{abs}(E_{x-D} + aE_{x-R} \exp(i\Psi))^2 + \text{abs}(E_{y-D} + aE_{y-R} \exp(i\Psi))^2 + \text{abs}(E_{z-D} + aE_{z-R} \exp(i\Psi))^2. \quad (6)$$

The coefficient a and the phase Ψ correspond to the ability of the OPCM to adjust the relative amplitudes and the phase difference between the two beams. In all simulation results presented in this article, $a = 1$ and Ψ is used as parameter.

4. CELL STRUCTURE, GOLD NANOPARTICLE MODEL AND SIMULATION RESULTS

4.1. Cell structure

The cell is modeled as a dielectric sphere with a realistic radius $R_c = 5 \mu\text{m}$. It is critically important to pay special attention to the membrane model since assigning the membrane the precisely desired thickness value leads to inadequate modeling of optical immersion experiments. This is due to the fact that the FDTD technique averages out the refractive index values at the interface of two different materials effectively reducing the membrane thickness value and eventually, due to the staircase approximation error, destroying the continuity of the membrane. This is the reason for us to select a membrane thickness $d = 20 \text{ nm}$ which corresponds to effective thickness of approximately 10 nm . The cell nucleus is also spherical with a radius $R_n = 1.5 \mu\text{m}$ centered at a position which is $2.0 \mu\text{m}$ shifted from the cell center in a direction perpendicular to the direction of light propagation. The refractive index of the cytoplasm is $n_{\text{cyto}} = 1.36$, of the nucleus $n_{\text{nuc}} = 1.4$, of the membrane $n_{\text{mem}} = 1.47$, and of the extracellular material $n_{\text{ext}} = 1.33$ (no refractive index matching) or 1.36 (refractive index matching).

4.2. Optical properties of gold nanoparticles

Gold NPs exhibit the ability to resonantly scatter visible and near infrared light due to the excitation of surface plasmon resonances (SPRs). The scattering ability is extremely sensitive to their size, shape, and aggregation state offering a great potential for optical cellular imaging and detection labeling studies [15–19]. Our FDTD approach uses the dispersion model for gold derived from the experimental data provided by Johnson and Christy [7, 20] where the total, complex-valued permittivity is given as

$$\varepsilon(\omega) = \varepsilon_{\text{REAL}} + \varepsilon_L(\omega) + \varepsilon_P(\omega). \quad (7)$$

Each of the three contributions to the permittivity arises from a different material model. The first term represents the contribution due to the basic, background permittivity.

The second and third terms represent Lorentz and plasma contributions:

$$\varepsilon_L(\omega) = \frac{\varepsilon_{\text{LORENTZ}} \omega_0^2}{\omega_0^2 - 2i\delta_0\omega - \omega^2}, \quad (8)$$

$$\varepsilon_P(\omega) = \frac{\omega_p^2}{i\omega\nu_C + \omega^2},$$

where all material constants are summarized in Table 1.

We have modeled two different cases—resonant and nonresonant. The ability to model both these cases together with the effect of optical clearing effect provides the opportunity to numerically study the possibility for imaging of the uptake of clusters of NPs—a scenario which, to the best of our knowledge, was not studied before. We used the FDTD technique to calculate the scattering and absorption cross-sections over a 400–900 nm wavelength range for a single 50 nm diameter gold NP immersed in a material having the properties of the cytoplasm ($n = 1.36$) and resolution $dx = dy = dz = 10 \text{ nm}$. The scattering cross-section is defined as

$$\sigma_{\text{scat}} = \frac{P_{\text{scat}}(\omega)}{I_{\text{inc}}(\omega)}, \quad (9)$$

where P_{scat} is the total scattered power and I_{inc} is the intensity of the incident light in (W/m^2). It was calculated by applying the total field/scattered field FDTD formulation [13] and by creating 12 field power monitoring planes around the nanoparticle in the form of a box: 6 in the total field region and 6 in the scattered field region. The total scattered power is calculated by summing up the power flowing outward through 6 scattered field power monitors located in the scattered field region.

The absorption cross-section is similarly defined as

$$\sigma_{\text{abs}} = \frac{P_{\text{abs}}(\omega)}{I_{\text{inc}}(\omega)}, \quad (10)$$

where P_{abs} is the total power absorbed by the particle. The power absorbed by the particle is calculated by calculating the net power flowing inward through the 6 total field power monitors located in the total field region. The extinction cross-section is the sum of the absorption and scattering cross-sections

$$\sigma_{\text{ext}} = \sigma_{\text{scat}} + \sigma_{\text{abs}}. \quad (11)$$

Figure 4 shows that the extinction cross-section has a maximum of 3.89 at around 543.0 nm corresponding to one of the radiation wavelengths of He-Ne lasers. In this article, we also present results for $\lambda = 676.4 \text{ nm}$ (a Krypton laser wavelength) which corresponds to the nonresonant case (extinction cross-section value 0.322, ~ 12 times smaller than 3.89). The FDTD results are compared with the theoretical curve calculated by Mie theory. The main reason for the slight discrepancy between the theoretical and FDTD results for the extinction cross-section is the finite mesh size.

To consistency of the results could be improved by reducing the mesh size. In the FDTD simulations including both the cell and the nanoparticles, the numerical resolution

TABLE 1: Optical material constants of gold [20].

Background permittivity	Lorentz dispersion	Plasma dispersion
$\epsilon_{\text{REAL}} = 7.077$	$\epsilon_{\text{LORENTZ}} = 2.323$	$\omega_p = 1.391 \times 10^{16}$ Hz
	$\omega_0 = 4.635 \times 10^{15}$ Hz	$\nu_c = 1.411 \times 10^7$ Hz
	$\delta_0 = 9.267 \times 10^{14}$ Hz	

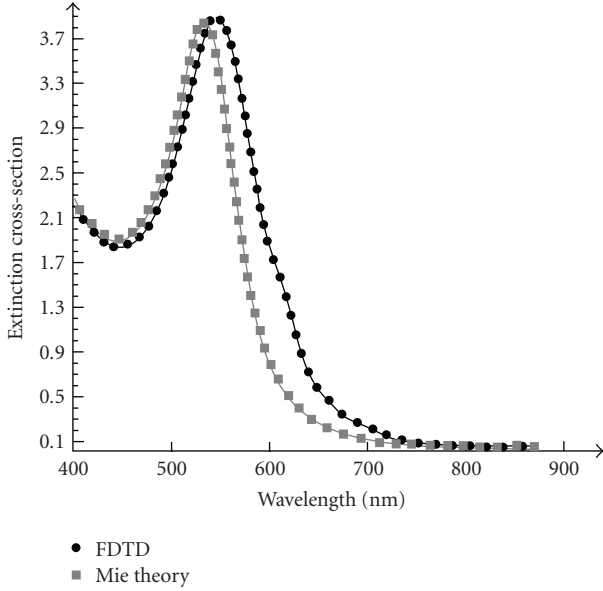


FIGURE 4: Extinction cross-section of a 50 nm gold nanoparticle immersed in material having the optical properties of the cytoplasm: $n = 1.36$. The optical properties of gold are described by (7) and (8) and the parameters given in Table 1.

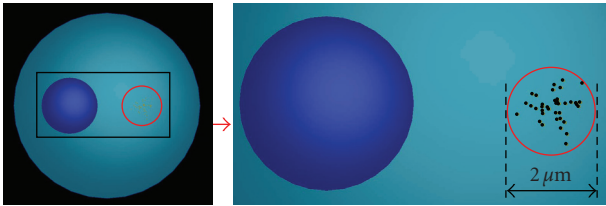


FIGURE 5: A cluster of 42 gold nanoparticles randomly distributed in a spatial sphere with a radius of $1 \mu\text{m}$ at a cell location opposite to the location of the nucleus ($x = 2 \mu\text{m}$, $y = 0$, $z = 0$). The nucleus is located at $x = -2 \mu\text{m}$. The gold nanoparticle size (diameter = 50 nm) on right-hand graph is slightly exaggerated.

of the nanoparticles was hard-coded to $dx = dy = dz = 10$ nm to make sure that their numerically manifested optical resonant properties will be the same as the ones shown in Figure 4. However, Figure 5 visualizes the positioning of a cluster of 42 nanoparticles in the cytoplasm that was used to produce the FDTD simulation results presented in Section 5. It was randomly generated without controlling the possibility for spatial overlaps or contacts between the nanoparticles.

The closer visual inspection showed that there were no such overlaps and contacts.

4.3. OPCM image simulation results

The simulation results presented here are based on the 3D FDTD OPCM model. The simulations use nonuniform meshing where the number of mesh points in space is automatically calculated to ensure a higher number of mesh points in materials with higher values of the refractive index [14]. The realistic cell dimensions (including both cell radius and membrane) require a very fine numerical resolution making the simulations computationally intensive. The locally refined resolution of the nanoparticles leads to additional requirements for the CPU time and memory (~ 120 Gbs RAM) requiring high performance computing resources. The time step used during the simulation was defined by means of a factor of 0.99 in the Courant stability limit: $c\Delta t = 0.99 \times (1/\Delta x^2 + 1/\Delta y^2 + 1/\Delta z^2)^{-1/2}$. The cell center is located in the middle ($x = y = z = 0$) of the computational domain with dimensions $15 \mu\text{m} \times 12 \mu\text{m} \times 15 \mu\text{m}$. The nucleus' center is located at $x = -2 \mu\text{m}$, $y = z = 0 \mu\text{m}$. The cluster of gold nanoparticles is located at $x = 2 \mu\text{m}$, $y = z = 0 \mu\text{m}$ (Figure 5).

The refractive index matching (RIM) between the cytoplasm and the extracellular medium leads to the optical clearing of the image and a significantly better OPCM image of the nucleus and of the membrane—the only sources of phase contrast at optical immersion conditions. Based on the fact that RIM enhances significantly the imaging of the cell components, we have used the FDTD OPCM model to create the OPCM images of the same cell at optical immersion conditions including the cluster of 42 gold NPs (Figure 5, see also Figure 1(b)) and for different phase offsets between the reference beam and the scattered beam (assuming $a = 1$). The insertion of the nanoparticles increases significantly the CPU and memory requirements. The dimensions of the computational domain are $15 \mu\text{m} \times 15 \mu\text{m} \times 12 \mu\text{m}$. The OPCM images in Figure 6 show that the gold NP cluster can be clearly identified at both the nonresonant ($\lambda = 676.4$ nm) and resonant ($\lambda = 543.0$ nm) wavelengths.

The graphs in Figure 7 compare the geometrical cross-sections of the three OPCM images shown at the bottom of Figure 6 at $y = 0 \mu\text{m}$ showing the relevant half of the images (right) where the gold NP cluster is located. At resonance, the optical contrast of the gold NP peak is ~ 2.24 times larger than the one at no resonance and 24.79 times larger than the background optical contrast corresponding to the case when there are no nanoparticles. The enhanced imaging of

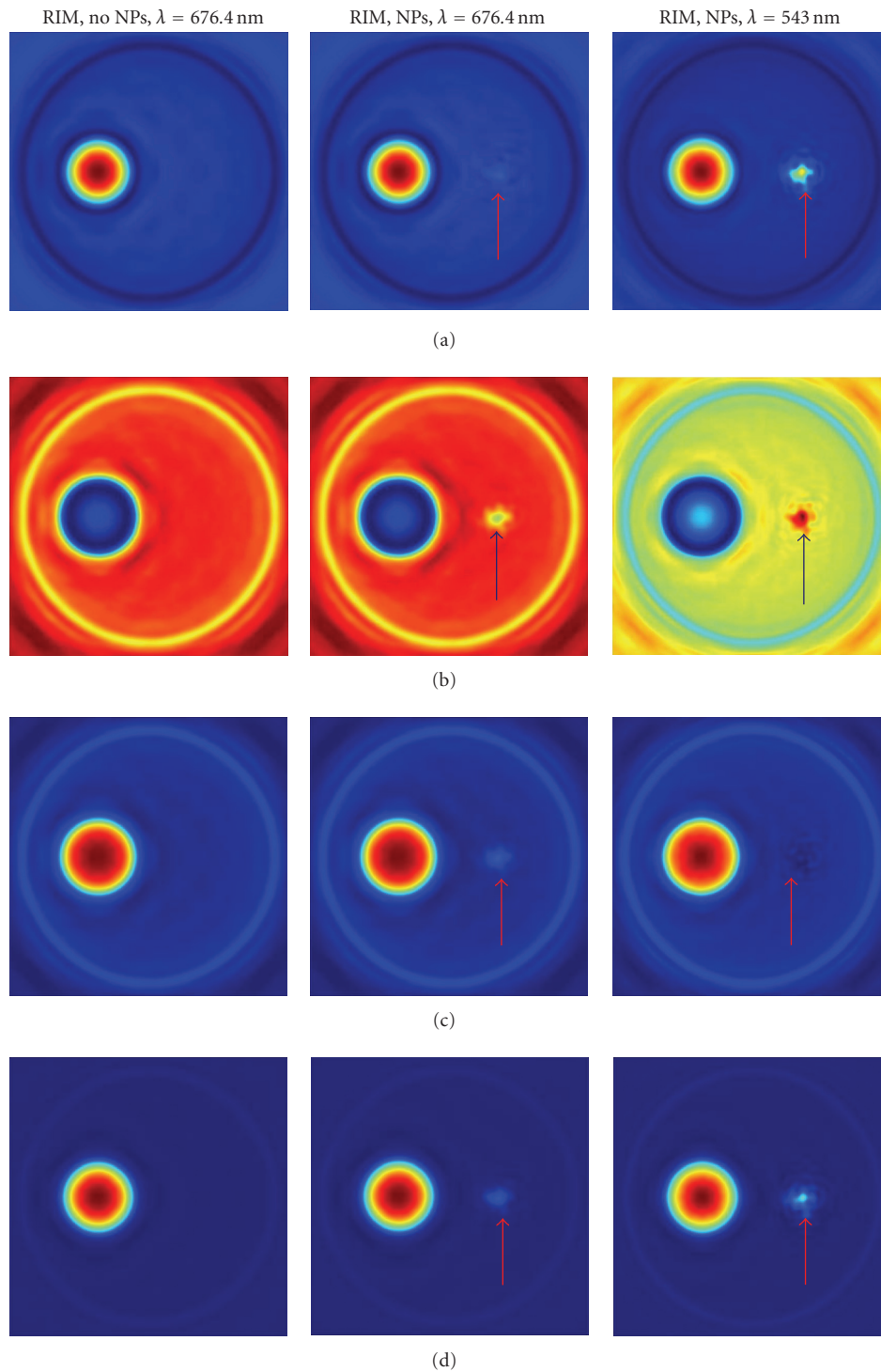


FIGURE 6: OPCM images of a biological cell for different values (a: -150° , b: -90° , c: 90° , d: 180°) of the phase offset between the reference and diffracted beam of the OPCM at optical immersion conditions (left) including a cluster of 42 gold NPs (middle: no resonance, right: at resonance) located in a position symmetrically opposite to the nucleus. The arrows indicate the position of the gold NP cluster.

the gold NP cluster at resonant conditions is of no surprise. It, however, needs to be further studied as a function of particular phase delay Ψ between the reference beam and the scattered beam. Figure 8 visualizes the optical contrast due to the gold nanoparticle cluster as a function of the phase offsets

between the reference (R) and the diffracted (D) beams of the optical phase microscope. It shows that the enhancement of the optical contrast due to the nanoparticle resonance changes significantly from a minimum of 0.0 ($\Psi = 0^\circ$) to a maximum of 3.60 ($\Psi = -150^\circ$).

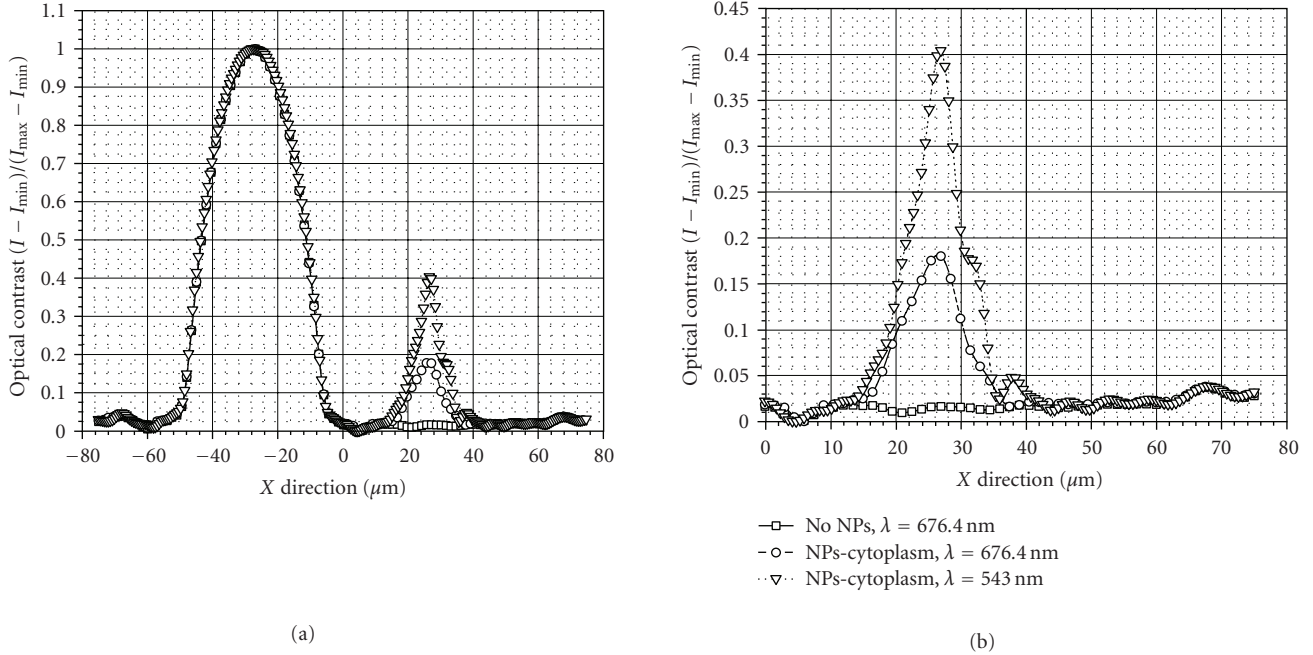


FIGURE 7: Comparison of the geometrical cross sections at $y = 0 \mu\text{m}$ of the three OPCM images corresponding to 180° phase delay between the reference and the diffracted beam (bottom row in Figure 6) in terms of optical contrast. The right-hand side graph illustrates the optical contrast enhancement due to the effect of the gold NP resonance at $\lambda = 543$ nm.

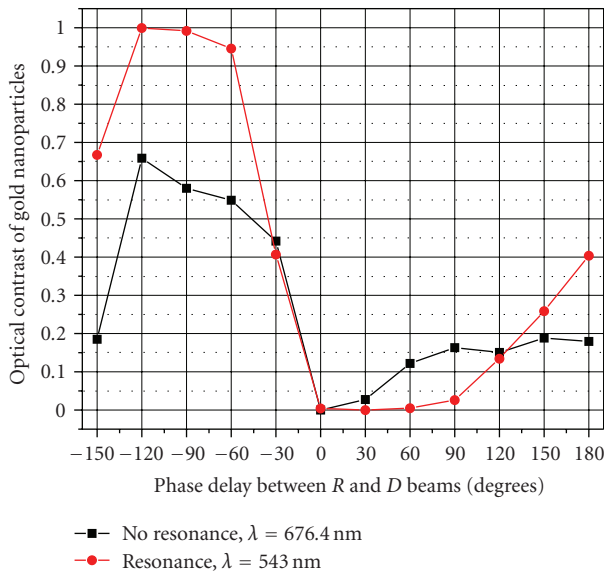


FIGURE 8: Optical contrast due to the gold nanoparticle cluster as a function of the phase offsets between the reference (R) and the diffracted (D) beams of the optical phase microscope.

The correct modeling of the gold NPs required making sure that the FDTD resolution is the same as in the calculation of their optical scattering/absorption properties, that is, $dx = dy = dz = 10$ nm. This was done by using the built-in features of our FDTD simulation software [14] enabling the possibility for using both nonuniform meshing

in the entire computational domain and local hard coding of the resolution of the NPs. The results presented in Figures 6–8 clearly demonstrate the capability of the proposed FDTD OPCM approach to model the visual effect of gold NPs at nonresonant and resonant conditions. A future extension of this research will be to study the capability of the model to provide valuable insights for the application of gold NPs in optical nanotherapeutics.

5. CONCLUSIONS

In this article, we provided simulation results on the application of the FDTD approach to the modeling of the OPCM imaging of gold NPs in single biological cells. We have first reproduced the effect of optical immersion on the OPCM images of a realistic size cell containing a cytoplasm, a nucleus, and a membrane. The model was then extended to include the presence of a cluster of gold NPs in the cytoplasm at optical immersion conditions as well as the enhancing imaging effect of the optical resonance of the nanoparticles. The results do not allow analyzing the scaling of the NP imaging effect as a function of the number of the NPs in the cluster. However, the validation of the model provides a basis for future studies of OPCM nanobioimaging including the effects of NP cluster size, NP size and number, as well as average dimension between the NPs. To the best of our knowledge, this is the first time that FDTD simulation results were post-processed in a way providing realistic OPCM images of biological cells including a cluster of gold NPs. The results demonstrate the potential of the FDTD approach to model advanced optical nanobioimaging instruments.

ACKNOWLEDGMENTS

S. Tanev, J. Pond, and P. Paddon acknowledge the use of the computing resources of WestGrid (Western Canada Research Grid)—a \$50-million project to operate grid-enabled high performance computing and collaboration infrastructure at institutions across Canada. V. V. Tuchin was supported by grants of Federal Agency of Education of RF no. 1.4.06, RNP.2.1.1.4473, RFBR no. 06-02-16740, and Photonics4Life of FP7. The authors are thankful to Dr. Vladimir P. Zharov for the initial discussion on the relevance of the problem of nanoparticle clustering in single cells.

REFERENCES

- [1] P. N. Prasad, *Introduction to Biophotonics*, chapter 7, John Wiley & Sons, New York, NY, USA, 2003.
- [2] V. V. Tuchin, *Tissue Optics: Light Scattering Methods and Instruments for Medical Diagnosis*, vol. 166 of *Press Monograph Series*, SPIE Press, Bellingham, Wash, USA, 2nd edition, 2007.
- [3] F. M. Kahnert, “Numerical methods in electromagnetic scattering theory,” *Journal of Quantitative Spectroscopy and Radiative Transfer*, vol. 79–80, pp. 775–824, 2003.
- [4] R. Drezek, A. Dunn, and R. Richards-Kortum, “A pulsed finite-difference time-domain (FDTD) method for calculating light scattering from biological cells over broad wavelength ranges,” *Optics Express*, vol. 6, no. 7, pp. 147–157, 2000.
- [5] T. Tanifuji and M. Hijikata, “Finite difference time domain (FDTD) analysis of optical pulse responses in biological tissues for spectroscopic diffused optical tomography,” *IEEE Transactions on Medical Imaging*, vol. 21, no. 2, pp. 181–184, 2002.
- [6] R. Drezek, M. Guillaud, T. Collier, et al., “Light scattering from cervical cells throughout neoplastic progression: influence of nuclear morphology, DNA content, and chromatin texture,” *Journal of Biomedical Optics*, vol. 8, no. 1, pp. 7–16, 2003.
- [7] S. Tanev, V. V. Tuchin, and P. Paddon, “Light scattering effects of gold nanoparticles in cells: FDTD modeling,” *Laser Physics Letters*, vol. 3, no. 12, pp. 594–598, 2006.
- [8] S. Tanev, V. V. Tuchin, and P. Paddon, “Cell membrane and gold nanoparticles effects on optical immersion experiments with noncancerous and cancerous cells: finite-difference time-domain modelling,” *Journal of Biomedical Optics*, vol. 11, no. 6, Article ID 064037, 6 pages, 2006.
- [9] X. Li, A. Taflove, and V. Backman, “Recent progress in exact and reduced-order modeling of light-scattering properties of complex structures,” *IEEE Journal on Selected Topics in Quantum Electronics*, vol. 11, no. 4, pp. 759–765, 2005.
- [10] R. Barer, K. F. A. Ross, and S. Tkaczyk, “Refractometry of living cells,” *Nature*, vol. 171, no. 4356, pp. 720–724, 1953.
- [11] B. A. Fikhman, “Microbiological refractometry,” *Medicine*, pp. 81–94, 1967 (Russian).
- [12] V. V. Tuchin, *Optical Clearing of Tissues and Blood*, vol. 154 of *Press Monograph Series*, SPIE Press, Bellingham, Wash, USA, 2005.
- [13] A. Taflove and S. Hagness, *Computational Electrodynamics: The Finite-Difference Time Domain Method*, Artech House, Boston, Mass, USA, 3rd edition, 2005.
- [14] The simulations were performed by the FDTD Solutions™ software developed by Lumerical Solutions Inc., Vancouver, BC, Canada, <http://www.lumerical.com>.
- [15] K. Sokolov, M. Follen, J. Aaron, et al., “Real-time vital optical imaging of precancer using anti-epidermal growth factor receptor antibodies conjugated to gold nanoparticles,” *Cancer Research*, vol. 63, no. 9, pp. 1999–2004, 2003.
- [16] I. H. El-Sayed, X. Huang, and M. A. El-Sayed, “Surface plasmon resonance scattering and absorption of anti-EGFR antibody conjugated gold nanoparticles in cancer diagnostics: applications in oral cancer,” *Nano Letters*, vol. 5, no. 5, pp. 829–834, 2005.
- [17] N. G. Khlebtsov, A. G. Melnikov, L. A. Dykman, and V. A. Bogatyrev, “Optical properties and biomedical applications of nanostructures based on gold and silver bioconjugates,” in *Photopolarimetry in Remote Sensing*, G. Videen, Ya. S. Yatskiy, and M. I. Mishchenko, Eds., vol. 161 of *NATO Science Series II: Mathematics, Physics and Chemistry*, pp. 265–308, Kluwer Academic Publishers, Dordrecht, The Netherlands, 2004.
- [18] V. P. Zharov, J.-W. Kim, D. T. Curiel, and M. Everts, “Self-assembling nanoclusters in living systems: application for integrated photothermal nanodiagnostics and nanotherapy,” *Nanomedicine: Nanotechnology, Biology and Medicine*, vol. 1, no. 4, pp. 326–345, 2005.
- [19] V. P. Zharov, K. E. Mercer, E. N. Galitovskaya, and M. S. Smeltzer, “Photothermal nanotherapeutics and nanodiagnostics for selective killing of bacteria targeted with gold nanoparticles,” *Biophysical Journal*, vol. 90, no. 2, pp. 619–627, 2006.
- [20] P. B. Johnson and R. W. Christy, “Optical constants of the noble metals,” *Physical Review B*, vol. 6, no. 12, pp. 4370–4379, 1972.